

**NASA CONTRACTOR
REPORT**

NASA CR-1790



NASA CR-17

NASA
CR
1529
v.2
c.1



**LOAN COPY RETURN
AFWL (DOGL)
KIRTLAND AFB, N. M.**

**STUDY OF 30 KM TO 200 KM
METEOROLOGICAL ROCKET
SOUNDING SYSTEMS**

Volume II - Recent Advancements

by Bruce Bollermann

Prepared by

SPACE DATA CORPORATION

Phoenix, Ariz. 85034

for George C. Marshall Space Flight Center



0060714

1. Report No. NASA CR-1790	2. Government Accession No.	3. Recipient's Catalog No.	
4. Title and Subtitle STUDY OF 30 KM to 200 KM METEOROLOGICAL ROCKET SOUNDING SYSTEMS (VOLUME II - RECENT ADVANCEMENTS)		5. Report Date May 1971	6. Performing Organization Code
		8. Performing Organization Report No.	
7. Author(s) Bruce Bollermann		10. Work Unit No.	
9. Performing Organization Name and Address Space Data Corporation 1331 South 26th Street Phoenix, Arizona 85034		11. Contract or Grant No. NAS8-24386	
		13. Type of Report and Period Covered Contractor Report	
12. Sponsoring Agency Name and Address National Aeronautics and Space Administration Washington, D. C. 20546		14. Sponsoring Agency Code 160-44-58	
		15. Supplementary Notes Contract Monitor: Mr. R. E. Turner, Aerospace Environment Division, Aero-Astroynamics Laboratory, Marshall Space Flight Center, Alabama.	
16. Abstract There have been a number of recent significant advances in the technology of 30 km to 200 km meteorological sounding systems. Rocketsonde temperature measurements have been improved and now show excellent agreement with conjunctive rawinsonde data. The passive falling-sphere density measurements are being improved by means of computer program advances, and the drag coefficient data are being refined by means of experiments and further theoretical investigations. Larger Starutes have been developed along with lighter telemetry packages to reduce the rocketsonde descent velocities to a ballistic coefficient on the order of 0.016 lb/ft ² . Further experimental investigations have been conducted for the Stokes flow decelerator. The AN/GMD-4 telemetry system has been successfully used to supply complete tracking data for transponder rocketsondes. A transponder instrument has been successfully flown with the Super Loki vehicle in a large diameter Dart to an altitude of over 75 km. Development efforts have continued for the Army RDT&E rocket. The Astrobee D vehicle has been successfully flown with heavy payloads. Improved accuracy in the density measurements above 60 km appears to be the most critical problem in the meteorological rocket field today. To improve the precision of the passive falling-sphere density measurements and eliminate the drag coefficient and vertical wind problems, a low-cost pitot probe system is proposed. This system employs small Super Loki rocket motors in a low-cost two-stage vehicle configuration and AN/GMD-2 telemetry and tracking instrumentation for data acquisition. A vibrating diaphragm pressure transducer is proposed as the sensor to measure ram impact pressure at the nose of the rapidly ascending vehicle from 50 km to 120 km altitudes.			
17. Key Words (Suggested by Author(s)) Rockets, Temperature, Pressure, Density, Sensors, Winds, Radars, Telemetering		18. Distribution Statement Unclassified - Unlimited	
19. Security Classif. (of this report) Unclassified	20. Security Classif. (of this page) Unclassified	21. No. of Pages 241	22. Price* \$3.00

FOREWORD

This study was made under Contract NAS8-24386 with the Aerospace Environment Division, Aero-Astroynamics Laboratory, Marshall Space Flight Center. Mr. Robert E. Turner was the Contract Monitor. Volume II, Recent Advancements, is a continuation of the study effort which resulted in Volume I, Literature and Data Review, published as NASA-CR-1529 Parts 1 and 2. Volume II presents a study of the recent advancements in rocket meteorology together with a design study for a pitot probe density measurement system.

ACKNOWLEDGEMENTS

Special recognition is expressed to the Meteorological Working Group of the Inter-Range Instrumentation Group, Range Commander's Conference, whose efforts brought about the formation of the Meteorological Rocket Network, and consequently the widespread distribution of its valuable data to the scientific community. The Network has grown worldwide, and has directly influenced developments in rocket meteorology.

Appreciation is expressed to Mr. Robert E. Turner and Mr. O. E. Smith of the Aerospace Environment Division, Aero-Astroynamics Laboratory, NASA-Marshall Space Flight Center for their support and guidance in presenting this study.

TABLE OF CONTENTS

	<u>Page</u>
FOREWORD	iii
ACKNOWLEDGEMENTS	iii
1. INTRODUCTION	1
2. RECENT SENSOR ADVANCEMENTS	2
2.1 General	2
2.2 Rocketsonde Temperature Measurements	2
2.3 Rocketsonde One-Point Pressure Switch	12
2.4 Passive Falling-Sphere Density Sensors	22
2.5 Sandia Pitot-Static Probe	48
2.6 Gamma-Ray-Backscatter Technique for Density Measurement	54
2.7 Bremsstrahlung X-Ray Technique for Density Measurement	59
2.8 Radio Frequency Mass Spectrometers	61
2.9 Ultraviolet Filter Rocket Ozonesonde	69
3. RECENT DECELERATOR ADVANCES	79
3.1 General	79
3.2 Ram-Air Decelerators	79
3.3 Stokes Flow Decelerators	81
3.4 Ringsail, Disk Gap Band, Cross Parachute Evaluations	85
4. RECENT TELEMETRY ADVANCES	88
4.1 General	88
4.2 AN/GMD-4 Telemetry and Tracking Systems	88
4.3 Tone Range/Interferometer Telemetry Tracking Systems	89
4.4 Loran C Radiosonde Tracking System	101
4.5 Micro-Miniature Voltage Controlled Oscillator	102

5.	RECENT ROCKET VEHICLE ADVANCEMENTS	104
5.1	General	104
5.2	Super Loki	104
5.3	Army RDT and E Rocket	104
5.4	Astrobee D	104
6.	PITOT PROBE DESIGN STUDY	107
6.1	General	107
6.2	Introduction	110
6.3	Requirements	111
6.4	Pitot Probe Sensor	122
6.5	Tracking and Telemetry Instrumentation	156
6.6	Vehicle Design	171
6.7	System Performance	192
6.8	Inflatable Sphere Sensor	208
6.9	System Operation	210
	REFERENCES	211

LIST OF FIGURES

<u>Figure</u>		<u>Page</u>
2.1	Thermal Entry Length Coefficient (after Hanks 1963)	5
2.2	Thermal Entry for 1 cm Diameter Shield	6
2.3	Thermal Entry for 10 cm Diameter Shield	6
2.4	View Half-Angle θ of a Sensor Placed at Depth 5 in Shield of Diameter d	7
2.5	Cross Plots of Data from Tables VI and VII, Relating Limiting Values of Shield Diameter d, Altitude z, View Half- Angle θ , and Thermal Entry Length L_{eT} for Safety Factors α	7
2.6	Relative Effect of Aerodynamic Heating for Three Shapes	9
2.7	Comparison of Time Constant for Three Sensor Shapes	9
2.8	$T_T - T_E$ as a Function of Static Pressure ($\alpha = 0$)	13
2.9	Thermistor Recovery Factor as a Function of Knudsen Number ($\alpha = 0$)	14
2.10	$T_T - T_E$ as a Function of Angle of Attack for Various Total Pressures	15
2.11	Sample Response Time Trace and Results of the Response Time Tests	17
2.12	Hasp Pressure Switch Cross-Sectional View	20
2.13	Pressure Switch Operating Point Deviation in Millibars as a Function of Temperature (18 samples)	21
2.14	Effect of Mass Correction on Density in the Case of an Early Deflation	24
2.15	Error in Sphere Drag Coefficient Due to Distortion	26
2.16	Viper Robin Density Profile	27
2.17	Density Ratio Between 2 FPS-16 Radars Tracking the same Sphere	28
2.18	Acceleration and Velocity Curves for Two Spheres Released at 144 and 153 km over Kauai in May 1968	31
2.19	Robin Falling Sphere Aerodynamic Flow Conditions	32
2.20	Typical Trajectory of Free-Falling Spheres	33
2.21	Drag Coefficients of a Sphere	34
2.22	Sphere Drag Coefficients	36
2.23	Drag Coefficient of a Sphere in Supersonic Flow as a Function of the Free-Stream Reynolds Number	37
2.24	Drag Coefficient of a Sphere in Subsonic Flow as a Function of the Free-Stream Reynolds Number	37
2.25	Viper 8, 9 May 1969, Density Departures from 1966 Standard Atmosphere, July, 30°N	38
2.26	Viper 8, Comparison of Density Between Sphere and Rocketsonde	39
2.27	Robin Reduced Temperature Profile	41
2.28	Robin Reduced Temperature Profile - Two Radars	42

2.29	Density Profile, Apollo 11 Launch Support, ETR, Cape Kennedy, Florida, 14 July 1969	44
2.30	Density Error Resulting from Vertical Winds as a Function of Altitude - Escape Altitude, 125 km	46
2.31	Density Data, in Terms of Percent of Deviation from 1962 U. S. Standard Atmosphere, as Derived from Sphere and Grenade or Pitot-Tube Experiments Versus Altitude	47
2.32	Sketch of Cone-Cylinder Probe	49
2.33	Sketch of Sensor Element and Thermocouple Circuit Diagram	50
2.34	Schematic Drawing of Gamma Ray Backscatter Configuration for In-Flight Measurement of Atmospheric Density	55
2.35	Payload Of Nike-Apache Backscatter Density Sensor	56
2.36	Detected Counting Rate (Background Subtracted) and Density as a Function of Altitude for an Earth-Atmosphere Flight Test	57
2.37	Source Detector Sonde Geometry	60
2.38	System Operational Schematic	62
2.39	Schematic Diagram of Omegatron (RF Plates form End Caps to Shield Box which Surrounds Ionization Chamber)	65
2.40	Schematic Drawing of Gridded Spectrometer	66
2.41	Quadrupole Spectrometer	68
2.42	Block Diagram for Ozonesonde	71
2.43	Payload Assembly	72
2.44	Transmission Curves of Narrow-Band Filters	73
2.45	Photometer Signal During Ejection and Deployment Sequence	74
2.46	Intensity vs. Height Data	75
2.47	Ozone Concentration Measurement Precision vs. Height	76
2.48	Autumnal Ozone Distribution, Barking Sands Facility, Hawaii	77
3.1	Starute Descent Rates	80
3.2	Stokes-Flow Parachute Concepts	82
3.3	Ballistic Coefficients, b , for ARCAS and DART Payload Delivery Systems	83
3.4	Geometry of mesh, solidity 0.2 (Full Scale)	84
3.5	Parachute Configurations	86
3.6	Summary of Faired Drag Histories	87
4.1	Tone Range/Telemetry Interferometer Systems	93
4.2	Interferometer Geometry	96
4.3	Interferometer System - Simplified Block Diagram	96
4.4	Loran C Radiosonde System	103

5.1	Astrobee D - Thrust vs. Time	106
6.1	Pitot Probe Density Measuring System	109
6.2	Typical Atmospheric Density Measurement Accuracy Requirement	112
6.3	Normal Shock Wave	113
6.4	Pitot-Static Pressure Ratio for Supersonic Flow of Air ($\gamma = 1.4$)	116
6.5	Pitot Probe Sensor	123
6.6	Variation of Pressure Coefficient on a Hemisphere at $\alpha = 0$	124
6.7	Variation of Pressure Coefficient on a Hemisphere at $\alpha = 5^\circ$	126
6.8	Variation of Pressure Coefficient along Meridian Lines on a Hemisphere at $\alpha = 10^\circ$, $N \geq 15$	127
6.9	Variation of Pressure Coefficient along Meridian Lines on a Hemisphere at $\alpha = 15^\circ$	128
6.10	Physical Layout of Sensor Assembly	130
6.11	Simplified Sketch of the Original Embodiment	133
6.12	Principle of Operation	134
6.13	Transducer Assembly Details	142
6.14	Block Diagram for the Vibrating Diaphragm System	144
6.15	Vibrating Diaphragm Pressure Cell Electronics Systems	145
6.16	Performance Curves Obtained for Air, Corrected for Mechanical and Electrical Losses	147
6.17	Vibrating Diaphragm Transducer Rms Deviation from Standard Gage Techniques	148
6.18	Output Stability Shown as a Function of Pressure	150
6.19	Transducer Q plotted against Pressure	150
6.20	Time Constant Plotted Against Pressure	151
6.21	Pressure Calibration for a New Transducer Design	153
6.22	Typical Vacuum Calibration System	155
6.23	Telemetry Block Diagram	157
6.24	Voltage Controlled Blocking Oscillator Schematic	159
6.25	Modulator-Transmitter Schematic	160
6.26	Super-Regenerative Receiver and Tuned Amplifier Schematic	162
6.27	Antenna Schematic	163
6.28	Power Supply Schematic	165
6.29	Telemetry Module Assembly	166
6.30	Telemetry Module Subassemblies	167
6.31	Centrifugally Erected Antenna System	168
6.32	Ground Equipment Block Diagram	170
6.33	Two-Stage Super Loki Vehicle Configuration	172

6.34	Interstage Coupling Design	173
6.35	Super Loki Rocket Motor	176
6.36	Cross Section View of First Stage Super Loki Motor	177
6.37	Proposed Payload Design	178
6.38	Two-Stage Super Loki Drag Coefficients	182
6.39	Two-Stage Super Loki Pitot Probe Apogee Altitude vs. Interstage Coast Time	183
6.40	Two-Stage Super Loki Pitot Probe Impact Range vs. Interstage Coast Time	184
6.41	Two-Stage Super Loki Pitot Probe Altitude vs. Time	187
6.42	Two-Stage Super Loki Pitot Probe Altitude vs. Range	188
6.43	Two-Stage Super Loki Pitot Probe Altitude vs. Velocity	189
6.44	Two-Stage Super Loki Pitot Probe Altitude vs. Mach No.	190
6.45	Two-Stage Super Loki Pitot Probe Altitude vs. Altitude Parameters	191
6.46	Two-Stage Super Loki Pitot Probe Vehicle Static Stability Data	200
6.47	U.S. Standard Atmosphere, 1962, Density and Pressure vs. Altitude	201
6.48	U.S. Standard Atmosphere, 1962, Mean Free Path vs. Altitude	202
6.49	Two Stage Super Loki Pitot Probe Expected Ideal Impact Pressure vs. Altitude	206
6.50	Random Gage Error vs. Altitude for Pitot Probe Flight Conditions	209

LIST OF TABLES

<u>Table</u>		<u>Page</u>
2.1	Entry Length Coefficient, C , for Rarefied Flow	5
2.2	Numerical Results	11
2.3	Response Time Test Conditions and Results	16
2.4	Maximum Altitude of Satisfactory Radar Performance with a 66 cm Aluminized Sphere (University of Michigan, McWatters and Peterson)	29
2.5	Drag Coefficient Differences	35
2.6	Approximate Errors for Robin Using the AN/FPS-16 Radar and the "March 65" Data Reduction Program	45
2.7	Low-Density Corrections for Pitot Pressure Data	51
2.8	Error in Density Calculation with Assumed Static Pressure Errors	52
2.9	Static Pressure Measurement Parameters	52
2.10	Static Pressure Errors	53
2.11	Characteristics of RF Mass Spectrometer	63
2.12	Average Ozone Concentrations, atm-cm/km	78
4.1	Transponder Flight Analysis (Error Data)	90
4.2	Flight Analysis at 5 Kilometer Altitude Intervals	90
4.3	Summary of Error Contributions to Tone Ranging	98
4.4	Relative Design Precisions for Several Tracking Systems	99
4.5	Standard Deviation in X, Y, and Z Coordinates with Range Measurement Assumed Perfect	100
4.6	Comparative Direction Cosine Precision Granularity for TM Interferometer, FPS-16 and FPQ-6 Radars	100
6.1	Summary of Error Sources in Pitot-Tube Method	118
6.2	Transducer Measurements	152
6.3	Super Loki Rocket Motor Design Characteristics Summary	175
6.4	Two-Stage Super Loki Weight Breakdown	179
6.5	Super Loki Thrust and Propellant Weight vs. Time	180
6.6	Two-Stage Super Loki Drag Coefficient Data	181
6.7	Two-Stage Super Loki Pitot Probe Vehicle Performance Summary 85° QE Sea Level Launch with Various Interstage Coast Times	185
6.8	Two Degree of Freedom - Point Mass Simulation	193
6.9	Two Stage Super Loki Second Stage	197
6.10	Pitot Probe Density Measurement Parameters	204

INTRODUCTION

Routine meteorological rocket measurements today are being made with the Arcas and Loki rocketsondes to an altitude of 65 km and by the Viper Dart with a passive falling sphere payload to 100 km. So far other proven systems such as the active falling spheres, the pitot probe and the grenade experiments have been limited by high costs for both the vehicles and the payloads to a few soundings for research applications. Even the Arcas is being phased out for routine soundings by most agencies because of a significantly higher cost than the booster-dart systems. Consequently, most of the recent efforts within the past year have been to refine the rocketsonde temperature measurements and to determine the errors associated with the passive falling sphere technique. The literature over the past year reflects this interest.

Currently the most important requirement for meteorological rocket development appears to be for a density measurement system which is more accurate than the passive falling sphere. A relatively low cost pitot probe system is proposed to significantly improve the falling sphere density measurement. Such a system should find use in aerospace test support applications and perhaps in calibrating the inherently more economical passive falling sphere data. For these reasons a fairly detailed design study for a pitot probe system is reported in this volume.

2.

RECENT SENSOR ADVANCEMENTS

2.1 General.

Over the past year there have not been any significantly new meteorological sensors developed. The two major efforts which are reported in the literature are theoretical and experimental studies of the errors associated with the rocketsonde temperature measurement and the higher altitude passive falling sphere density measurement. A review of this work is presented in the following sections together with information on other sensor techniques of potential interest.

2.2 Rocketsonde Temperature Measurements.

Over the past year several papers concerning rocketsonde temperature measurements have been published. The salient features of these papers are presented in the following paragraphs. A rather complete background of the rocketsonde temperature measurement factors is presented in NASA-CR-1529 Part 1.

Disagreements between rocketsonde and conjunctive radiosonde temperatures in the overlap altitude region of about 25 km were investigated by the Navy at PMR in conjunction with Space Data Corporation. The report of this investigation is included as Appendix A. It was found that the rocketsonde temperatures were 3° C to 6° C too warm in the overlap region for rocketsonde sensors which had the bead thermistors pressed down into intimate contact with the mylar film mounting structure. Sensor configurations with the thermistors extended a short distance above the mylar film agreed quite well with the radiosonde data. The cause of the warm temperature biases for the depressed thermistor configurations has been attributed to albedo and instrument infrared radiation effects upon the mylar film. During nighttime this bias decreased to about 2° C, and this has been attributed to the instrument infrared heating of the film. Temperature oscillations found during the daytime flights of the depressed thermistor configurations disappear at night and were not found for the extended bead configurations. This effect has been attributed to the direct solar radiation heating of the film. The oscillations are created by the rotating descent system so that the sun is periodically blocked by the aluminized side film of the loop

mount as the sonde descends. The oscillation period was found to be correlated with the descent rate which would influence the induced spin of the decelerator. The oscillation amplitude was correlated with sun angle. Oscillation amplitudes were minimum at high solar elevation angles where the decelerator and sonde would block the sunlight, and at very low solar elevation angles where the incidence angle would be very small. Maximum temperature amplitudes were found during late morning and early afternoon flights where the sunlight incidence angle on the film at the sensor location was maximum. These oscillations disappear at night and were not evident in any of the data from the extended thermistor configurations. Although the obvious choice is to use the extended thermistor configuration for routine rocketsonde measurements, it may be advantageous to use the depressed configuration to extend the measurement ceiling above 60 km. The time constant of the film is about forty percent of the bead time constant, at an altitude of 60 km, and the film becomes more advantageous as altitude is increased. To take advantage of this faster response, however, the film in the sensor location must be screened from solar, albedo and instrument radiation heating. Methods of screening with thin-film mylar are currently under investigation.

A cylindrical radiation shield has been investigated theoretically by Staffanson, Alsaji and Fazzio at the University of Utah (reference 1) for the Arcasonde parallel-plate thin-film sensor mount. An expression was derived for the depth the sensor may be placed within the shield without incurring convective heat transfer between the shield and sensor. It was concluded that a 4-inch diameter shield should provide significant screening to 80 km. In the continuum flow regime, the entry length is given by

$$Le_T = 0.0288 d Re$$

where d = shield diameter

Re = Reynold's Number based upon d

In the rarefied flow region where

$$0.01 < \frac{M}{Re} \quad , \quad Re < 1$$

and

$$0.01 < \frac{M}{\sqrt{Re}} \quad , \quad Re > 1$$

$$Le_T = c d Re$$

where M = Mach Number

c = entry length coefficient

The entry length coefficient, c , for rarefied flow is a function of the Knudsen number, $Kn = \frac{\lambda}{d}$, as shown in Table 2.1 and Figure 2.1 where λ is the atmospheric mean free path and d is the shield diameter. As can be seen from the above expressions, deeper entry lengths are possible with larger diameter shields and the entry length decreases with increasing altitude of the rocketsonde. Examples of the dependence of entry length upon altitude for various decelerator ballistic coefficients M/A_{cr} are presented in Figures 2.2 and 2.3.

Since the above expressions represent a theoretical maximum entry length, a safety factor, α , should be introduced to allow for the thermal boundary layer perturbations under real conditions. When consideration is made of the radiation screening geometry, as shown in Figure 2.4, it follows that

$$s = \frac{d}{2 \tan \theta}$$

Let $s = \alpha L_e$

so that

$$\tan \theta = \frac{\mu}{2\rho} \cdot (\alpha C_d V)^{-1}$$

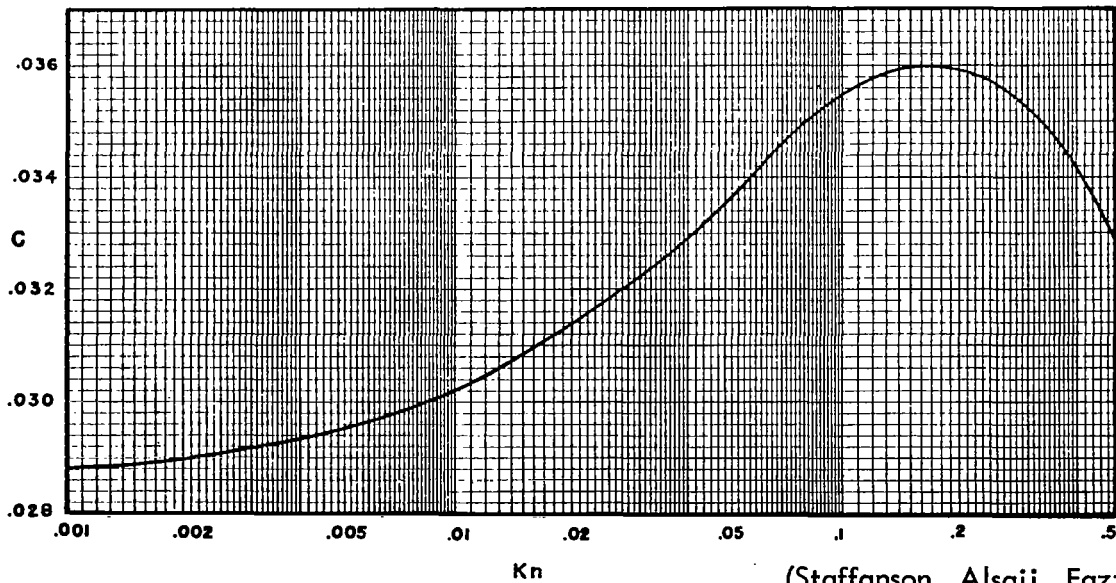
It is desired to minimize θ for maximum screening from incident radiation. From an inspection of the above expression it appears, that θ becomes smaller as d and C become larger. But C is a function of the Knudsen number which is inversely proportional to the shield diameter. Thus, there is an optimum shield diameter for a given altitude and descent velocity. As altitude increases, the entry length decreases. Limiting values of shield diameter, altitude, view half-angle and thermal entry length are plotted for several values of safety factor in Figure 2.5. The above discussion concerns shielding effects only for a cylindrical or tubular shape shield. Other geometries or shapes may offer significant advantages over that discussed above.

Staffanson (reference 2) has theoretically compared thermistor beads, wires and films as rocketsonde sensors. He finds that the thin-film mount rather than the thermistor bead dominates the performance of the sensor in the higher altitudes of operation where the bead tends to measure film temperature. Similarly the bead thermistor with long wires depends on the heat transfer properties of the wire at the higher altitudes. Generally, the time lag of a sensor is proportional to its volume-to-surface ratio and, therefore, to its thickness. Thinness is needed to minimize heat conduction along the structure and to improve response speed. In addition, sensor shape influences the air flow temperature rise, convective heat transfer and incoming radiation cross-section.

Table 2.1 Entry Length Coefficient, C , for Rarefied Flow

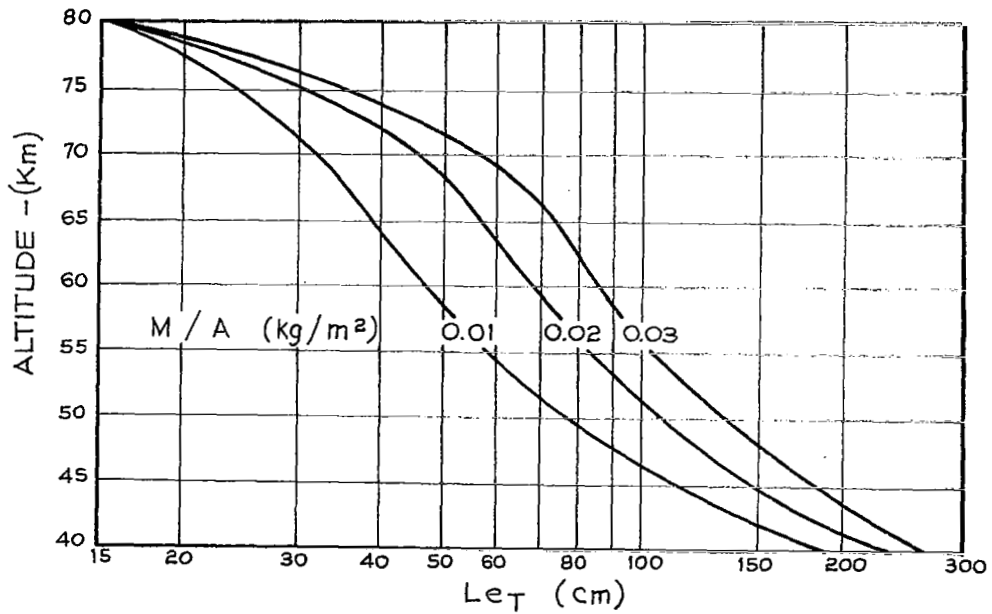
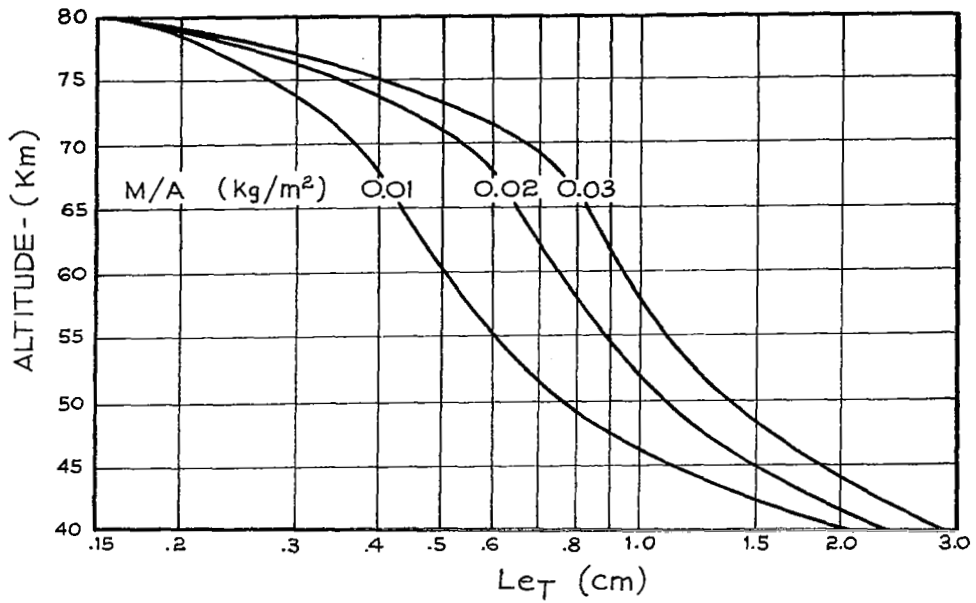
Kn	C
0	0.0288
0.00100	0.0288
0.00500	0.0295
0.0100	0.0302
0.0500	0.0335
0.0556	0.0338
0.0625	0.0342
0.0714	0.0346
0.0833	0.0350
0.100	0.0354
0.125	0.0358
0.1667	0.0360
0.250	0.0357
0.500	0.0329

(Staffanson, Alsaji, Fazzio)



(Staffanson, Alsaji, Fazzio)

Figure 2.1 Thermal Entry Length Coefficient (After Hanks 1963)



(Staffanson, Alsaji, Fazzio)

Figures 2.2 and 2.3 Thermal Entry for 1 cm (upper) and 10 cm (lower) Diameter Shields

Figure 2.4 View Half-Angle θ of a Sensor Placed at Depth S in Shield of Diameter d .

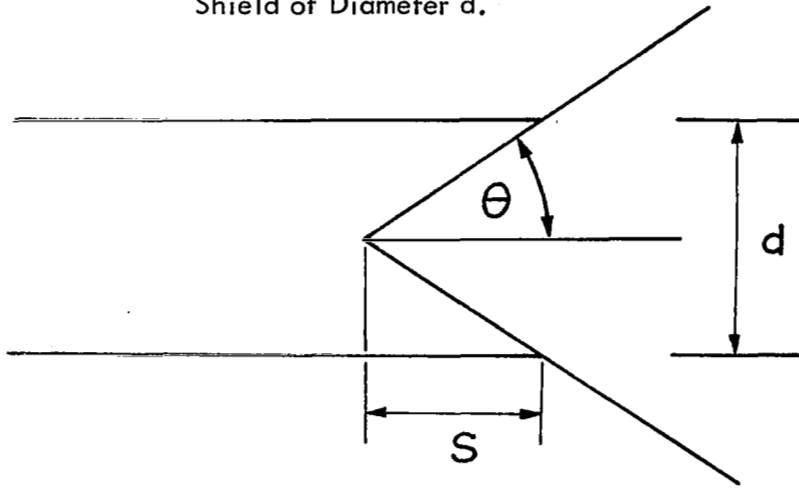
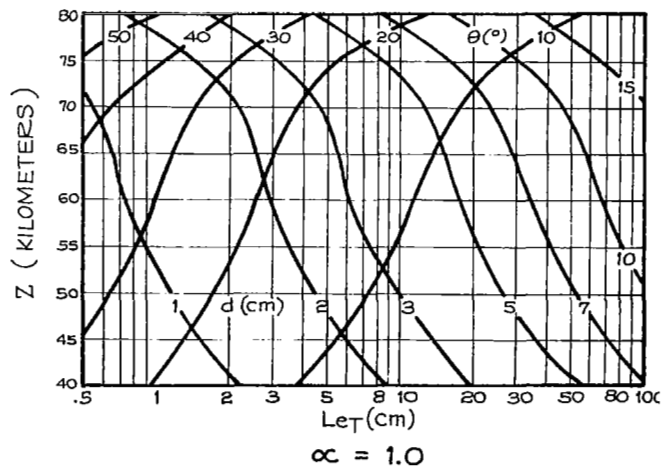
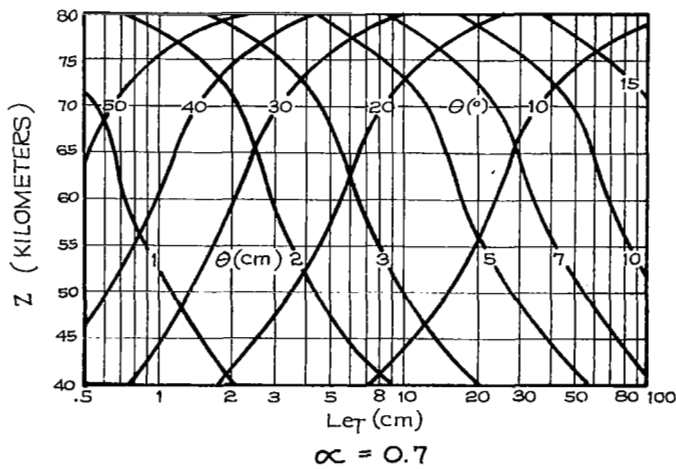
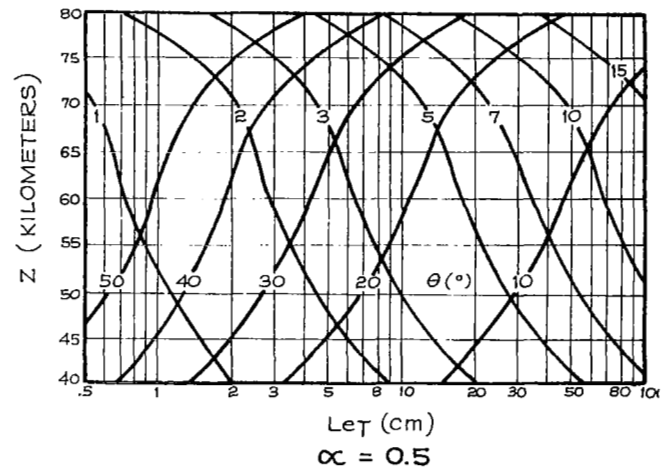
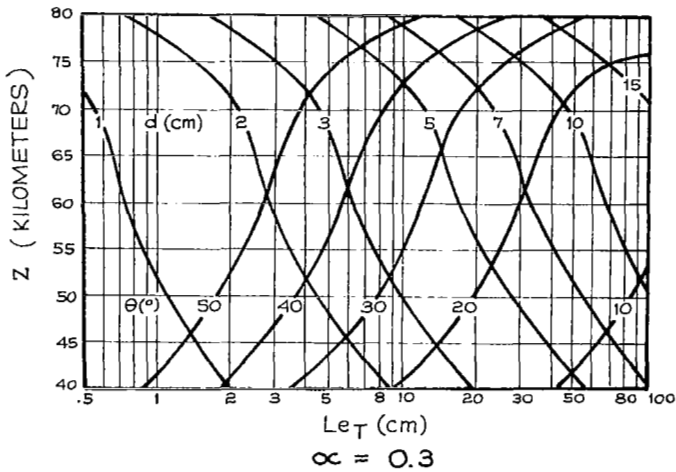


Figure 2.5 Cross plots of data from Tables VI and VII, relating limiting values of shield diameter d , altitude z , view half-angle θ , and thermal entry length Le_T for safety factors α .



(Staffanson, Alsaji, Fazzio)

The temperature rise in the air stream due to aerodynamic heating or viscous dissipation is given by

$$\Delta T = r \frac{V^2}{2 c_p}$$

where ΔT = air stream temperature rise

V^2 = sensor velocity

c_p = specific heat of air

r = recovery factor

The recovery factor depends upon the shape of the sensor and the flow regime. The effect of sensor shape is shown for a typical rocketsonde application in Figure 2.6. Since the error or uncertainty in aerodynamic heating can be expected to be proportional to the magnitude of the temperature rise, the plate geometry appears to be superior. This results from the larger plate dimension which keeps the plate in the continuum flow region to a higher altitude with a lower recovery factor value.

The sensor time constant is given by

$$\tau = \frac{(\rho c) (V/A)}{h + 4 \epsilon \sigma T_a^3}$$

where ρ = mass density
 c = specific heat
 V = sensor volume
 A = total sensor surface area
 h = convective heat transfer coefficient
 ϵ = emissivity
 σ = Boltzmann constant
 T_a = nominal temperature of sensor

which depends on sensor shape through the thickness parameter (V/A) and the convection coefficient h . The convection coefficient increases with decreasing body length until the body length becomes small relative to the molecular mean free path where it is independent of body length. At the higher altitudes the deterioration of the plate convection coefficient is not as rapid as those of the cylinder and sphere. The most important factor in the time constant is the thickness parameter or mass-to-surface area ratio. The thin-film flat plate is superior in this parameter. The effect of sensor shape on the thermal time constant is shown in Figure 2.7.

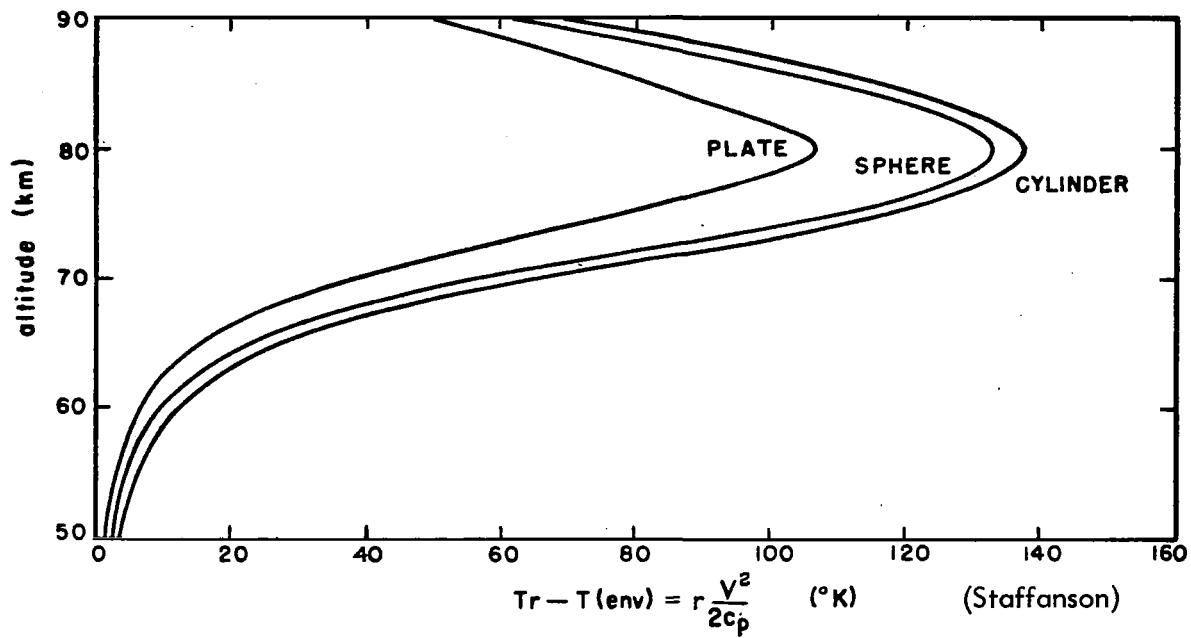


Figure 2.6 Relative Effect of Aerodynamic Heating for Three Shapes

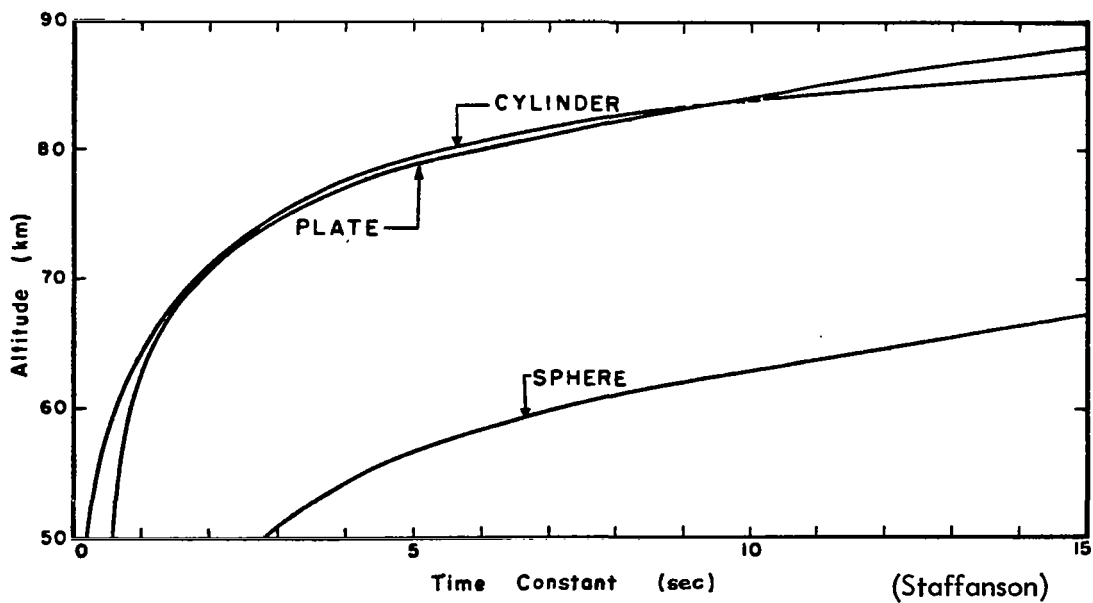


Figure 2.7 Comparison of Time Constant for Three Sensor Shapes

The equilibrium temperature is determined by competition between the convective and radiative heat transfer processes. The convective temperature is given by

$$T_r = T(\text{env}) + r \frac{V^2}{2 c_p} \quad \text{and}$$

the radiative temperature is given by

$$T_R = \frac{(q_r/A) + 3 \epsilon \sigma T_a^4}{4 \epsilon \sigma T_a^3}$$

where

T_r	=	recovery temperature
$T(\text{env})$		atmospheric temperature
q_r	=	radiation heat input

The sensor temperature lies between the above values according to the ratio

$$u = \frac{h}{4 \epsilon \sigma T_a^3}$$

and

$$T_e = \frac{u T_r + T_R}{u + 1}$$

where

u	=	$h/4 T_a^3$
T_e	=	equilibrium temperature ($T = 0$)
T_R	=	radiation temperature

The sensitivity to radiation is greatest in the plate geometry, although at the higher altitudes the superior convective heat transfer from the plate as compared to the sphere and cylinder tends to offset this effect. Although the direct radiation from the sun is a significant error source, an oscillating or rotating sonde would produce an oscillating temperature record with the minima representing temperature in absence of direct sunlight. This is providing the thermal time constant is sufficiently short. Direct radiation on the bead would lead to a bias.

Numerical results for typical bead, wire and film geometries are presented in Table 2.2.

Table 2.2 Numerical Results

Z(Km)		50	60	70	80	90
T(env)		271	256	220	181	181
V(m/sec)		60.9	121	291	444	300
L _f (cm)		0.22	0.22	0.35	0.66	0.87
h watt °K -m ²	b	63.8	24.4	7.72	2.17	.28
	w	91.8	26.9	8.89	2.51	.31
	f	24.9	14.6	5.98	1.60	.25
r	b	1.17	1.35	1.39	1.34	1.43
	w	1.66	1.68	1.54	1.39	1.51
	f	.86	.89	.92	.98	1.09
T _r - T(env) (°K)	b	2.16	9.84	58.9	133	64.2
	w	3.08	12.2	65.2	138	68.0
	f	1.60	6.44	39.0	97.2	48.8
τ (sec)	b	2.8	7.1	22.0	65	265
	w	.18	.62	1.8	5.5	29.3
	f	.46	.78	1.9	5.8	19
T _e (°K)	b	273	266	280	310	277
	w	274	269	286	315	277
	f	273	263	261	282	271
u	b	173	72	19.5	4.0	.77
	w	247	77	21.0	4.4	.80
	f	68	44	18.5	3.9	.69
(u + 1) ⁻¹	b	.0057	.014	.044	.20	.58
	w	.0040	.013	.045	.18	.56
	f	.0145	.022	.051	.20	.59
T _R (°K)	b	301	304	299	298	300
	w	301	303	299	299	300
	f	300	304	305	298	300

(Staffanson)

Wind tunnel calibrations were made by Haak and Noreen (reference 3) University of Minnesota for the Arcasonde thin-film flat plate temperature sensor configuration. Total temperature minus thermistor equilibrium temperature data at zero degrees angle-of-attack are presented in Figure 2.8 as a function of static pressure. The resulting recovery factors are plotted against the Knudsen number in Figure 2.9. It appears that the recovery factor is primarily a function of the Knudsen number. The effect of the angle-of-attack upon measured temperature is slight as shown in Figure 2.10. The thermal time constant, τ , is presented for various pressure levels and Mach Numbers in Table 2.3 and Figure 2.11.

Morrissey (reference 4) reports a possible bias between Arcasonde and radiosonde data at 25 mb (80,000 feet) where on the average the rocketsonde temperatures are warmer by 1.1°C . He reports that with the current systems a bias of $+2.4^{\circ}\text{C}$ would be incurred by raising the radiosonde tie-on point to the 10 mb (100,000 feet) level. These biases and 1.2°C temperature oscillations found in rocketsonde records can be reduced by employing longer thermistor leads on the rocketsondes and by correcting the radiosonde rod thermistor measurements for both solar and longwave radiation effects. Other experimenters have found larger errors due to the radiosonde altitude errors.

2.3 Rocketsonde One-Point Pressure Switch

Atmospheric density and pressure profiles are derived from rocketsonde temperature profiles by means of the ideal gas law and the hydrostatic equation. However, a base pressure and altitude must be used to initiate the calculations. Currently this base pressure and altitude are obtained from a conjunctive rawinsonde at an altitude level of about 25 km. Objections to the use of the rawinsonde data are the possible timewise and location differences between the rawinsonde and the rocketsonde measurements. The incorporation of a calibrated one-point pressure switch in the rocketsonde payload would overcome these objections. The problem is to obtain a reasonably economic pressure switch which is sufficiently accurate to replace the rawinsonde measurement.

PRESSURE ALTITUDE $\left(\begin{matrix} m \times 10^3 \\ ft \times 10^3 \end{matrix} \right)$

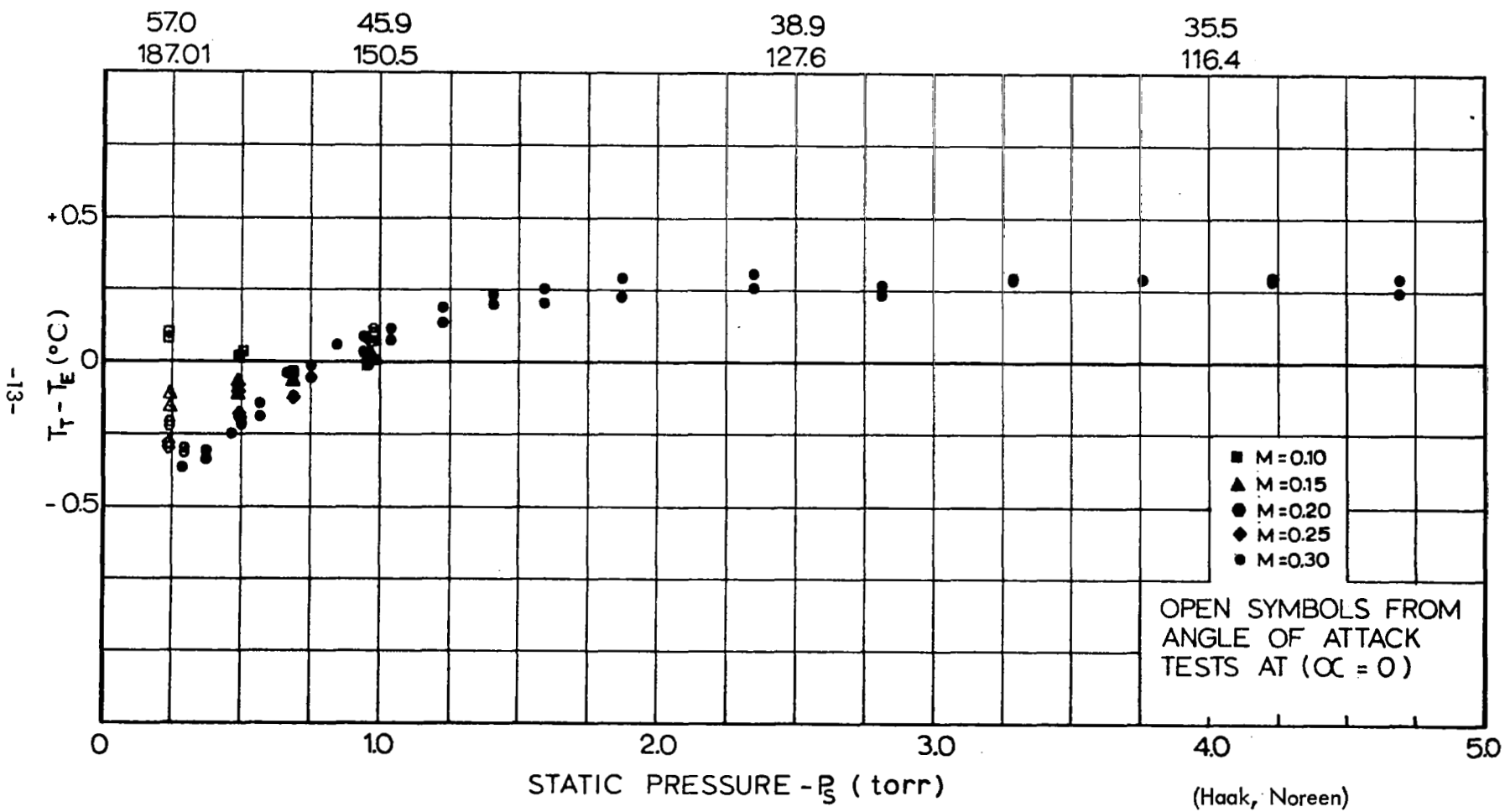
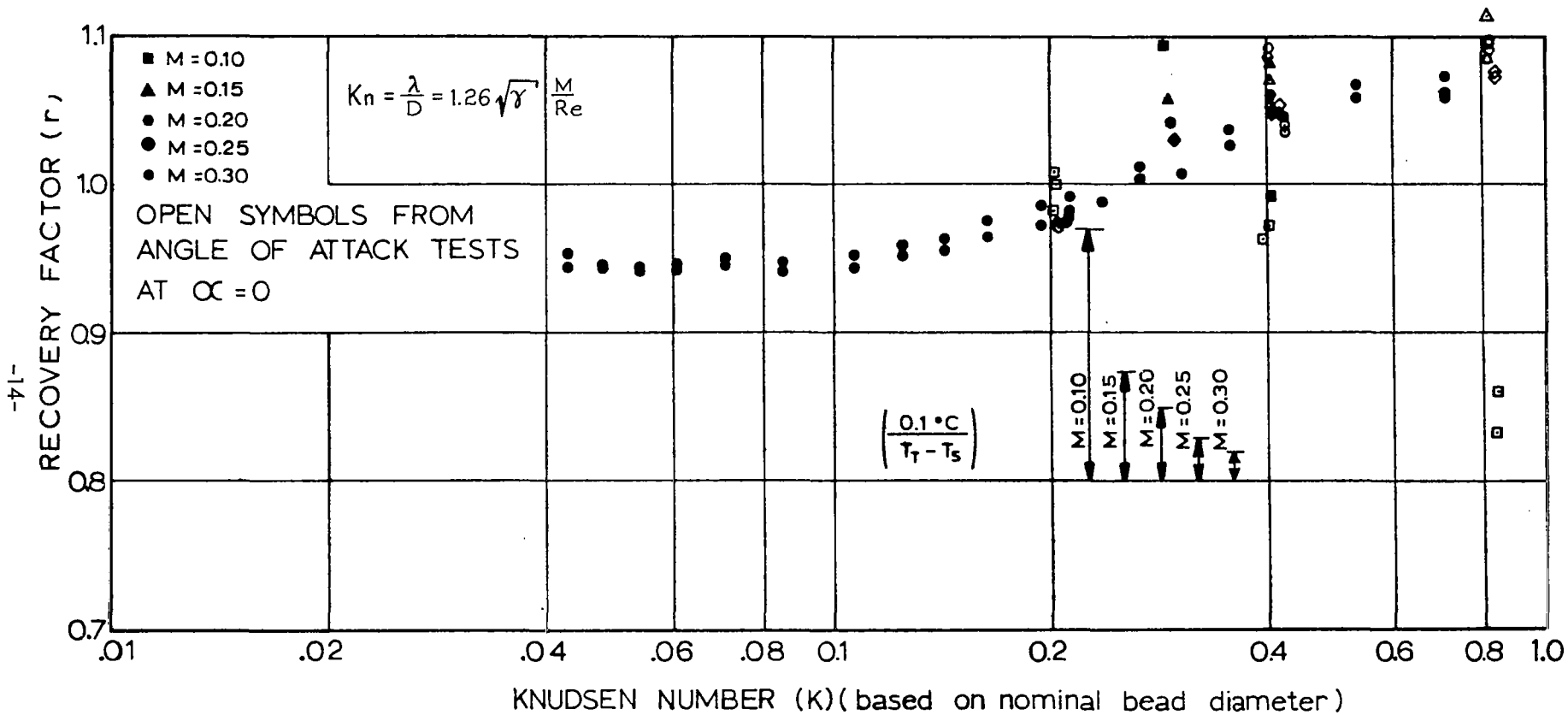
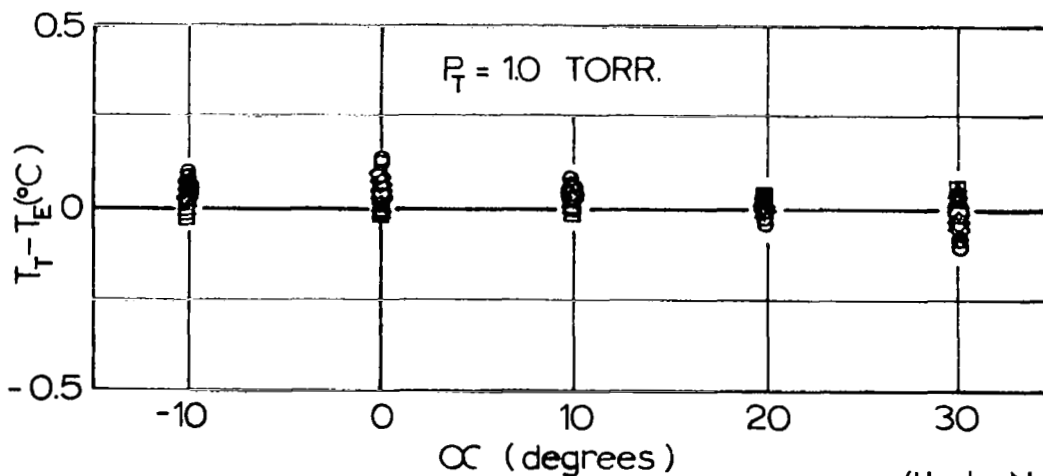
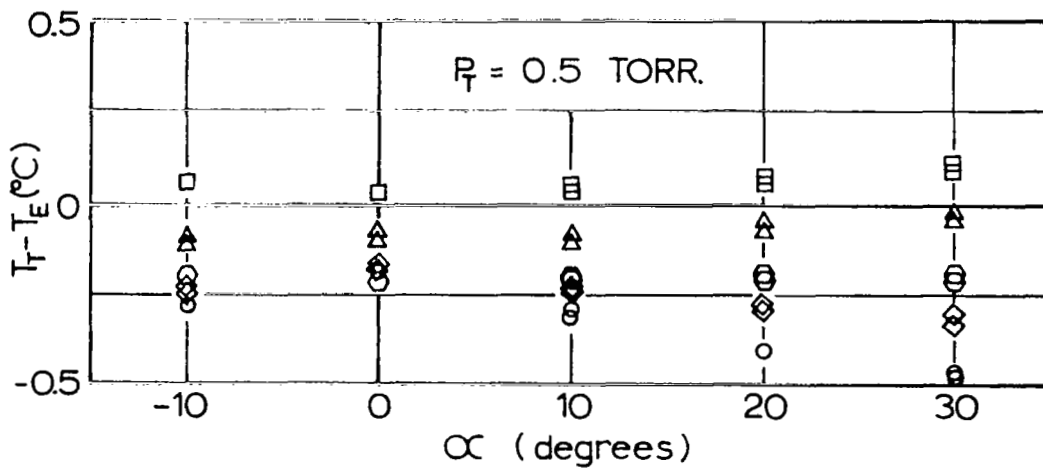
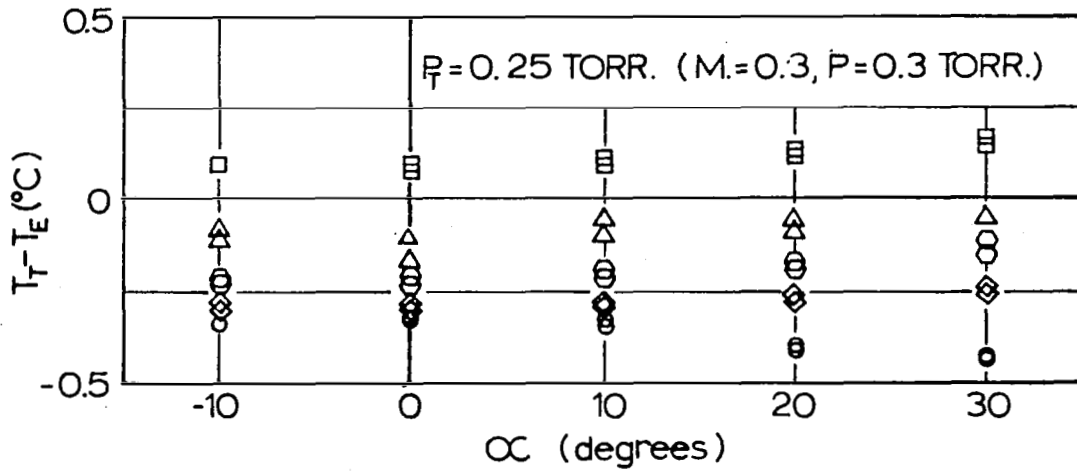


Figure 2.8 $T_T - T_E$ as a Function of Static Pressure ($\alpha = 0$)



(Haak, Noreen)

Figure 2.9 Thermistor Recovery Factor as a Function of Knudsen Number ($\alpha = 0$)



(Haak, Noreen)

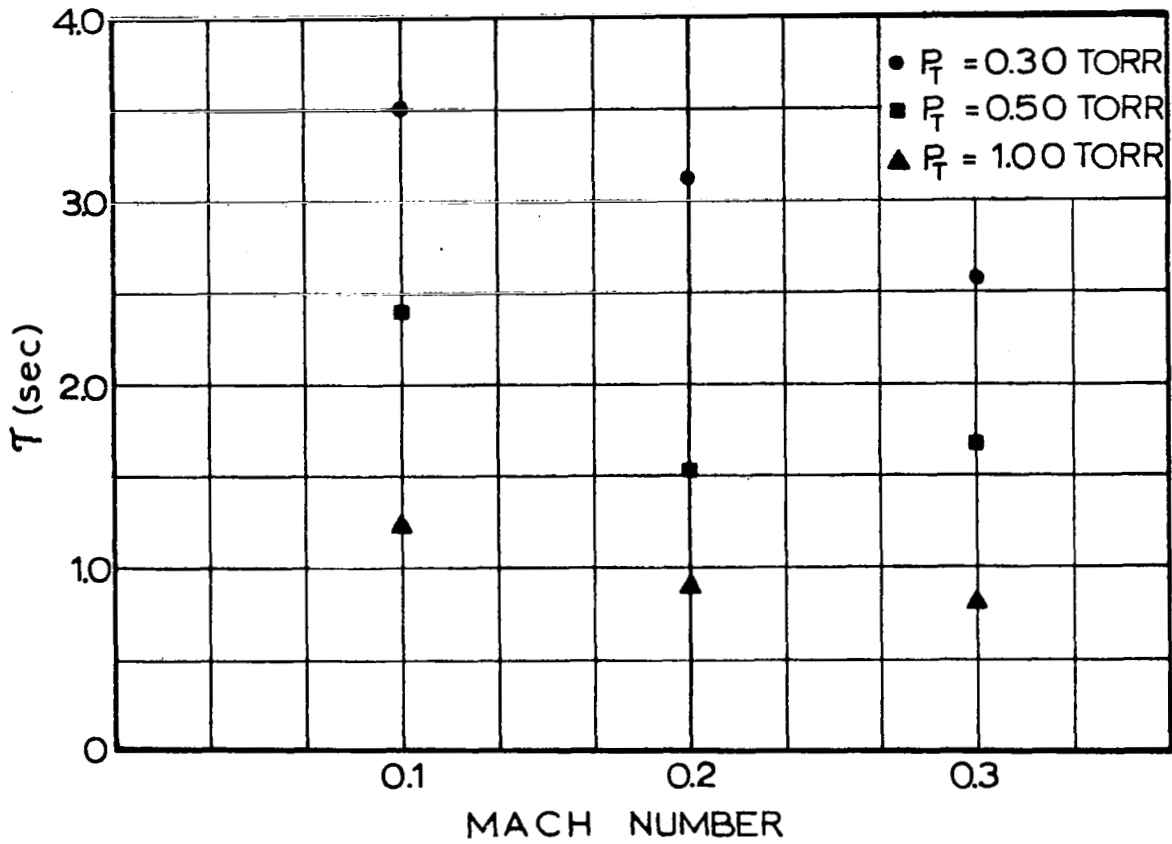
□ $M=0.10$ ○ $M=0.20$ ◐ $M=0.30$
 Δ $M=0.15$ ◇ $M=0.25$

Figure 2.10 $T_T - T_E$ as a Function of Angle of Attack for Various Total Pressures

Table 2.3 Response Time Test Conditions and Results

M	P _T (torr)	R _I (ohm)	T _I (C)	R _E (ohm)	T _E (C)	T(C)	T(sec)
0.10	0.30	3780	51.78	10268	23.70	34.03	3.51
	0.50	3720	52.11	9724	25.12	35.05	2.39
	1.00	1890	73.67	8942	27.30	44.36	1.22
0.20	0.30	2195	68.69	8908	27.42	42.60	3.12
	0.50	2470	64.89	9180	26.63	40.70	1.51
	1.00	2530	64.11	9452	25.87	39.93	0.88
0.30	0.30	2700	62.05	8636	28.26	40.69	2.58
	0.50	2700	62.05	8976	27.22	40.03	1.66
	1.00	2770	61.28	9520	25.68	38.77	0.80

(Haak, Noreen)



(Haak, Noreen)

Figure 2.11 Sample Response Time Trace and Results of the Response Time Tests

The ideal gas law or equation of state is given by

$$\rho = \frac{M P}{R T} \quad (1)$$

and the hydrostatic equation is given by

$$dP = -\rho g dz \quad (2)$$

where

- ρ = atmospheric density
- P = atmospheric pressure
- T = atmospheric temperature
- M = mean molecular weight of air
- R = universal gas constant
- z = altitude
- g = acceleration due to gravity

By combining equations 1 and 2 the variable ρ can be eliminated as

$$\frac{dP}{P} = -\frac{Mg}{R} \cdot \frac{dz}{T} \quad (3)$$

Assuming that the temperature is constant over a small altitude layer, and the temperature can be represented by an average, T_a , equation 3 can be integrated to

$$\ln P_2 = \ln P_1 - \frac{Mg}{R} \cdot \frac{Z_2 - Z_1}{T_a} \quad (4)$$

where the constant $\frac{Mg}{R}$ can be represented by either

0.0338 °K/meter or

0.0103 °K/foot.

Equation 4 can be transformed to base ten logarithms for computing as

$$\log P_2 = \log P_1 - 0.00448 \frac{Z_2 - Z_1}{T_a} \quad (5)$$

Thus the rocketsonde pressure switch closure would indicate the altitude, Z_1 , and the calibrated pressure, P_1 , for the first step calculation utilizing equation 5.

The U.S. Navy at NOL has experimented with a one-point pressure switch in the WOX-2A Hasp system. The Hasp pressure switch is shown in Figure 2.12. These switches were designed to close at about 36 mb or 75,000 ft. Two problems encountered with this system were a changing closure point calibration with time (about 0.085 mb per month) and temperature (about 0.0244 mb per °C). See Figure 2.13. In addition a \$200 increase in the cost of the Hasp system was estimated by the Navy to incorporate the pressure switch. Since subsequent flight tests indicated that the rawinsonde and the pressure switch data were in close agreement, they decided to continue to use the rawinsonde data.

At certain locations there appears to be a need for an on-board one-point pressure switch because near-time and near-location rawinsonde measurements are not available. Of the two sources of variation the near-time factor has been found to be the more important in the differences between rawinsonde and rocketsonde data. The stated pressure measurement rms accuracy for hypsometer equipped rawinsondes is ± 0.35 mb at 75,000 ft (35.43 mb). However, hypsometer flight test data comparisons with FPS-16 radar show differences as great as 600 meters or 3.131 mb at a level of 20 mb. Thus a rocketsonde pressure switch should be about as accurate to be worthwhile. Relatively inexpensive baroswitches are available which are accurate to about ± 1 mb at 75,000 feet (pressure gradient 1.591 mb/1,000 ft) providing the baroswitch temperature is known. An inexpensive thermister could be mounted on the baroswitch structure. Upon switch closure the temperature could be telemetered instead of the regular rocketsonde temperature.

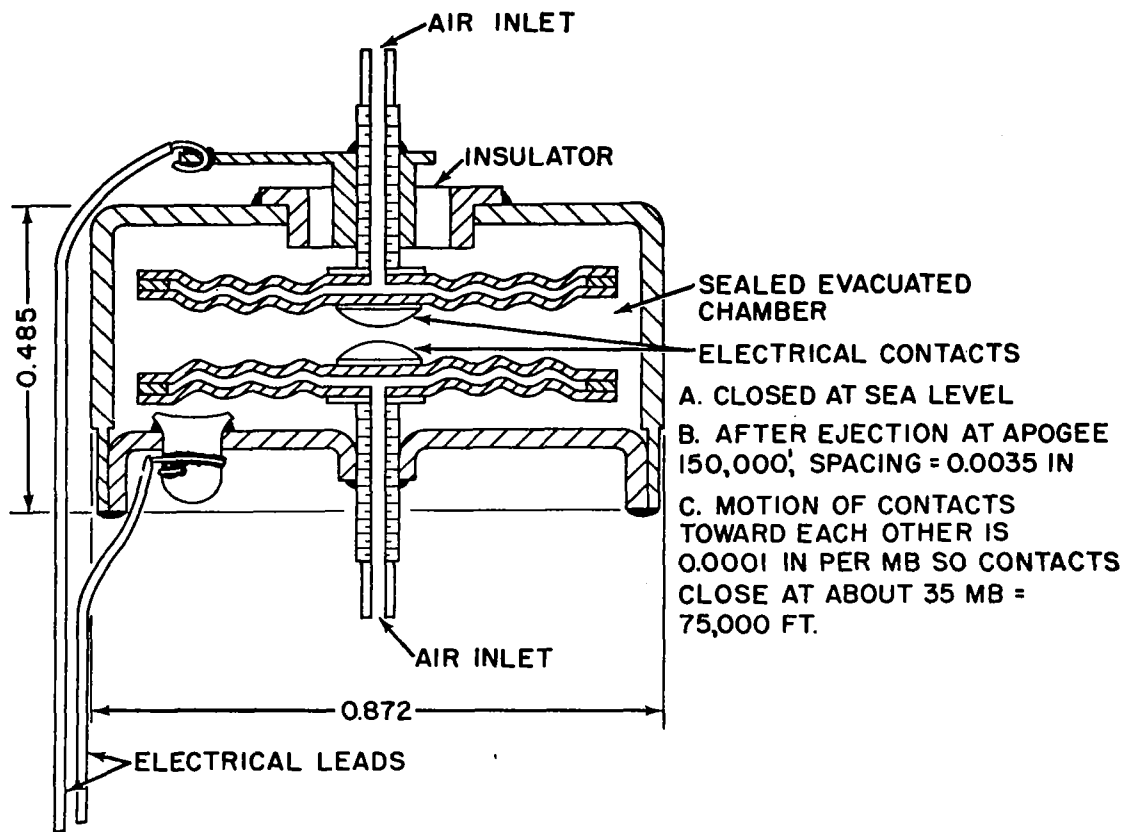


Figure 2.12 Hasp Pressure Switch Cross-Sectional View

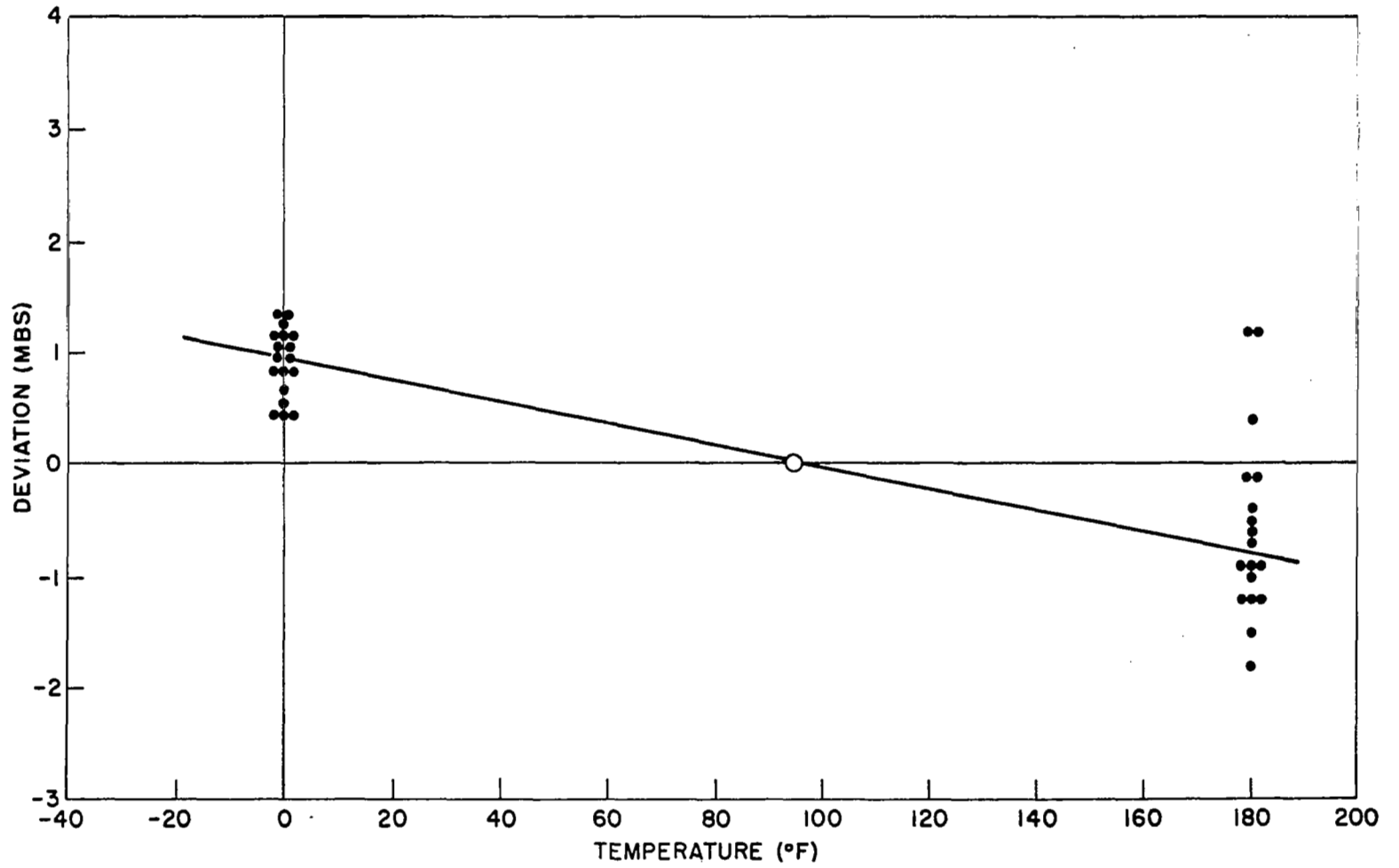


Figure 2.13 Pressure Switch Operating Point Deviation in Millibars as a Function of Temperature (18 samples)

2.4 Passive Falling-Sphere Density Sensors.

2.4.1 General.

Over the past year a great deal of information has been published concerning passive inflatable falling-sphere technology. Since most of this information has been published in NASA SP-219, Status of Passive Inflatable Falling-Sphere Technology for Atmospheric Sensing to 100 km, as a result of a symposium held at Langley Research Center, 23-24 September 1969, only a brief summary will be presented in the following sections.

Currently there are a handful of slightly different passive falling-sphere systems, i.e., vehicles, spheres, and data reduction techniques. Although the density data derived from these different systems tend to agree in a gross sense, significant differences have been found among the various techniques. Error sources include the physical sphere parameters, radar error, drag coefficient error, and data reduction error. Leakage of the sphere inflatant potentially could lead to a significant density error; however, this factor at present is a supposition. It has been demonstrated that the error introduced by the AN/FPS-16 radars is generally quite small. The largest source of error appears to be in the drag coefficient - in fact, the various experimenters use widely different drag coefficient values in certain regions of the drag table. The error due to data reduction techniques does not appear to significantly affect the density data; however, it appears that data reduction techniques introduce sizeable errors into the reduced temperature profiles. The wind data appears to be quite acceptable up to an altitude of about 85 km.

2.4.2 Physical Sphere Parameters.

The inflated sphere shape, mass and size enter into the calculation of atmospheric density as indicated by

$$\rho = \frac{2 m}{C_D A} \cdot \frac{a}{V^2}$$

where

m	=	sphere mass
A	=	sphere cross section area
C _D	=	sphere drag coefficient
a	=	sphere acceleration
V	=	sphere velocity
ρ	=	atmospheric density

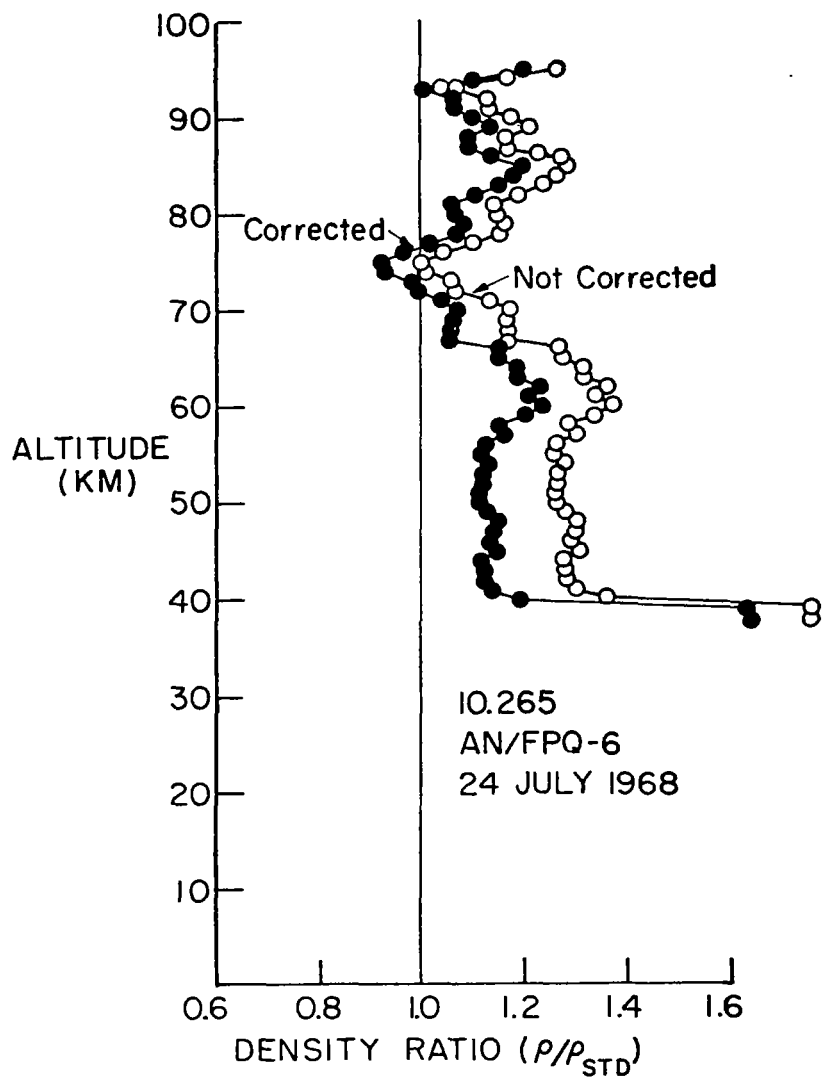
Although various sizes and weights of spheres are utilized, both the diameter and the mass are accurately controlled and measured during fabrication. The sphere diameters, and hence cross-section areas, are closely controlled during production. Each sphere is accurately weighed, and this weight is used as an input in the data reduction program. In addition, the spherical shape is accurately controlled during fabrication. Therefore, the as-manufactured spheres should not introduce any significant error into the density calculations ($\sim 0.2\%$). However, after sphere deployment into the atmosphere, the mass may decrease due to leakage of the isopentane inflatant through pin holes in the mylar skin, and the balloon may become soft so that it may not maintain a spherical shape. McWatters and Peterson, University of Michigan, (reference 5) have hypothesized that premature sphere deflations may be caused by pin hole leaks in the mylar skin, and that this would cause a gradual loss of inflatant mass during the sphere descent. They have attempted to correct the sphere mass as a function of descent time by means of

$$\frac{m}{m_0} = e^{-\frac{t - t_e}{t_d - t_e} \ln \frac{P'}{P_d}}$$

where

- m = sphere mass
- m_0 = initial sphere mass
- t = time
- t_e = ejection time
- t_d = deflation time
- P' = design deflation pressure
- P_d = actual deflation pressure

The corrected mass as a function of time is used as an input to the density data reduction program with a resulting correction in the density profile such as indicated in Figure 2.14. This correction technique assumes a sonic jet leak through a constant size orifice. Of course, the concept of a slow leak is only an hypothesis at this time since the existence of such has not as yet been proven. However, this mass correction technique is quite interesting and should be pursued further. If slow leaks are proven to be a problem, physical redesign of the spheres should be undertaken as the real solution, i. e., heavier gage mylar.



(McWatters, Peterson)

Figure 2.14 Effect of Mass Correction on Density in the Case of an Early Deflation

If the spheres are reasonably inflated, leading edge dynamic pressure during descent should not appreciably distort their shapes. However, if the internal pressure becomes low enough for the sphere to go soft, a flattening of the shape can take place with a resulting change in the drag coefficient as indicated in Figure 2.15. Experience has shown that when the sphere has reached this stage of deflation, it very soon becomes completely deflated. This becomes quite obvious from the radar fall rate data. Since the data in this region would automatically be rejected, this factor offers no real error in the density data. Premature deflation, however, is a problem in that the measured density profile is not extended as low in altitude as desired. Design deflation altitudes are about 30 km, and many sphere flights have terminated from 40 to 60 km. If pin hole leaks are not the problem, it appears that low temperature effects cause the premature deflations.

2.4.3 Radar Error.

Radar position data has long been credited with contributing a major share of error in the sphere technique. Recent flights, however, with well-maintained FPS-16 radars have produced density profiles which show remarkable agreement. See Figures 2.16 and 2.17. In general the agreement among well-maintained FPS-16 radars has been within 1%.

The classical radar range equation may be written as

$$\frac{S}{N} = \frac{P_t G_t G_r \lambda^2 \sigma}{R^4 B F_o L}$$

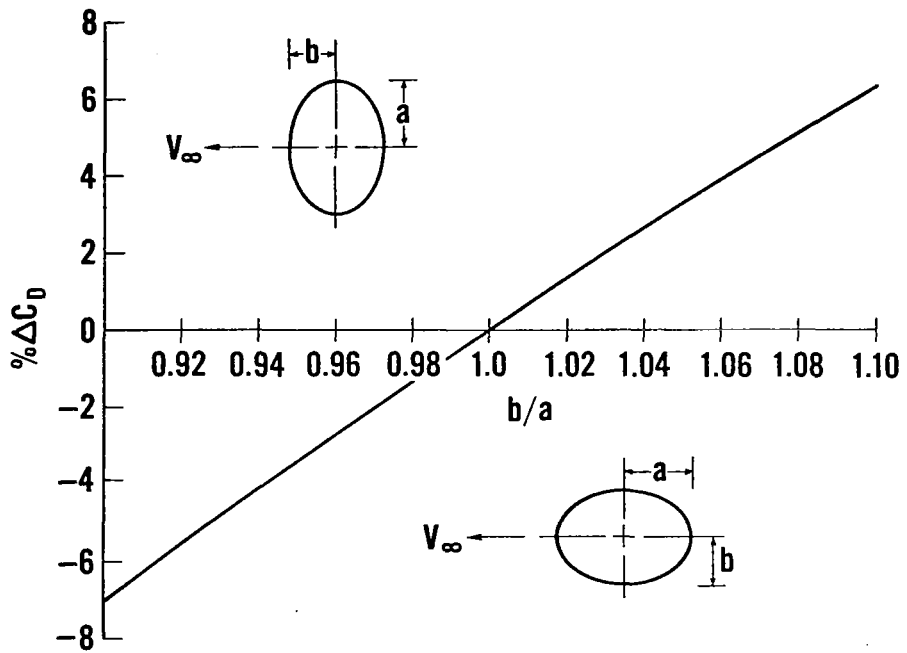
and range and elevation angle standard deviations per single pulse are

$$\sigma_R = \frac{137 \tau}{\sqrt{S/N}}$$

$$\sigma_E = \frac{\theta}{2\sqrt{S/N}}$$

where

S/N	=	effective signal-to-noise ratio
P _t	=	radiated power
G _t	=	transmitting antenna gain
G _r	=	receiving antenna gain
λ	=	wavelength of radar
σ	=	radar cross section of target
R	=	slant range
B	=	receiver bandwidth
F _o	=	receiver noise figure
L	=	tracking system losses



(Lyons)

Figure 2.15 Error in Sphere Drag Coefficient Due to Distortion

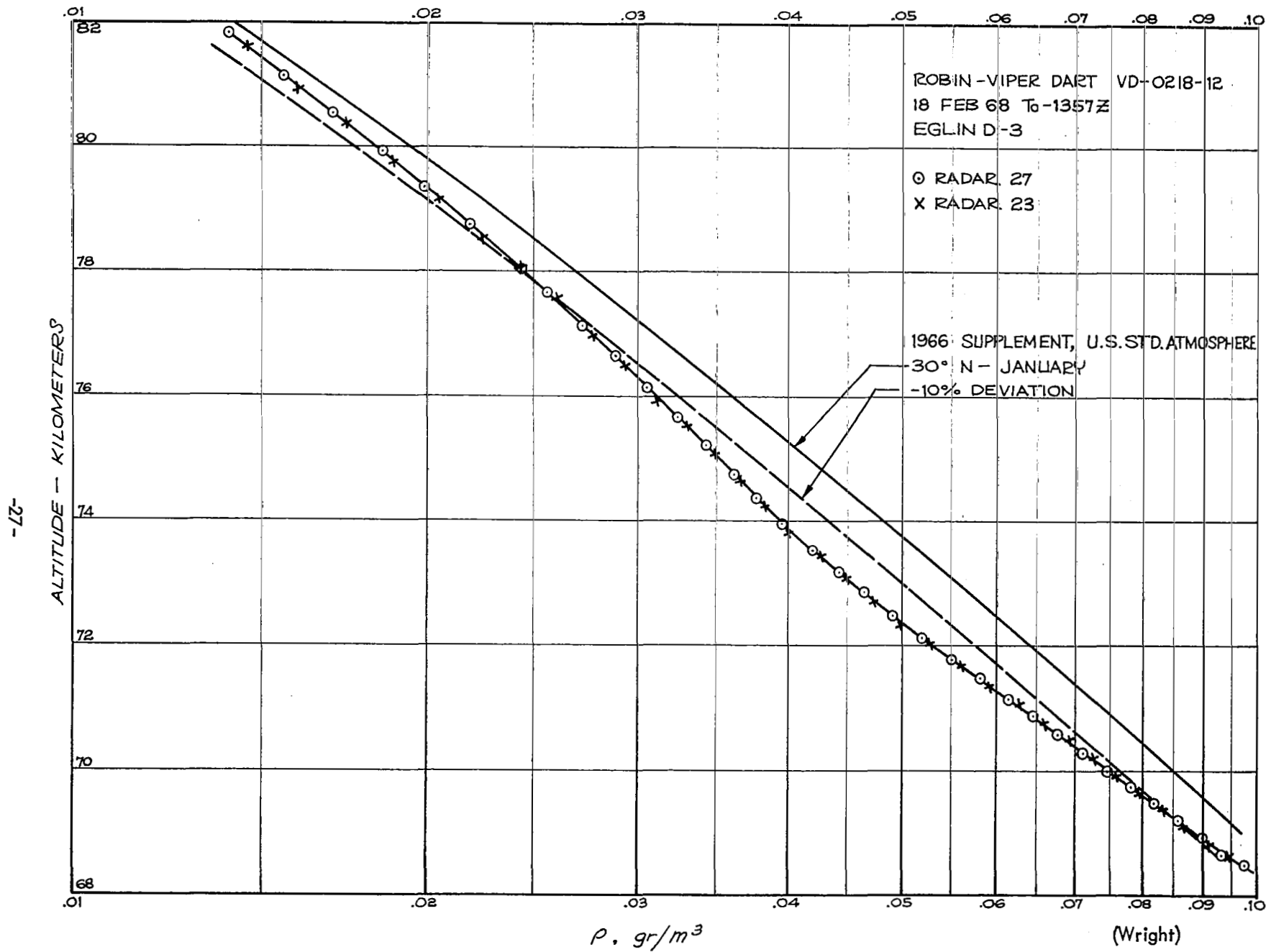


Figure 2.16 Viper Robin Density Profile

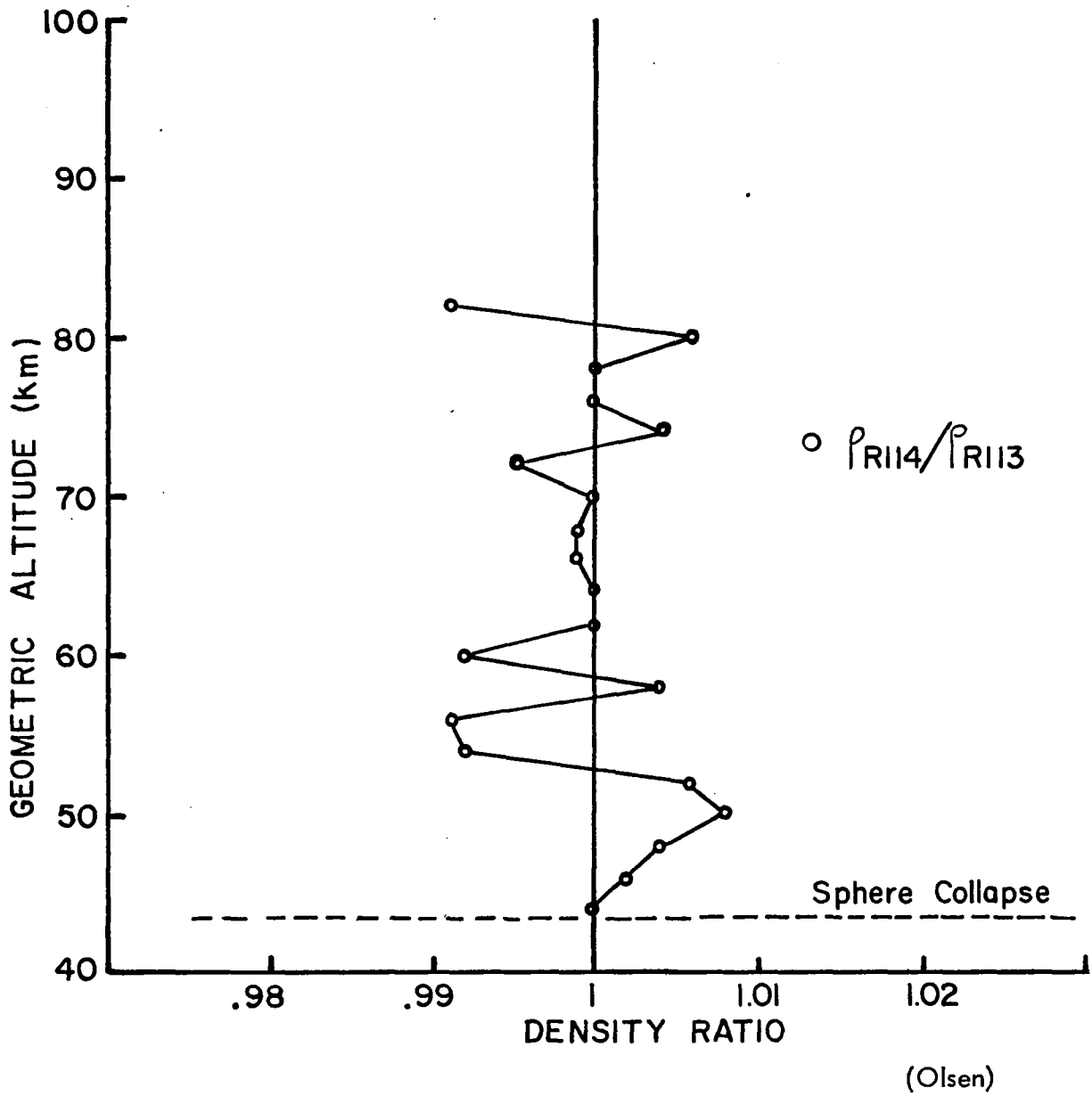


Figure 2.17 Density Ratio Between 2 FPS-16 Radars Tracking the Same Sphere

- τ = pulse width (in seconds)
- θ = antenna beam width
- σ_R = standard deviation in range
- σ_E = standard deviation in elevation angle

Since the resulting error in density is a function of both the range and elevation angle error, more accurate densities can be obtained when the elevation angle is held constant, i.e., on the upleg portion of the trajectory. In this case the elevation angle velocity and acceleration are zero, and elevation errors drop out from the density computations. Simultaneous tracks by independent FPS-16 and FPQ-6 radars have upon numerous occasions shown a fine structure in the falling sphere data which was duplicated by each radar. Therefore, it appears that these radars are capable of discerning fine structure in the atmosphere. As indicated by the equations above, the range and elevation errors are a function of the radar-target signal-to-noise ratio which in turn is directly related to target radar cross-section. Therefore, the larger the radar cross-section, the more accurate the radar data will be. Although it is well-recognized that different types of radars produce falling sphere data of different accuracies, it has been found that even for one type of radar the accuracies may be significantly different because of radar modifications and maintenance variations. The radar accuracy is a function of the radiated power, antenna systems gains, receiver bandwidth setting, receiver noise figure and the various tracking system losses. In general, however, radar accuracies introduce an rms density error of 1-2% below 80 km and 3% up to 120 km providing the radar tracking modes of Table 2.4 are employed.

Table 2.4 Maximum Altitude of Satisfactory Radar Performance With A 66 cm Aluminized Sphere (University of Michigan, McWatters and Peterson)

Technique	Max. Altitude
FPQ-6 Ascent (range-rate)	120 km
FPQ-6 Ascent (range, angles)	108 km
FPQ-6 Descent (range, angles)	94 km
FPS-16 Ascent (range, angles)	102 km
FPS-16 Descent (range, angles)	80 km

2.4.4 Drag Coefficient

Typical inflatable falling sphere fall rate data are presented in Figures 2.18 and 2.19 for two slightly different sphere designs. Although the fall rate profiles above 80 km are dependent upon the sphere apogee altitudes, the sphere deceleration appear to be fairly independent. During descent, the typical inflatable sphere passes through various fluid dynamic flow regions such as free molecule, transitional, slip and continuum as shown in Figure 2.20. The spheres accelerate to low supersonic speeds and then decelerate through the Mach 1 transition region at an altitude slightly above 70 km. Below 70 km the spheres descend at subsonic fall rates.

The sphere drag coefficients depend upon both the Mach and Reynold's numbers as indicated in Figure 2.21. Disagreements among various investigators as to the proper values to use for drag coefficients has led to sizeable differences in the reduced density profiles. Since the computed density is inversely proportional to the drag coefficient, a given percent error in the drag coefficient causes the same percent error in the computed density. Differences in the drag coefficient values used by the various investigators are presented in Table 2.5. Various experimental values are presented in Figure 2.22. The most recent drag coefficient data presented by the University of Minnesota is shown in Figures 2.23 and 2.24. Currently there is a coordinated effort among various government agencies to improve the sphere drag coefficient data so that a universal table can be constructed which meets widespread approval. If this is accomplished and the resulting density profiles agree with the rocketsonde, pitot and grenade data, a significant improvement in the falling sphere data will have been made.

The effect which two different sets of drag data has upon the computed density profiles is shown in Figures 2.25 and 2.26. Although it is difficult to judge which set of data is more valid at the higher altitudes, a comparison with the rocketsonde data below 60 km indicates that the Sandia data is more accurate below 60 km. Referring back to Figure 2.16, a curious deviation in the computed density profile is apparent from about 71 km to 76 km. This deviation or "bump" in the density profile is apparent in many of the falling sphere data. Since the spheres are traversing the transonic flow region at this altitude, it has been hypothesized that this "bump" is due to erroneous drag coefficient data in the transonic region where it is difficult to either predict or measure. One suggestion is to refine the drag coefficient data from the flight data by smoothing through the deviation zone. If the corrected drag coefficients are similar over a number of soundings, the corrected coefficients in this transonic region could be adopted as universal values.

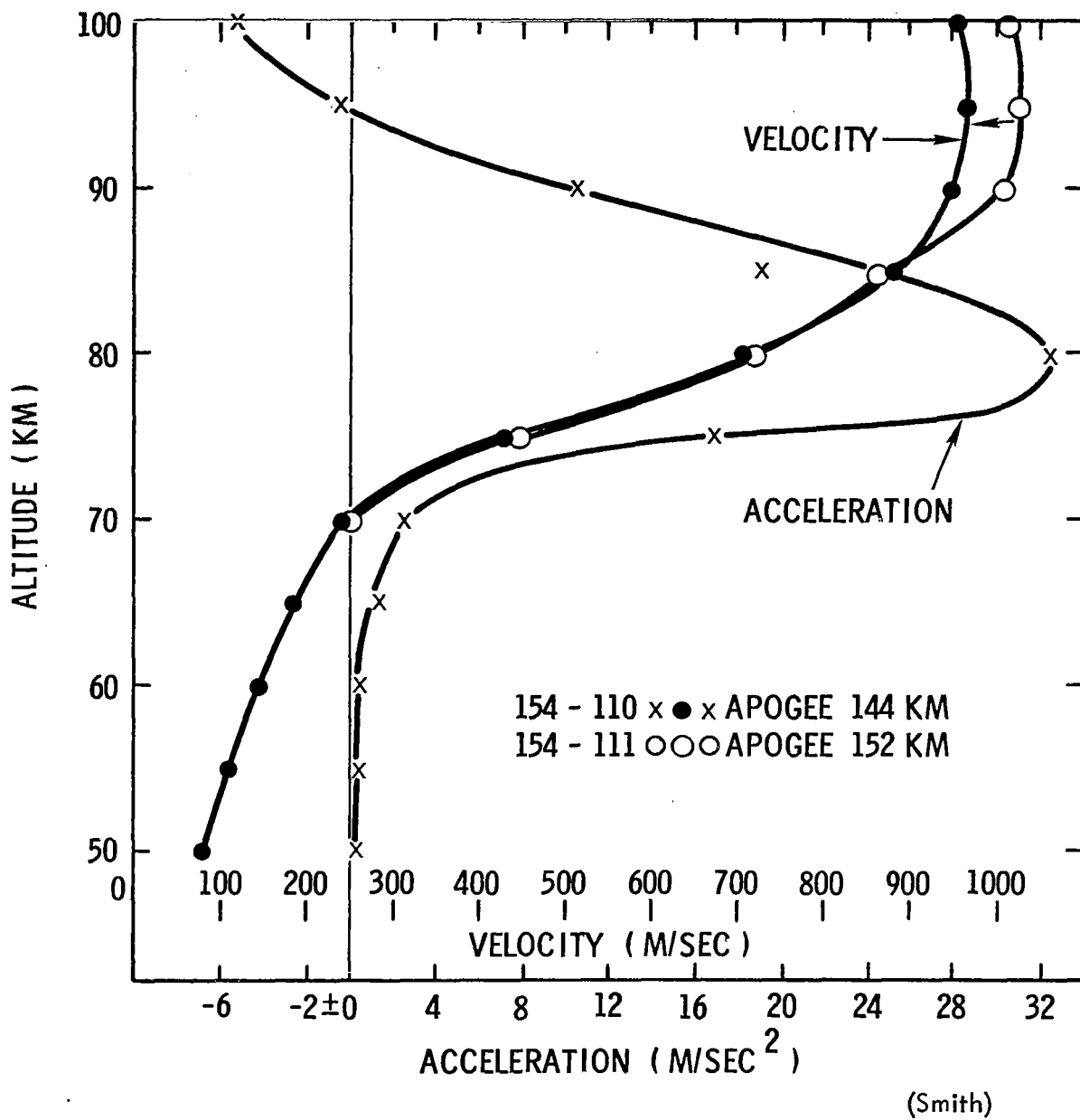


Figure 2. 18 Acceleration and Velocity Curves for Two Spheres Released at 144 and 152 km over Kauai in May 1968

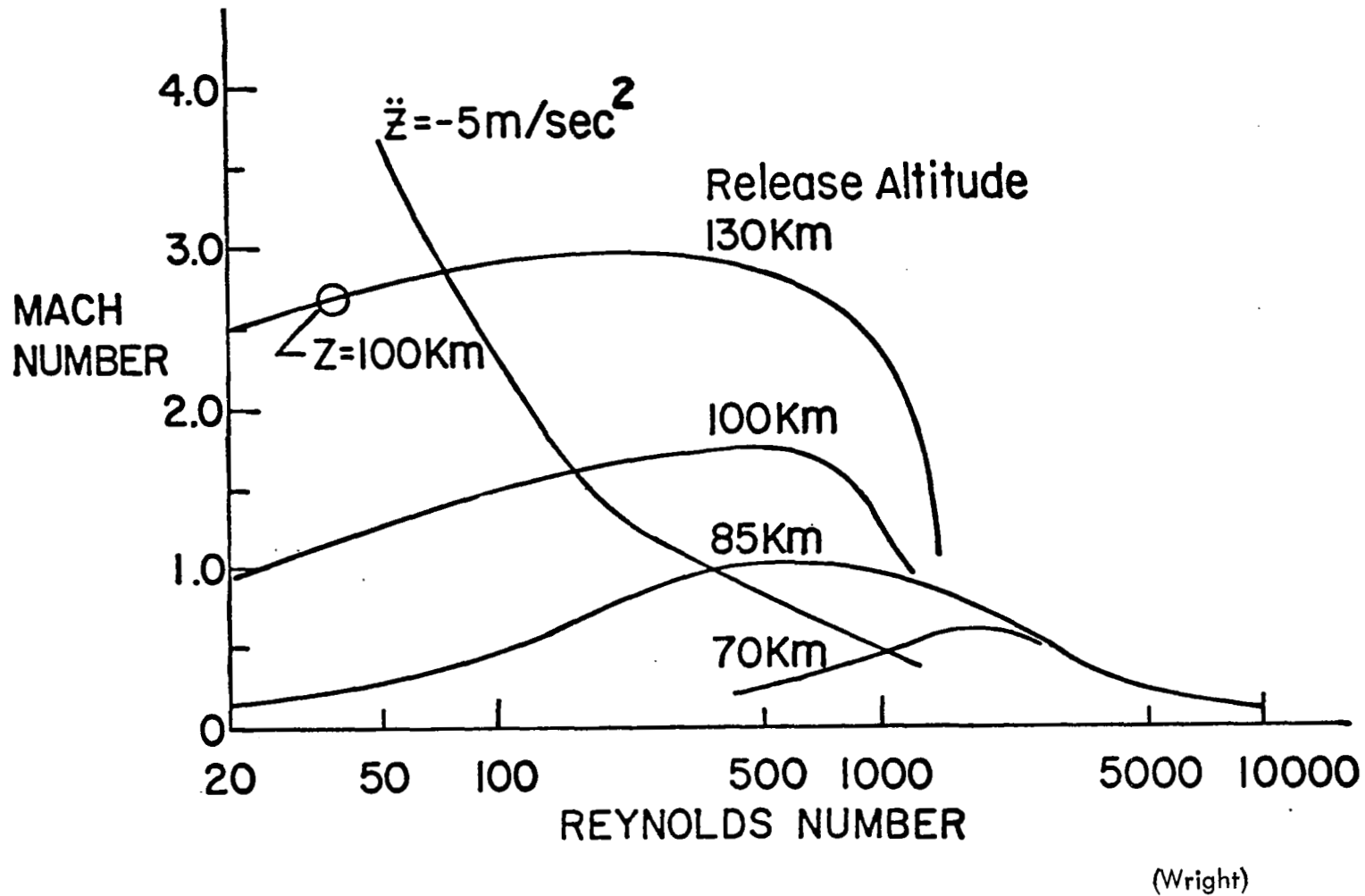


Figure 2.19 Robin Falling Sphere Aerodynamic Flow Conditions

(Wright)

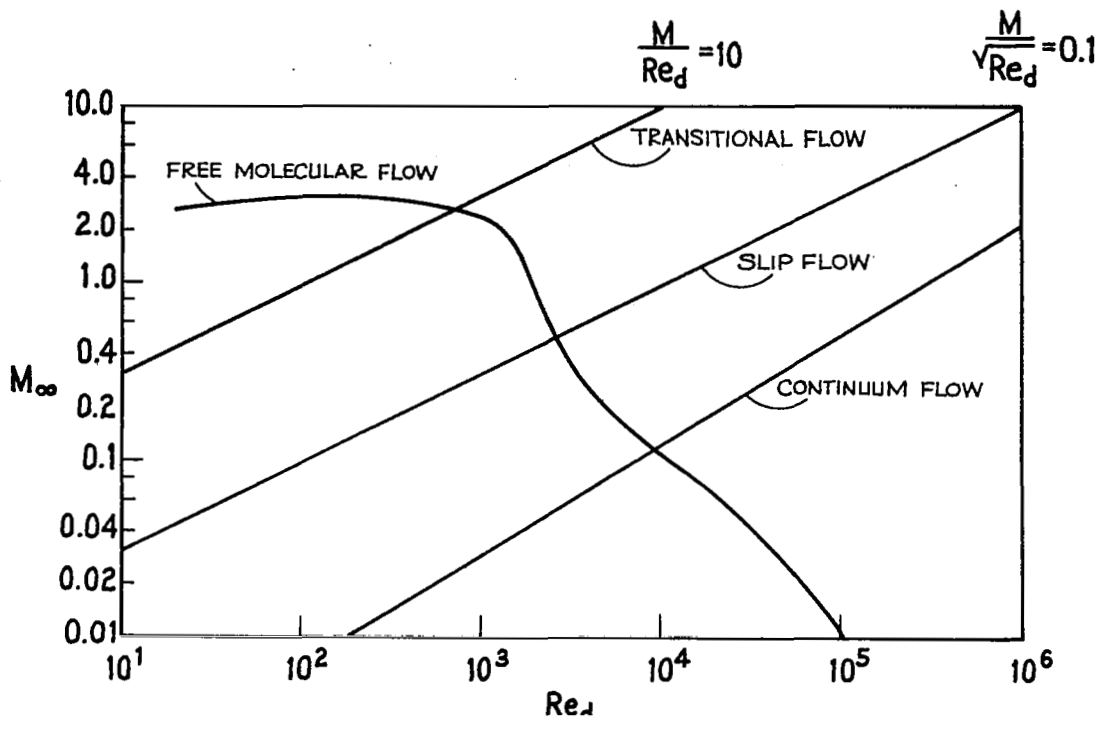
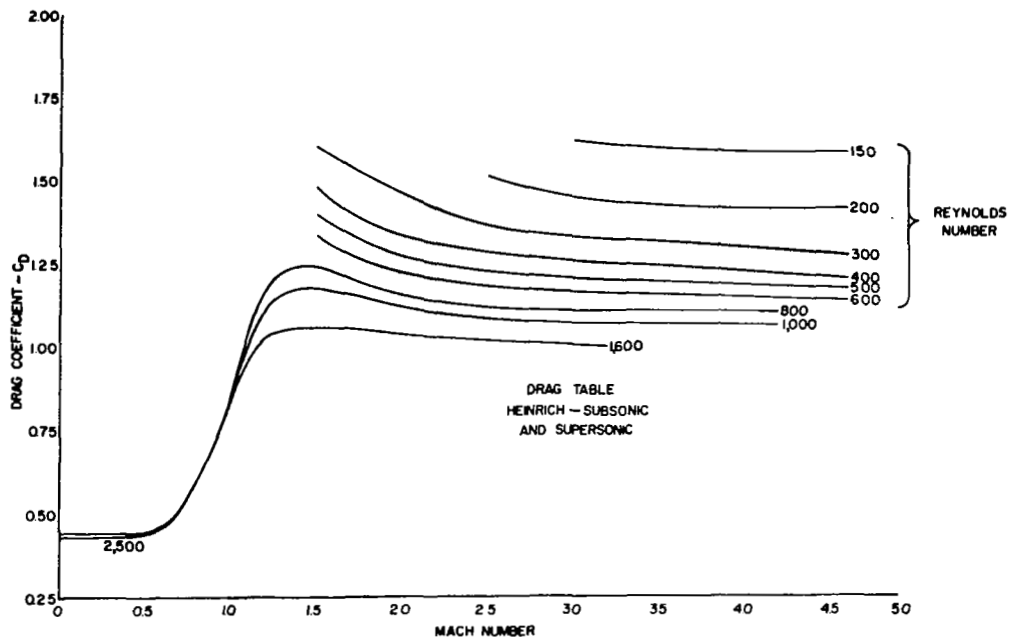
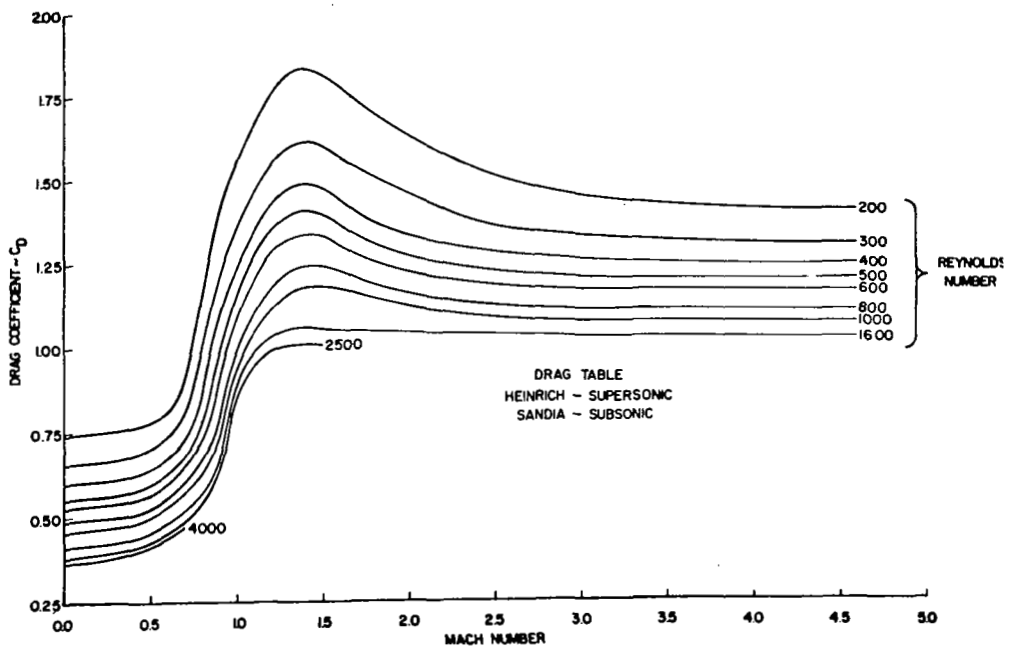


Figure 2.20 Typical Trajectory of Free-Falling Spheres



(a) Utilized in "March 65" Computer Program.



(b) Experimental.

(Wright)

Figure 2.21 Drag Coefficients of a Sphere

Table 2.5 Drag Coefficient Differences

Altitude (km)	M	R	March 1965 ROBIN Program (Heinrich)	University of Michigan		Sandia	
			C_D	C_D	Diff.	C_D	Diff.
87	2.5	260	1.42	1.3	- 8.5%	--	--
79	2.0	860	1.15	1.12	- 2.5%	--	--
76	1.5	925	1.2	1.06	- 11%	--	--
73	1.2	1120	1.09	.98	- 10%	--	--
70	1.0	1650	.82	.87	+ 6%	.9	+ 10%
68	.8	1700	.62	.57	- 8%	.64	+ 3%
62.5	.6	2680	.457	.46	0	.46	0
58	.4	3300	.434	.44	+ 1.5%	.41	- 5.5%

(Wright)

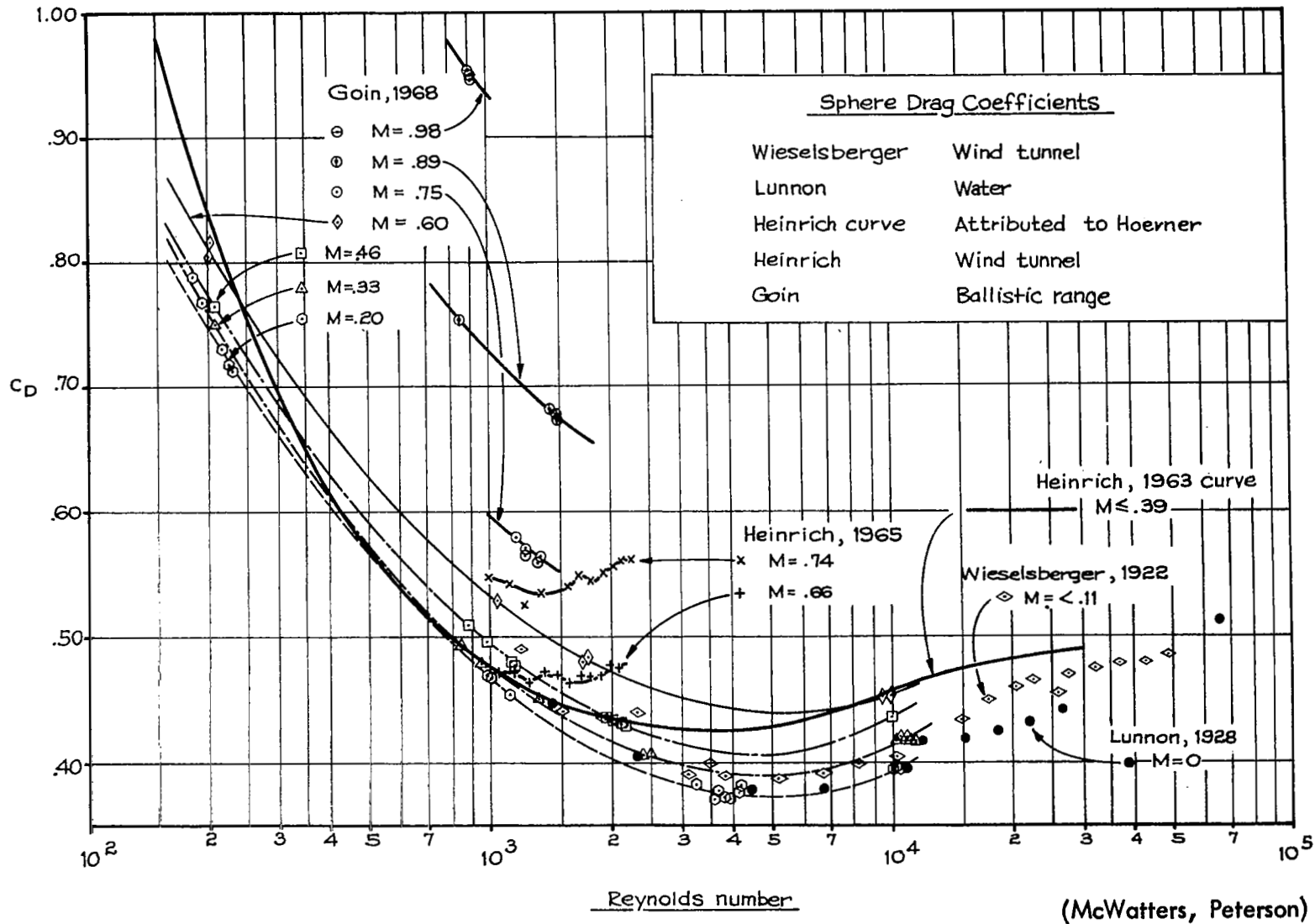


Figure 2.22 Sphere Drag Coefficients

(McWatters, Peterson)

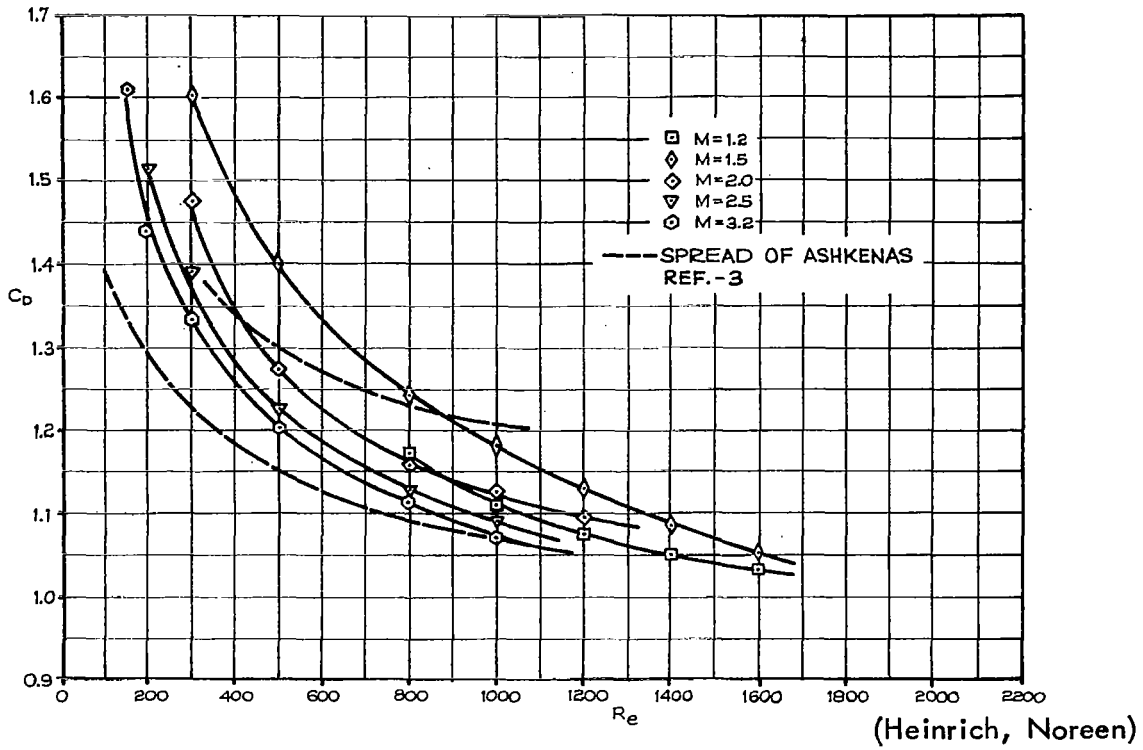


Figure 2.23 Drag Coefficient of a Sphere in Supersonic Flow as a Function of the Free-Stream Reynolds Number

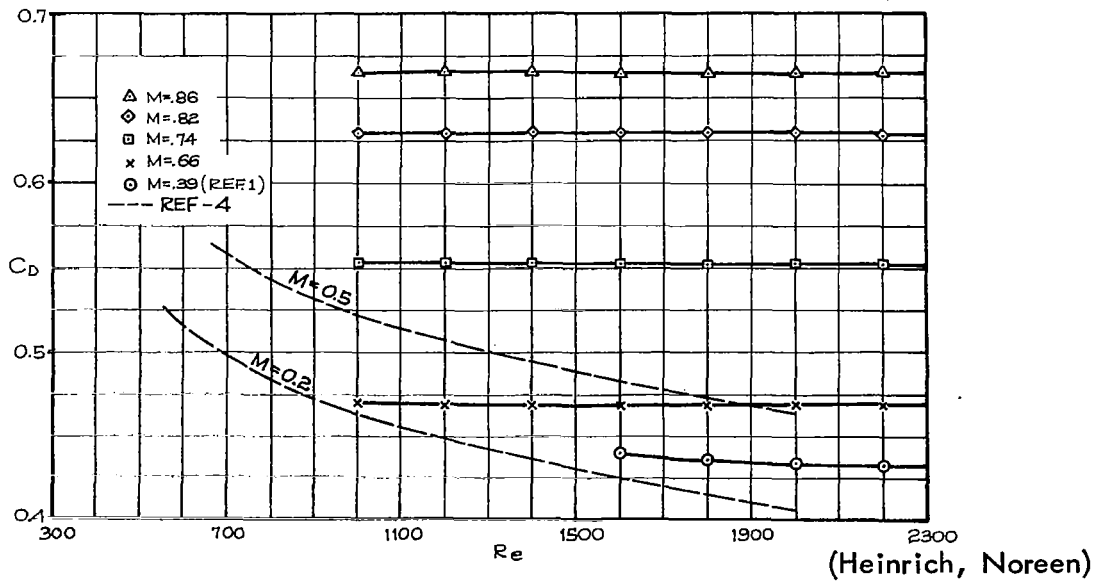


Figure 2.24 Drag Coefficient of a Sphere in Subsonic Flow as a Function of the Free-Stream Reynolds Number

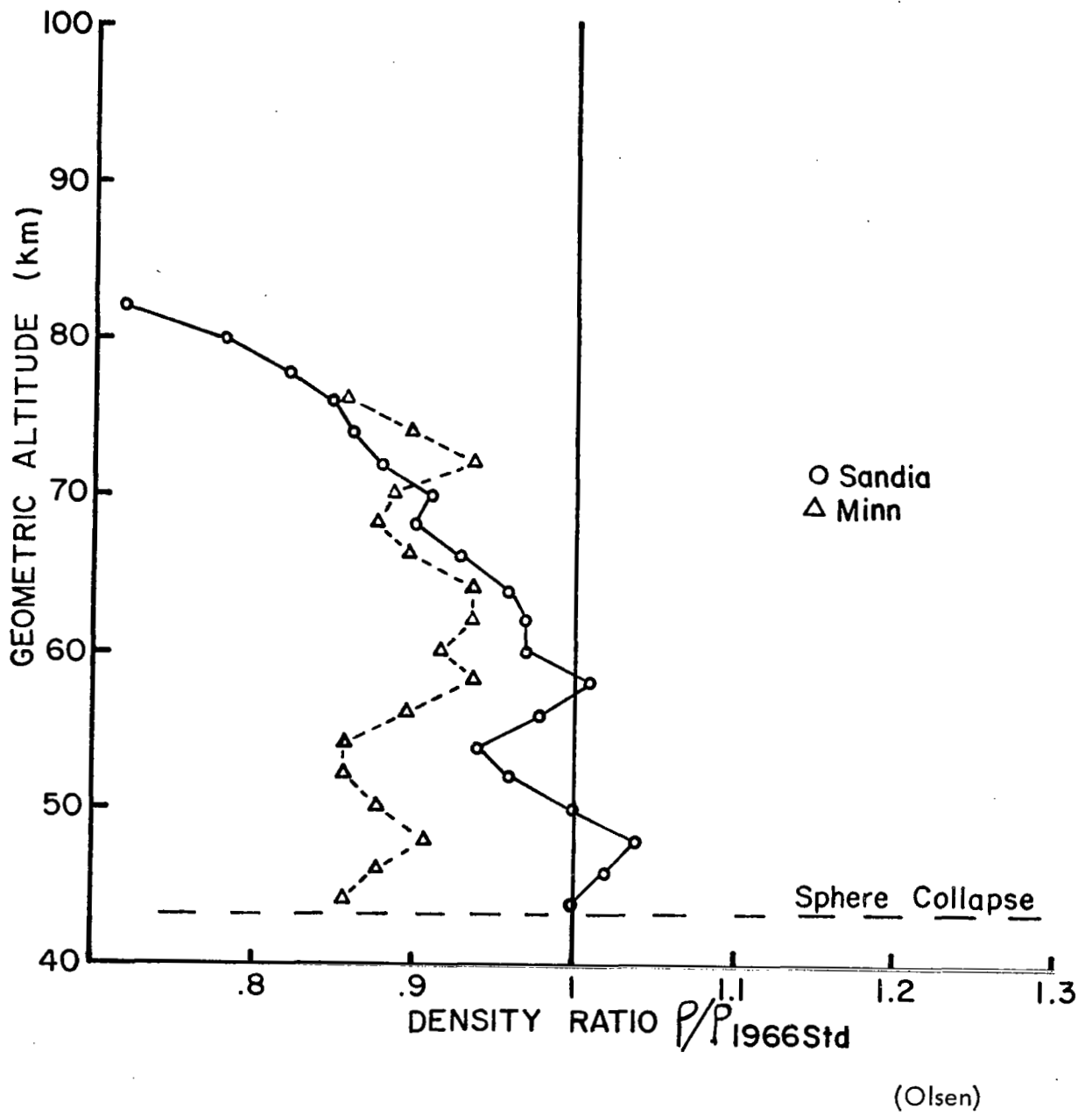


Figure 2.25 Viper 8, 9 May 1969, Density Departures from 1966 Standard Atmosphere, July, 30°N

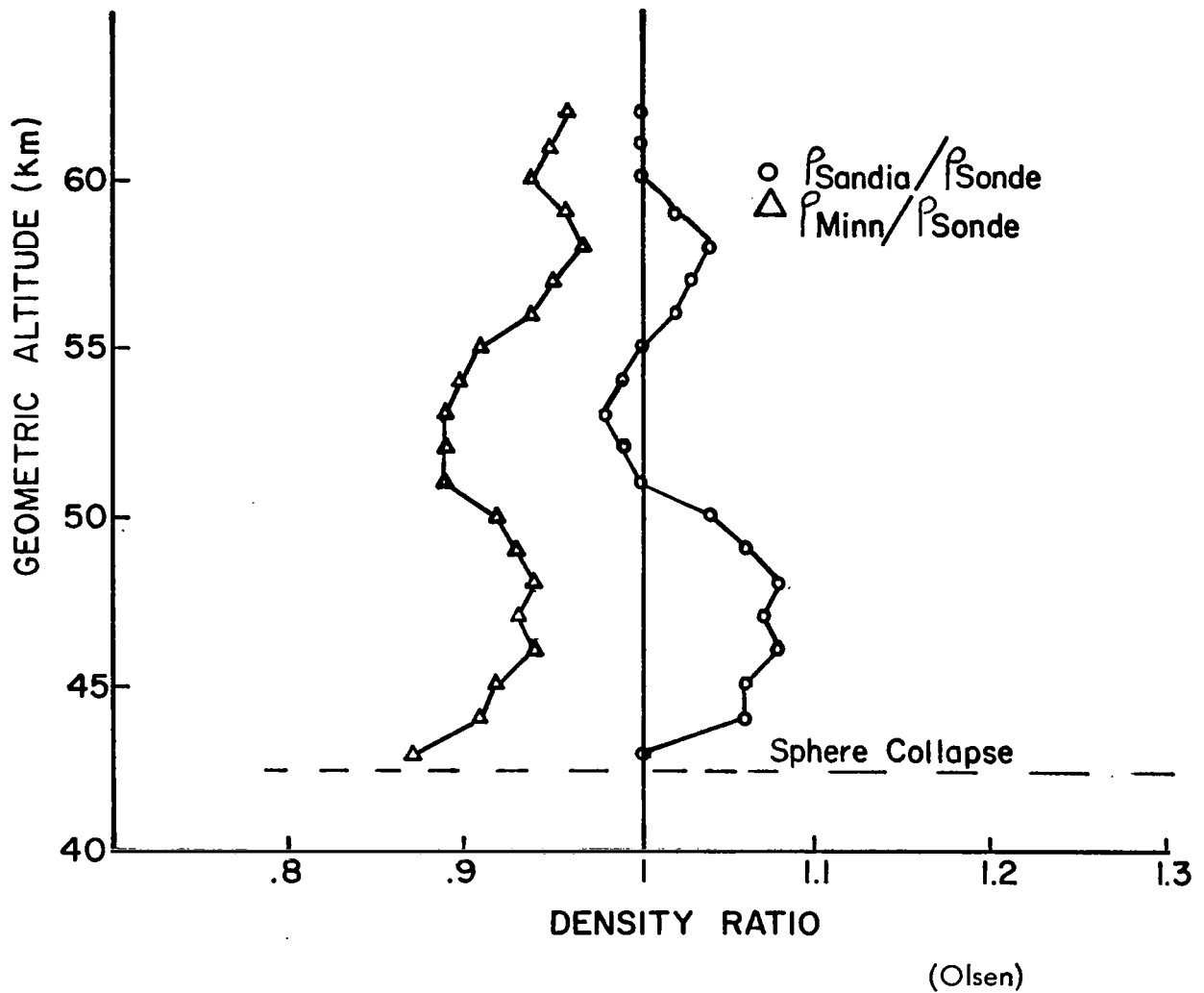


Figure 2.26 Viper 8, Comparison of Density Between Sphere and Rocketsonde

2.4.5 Data Reduction Techniques.

When optimum smoothing intervals are used for the radar data, there appears to be only a 1% bias error in computed density from 30 to 70 km and an rms noise error of 3%. From 70 to 95 km the bias would be 3% - 5%, and the rms noise error would be less than 3%. These accuracies do not include the unknown accuracies of the drag tables nor the effect of vertical winds. The smoothing intervals generally have been selected to optimize the computed density data. It appears that oscillations in the reduced temperature profiles as shown in Figures 2.27 and 2.28 may be caused by the data reduction techniques since independent radar tracks of the same sphere have produced similar oscillations in the reduced temperatures but vary in phase as the flight progresses. This may indicate a data reduction problem or possibly vertical winds.

2.4.6 Summary.

The inflatable passive falling-sphere technique appears to be adequate for determining atmospheric density profiles to 100 km providing adequate radars are available. By combining the falling sphere data with rocketsonde and rawinsonde data, density profiles to 100 km such as in Figure 2.29, can be economically measured on a routine basis. Typical accuracies for the falling sphere densities and winds are as indicated in Table 2.6. The major sources of unknown error in the derived density profiles appear to be due to errors in the drag coefficient data and the presence of vertical winds. Drag coefficient discrepancies on the order of ten percent have been found among various investigations in certain regions of the drag tables. This problem should be solved in the near future by the adoption of a universal drag table with more accurate data. In the falling sphere technique it is not possible to distinguish between density effects and vertical winds. These winds have been estimated from other experiments to be as great as 25 m/s above 80 km. Vertical winds on the order of 3 m/s may have been detected on a number of inflatable sphere flights. The density errors due to vertical winds are indicated in Figure 2.30.

A comparison between inflatable falling-sphere data and the results from the pitot probe and grenade experiments have been made by NASA-GSFC as shown in Figure 2.31. In general the sphere densities show good agreement above 70 km, but diverge as much as 10-15% below. This may be due to the subsonic drag coefficient disparities previously discussed.

FIGURE 2.27 ROBIN REDUCED TEMPERATURE PROFILE

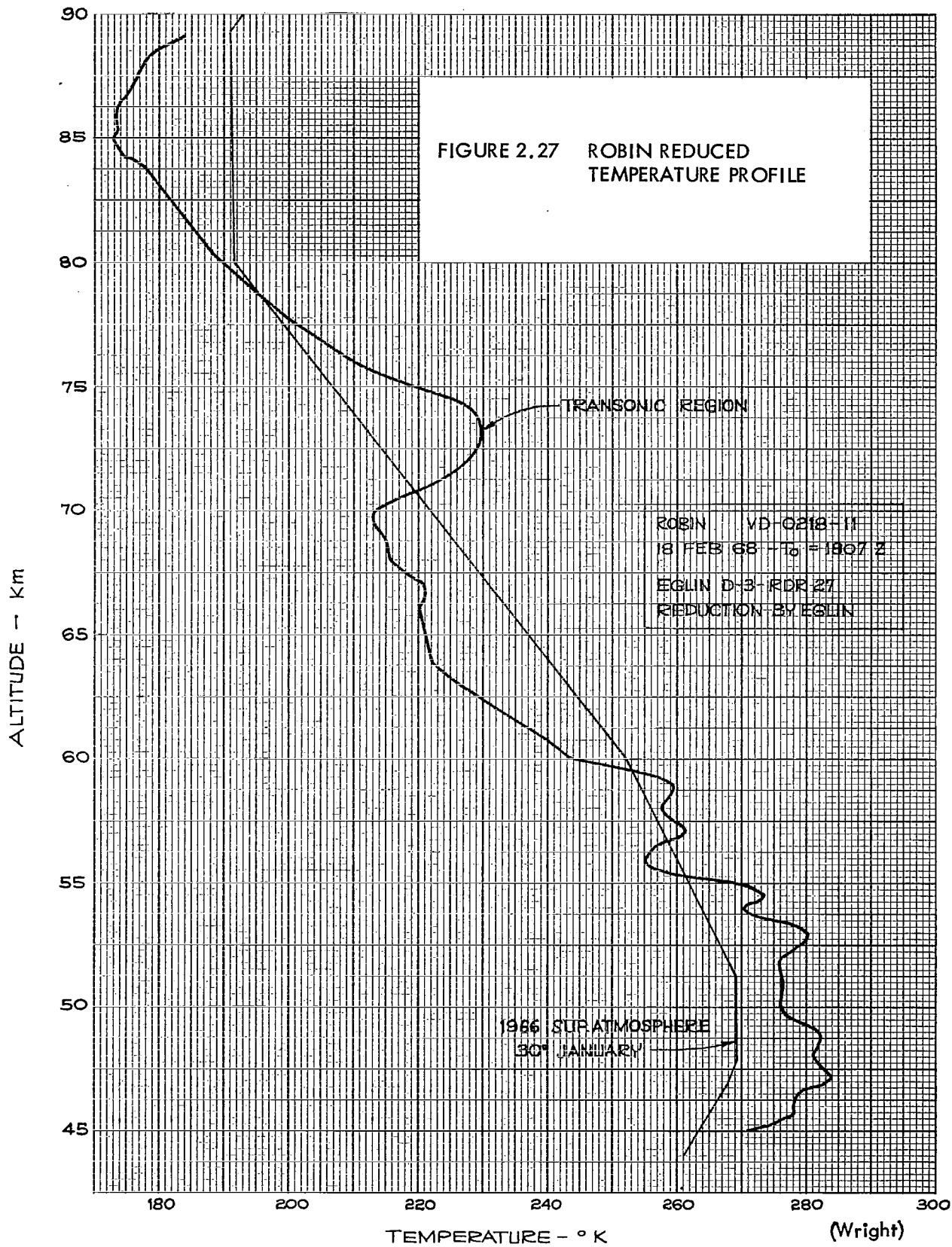
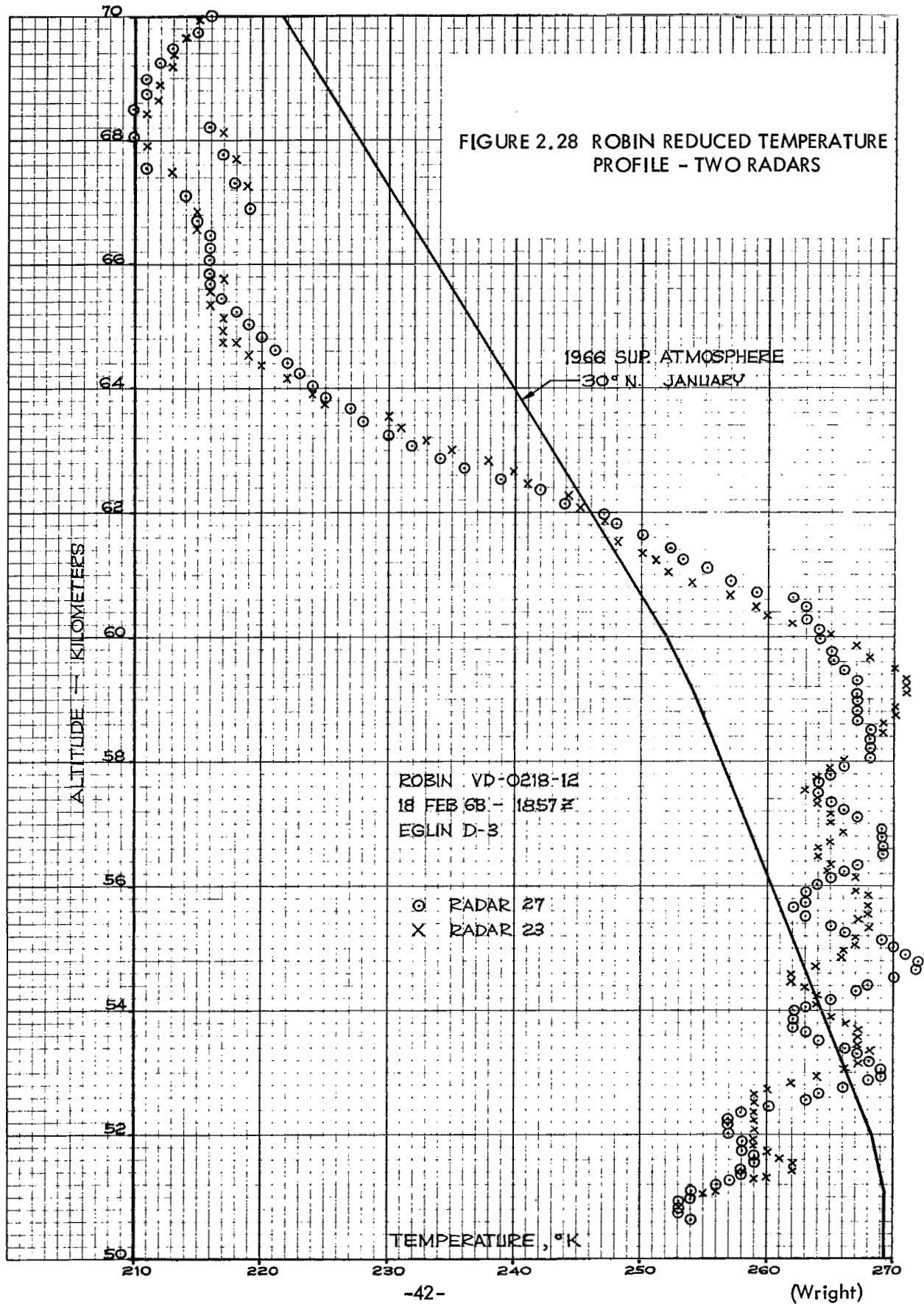
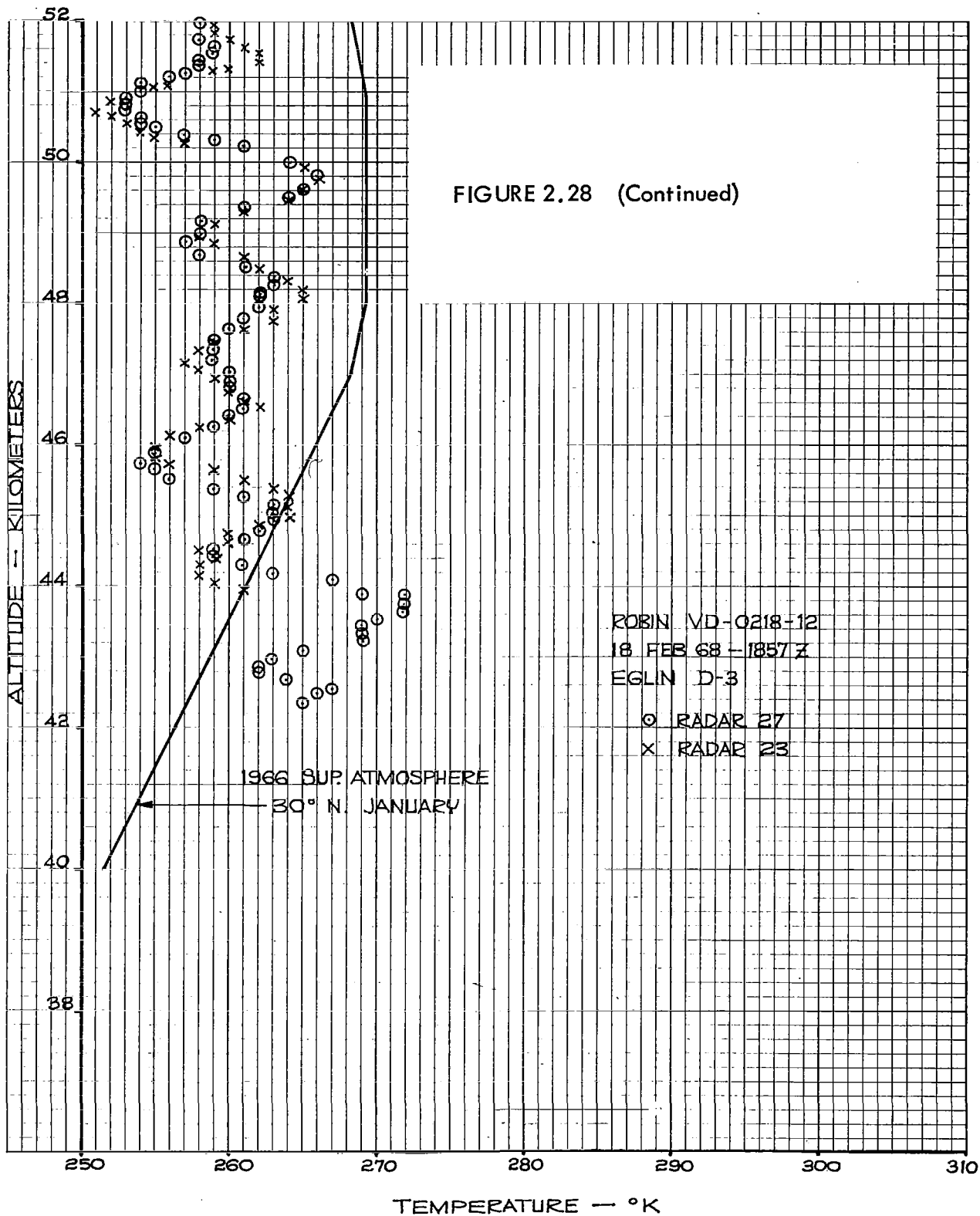


FIGURE 2.28 ROBIN REDUCED TEMPERATURE PROFILE - TWO RADARS





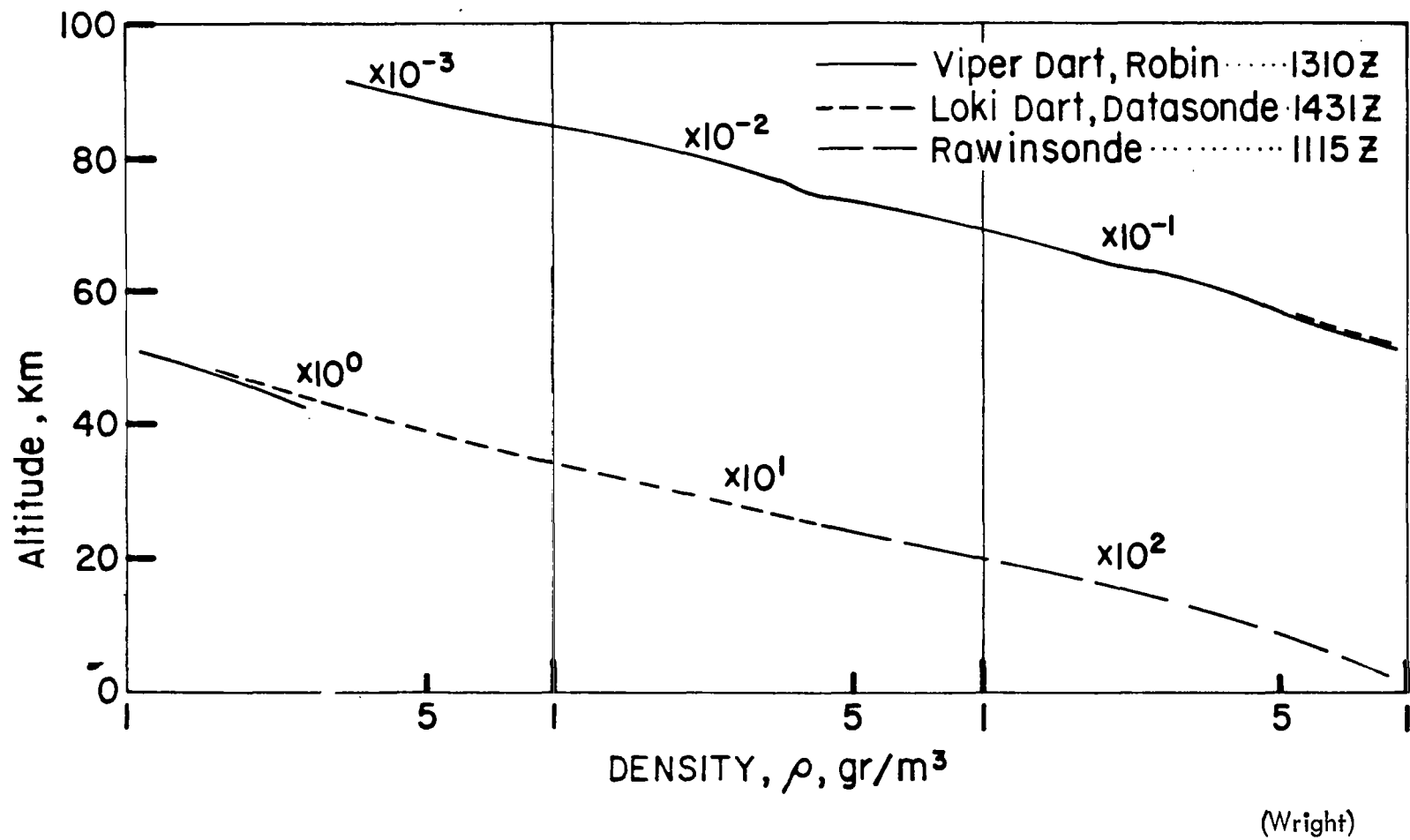


Figure 2.29 Density Profile, Apollo II Launch Support, ETR, Cape Kennedy, Florida, 14 July 1969

Table 2.6 Approximate Errors for Robin Using the AN/FPS-16 Radar and the "March 65" Data Reduction Program

Meteorological Parameter	Altitude		
	90 Km	80 Km	70 Km
Wind			
RMS Noise Error, m/sec.	20	5	4
Bias Error, m/sec.	3	3	2
Sinusoidal Wind Field Bias Error, % of Amplitude Measured			
4 Km Sinusoidal Wind	1	5	20
10 Km Sinusoidal Wind	16	40	80
Density			
Random Error, %	5	3	4
Bias Error, %	14	2	0

(Wright)

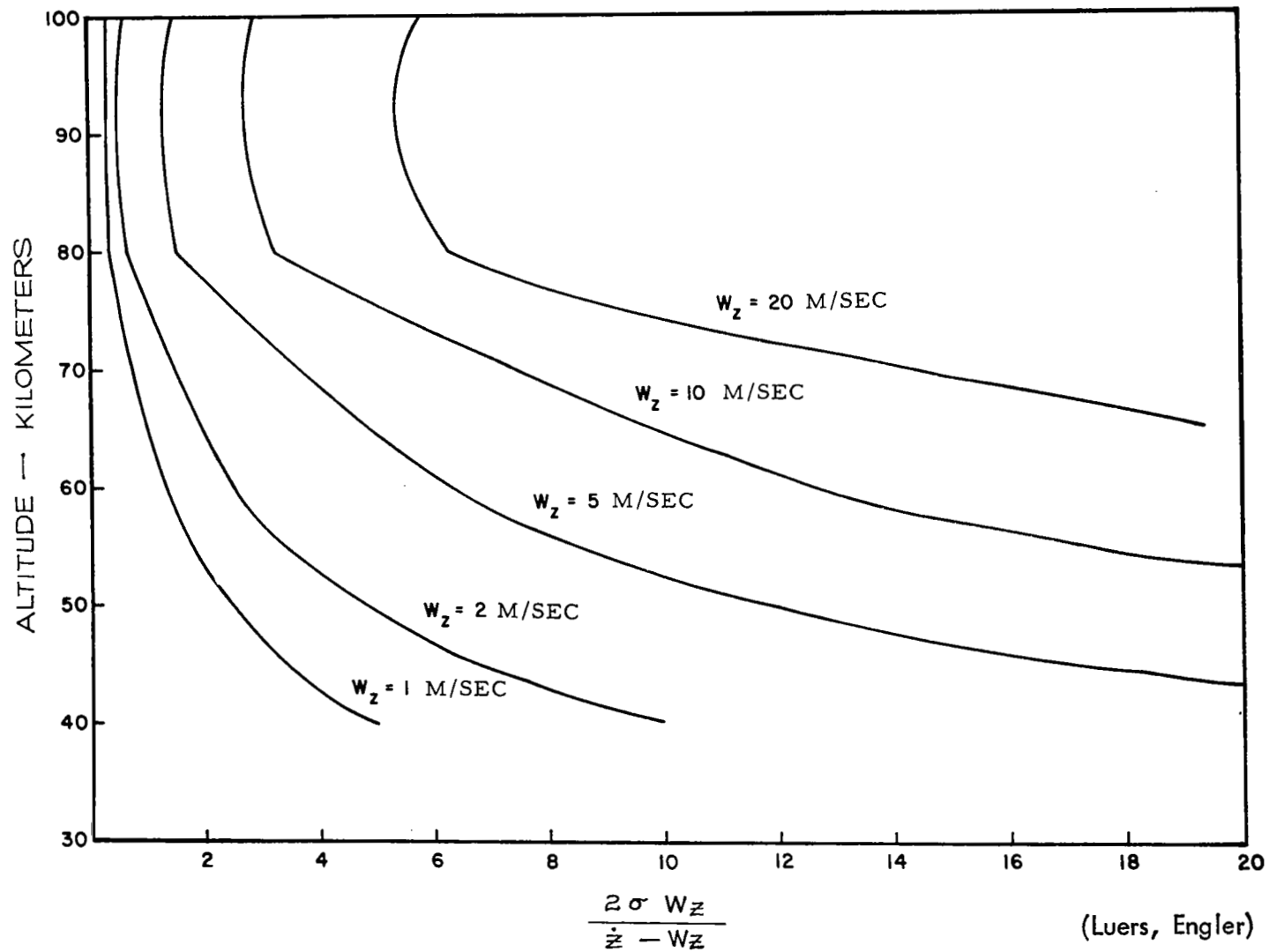
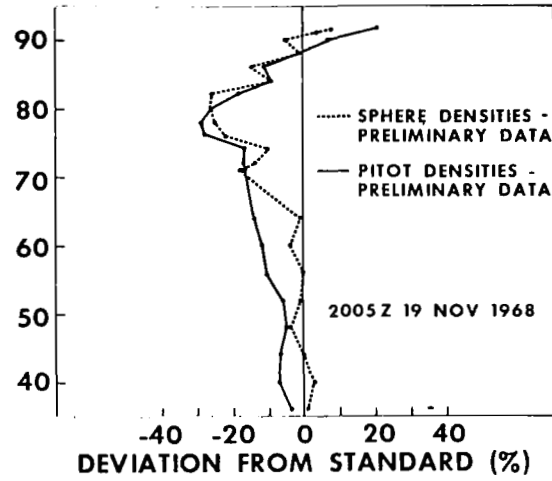
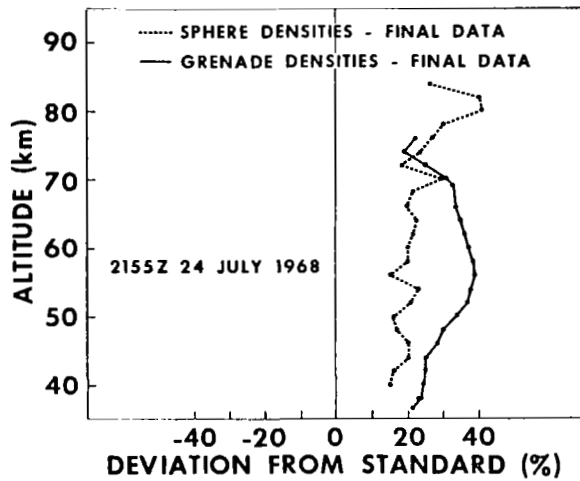
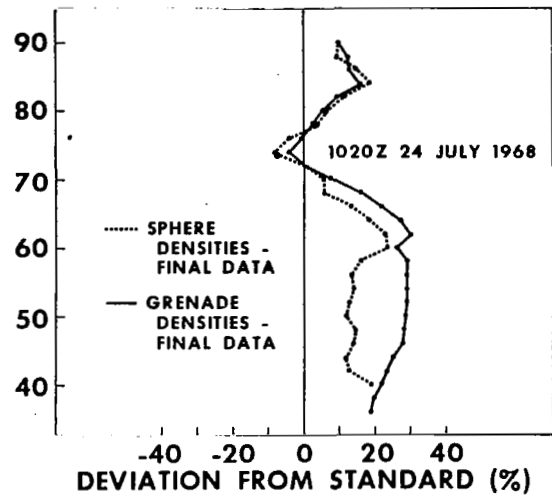
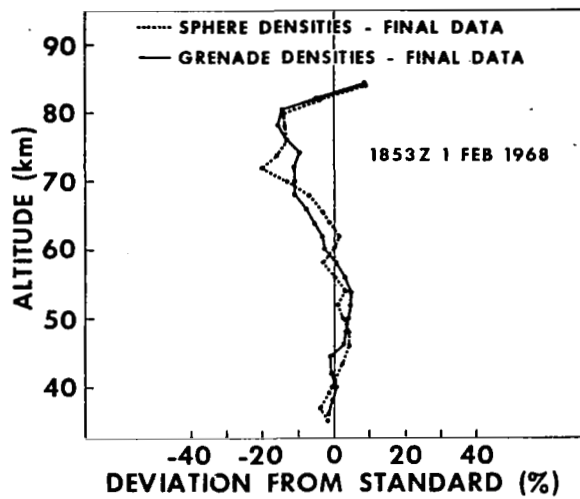


Figure 2.30 Density Error Resulting from Vertical Winds as a Function of Altitude - Escape Altitude, 125 km



(Smith)

Figure 2.31 Density Data, in Terms of Percent of Deviation from 1962 U. S. Standard Atmosphere, as Derived from Sphere and Grenade or Pitot-Tube Experiments Versus Altitude

2.5 Sandia Pitot-Static Probe.

Atmospheric density measurements have been made between the altitudes of 30 km and 90 km by D.J. Rigali and K.J. Touryan (reference 6), with a cone-cylinder pitot-static pressure probe using special thermoconductivity gauges as the sensors. The Nike-Apache two-stage solid-propellant sounding rocket was used together with a 14-channel FM-FM telemetry system, a roll-stabilized gyro platform, and a DME receiver for tracking information. The payload weighed 82 lbs and apogee altitude was 170 km.

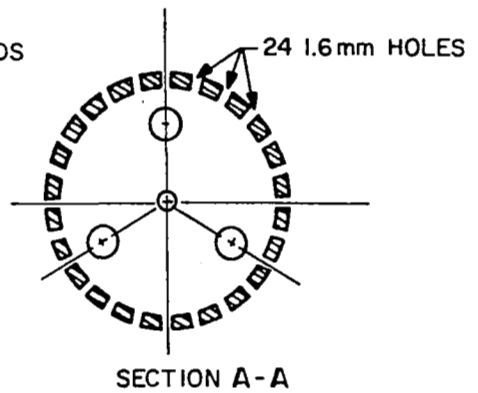
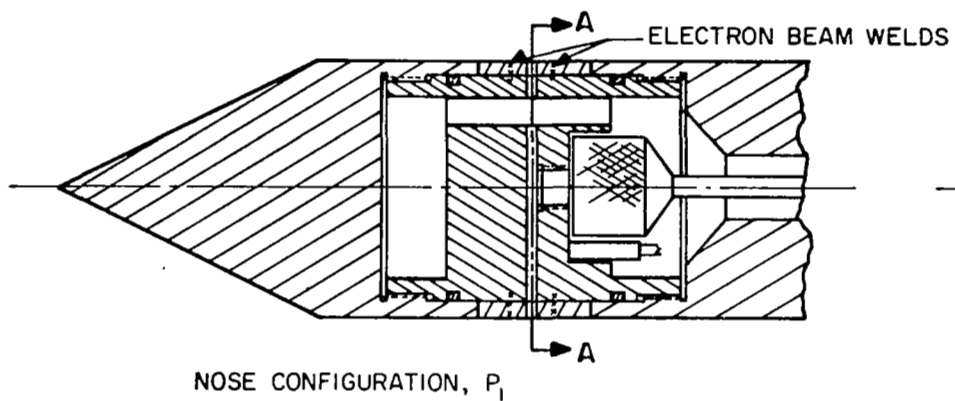
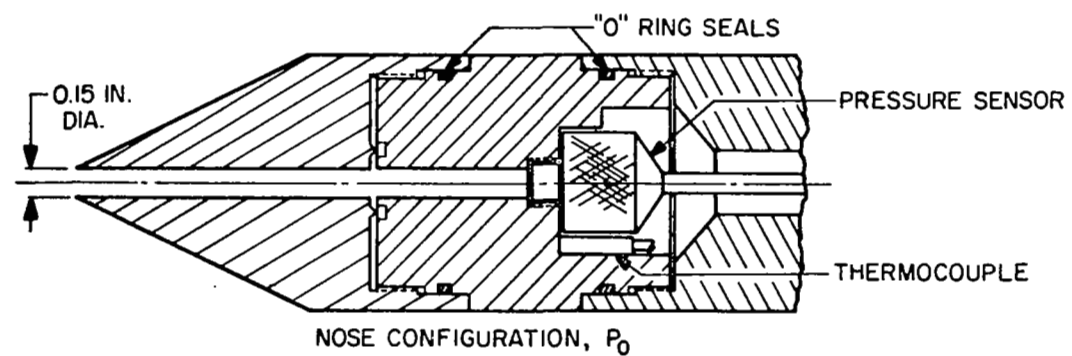
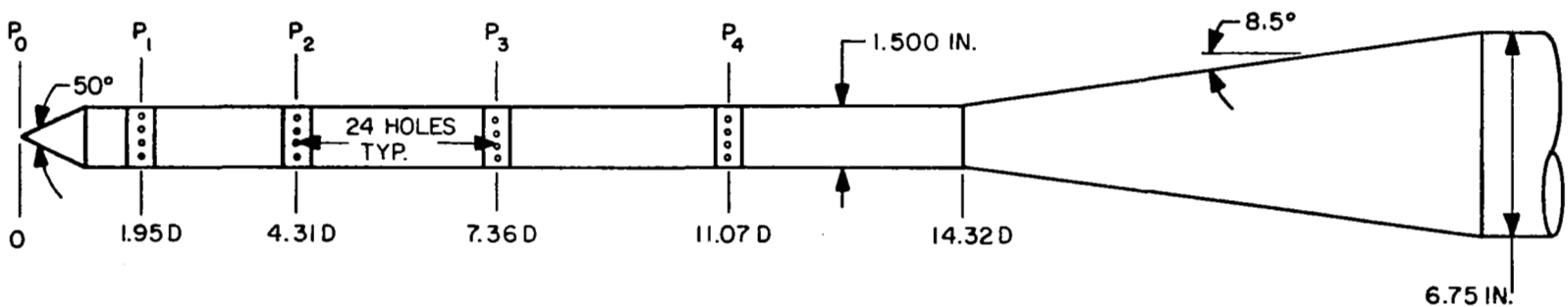
The payload configuration is shown in Figure 2.32. Twenty-four 0.062 inch diameter holes were located circumferentially at each of four probe stations to sample static pressure. Under low-density supersonic flow conditions the optimum location for these ports would be as far aft of the conical forebody as possible; however, interference from the aft payload flare due to boundary layer separation restricts the aftwise placement. On some of the flights, ram pressure was measured at the conical nose tip of the probe.

Probe pressures were sensed by 0.001 torr to 30 torr heated thermocouple gages. The output of each gage was divided into six pressure ranges yielding 0-5 volt dc outputs. Thermal conductivity of the atmosphere varies as a function of pressure, so that the equilibrium temperature of the heated thermocouple decreases with increasing pressure. The thermocouples are part of a bridge circuit which develops a dc potential which is directly proportional to the temperature. The sensor element is shown in Figure 2.33. The sensing element is made up of four heated fine-wire thermocouples mounted on a miniature header within a reflective housing to prevent heat loss by radiation. The housing is surrounded by a heater which is controlled by a thermostat. The pneumatic response time of the chamber has been determined to be 15 ms for a pressure step from 0 to 0.3 torr.

The raw pressure data obtained from each gage is corrected for low-density effects by means of wind tunnel calibration data. The ram pressure corrections include such factors as viscous effects, low Reynolds number effects and transpiration effects. The static pressure data must also be corrected for shock interaction effects, transverse curvature corrections and angle of attack effects. These corrections are significant above 60 km; however, the first station static measurement is influenced by the overexpansion around the forebody shoulder at even lower altitudes. Transpiration effects enter the pitot pressure data at low densities because of large differences between temperature at the probe stagnation point, T_o , and the temperature at the pressure sensor, T_g . For Knudsen numbers relative to probe radius, r , greater than 0.01 this temperature gradient can maintain a pressure gradient as

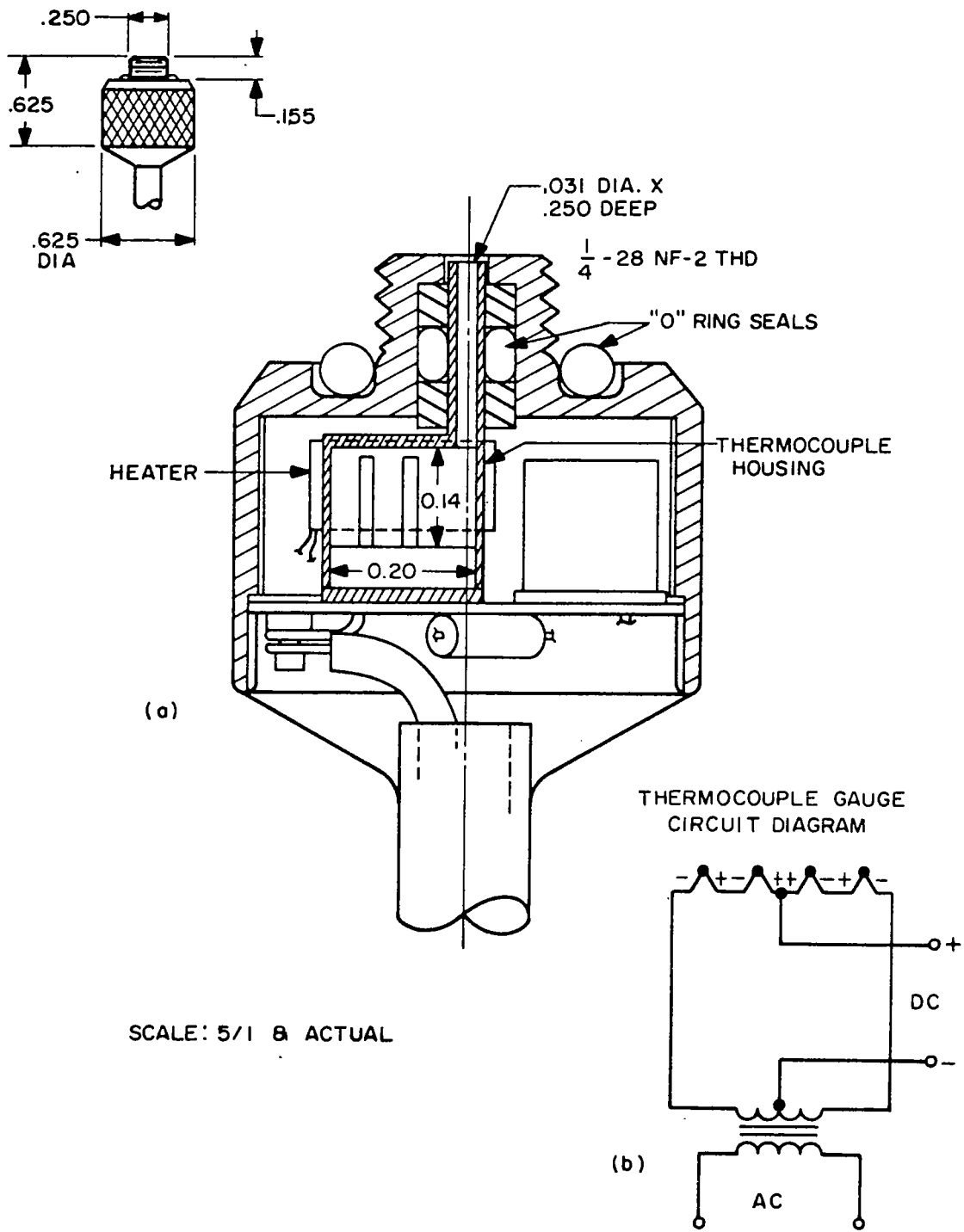
$$\frac{P_{\text{gauge}}}{P_o} = F(\text{Kn}) \sqrt{\frac{T_g}{T_o}},$$

where $F(\text{Kn})$ has been determined experimentally. Thermocouples located at T_g and



(Rigali, Touryan)

Figure 2.32 Sketch of Cone-Cylinder Probe



SCALE: 5/1 & ACTUAL

(Rigali, Touryan)

Figure 2.33 Sketch of Sensor Element and Thermocouple Circuit Diagram

heat transfer estimates to the probe tip yield $T_o/T_g \leq 3.0$. At 85 km the Knudsen number relative to r at the gauge is about 0.13 and the corresponding pressure ratio $p_{gauge}/p_o \simeq 0.93$, which is a lower bound for the current configuration. This 7 percent correction is in the opposite direction to changes in p_o introduced by viscous-rarefaction effects; it is lower in magnitude and is within the 10 percent uncertainty band of the rarefaction corrections.

A list of low-density corrections for the pitot pressure data obtained on a typical flight is presented in Table 2.7. The second column lists corrections arising from low Reynolds number effects, where p'_o is the measured pressure and p_o is the corresponding Rayleigh-pitot pressure. The fourth column is the temperature ratio between the stagnation point and the gauge corresponding to the Knudsen number Kn at the gauge. The fifth column gives the resulting pressure change caused by this temperature gradient, and the last column is the net correction.

Table 2.7 Low-Density Corrections for Pitot Pressure Data

Altitude (km)	p'_o/p_o	Kn_{gauge}	T_o/T_{gauge}	p_{gauge}/p'_o	p_{gauge}/p'_o
75	0.98	0.033	3.0	0.98	0.96
80	1.02	0.080	2.7	0.94	0.96
85	1.20	0.128	2.4	0.93	1.11
90	1.40	0.281	2.0	0.90	1.26

Pitot and static pressure data from the various launches are used in the corrected Rayleigh-pitot formula to yield the density as

$$\rho = \frac{0.144p_o - 0.066p_s}{V^2},$$

where V is the rocket velocity along its trajectory, p_o is the impact or pitot pressure, p_s is the static pressure. In accordance with the above equation and the typical flight conditions of a rocket pitot probe with an apogee on the order of 200 km, the errors in the static pressure are found to be negligible as in Table 2.8. Thus, it is evident that the static pressure measurements are unnecessary as long as ram pressure

is measured. The deviations in pressure from the standard atmosphere seldom exceed $\pm 20\%$, so by using the standard value for the above computation less than 0.3% error in density is incurred. For reasons of gage sensitivity, angle-of-attack variation and time response, the ram pressure measurement is superior, especially with a hemispherically typed probe. It appears that the Sandia experiments were much more complicated and costly than they needed to be.

Table 2.8 Error in Density Calculation with Assumed Static Pressure Errors

Assumed Static Pressure Error	Error in Calculated Density	
	60 km	90 km
10%	0.131%	0.117%
20%	0.260%	0.231%

Omitting low-density corrections and outgassing problems, some important sources of error in measuring static pressures by sounding rockets are inherent errors in the pressure sensors; errors in the TM system; time response in the pressure ports and chambers; and angle-of-attack variations. The TM data was received on FM-FM channels in analog form and converted into digital form with a maximum overall error of 2 percent. Table 2.9 lists the pressure ranges, the approximate gauge sensitivity, the responsibility of each range based on the 0.1 volt TM error, and the repeatability in percent of full-scale pressure.

Table 2.9 Static Pressure Measurement Parameters

<u>Pressure range (torr)</u>	<u>Nominal gauge sensitivity (torr/volt)</u>	<u>Repeatability* (% of each pressure range)</u>	<u>Repeatability* (% of full-scale pressure range)</u>
0-0.025	0.005	8	0.007
0.025-0.10	0.015	2.7	0.007
0.10-0.25	0.030	2	0.017
0.25-1.0	0.15	2	0.07
1.0-7.5	1.3	2	0.5
7.5-30	4.5	2	2

*Assuming a TM error of 0.1 volt or a gauge repeatability of 2 millitorr, whichever is the greater.

Two sources of error arise from time lag. The first is in the response of the thermoconductivity gauge to the changes in the chamber environment. This was estimated to be 70 msec below 70 km and 100 msec above 70 km. The second error is due to time lag between changes on the rocket exterior and the gauge housing. This lag was also estimated to be about 70 msec. At a maximum speed of 1500 msec this amounts to an error of 0.2 km.

The total angle of attack is found to be $0 \leq \alpha \leq 7^\circ$. Low-density wind tunnel calibrations show that the largest changes in p_s at $\alpha = 7^\circ$ occur for $M \geq 5$. For present test conditions this introduces a maximum deviation of 6 percent from the $\alpha = 0$ case in the magnitude of p_s for the flight conditions. By means of previous calibrations and recorded angle-of-attack data on the flights, this error can be reduced to 3 percent. Table 2.10 lists the various errors in the static pressure calculation of density.

Table 2.10 Static Pressure Errors

Type of error	Altitude in km	Percent error				
		Flight 154-64			Flight 154-65	
		P_0	P_3	P_4	P_1	P_3
Gauge	< 80	2	2	2	2	2
	> 80	5	8	8	8	8
Time lag		2	3	3	3	3
Angle of attack	< 60	0	2	2	2	2
	> 60	2	3	3	3	3
Low density and hypersonic flow corrections	< 70		None		10	None
	> 70	10	10	10	15	10
Over-all uncer- tainty in p_s (or ρ from Equation 4)	< 60	3.5	4.6	4.6	4.6	4.6
	> 60	11.7	13.6	13.6	17.3	13.6

The over-all uncertainty in p_s was obtained by taking the square root of the sums of squares of each error and dividing it into two altitude regions: below 60 km and above 60 km.

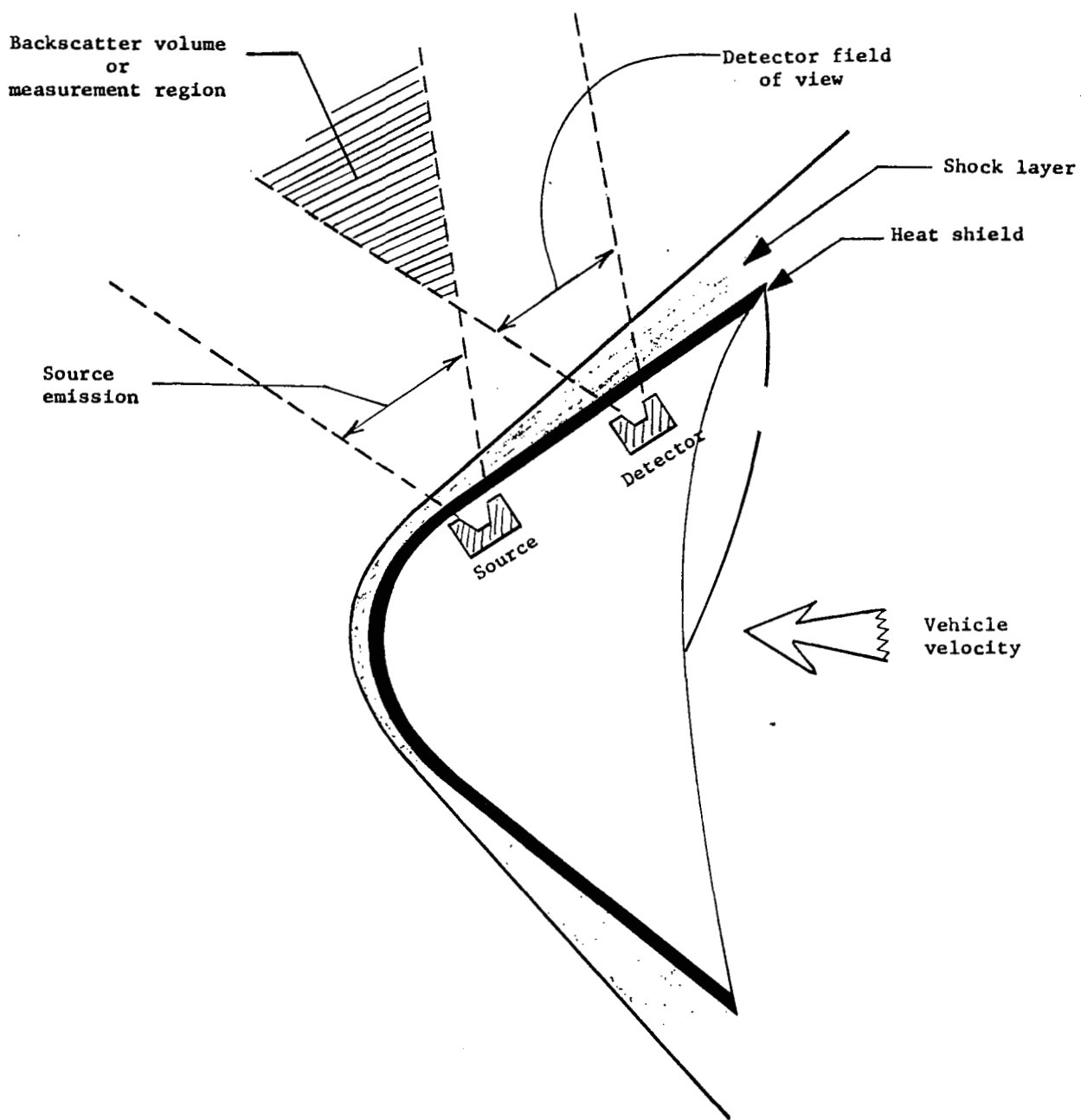
2.6 Gamma-Ray-Backscatter Technique for Density Measurement.

Studies have been made by LeBel (reference 7) of a technique which uses the backscattering of gamma radiation emitted by a radioisotope source to measure the ambient density from a rapidly moving rocket vehicle. Because of the penetrating ability of the radiation no probes or special windows are required in the rocket vehicle. The measurement is essentially unaffected by the composition of the atmosphere, by the shock layer, and by motions of the vehicle. As shown in Figure 2.34 the sensor consists of a source of gamma radiation, a detector and shielding material to eliminate the direct transmission between the two. The gamma rays propagate out through the wall of the vehicle without severe attenuation. A fraction of the emerging gamma radiation is backscattered by the atmosphere into the detector. The backscatter interaction, Compton scattering of gamma rays by atomic electrons, is linearly dependent upon the atmospheric density in the scattering region. By proper location of sensor components and collimation of the source emission and detector field of view, the effective scattering volume or measurement region can be located in the undisturbed ambient atmosphere beyond the shock wave. Advantages of this technique are as follows:

- a. The measurement is a direct, linear function of the ambient atmospheric density.
- b. No probes or special windows through the vehicle skin are required because of the penetrating ability of the radiation.
- c. Atmospheric composition measurements are not required for accurate density measurements.
- d. The shock layer and vehicle motions have a negligible effect upon the measurement.

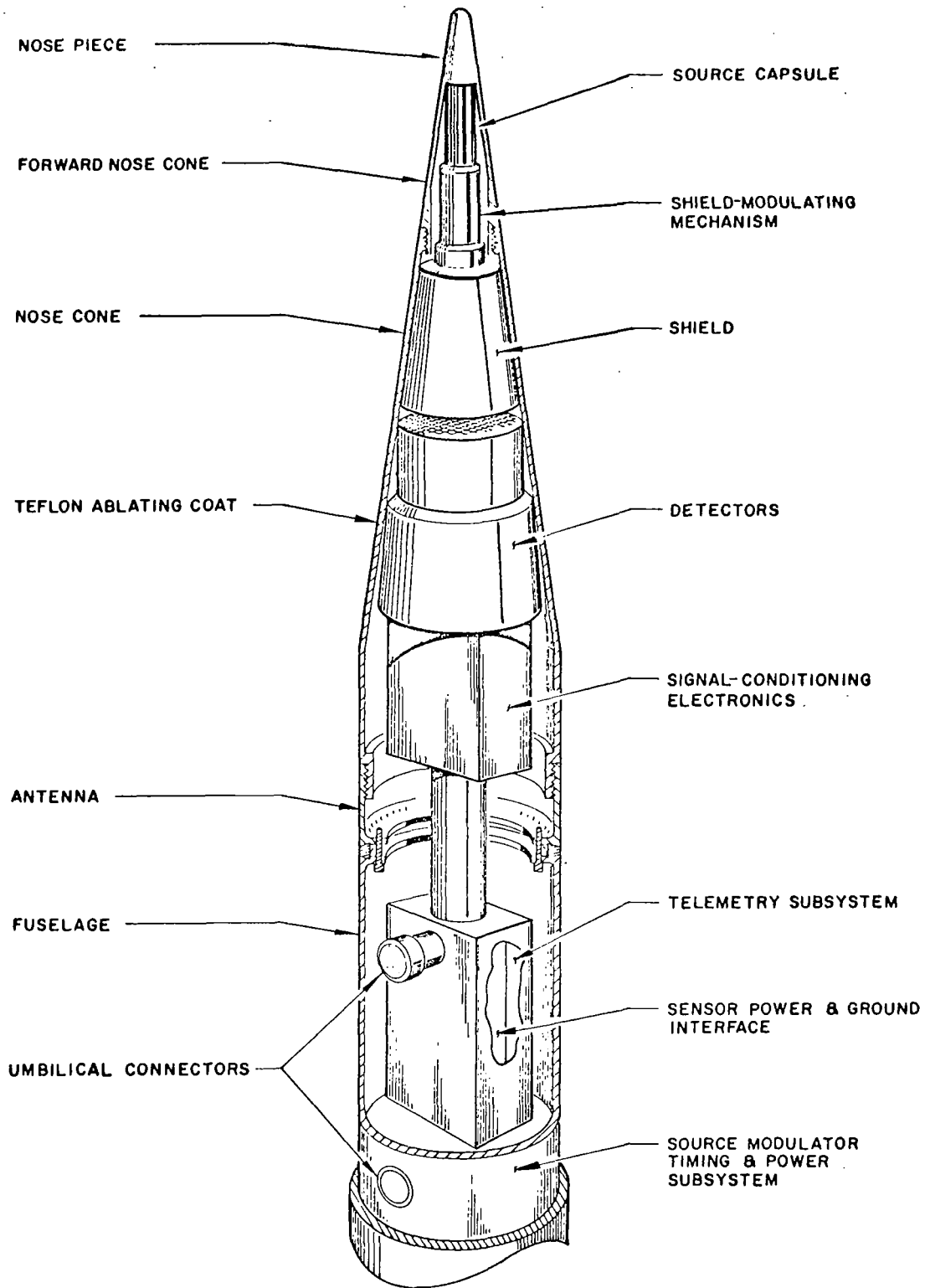
In the range between 10 KeV and 10 MeV Compton scattering is the primary mode of backscatter. This is incoherent scattering, in which the gamma ray acts like a particle and undergoes a collision with an electron. The electron absorbs some of the gamma ray energy and is freed from the atom. The scattered gamma ray has an energy which depends upon its original energy, the energy absorbed by the electron and the scattering angle.

Although this technique has been studied for Martian reentry measurements, prototype sensors have been flown with the Nike-Apache sounding rocket. The payload configuration for these flights is shown in Figure 2.35. A sodium iodide scintillation detector was used with 30 curies of the isotope cerium-144. The resulting data is presented in Figure 2.36. As a result of these flights, investigations have been initiated by NASA-RLC to reduce background noise and to develop a high-purity radioisotope source.



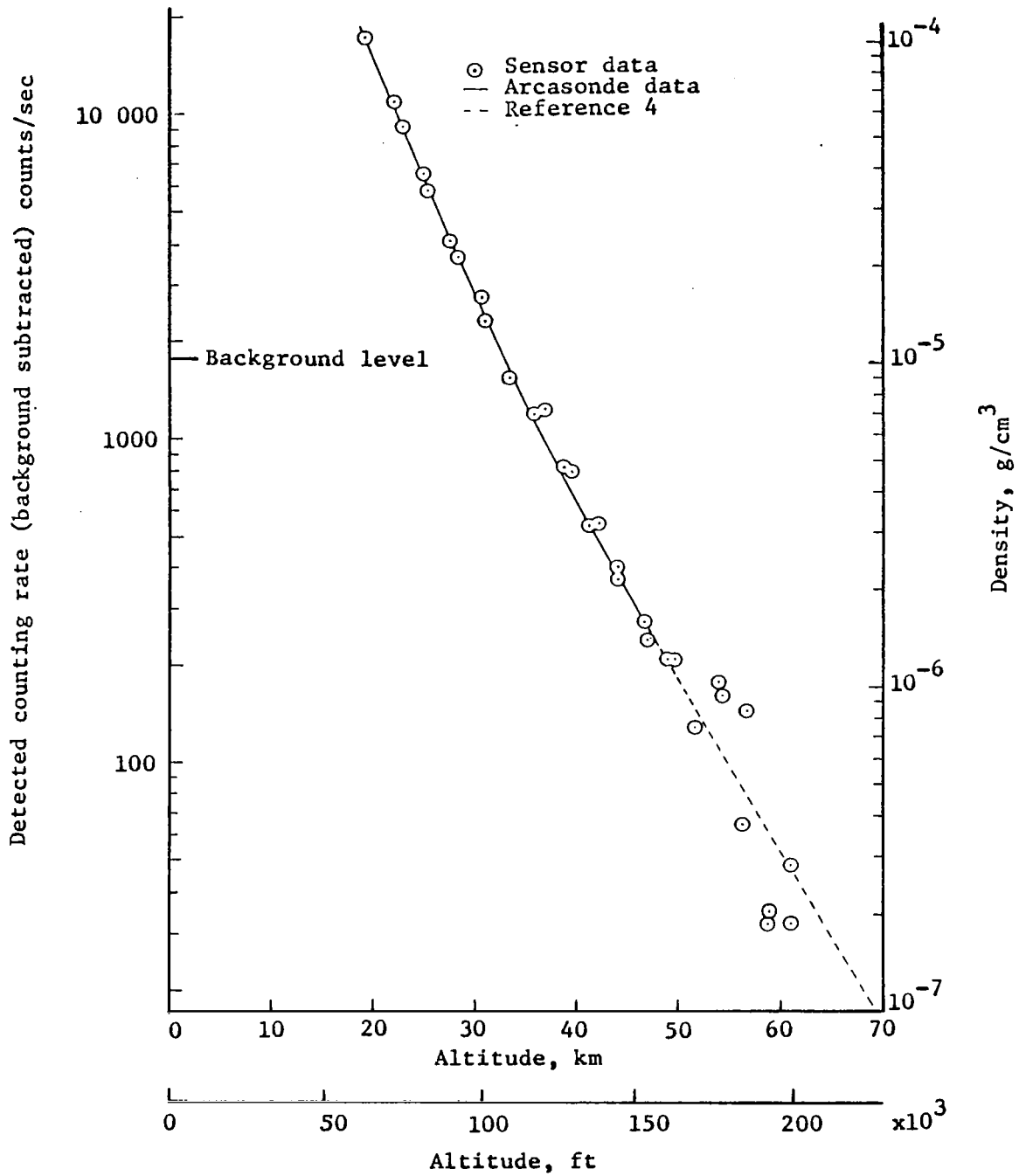
(LeBel)

Figure 2.34 Schematic Drawing of Gamma Ray Backscatter Configuration For In-Flight Measurement of Atmospheric Density



(LeBel)

Figure 2.35 Payload Of Nike-Apache Backscatter Density Sensor



(LeBel)

Figure 2.36 Detected Counting Rate (Background Subtracted) and Density as a Function of Altitude for an Earth-Atmosphere Flight Test

The backscattering counting rate, or signal, S is a function of the gamma ray flux emerging from the source, gamma ray energy, attenuation in the gamma ray path, Compton scattering cross section in the atmosphere, detector area and efficiency, and the geometry parameters, such as the source-detector separation and the collimation angles. For fixed source, detector, and geometry, all these parameters are constant, with two exceptions, attenuation in the shock layer and the atmospheric Compton scattering cross section σ . Although not constant the attenuation in the shock layer is expected to be very small and can be neglected. The total atmospheric Compton scattering cross section is given by

$$\sigma_s = \sigma_{s,e} N \rho \frac{Z}{A}$$

where $\sigma_{s,e}$ and N are constant,

Thus, the backscattered counting rate, or signal, can be represented by

$$S = K \rho \frac{Z}{A}$$

where K is a proportionality constant which includes the source, detector, and geometry parameters previously mentioned.

This expression shows that the response of the device is a direct function of atmospheric density. The only other atmospheric parameter which affects the signal is the ratio of atomic number to atomic weight. This ratio is equal to 0.5 for all the significant gases in the atmosphere up to an altitude level of 100 km.

Background radiation contributes to the total counting rate. Therefore, it is important to reduce the background noise for maximum measurement sensitivity and to precisely measure background counting rate for maximum measurement accuracy. The background counting rate is subtracted from the total counting rate so that the backscattered counting rate or signal can be determined.

Three factors which contribute to the background noise are:

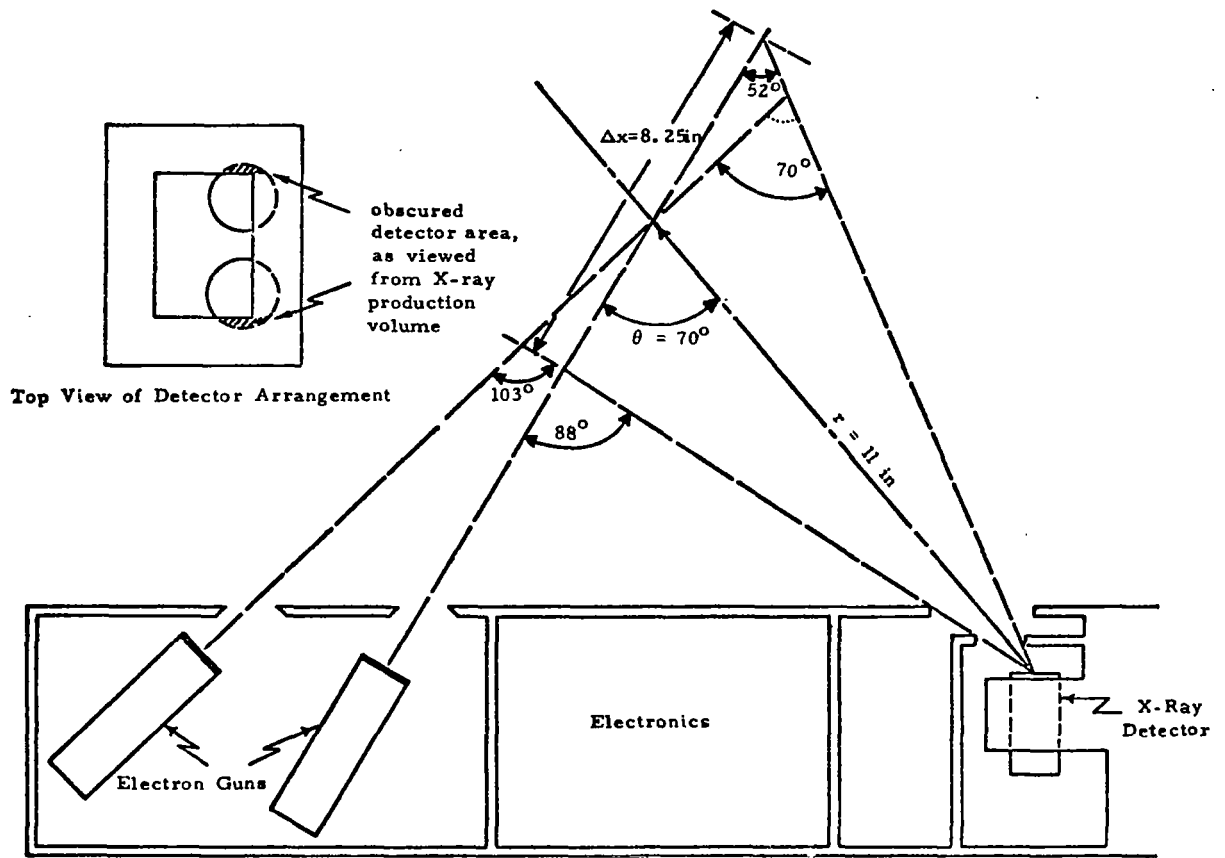
- a. Natural background radiation due to cosmic rays and other sources would contribute on the order of 50 counts per second to the total counting rate for a typical detection system and measurement geometry.
- b. Direct transmission noise caused by gamma rays traveling directly between the source and detector.
- c. Skin scatter noise. This is caused by multiple scattering of gamma rays within the vehicle skin and into the detector. This can be reduced considerably by choosing a geometry that requires the gamma ray to undergo a third scatter before being detected. Skin scatter noise has also been found to be a strong function of the source to detector separation distance. Small increases in this separation distance will significantly reduce the noise without appreciably affecting the back-scattered signal.

Although a feasible gamma ray energy level is required to penetrate the vehicle skin, as low as possible gamma ray energies are desirable so that shielding weight is minimized and the cross section for scattering at large angles is a maximum at low energies. Most ideal source would be mono-energetic so that a narrow energy discrimination window could be established to increase the signal-to-noise ratio. The radioisotope comes closest to being the ideal monoenergetic source. The source half-life is important from the standpoint of feasible shelf life.

The detection system consists of a scintillation-crystal-photomultiplier-tube detector. The detector area should be maximized consistent with such factors as the increased shielding weight and the increased susceptibility of large crystals to physical damage from shock and vibration. Some form of automatic gain control will be necessary to compensate for the poor gain stability of a scintillation detector with temperature. Calibration in a vacuum chamber where gas density can be carefully controlled and varied is necessary. Calibration should take place in as large a vacuum chamber as possible to minimize scattering of gamma rays from the chamber walls and into the detector. Gas pressure and temperature measurements should be taken to monitor the gas density. Scaling down the source intensity for the calibrations will probably be required since wall scattering on the calibration chamber may be too great for the full intensity flight source. Scaling technique requires that the ratio of the gamma ray outputs of the two sources be precisely known.

2.7 Bremsstrahlung X-Ray Technique For Density Measurement.

The detection of Bremsstrahlung x-rays generated by the injection of an electron beam from a rocket vehicle into the atmosphere has been used by Sellers and Ziegler (reference 8) as a basis of atmospheric density measurement between the altitudes of 100 and 200 km. It has been found that the detected x-ray flux is linearly related to the ambient air density. In this technique an electron gun aboard a rocket vehicle fires out into space at the side of the vehicle, as shown in Figure 2.37, an electron beam interacts with the atmospheric molecules and causes the generation of Bremsstrahlung x-rays. The intensity of these generated x-rays is measured with on-board x-ray detector equipment. The number of Bremsstrahlung x-rays generated within a selected segment of the beam via electron-gas atom interaction is directly proportional to atomic density. The systems response is dependent upon the average atomic number of the atoms which constitute the gas but is independent of chemical form, degree of ionization and temperature of the gas. With this method air density can be determined to better than 10% accuracy over the range from 100 to 200 km. The lower altitude limit is set by the requirement that the electron gun not be exposed to pressures above about 10^{-3} torr. The upper limit is that altitude at which the detector counting



(Sellers, Ziegler)

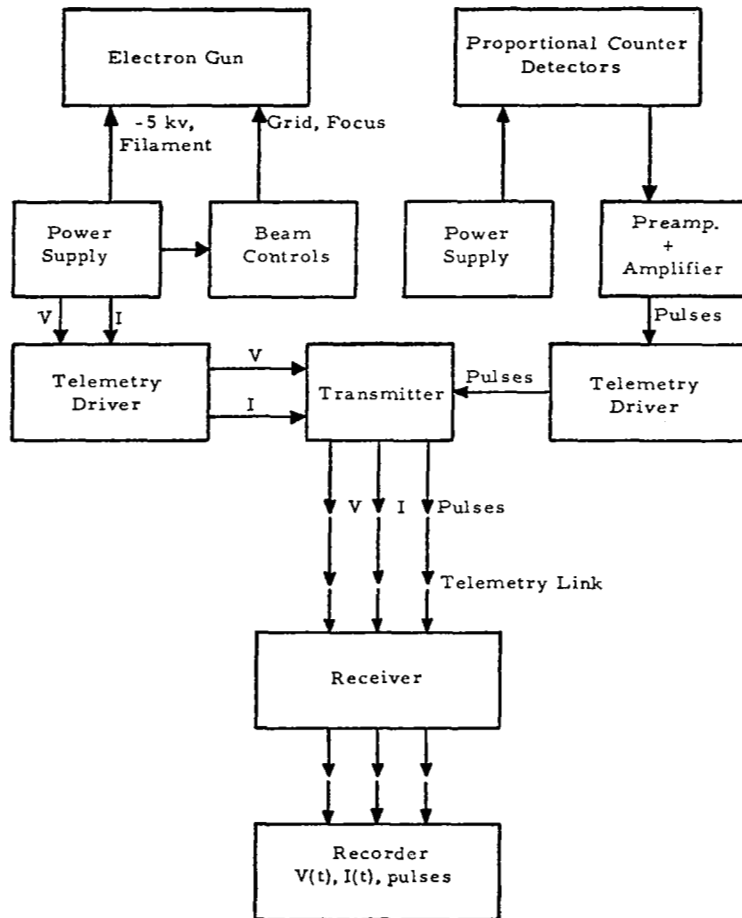
Figure 2.37 Source Detector Sonde Geometry

rates become comparable to the background rate. The advantage of this method is that the "sensed volume" can be selected outside of the shock wave effects. At an altitude of about 100 km the panels covering the electron gun and detector ports are ejected and the end of the electron gun is cut off; thereby the electron gun cathode has been protected from the adverse effects of the high density and high pressure atmosphere. Electron beam voltage and electron beam currents are telemetered with the pulses resulting from detection of the x-rays. The maximum counting rate expected is less than 800 counts per second which offers no problem for the telemetry system. A block diagram of the telemetry system is presented in Figure 2.38.

2.8 Radio Frequency Mass Spectrometers.

Radio frequency mass spectrometers have been used for measuring many properties of the upper atmosphere, such as neutral gas composition from 100 km to 250 km. This is the altitude at which diffusive separation starts as determined by measuring the ratio of argon to molecular nitrogen, and the positive ion composition of the atmosphere. Basically, three RF mass spectrometers have been used for sounding rocket flights into the upper atmosphere. These are the omegatron, the gridded spectrometer and the quadrupole spectrometer. A comparison presenting the important characteristics of these three RF spectrometers by Gilmour (reference 9) is presented in Table 2.11. It appears that the quadrupole spectrometer is the most useful for sounding rocket flights because of its simplicity, light weight, ruggedness and excellent performance.

A major problem encountered with the use of all of these spectrometers has been contamination due to residual gases in the spectrometers as well as various components of the probe. It has been shown that all components must be thoroughly out-gassed prior to measuring gas constituents at low pressures. All exposed surfaces should be out-gassed in a high vacuum chamber at a temperature of at least 450° C until the pressure in the chamber is below 10^{-8} torr. After all exposed surfaces are properly out-gassed, they must not come into contact with a gas at a temperature above 10^{-4} torr; enough absorption will occur to cause contamination and errors in the data. For practical measurements the components must be out-gassed by a pressure level at least a couple of orders of magnitude below that of the intended region.



(Sellers, Ziegler)

Figure 2.38 System Operational Schematic

Table 2.11 Characteristics of RF Mass Spectrometer

CHARACTERISTICS	TYPE OF RF SPECTROMETER		
	OMEGATRON	GRIDDED SPECTROMETER	QUADRUPOLE SPECTROMETER
RESOLVING POWER	$\frac{1}{\text{MASS}}$, 40 AT MASS 28	100	1500
PRESSURE RANGE (ASSUMING 10^{-13} AMPERES IS LIMIT OF CURRENT METER)	$10^{-5} - 10^{-10}$ TORR	$10^{-4} - 10^{-8}$ TORR	$10^{-4} - 10^{-10}$ TORR
FREQUENCY RANGE (CORRESPONDING TO MASS RANGE OF 1 - 100)	6 MC/S - 40 KC/S	5 MC/S - 500 KC/S	5 MC/S - 500 KC/S
RF VOLTAGE REQUIRED	3 VOLTS	100 VOLTS	1000 VOLTS
MAGNETIC FIELD REQUIRED	4000 GAUSS	NONE	NONE
WEIGHT (INCLUDING CIRCUITRY NECESSARY TO PROVIDE INPUT SIGNAL FOR TELEMETRY EQUIPMENT)	25 POUNDS	5 POUNDS	5 POUNDS
POWER REQUIRED	15 WATTS	15 WATTS	15 WATTS

(Gilmour)

2.8.1 Omegatron.

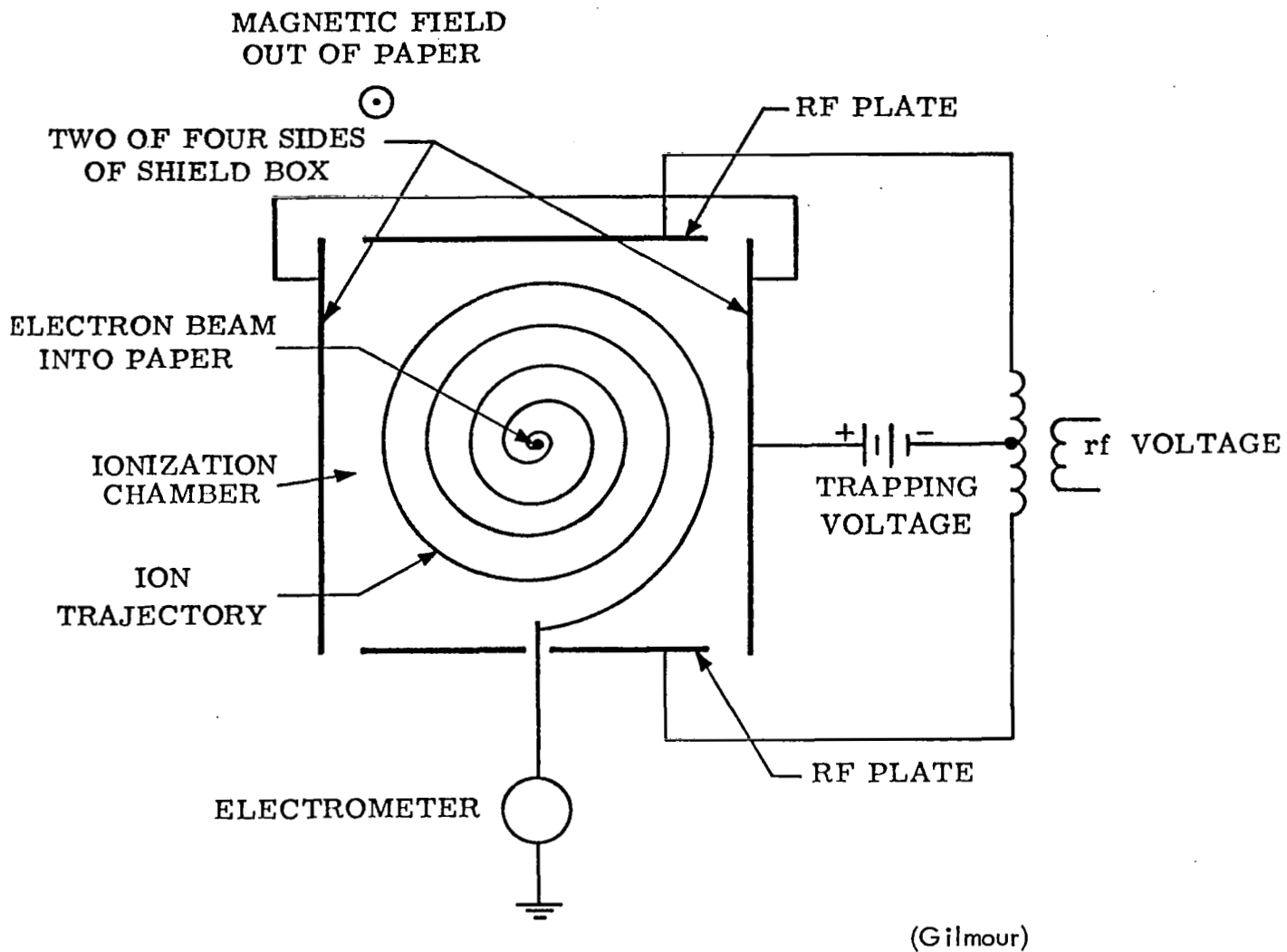
The omegatron is the simplest of the mass spectrometers and is shown schematically in Figure 2.39. A low density electron beam containing a few microamperes of current is formed by accelerating electrons from a hot filament through an aperture in the center of the side of a metal box which has the shape of a 2 cm cube. This beam travels across the box, ionizing gas molecules, and exits through an aperture in the opposite side. It is collected by a plate which is at a positive potential with respect to the box.

The ions formed by the electron beam are acted upon by an RF field created by plates on two opposite sides of the box and attached to a common RF signal source. Because the omegatron is immersed in a magnetic field that is parallel with the direction of flow of the electron beam and perpendicular to the RF electric field, the ions are accelerated in spiral orbits of increasing size, provided that the frequency of the electric field is the same as the cyclotron frequency of the ions. A positive trapping voltage is applied to the shield box to prevent ions from moving in a direction parallel with the magnetic field and being lost to the box. Thus those ions with a cyclotron frequency equal to the frequency of the applied field are collected by a small metal plate in the center of one of the RF plates. The ion current is a measure of the partial pressure of the selected gas.

Mass scanning can be accomplished by varying either the frequency of the RF voltage or the intensity of the magnetic field. The pressure range over which the omegatron can be used has been found to be from 10^{-5} torr to 10^{-11} torr, the upper limit being imposed by scattering of the ions from gas molecules and the lower limit by measuring the minute ion currents at the ion collector. Resolving power for the omegatron is defined by the midpeak frequency divided by the width of the resonant peak. A typical value is 40. The resolving power varies inversely with mass so that the omegatron is useful only for analyzing ions of low mass. The magnetic field required is about 4000 gauss, so that the magnets required for the omegatron are relatively heavy.

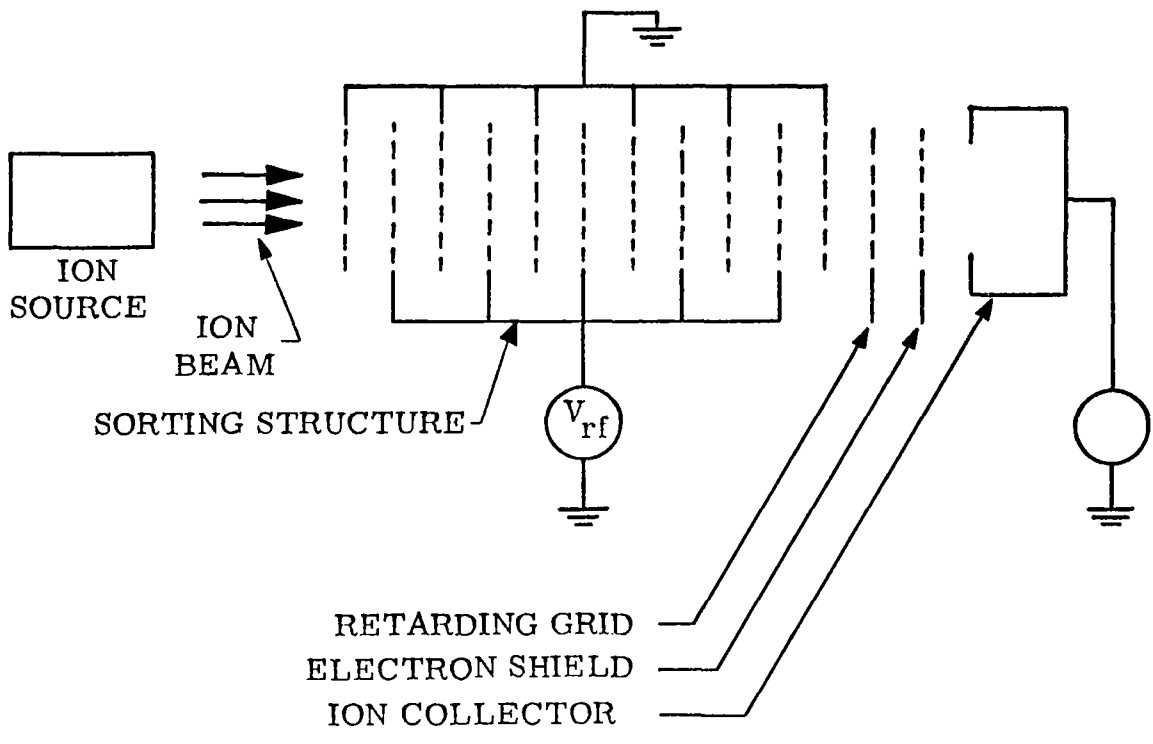
2.8.2 Gridded Spectrometer.

The gridded spectrometer as shown in Figure 2.40 consists of an ion source, and a sorting structure of equally spaced parallel-plane grids. RF voltage is applied to alternate grids of the sorting structure. All ions entering the sorting structure from the ion gun have nearly the same energy, but their velocities depend on their masses. All ions are assumed to be singly charged. Those ions entering the sorting structure during the proper phase angle and having transit times between adjacent grids near the half-period of the applied RF voltage are accelerated as they pass through the sorting structure and are able to pass the



(Gilmour)

Figure 2.39 Schematic Diagram of Omegatron (RF Plates Form End Caps to Shield Box which Surrounds Ionization Chamber)



(Gilmour)

Figure 2.40 Schematic Drawing of Gridded Spectrometer

retarding grid and reach the ion collector. By varying either the frequency of the RF voltage or the initial energy of the ion beam, one can select ions of various masses. The ion current at the collector indicates the rate of formation of ions of a particular gas in the ion gun and therefore, after calibration of the spectrometer, is a measure of the partial pressure of that gas. The pressure range in which the RF spectrometer may be used is presently from 10^{-4} to 10^{-8} torr. The upper limit is imposed by the mean-free path length of the ions and the lower limit by the difficulty of measuring the minute collected ion currents. Typical resolving powers for the gridded spectrometer are from 50 to 100. The major disadvantages of this device are: (1) the ion current of a desired mass arriving at the ion collector is a small fraction of that leaving the ion gun, because of ion interceptions by the sorting structure and because only those ions entering the sorting structure during a small part of the RF cycle are accelerated; (2) the resolving power is degraded by an energy spread of the ion beam leaving the ion gun; (3) since both the resolving power and the calibration of partial pressure are functions of the ratio of the retarding voltage to the RF voltage, this ratio must be controlled to an accuracy of a fraction of one percent over the frequency range of the spectrometer to obtain reasonable results.

2.8.3 Quadrupole Spectrometer.

The quadrupole spectrometer, as shown in Figure 2.41, consists of an ion source and an ion detector similar to those used in the gridded spectrometer as well as a sorting structure that consists of four circular rods parallel with one another and positioned on the four corners of a square. By applying the proper RF and DC voltages to the sorting structure, one obtains a mass filter that has a band-pass characteristic. The ion mass-to-charge ratio at the center of the pass band and the width of the pass band can be varied by adjusting the voltages, amplitude or frequency, applied to the four circular rods. Thus ions having the proper mass-to-charge ratio can pass through the quadrupole filter along its axis and be collected by the ion detector.

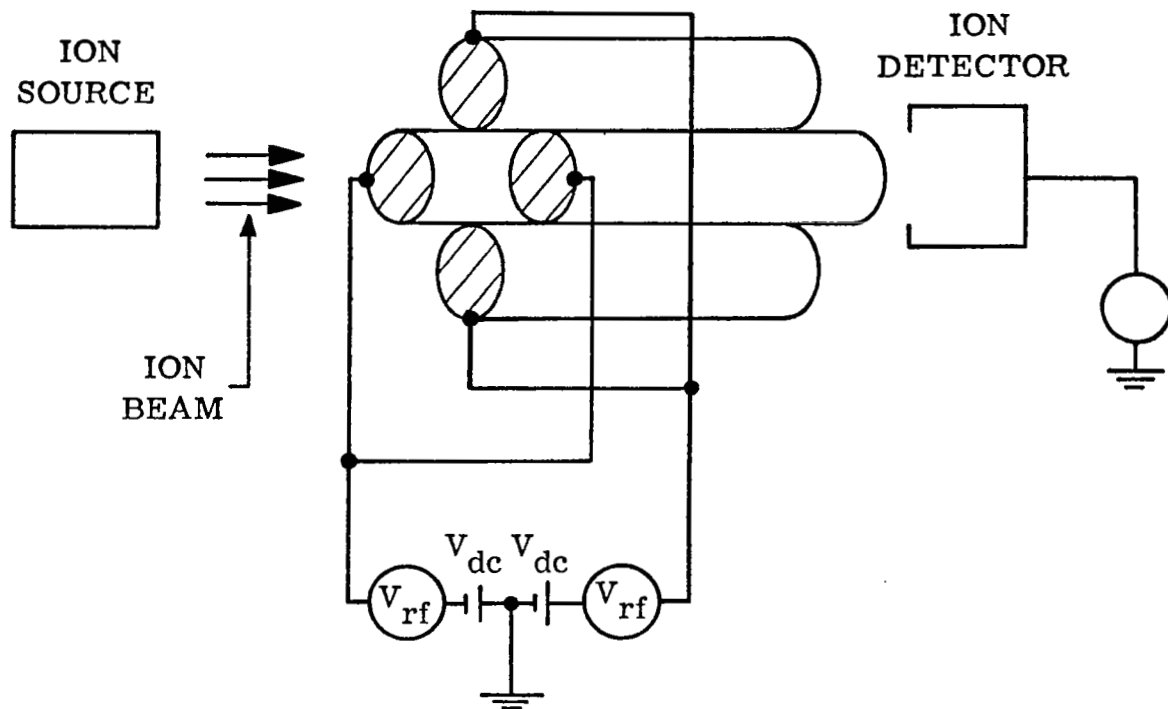


Figure 2.41 Quadrupole Spectrometer

2.9 Ultraviolet Filter Rocket Ozonesonde.

A rocketborne ozonesonde based upon the selective absorption of ultraviolet sunlight has been developed and successfully flight tested by Arlin J. Krueger (references 10, 11, 12). This instrument has been developed for the Arcas rocket. It measures the ultraviolet intensity from the sun at various wavelengths during descent with the rocketsonde parachute. The data is telemetered via the AN/GMD-1 system with some ground-station modifications to recover and digitize the output information.

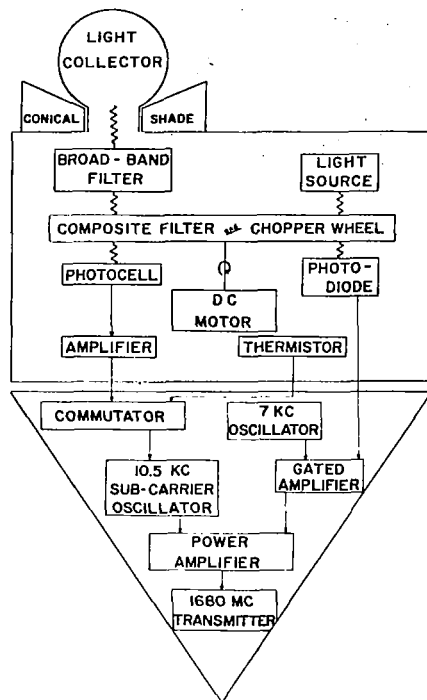
A block diagram for the ozonesonde is presented in Figure 2.42 and the rocket payload layout is shown in Figure 2.43. Upon ejection from the rocket, the instrument is deployed 15 meters below the parachute on a lanyard to minimize the problems of obscuration of the sun and backscattered light from the parachute. To avoid the complexity of an active pointing control system, a transmission-type integrating sphere is used to collect the sunlight from a fairly wide field of view. To reduce errors due to the reception of scattered light from low incidence angle illumination, a conical shade is employed to limit the view to elevation angles above 30 degrees. A broad-band filter is used to pass the ultraviolet region of interest and block the visible spectrum.

Four narrow band (40-50 Å half-widths) optical filters centered near 2700, 2950, 3050, and 3300 Å are used to obtain data at various altitude regions from 20 to 55 km. These filters are sampled sequentially to provide 8 complete samplings per kilometer. The transmission curves of the narrow band pass filters are shown in Figure 2.44. A typical telemetry record presented in Figure 2.45 shows the output sequence from each of these filters during flight. The 3287 Å filter is used as a reference, and the outputs of the other filters are ratioed with it as a measure of total ozone content as indicated in Figure 2.46.

An RCA C70129C ultraviolet photomultiplier is used as the photodetector. A rotating sampling wheel is used to sample the narrow band filters, a blank for dark current measurement, an internal light source for marker pulses which are used during the automatic data digitizing at the ground-station. To obtain absolute intensity values photometer temperature is monitored with a bead thermistor. Two subcarrier oscillators are used to modulate a 1680 MHz transmitter.

The overall ozone concentration measurement accuracy depends upon the accuracy of the ozone absorption coefficient at the filter wavelengths employed and the precision of the telemetered intensity vs. height data. Calculated fractional

errors in ozone concentration are plotted vs. altitude for three different filters with absorption coefficients as shown in Figure 2.47. For each optical filter the errors grow rapidly outside of a central region. Generally, 10 percent accuracies can be obtained over a 12 to 15 km height region with a given filter. Ozone concentration profiles are derived from the spectral intensity measurements by a method of differentiation since the intensity values indicate total ozone content between the sensor and the highest reference altitude. A typical set of rocket data (ROCOZ) and balloon data are presented in Table 2.12. Rocket derived ozone profiles are indicated in Figure 2.48.



(Krueger)

Figure 2.42 Block Diagram for Ozonesonde

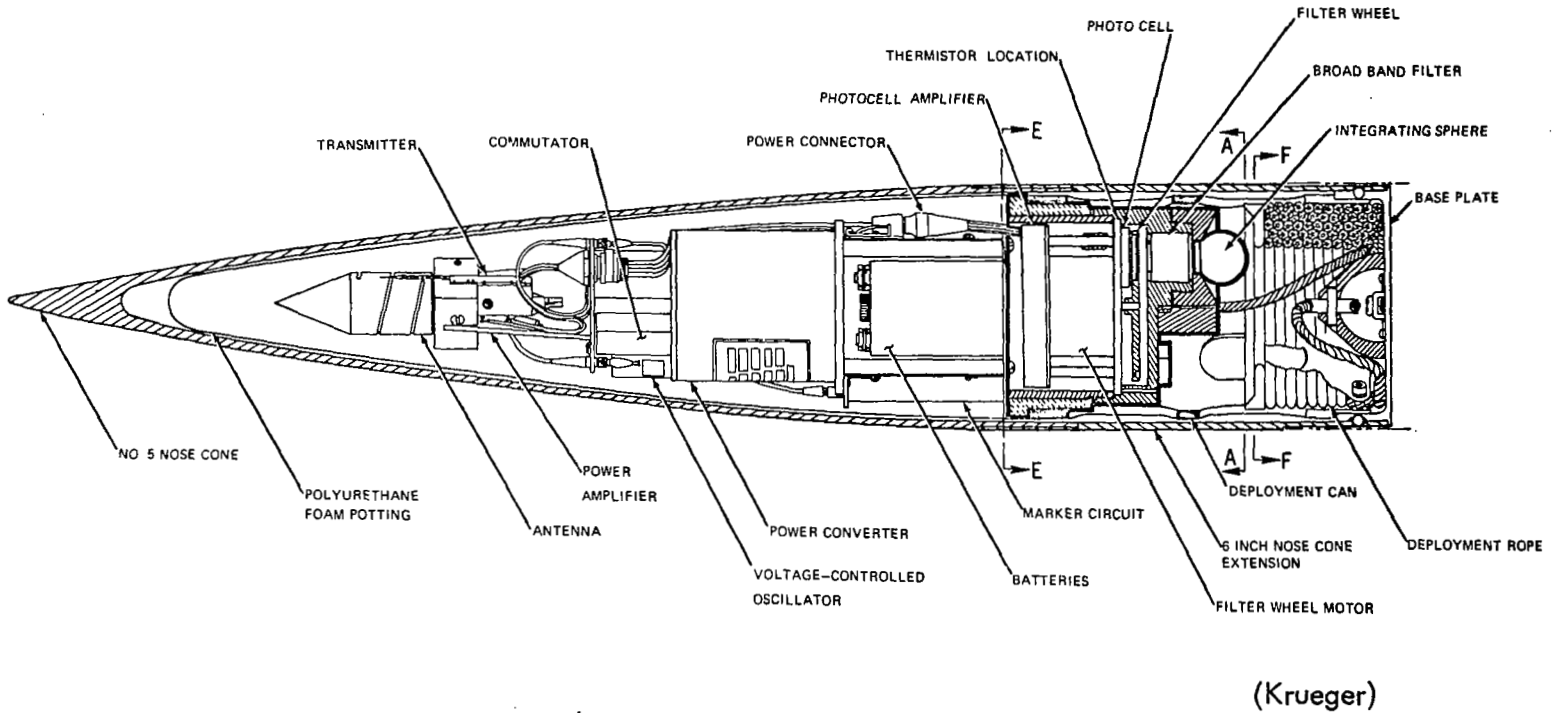
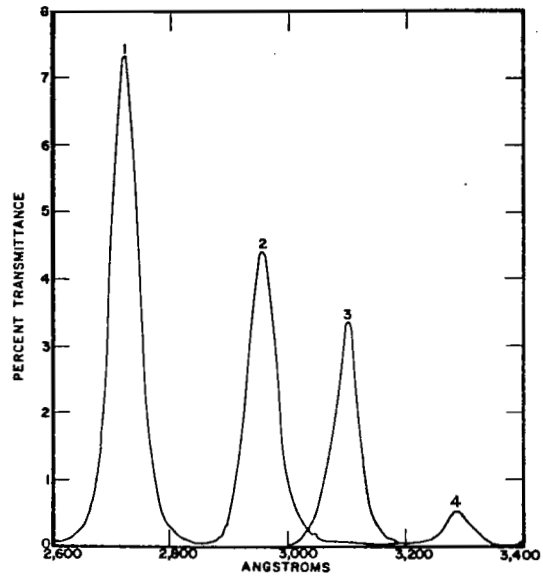
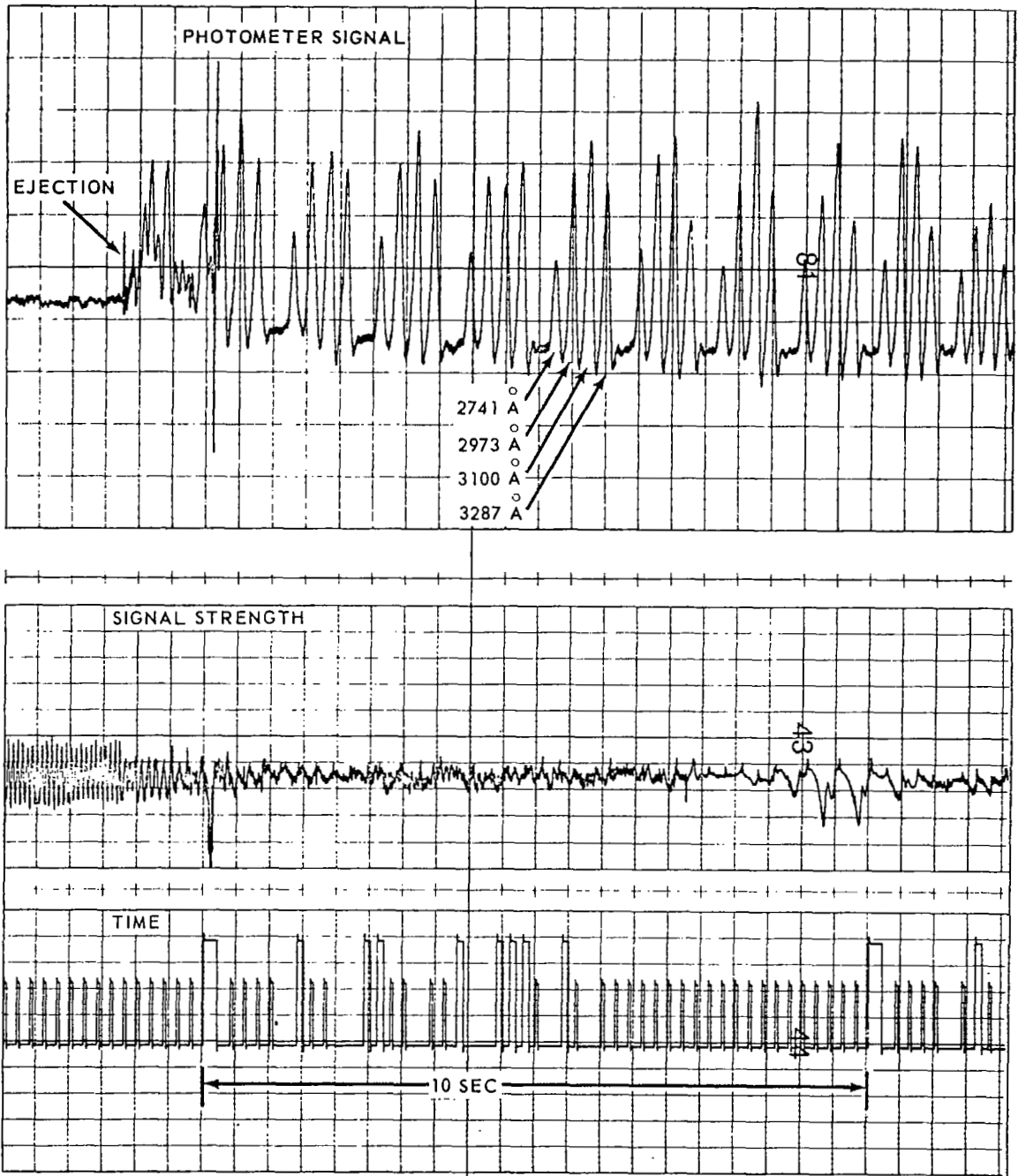


Figure 2.43 Payload Assembly



(Krueger)

Figure 2.44 Transmission Curves of Narrow-Band Filters



(Krueger)

Figure 2.45 Photometer Signal During Ejection and Deployment Sequence

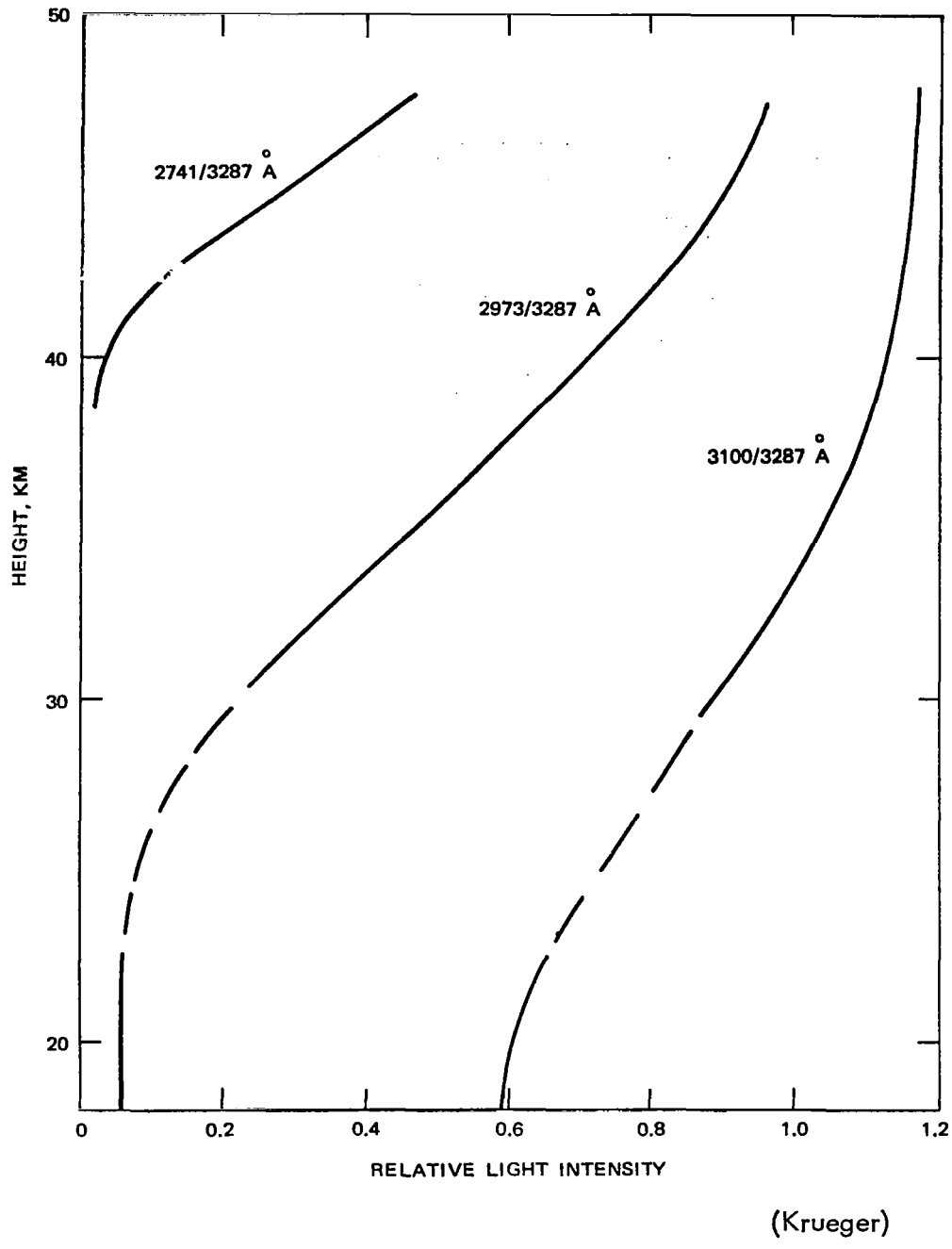
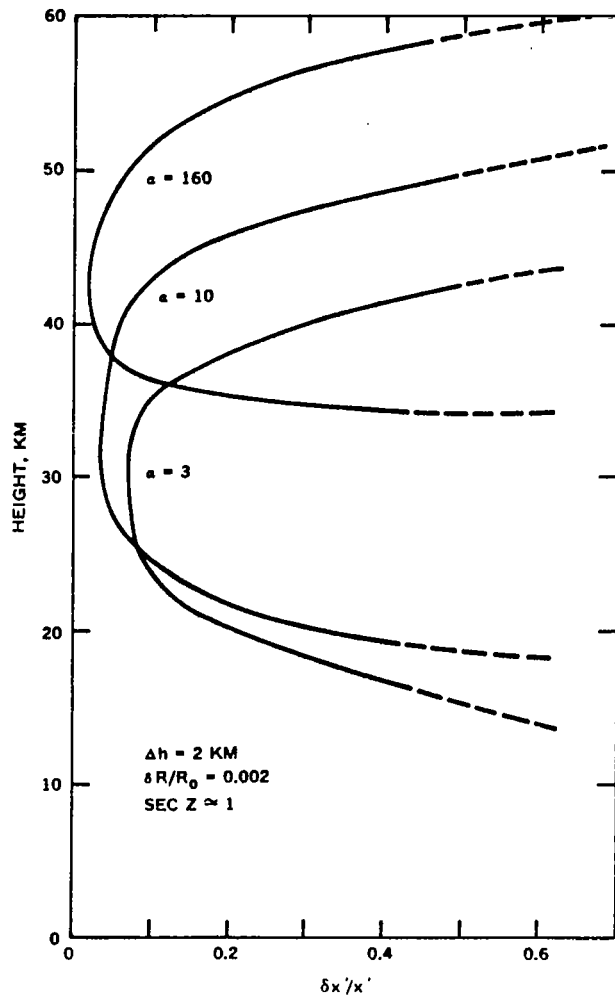
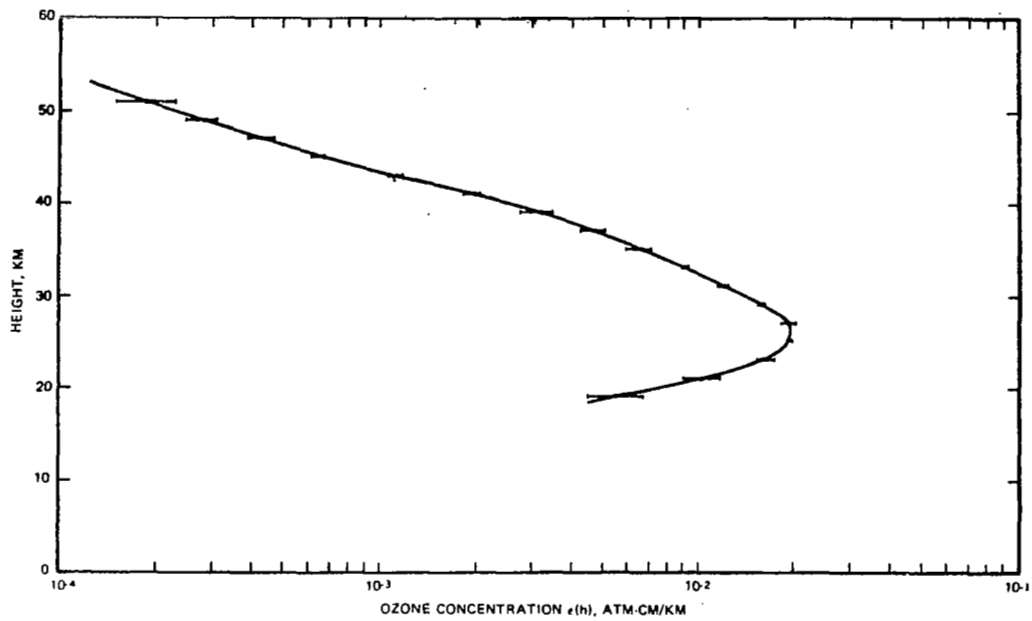


Figure 2.46 Intensity vs. Height Data



(Krueger)

Figure 2.47 Ozonde Concentration Measurement Precision vs. Height



(Krueger)

Figure 2.48 Autumnal Ozone Distribution, Barking Sands Facility, Hawaii

Table 2.12 Average Ozone Concentrations, atm-cm/km

Height, km	ROCOZ				Balloon		
	Mean $\Delta x/\Delta h$	Average deviation	% deviation	Mean $\epsilon(h)$	Mean $\Delta x/\Delta h$	Average deviation	% deviation
19	0.0056
20	0.0066	+0.0011	17.	0.0081	+0.0009	11.
21	0.0104
22	0.0123	+0.0014	11.	0.0129	+0.0010	7.8
23	0.0162
24	0.0176	+0.0010	5.7	0.0163	+0.0003	1.8
25	0.0192
26	0.0198	+0.0005	2.6	0.0175	+0.0005	2.8
27	0.191
28	0.0186	+0.0010	5.3	0.0148	+0.0004	2.7
29	0.0157
30	0.0149	+0.0004	2.4	0.0116	+0.0013	11.
31	0.0120
32	0.0112	+0.0004	3.6	0.0074	+0.0014	19.
33	0.0091
34	0.0085	+0.0002	2.7
35	0.0065
36	0.0060	+0.00055	9.1
37	0.00463
38	0.00421	+0.00041	9.7
39	0.00312
40	0.00284	+0.00036	12.7
41	0.00193
42	0.00169	+0.00010	5.9
43	0.00112
44	0.00098	+0.00006	6.1
45	0.00064
46	0.00056	+0.00003	5.4
47	0.00043
48	0.00039	+0.00004	10.2
49	0.00028
50	0.00025	+0.00003	12.
51	0.00019
52	0.00017	+0.00004	23.

(Krueger)

RECENT DECELERATOR ADVANCES

3.1 General.

Recent decelerator advances in the meteorological rocketsonde application include the scaling of the ram-air inflated starute and chamber testing of the Stokes flow parachute. Ballistic coefficients as low as 0.016 lb/ft^2 have been achieved in flight tests with the Super Loki system. Deployment and fabrication problems have been investigated for the Stokes flow parachute.

3.2 Ram-Air Decelerators.3.2.1 General.

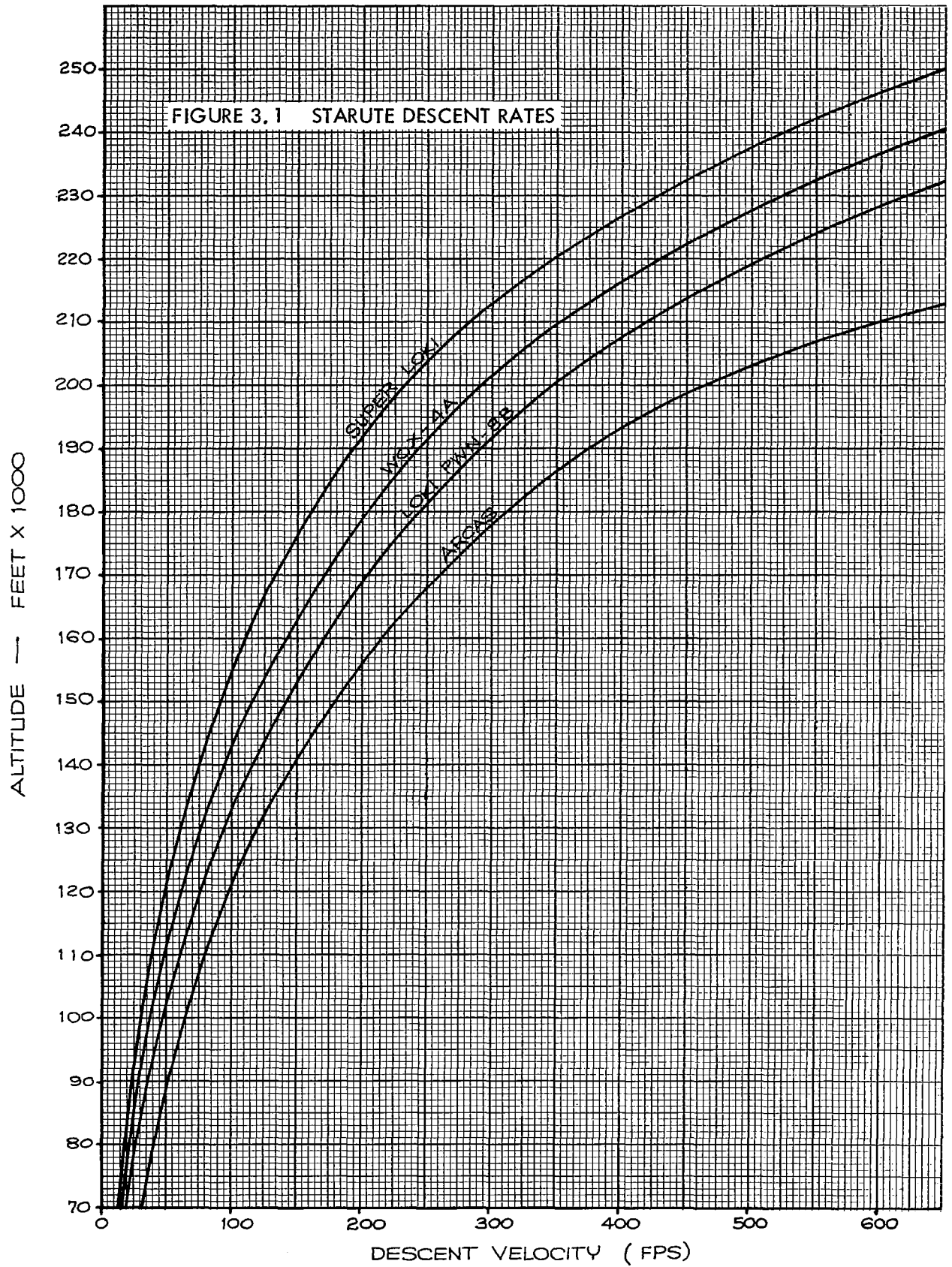
The Starute ram-air decelerators, as described in NASA CR-1529 Volume I Part 2, were originally developed for the Arcas and Loki systems. These designs have been modified for the WOX-4A and Super Loki instrumented dart systems to provide slower fall rates. The Arcas 14 foot diameter Starute achieves a ballistic coefficient of about 0.060 lb/ft^2 with the Arcasonde payload. The Loki 7 foot square Starute achieves a ballistic coefficient of 0.030 lb/ft^2 with the Datasonde payload. The WOX-4A and Super Loki units have achieved considerably slower fall rates with their respective instrumented payloads.

3.2.2 WOX-4A Starute.

The WOX-4A Starute has been developed for NOL for the 1 3/8 inch dart and the WOX-4A instrument payload. This unit is designed with a 6 foot square burble fence, and is a scale-down (160 gm) of the standard Loki (PWN-8B) Starute. Since the WOX-4A payload weight has been reduced to 160 gm for the vacuum-tube transmitter version and 135 gm for the solid-state transmitter version, the system ballistic coefficient has been reduced to 0.022 lb/ft^2 and 0.021 lb/ft^2 respectively.

3.2.3 Super Loki Starute.

The Super Loki Starute has been developed for AFCRL for the 2 1/8 inch Super Loki dart and the GMD-2 transponder payload. This unit is designed with a 12 foot square burble fence, and is a scale-up of the standard Loki (PWN-8B) Starute. The transponder instrument weighs 1.06 lb and the Starute weight is 1.10 lb. This Starute has demonstrated reliable performance to an altitude of 250,000 feet (76 km). The ballistic coefficient for this system is about 0.016 lb/ft^2 . A summary of the various Starute systems descent rates is presented in Figure 3.1.



3.3 Stokes Flow Decelerators.

Development efforts by Astro Research Corporation for NASA-LRC have continued toward demonstrating the feasibility of ribbon mesh Stokes flow decelerators for meteorological rocketsonde applications. Performance calculations indicate the possibility of subsonic descents from altitudes up to 80 km. Although there have not as yet been any flight tests of the proposed decelerators, vacuum chamber deployment tests have indicated problems such as shroud line tangling and pin-hole leaks in the inflatable brace struts.

Cross-brace and toroidal-shaped canopies as shown in Figure 3.2, were investigated for both the Arcas and Loki systems. A performance comparison between these systems and other decelerators in current use is presented in Figure 3.3. The Super Loki 12 foot Starute has achieved a ballistic coefficient of 0.073 kg/m^2 with a 0.460 kg payload. The theoretical performance of the proposed Stokes flow decelerators is slightly better.

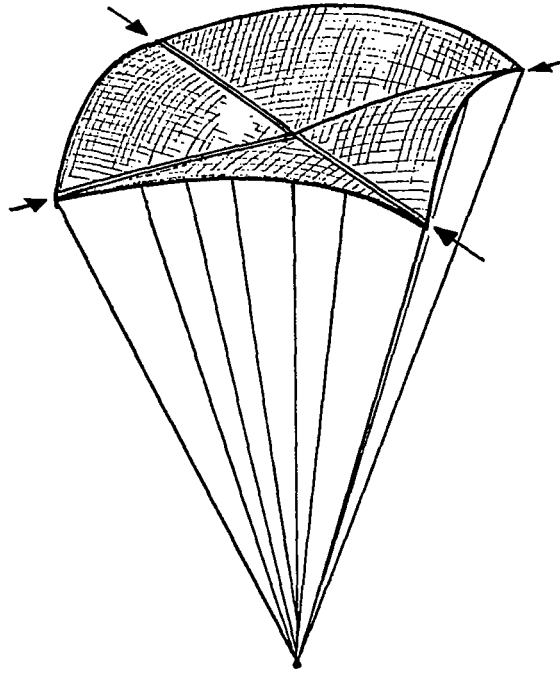
Canopy construction consists of a punched-out grid pattern in thin Mylar film as shown in Figure 3.4. The canopies are characteristically flat, with a minimum of billowing out to prevent the occurrence of excessive stresses due to aerodynamic loading. The mesh of the canopy consists of a thin polyester-type foil such as 1/4 mil Mylar, aluminized for radar tracking purposes. The foil is punched out with square holes, leaving a rectangular network of tapes typically 2 mm wide and 20 mm apart, for a solidity of 20 percent. The canopies are composed of several gores, the joining lines of which not only serve as reinforcements, but also as "rip-stop" lines.

The X-brace parachute has a projected area of a square. Two straight braces are placed along its diagonals. The four triangular sails of the canopy are each attached to adjacent brace legs. The payload is carried by a number of suspension lines originating from the braces.

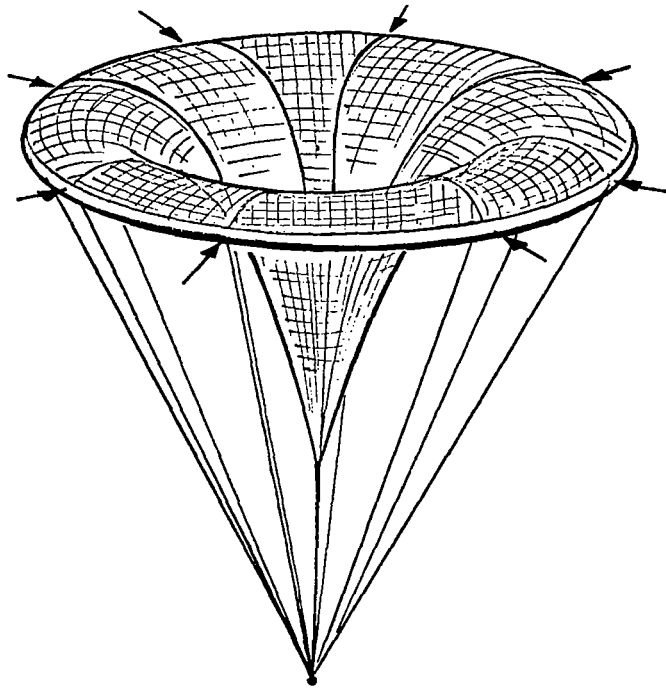
The toroid parachute has a circular projected area framed by an annular brace. The apex of the canopy is pulled in by a central suspension line carrying part of the payload. Additional suspension lines, evenly distributed along the toroid, carry the remaining part of the payload.

The braces are designed as compression restraint structures which also carry bending loads. They supply the forces to deploy the canopy from its tightly packaged state and they subsequently prevent it from collapsing. Their weight and volume contribute significantly to the overall weight and packaged volume of the parachute.

Thin-walled inflatable brace tubes or struts were investigated as a means of deployment and of rigidizing the canopies. Several liquids such as Freon 11, isopentane, methanol and water were considered as inflatants. Pin hole leaks occurred generally at the intersection of the two-fold crease marks during the inflation tests. During the deployment tests it was found that the shroud lines tended to tangle and the fine mesh of the dart-size canopies tended to tangle and tear.



X-Brace Parachute



Toroid Parachute

Figure 3.2 Stokes-flow Parachute Concepts

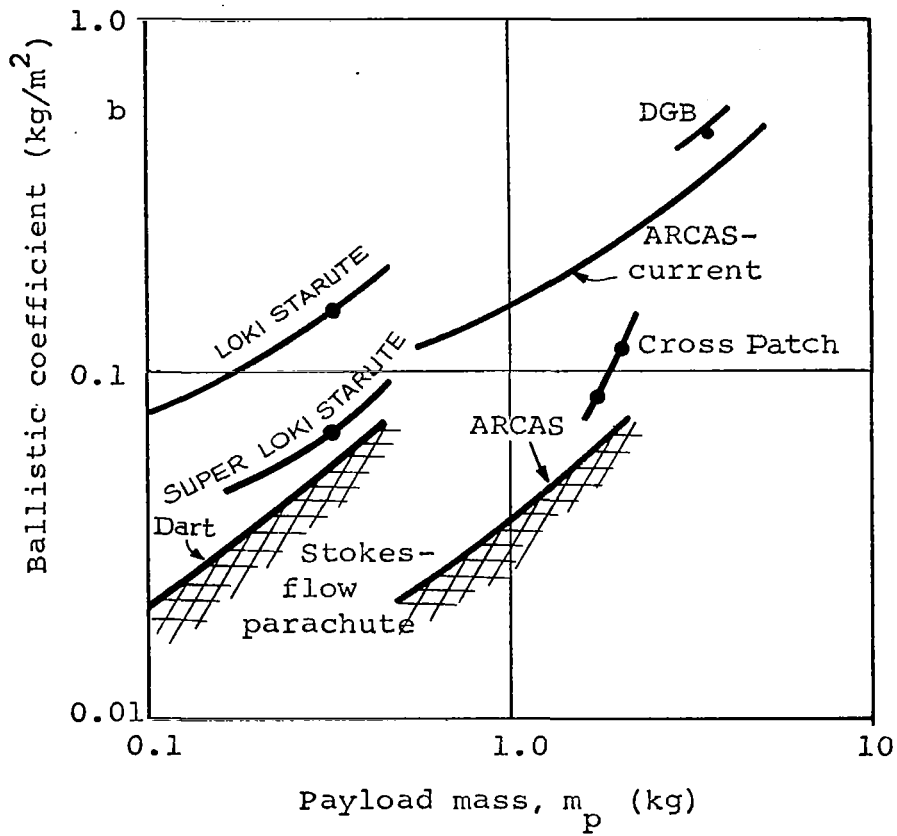


Figure 3.3 Ballistic Coefficients, b , for ARCAS and DART Payload Delivery Systems

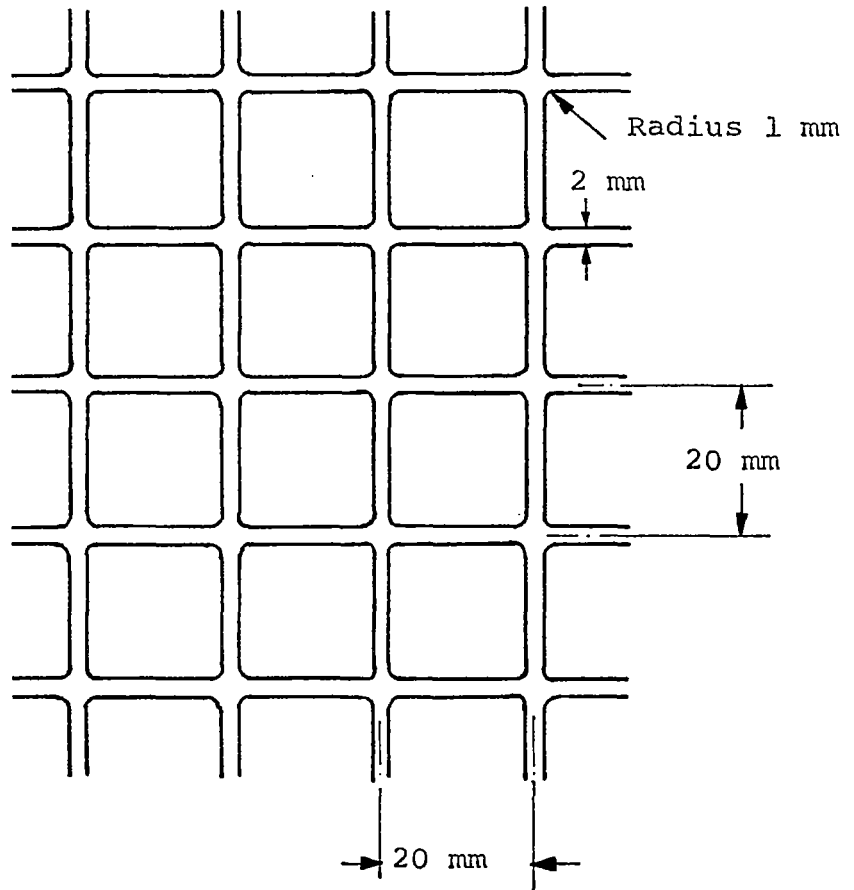
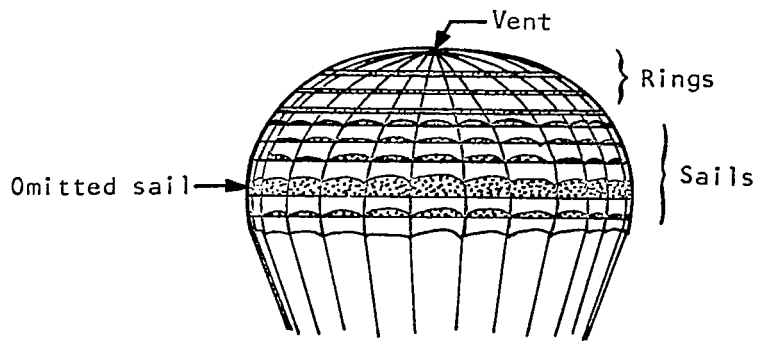


Figure 3.4 Geometry of Mesh, Solidity 0.2 (Full Scale)

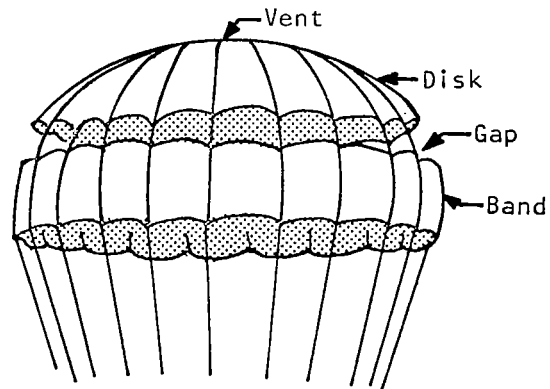
3.4 Ringsail, Disk Gap Band, Cross Parachute Evaluations.

A flight test series to determine and compare the supersonic low-density deployment and inflation characteristics of three parachute shapes was conducted by NASA-LRC (reference 7) for heavy payload applications. The results of this flight series may be of some interest for future meteorological rocketsonde systems design.

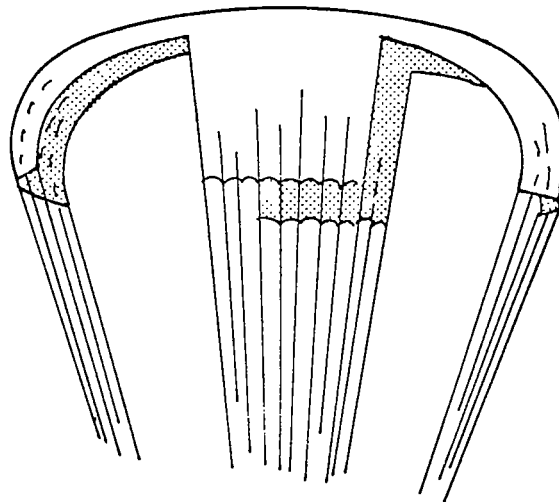
Various sizes of the three parachute configurations as shown in Figure 3.5 were deployed at Mach numbers from 1.39 to 2.72 and at dynamic pressures of about 10 lb/ft². All parachutes were characterized by a partial collapse and fluctuations of the canopy immediately after the first inflation peak. The partial collapse was most severe for the disk gap band configuration and least severe for the modified ringsail. The cross parachute never achieved a stable configuration during the data periods and was characterized by a scissoring motion. Both the modified ringsail and the disk gap band were stable for Mach numbers below 1.4 once deployment dynamic effects had diminished. Even though the canopies of the cross and disk gap band configurations exhibited fluctuations at high Mach numbers, both systems were good drag-producing devices. As indicated in Figure 3.6, the cross parachute produced the highest drag coefficients even if all values were based upon fabric area.



(a) Modified ringsail.



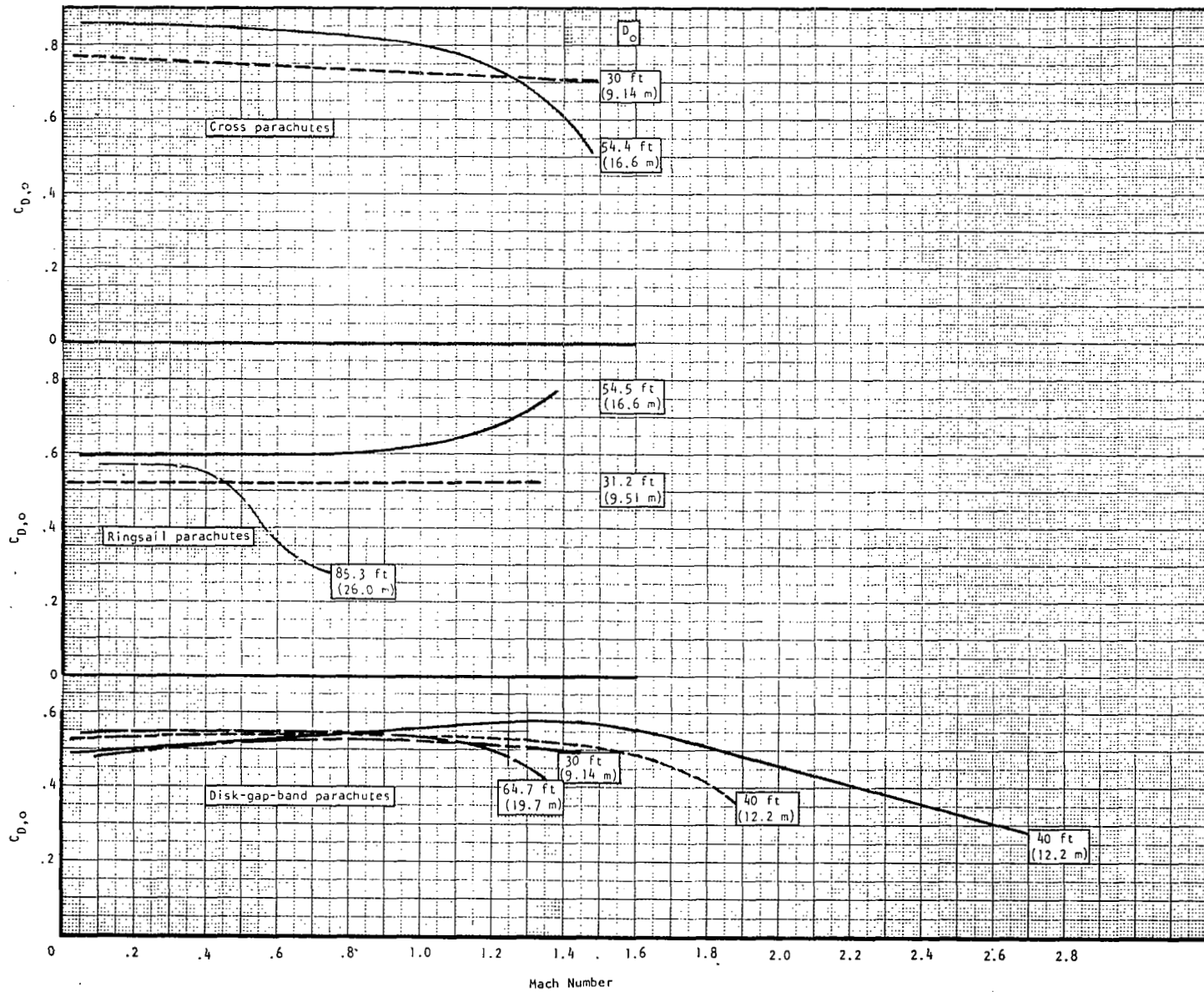
(b) Disk gap band.



(c) Cross.

(Whitlock, Bendura)

Figure 3.5 Parachute Configurations



(Whitlock, Bendura)

Figure 3.6 Summary of Faired Drag Histories

RECENT TELEMETRY ADVANCES

4.1 General.

The AN/GMD-4 telemetry and tracking system has been successfully used with the Arcas AN/DMQ-9 transponder instrument; however, parachute oscillations have caused signal dropout problems for a majority of the flights. Although this system is in routine use, the overall reliability has been poor. Currently the USAF-CRL are developing a transponder instrument for the Super Loki system with a 2 1/8" diameter dart and a 12 foot scale-up of the Starute decelerator. Initial flight tests have shown promising results. Advantages of this system over the Arcas are a stable descent with the elimination of the signal dropouts, a higher altitude (250,000 feet) and a lower cost (less than half that of the Arcas system). In addition to the GMD-4 system efforts, AMSS rocketsonde payloads were successfully flight tested in the Super Loki vehicle with the Motorola phase-lock AMSS system. Both ranging and meteorological data were reliably received during the initial flight tests with this system. NASA-GSFC is currently developing a tone range and interferometer telemetry tracking system which may be adaptable to meteorological rockets. Standard IRIG telemetry and a passive antenna array are main features of this system. The ESSA is currently investigating a radiosonde tracking system which makes use of the Loran C system for obtaining position information. Since it may be possible to incorporate altitude data into this system, it may be a candidate for a meteorological rocketsonde application.

4.2 AN/GMD-4 Telemetry and Tracking Systems.

The AN/GMD-4 telemetry and tracking system has successfully been used with rocketsonde payloads. It basically consists of an AN/GMD-2 modified rawinsonde set with the addition of a meteorological data processor. In addition to the automatic processing of the meteorological and tracking data, major advantages of this system for rocketsonde flights are the coarse-ranging provision and the manual entry of preset data prior to launch.

The Arcas AN/DMQ-9 transponder rocketsonde payload has been successfully flight tested with the GMD-4 ground station. Recent improvements in the DMQ-9 consist of insulating the 403 mHz receiving antenna from shorting and changing the ranging modulation of the sonde transmitter from cathode to plate modulation to incorporate a feedback system into the super-regenerative receiver to provide

additional range signal gain control. A major problem, however, is interference from external sources at about 400 MHz. Typical accuracies of the DMQ-9 flight test data as compared with the FPS-16 radar as a standard are presented in Tables 4.1 and 4.2.

AFCRL is currently developing a transponder instrument similar to the DMQ-9 for the Super Loki dart application. Preliminary flight tests have been encouraging. However, one of the main problems has been external interference at about 400 MHz. Efforts are underway to reduce the receiver bandwidth to reduce the interference problem.

4.3 Tone Range/Interferometer Telemetry Tracking System.

4.3.1 General.

The Tone Range/Interferometer Telemetry Tracking System (reference 13) utilizes a standard IRIG telemetry transmitter with a tone range receiver. Slant range is determined by the phase shift of the tone signal which is transmitted from the ground station to the payload and then back again to the ground station. Angular tracking data is acquired by measuring the difference in phase of the signal transmitted from the payload at various antennae in the ground station receiving antenna array. Thus with the addition of only a receiver to a standard IRIG telemetry payload, telemetry and tracking data may be received.

4.3.2 Ranging System.

In the tone range system a sinusoidal signal $FCN_I(t) = \sin(W_I t + \phi_0)$ is generated and transmitted from the ground station to the receiver in the payload which is at a distance R. This signal is retransmitted back to the ground station for a round trip distance 2R. The instantaneous phase of the signal is $\phi_I = W_I t + \phi_0$ where ϕ_0 is the accumulation of fixed phases throughout the system. If ϕ_0 is assumed to be zero, for convenience in this description, the round trip range tone phase will be $\phi_R = W_I (t - \frac{2R}{C})$ and the range may be found from a measurement of the phase difference as

$$R = \frac{C \Delta \phi}{2 \omega_I} \text{ or } \frac{C}{2 f_I} \cdot \frac{\Delta \phi}{2 \pi} .$$

As with other sinusoidal ranging systems there is a potential ambiguity in the range data if the number of complete phase shifts are not counted. Since to include the expected range within the interval represented by $\Delta \phi < 2\pi$ would lead to a too coarse measurement of R, a multiple frequency method is used. A high frequency

Table 4.1 Transponder Flight Analysis (Error Data)

Fil. No.	No. Obs.	RMS ERROR				AVERAGE ALGEBRAIC ERROR				STANDARD DEVIATION		AVERAGE ABSOLUTE ERROR			
		Altitude	Slant Range	El. Angle	Az. Angle	Altitude	Slant Range	El. Angle	Az. Angle	Altitude	Slant Range	Altitude	Slant Range	El. Angle	Az. Angle
1	60	145	31	0.20	0.13	+87	+25	+0.06	+0.06	117	17	119	26	0.15	0.11
2	65	183	79	0.20	0.73	+10	-38	-0.01	-0.71	183	69	137	66	0.15	0.71
3	68	189	76	0.42	0.28	+105	-68	+0.26	-0.13	159	35	135	68	0.29	0.20
4	67	147	101	0.16	0.17	+59	+48	-0.04	-0.04	133	91	112	49	0.12	0.14
5	67	340	497	0.19	0.15	+287	+492	-0.09	+0.02	188	105	301	501	0.15	0.11
6	69	205	228	0.28	0.32	+75	+209	-0.14	+0.08	191	89	134	224	0.16	0.23
7	66	107	160	0.18	0.14	+54	+151	-0.12	+0.07	93	59	80	151	0.13	0.13
8	70	129	180	0.21	0.25	+68	+177	-0.14	+0.01	110	32	91	177	0.18	0.15
9	71	139	140	0.13	0.14	+92	+70	+0.03	-0.09	94	77	129	110	0.11	0.11
10	71	93	125	0.17	0.18	+39	+58	-0.07	-0.09	118	112	91	85	0.12	0.15
11	70	202	202	0.12	0.26	+168	+177	0	-0.09	97	46	169	177	0.09	0.21
12	62	119	135	0.11	0.16	-28	-60	-0.01	-0.07	116	122	75	76	0.09	0.11
AVERAGE		151	132	0.20	0.24	+66	+68	-0.02	-0.09	128	68	116	110	0.14	0.20

Altitude & Slant Range in Meters
 Elevation & Azimuth Angles in Degrees
 *The data from Flight No. 5 are not used in the average computations

(Georgian)

Table 4.2 Flight Analysis at 5 Kilometer Altitude Intervals

Altitude Interval (Km)	No. Obs.	RMS ERROR				AVERAGE ALGEBRAIC ERROR				AVERAGE ABSOLUTE ERROR			
		Alt.	Slant Range	El. Angle	Az. Angle	Alt.	Slant Range	El. Angle	Az. Angle	Alt.	Slant Range	El. Angle	Az. Angle
65-60	13	341	133	0.65	0.61	+318	+60	+0.55	-0.51	318	83	0.55	0.57
60-55	71	279	160	0.38	0.34	+162	+59	+0.09	-0.22	226	112	0.23	0.25
55-50	111	196	142	0.23	0.29	+126	+67	+0.08	-0.10	169	110	0.17	0.20
50-45	122	136	155	0.14	0.28	+63	+74	-0.04	-0.16	114	124	0.11	0.19
45-40	53	92	122	0.12	0.20	+61	+80	-0.05	-0.07	75	101	0.10	0.14
40-35	72	97	116	0.16	0.26	+40	+58	-0.04	-0.04	80	96	0.12	0.16
35-30	101	88	123	0.16	0.28	+20	+64	-0.09	-0.04	67	103	0.13	0.19
30-25	163	119	134	0.16	0.30	+23	+80	-0.09	-0.02	83	112	0.12	0.21
AVERAGE		169	136	0.25	0.32	+102	+68	+0.05	-0.15	142	105	0.19	0.24

Altitude & Slant Range in Meters
 Elevation & Azimuth Angles in Degrees
 The data from Flight No. 5 are not included in this table

(Georgian)

LIST OF SYMBOLS

c	velocity of propagation
$FCN_I(t)$	initial sinusoidal periodic function of time
f_I	initial reference frequency
N	integer
R	range
t	time
v	velocity
θ	angle of arrival
λ	wavelength
ϕ	phase
ϕ_I	initial phase
ϕ_O	accumulation of fixed phases throughout the system
ϕ_R	range-tone phase
$\Delta\phi$	range-phase difference
$\omega = 2\pi f$	
ω_C	carrier frequency
$\omega_I = 2\pi f_I$	

is used for high range resolution and a low frequency is used to resolve the ambiguities in the higher frequency tones. The ranging frequencies or tones selected were based primarily on noninterference with standard IRIG FM/FM data channels. The fine ranging tone is 100 kHz (1.5 km), and the coarse ranging tone is selected at either 2 kHz (75 km) or 4.5 kHz (33.3 km). Since neither of these coarse frequencies gives unambiguous range in excess of the maximum expected range, some knowledge of the trajectories is required to find the exact range. These range tones are used to modulate a 550 MHz carrier. The tone range/TM interferometer system uses beamwidths on the order of 60° and thus acquisition problems are minimized.

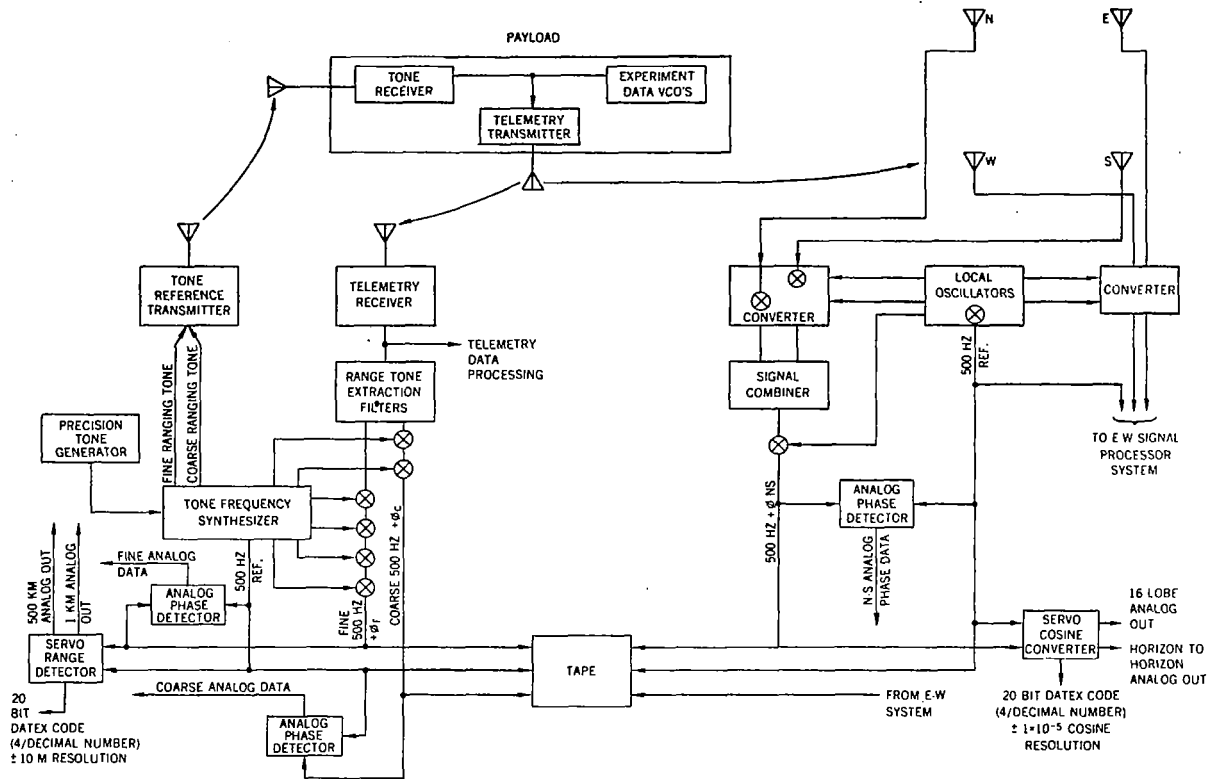
The tone range system is comprised of several subsystems as follows:

- Telemetry receiver, antenna, and preamplifier
- Precision tone generator and synthesizer
- Tone reference transmitter and antenna
- Tone translator
- Analog phase comparator and recorder
- Servo phase comparator and grey code to BCD converter
- Airborne receiver and telemetry transmitter

A simplified block diagram of the Tone Range/TM Interferometer system is shown in Figure 4.1. The heart of this system is the precision tone generator. This is normally a Hewlett-Packard HP 5245L counter from which a 1-MHz output is used to synthesize the required frequencies. Other counter functions include driving the timing and digital systems.

In the tone frequency synthesizer, the 1-MHz input is applied to divider chains to produce several phase coherent frequencies. The tone translator accepts the received mixed video and extracts the 100 kHz and 104.5 kHz range tones from the telemetry data via a 102.5 kHz, 6 percent bandwidth filter. These multiplexed range tones, dc referenced to signal common at the filter output, are applied to a diode limiter. This serves to establish a fixed signal level, as well as to establish the nonlinear function for separation of the coarse 4.5 kHz range tone. The limiter output is applied through buffer amplifiers to a 100 kHz, 2 percent bandwidth filter and a 4.5 kHz, 6 percent bandwidth filter for separation of the Fine and Coarse range tones. The 100 kHz and 4.5 kHz tones are mixed with the phase-coherent translating frequencies.

The analog phase detectors generate asymmetrical square waves, the degree of asymmetry of which is linearly proportional to the phase difference $\Delta\phi$ between the 500 Hz reference and $500 \text{ Hz} + \phi$ range tones. This square wave is integrated to form an output voltage linearly proportional to $\Delta\phi$. The outputs of the analog phase detectors are presented versus time by a Brush MK 280 Analog Recorder.



(Hudgins, Lease)

Figure 4.1 Tone Range/Telemetry Interferometer Systems

The 500 kHz reference and range tones are also applied to the servo phase detector. Here these two signals are compared in phase by a synchro-resolver, the output of which is a voltage proportional to the phase difference. This resolver is coupled by a gear train to a motor, the control of which is derived from the resolver output. Feedback is obtained in this manner and maintains, through mechanical rotation, zero phase difference between reference and range tone resolver windings.

In the airborne portion of the system, the only special equipment required is the tone receiver and its associated antenna. The received signal, generally 550 MHz, is demodulated and the resultant range tone signals are multiplexed with the data VCO outputs. The range tone signals are not preemphasized in accordance with their frequency relationship to the VCO frequencies. They are generally accorded 15 to 20 percent of the total telemetry transmitter deviation or ± 15 kHz, whichever is less. This is done to limit the effect of tracking on data acquisition, that is, placing the priority on the acquisition of experimental data.

4.3.3 Interferometer System

The interferometer system of determining incoming signal arrival angles is based upon the measurement of the differences in the times of arrival for the various antennae in the ground station receiving antenna array. Figure 4.2 depicts one axis of the interferometer antenna array. In the time period taken for the wave to arrive at the west antenna, the phase at the east antenna will have changed. If the antennas are spaced exactly one wavelength apart, the electrical phase difference of the signals received simultaneously at the two antennas is representative of the cosine of the space angle of arrival of the wave front with respect to the plane of the Interferometer. As the antenna spacing is opened up to 2 wavelengths, ambiguities begin to appear since the same electrical phase, 0° , is present for wave arrivals from the east and west horizons as well as that arriving parallel to the Interferometer axis. Although ambiguous, the electrical phase angle in degrees now represents half the space angle. As the axis increases in numbers of wavelength, ambiguities increase; however, the precision of measurement also increases proportionally. Each ambiguity is termed a "lobe". There are 32 such lobes in a 16 wavelength interferometer. Two mutually normal interferometer axes are used; their combined output defines a vector which includes the center of the interferometer array, the object being tracked, and results from the intersection of two conical surfaces of constant phase, one associated with each interferometer. Removing ambiguities by using close-spaced antennas is not at present deemed necessary, since integrated tracking from launch to end of flight has proven effective.

The relationship between the measured phase difference and the space angle of arrival can be derived from Figure 4.2 as

$$\begin{aligned}\cos \theta &= \frac{ct}{N\lambda} \\ &= \frac{\phi}{2\pi N}\end{aligned}$$

The interferometer system consists of the antenna subsystem, the receiver subsystem, the servo phase measuring unit, and the Az-El plotter. A magnetic tape recorder and a digital system are also used in the operation of the interferometer ground station. Figure 4.3 presents a simplified block diagram of the interferometer ground station.

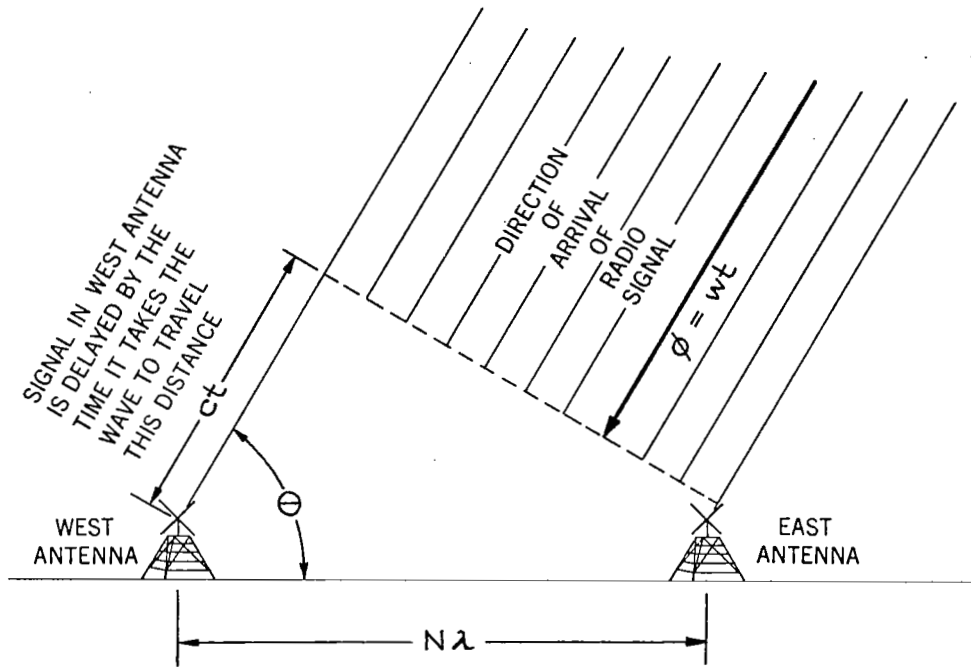
Each axis of the interferometer uses two antennas, 16 wavelengths apart; the antenna elements are spaced 1/4 wavelength above a ground plane. Each antenna is a pair of crossed dipoles, connected in circularly polarized configuration. Circularity of receiving, necessary because of the rotation of the rocket, is achieved by cutting the quarter-wave sections to a length that will cause them to be inductive, and coupling directly to two elements while connecting capacitively to the other two.

Low-noise preamplifiers provide about 30 dB gain for the incoming 244.3 MHz signals from the antennas plus conversion to 73.6 MHz. The preamplifiers are followed by mixer stages. The local oscillator signal to the north and east mixers is 67.12 MHz; to the south and west mixers it is 67.1205 MHz. The 6.48 and 6.4795 MHz outputs of the north and south mixers, respectively, are combined in an adder and sent through a common IF channel; likewise, the outputs of the east and the west. A second conversion is made, giving IF's of 465 kHz for the north and east mixers and 465.5 kHz for the south and west. The detected output for each axis is 500 Hz \pm phase difference between the two signals arriving at the antennas.

The phase of each of the two 500 Hz \pm phase signals is compared with that of the 500 Hz reference signal by means of two different types of phase-measuring equipment.

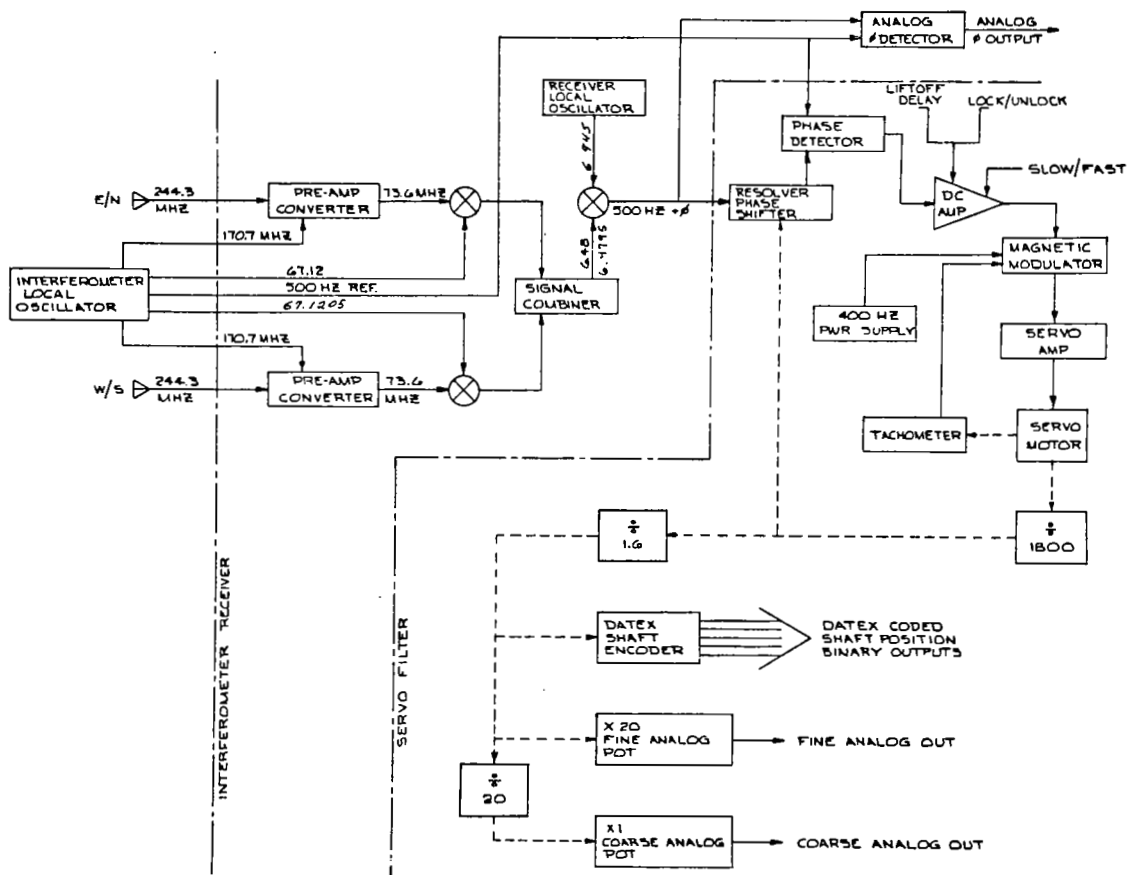
4.3.4 System Accuracies.

The systems accuracies cannot be defined, in general, since trajectory parameters, frequencies, specific components and systems delays affect the accuracy of the space-position measurement. For high radial velocities of the target, Doppler effects degrade the range accuracy. In addition to the system, electronic processing errors which effect both the range and angle accuracies, geometric variations play a dominant role in overall interferometer measurement accuracy.



(Hudgins, Lease)

Figure 4.2 Interferometer Geometry



(Hudgins, Lease)

Figure 4.3 Interferometer System - Simplified Block Diagram

These geometric variations include such factors as:

- Axis orthogonality and tilt
- Axial alinement with respect to geodetic coordinates
- Antenna spacing
- Antenna element alinement and tilt
- Antenna height
- Antenna circularity
- Antenna cross coupling

An indication of tone range errors is presented in Table 4.3. Doppler errors in range for typical sounding rocket flights can be as great as 25 m during the high speed portion of the flight. Near apogee the Doppler errors are more likely to be on the order of 3 m.

The precision of a tone range system is a function of the highest ranging frequency. In addition to ambiguity considerations, signal-to-noise and bandwidth factors limit the range data precision. The selection of the 100 kHz ranging frequency for the current system was based on the following:

- a. Minimum impact on the telemetry subcarrier format.
- b. Minimum requirement on the telemetry carrier power.
- c. Existing telemetry bandwidths limited to 100 kHz.

Typical precision estimates for various tracking systems are presented in Table 4.4. Examples of the interferometer accuracies and precisions are presented in Tables 4.5 and 4.6.

Table 4.3 Summary of Error Contributions to Tone Ranging

Source	Effect	Comments
Dynamic level	12.5 meters	Can be calibrated out from correlation with AGC record
Frequency stability offset	Negligible	Frequency source used is stable 5 parts in 10^{10} per day
Cross-coupling intermodulation	3 meters	40-dB separation in level for both cases
Propagation delay	$(R/3) \times 10^{-8}$ meter per m/sec	Can be all but eliminated by reiterative solutions
Equipment propagation delay	10^{-3} meter per m/sec	Can be all but eliminated by reiterative solutions
Differential phase delay:		
Velocity	75×10^{-3} meter per m/sec	Can be all but eliminated by reiterative solutions
Acceleration	7.6×10^{-3} m/sec per m/sec^2	Can be all but eliminated by reiterative solutions

(Hudgins, Lease

Table 4.4 Relative Design Precisions for Several Tracking Systems

TRACKING METHOD		DESIGN PRECISION	
GENERAL	SPECIFIC	RANGE	AZIMUTH & ELEVATION
DOPPLER INTERFEROMETER SYSTEMS	RADINT	± 1 METER	± .0029 DEGREES
	STONE RANGE-T.M. INTERFEROMETER	± 5 METERS (RESOLUTION LIMITED CASE)	± .0029 DEGREES AVERAGE
RADAR	AN/MPS -19	± 25 YDS = ± 22.8 METERS	± 1 MIL = ± .056 DEGREES
	AN/FPS -16	± 5 YDS = ± 4.58 METERS	± 1 MIL = ± .056 DEGREES
	AN/FPQ -11	± 25 YDS = ± 22.8 METERS	± 0.5 MIL = ± .028 DEGREES
	SPANDAR	± 25 YDS = ± 22.8 METERS	± 1 MIL = ± .056 DEGREES
	AN/FPQ -6	± 5 YDS = ± 4.58 METERS	± 0.05 MIL = ± .0028 DEGREES

(Hudgins, Lease)

Table 4.5 Standard Deviation in X, Y, and Z Coordinates with Range Measurement Assumed Perfect. (Data are Preliminary Results From a Radint-Interferometer-Accuracy Survey Made with Flight Model Nike-Apache 14.386 gm)

Flight time, sec	Elevation angle, deg	Slant range, km	σ_z , meters	$\sigma_x = \sigma_y$, meters
15	77	10.5	0.7	2.9
30	79	21.2	2.1	10.0
50	79	51.1	4.3	21.4
100	77	109	8.2	36.2
150	75	144	9.4	39.7
200	71	157	13.7	39.7
250	64	149	19.8	40.8
300	51	124	36	44
350	21	98	233	110

(Hudgins, Lease)

Table 4.6 Comparative Direction Cosine Precision Granularity for TM Interferometer, FPS-16 and FPQ-6 Radars

Az, deg	El, deg	Least significant value (parts per 10 ⁵)								
		Radint			FPS-16			FPQ-6		
		X	Y	Z	X	Y	Z	X	Y	Z
0	30	5	5	9	8	5	8	4	2	4
0	50	5	5	4	6	7	6	3	4	3
0	70	5	5	2	3	9	3	2	5	2
0	90	5	5	0	0	10	0	0	5	0
30	30	5	5	12	10	8	8	5	4	4
30	50	5	5	6	9	10	6	5	5	3
30	70	5	5	2	7	10	3	4	5	2
30	90	5	5	4	5	8	0	2	4	0
60	30	5	5	12	8	10	8	4	5	4
60	50	5	5	6	10	9	6	5	5	3
60	70	5	5	2	10	7	3	5	4	2
60	90	5	5	4	8	5	0	4	2	0
90	30	5	5	9	5	8	8	2	4	4
90	50	5	5	4	7	6	6	4	3	3
90	70	5	5	2	9	3	3	5	2	2
90	90	5	5	0	10	0	0	5	0	0

(Hudgins, Lease)

4.4 Loran C Radiosonde Tracking System.

4.4.1 General.

Measurements of winds aloft at sea has been a problem because of the need for a stabilized tracking antenna and the measurements must be made from a moving platform in most cases. To offset these problems the ESSA investigated the feasibility of utilizing the Loran C Navigation Aid as a radiosonde tracking system (reference 14). This method depends upon radio transmission of Loran C navigation information from fixed stations whose ground-wave signals extend out to 1500 miles. Possible utilization of the sky wave from these stations can increase this distance by a factor of two. Conventional 403 MHz radiosondes were modified by incorporating a miniaturized lightweight Loran C receiver to detect and retransmit the Loran information to the ground station. A flight test comparison with the standard GMD-1 type equipment showed typical wind speed and direction accuracies to be better than \pm one meter per second, \pm five degrees. With this system the accuracy is independent of distance between the balloon and the ground equipment as long as an adequate Loran C signal level can be received. Incremental displacements were measured better than \pm 20 meters, and a higher resolution is expected when the ground equipment is automated. The Loran C position data is independent of ground position motion. It also overcomes the problem of poor accuracy in the wind data when the GMD-1 elevation angles are lower than 6 degrees.

4.4.2 Loran C Principle.

The Loran C system consists of a chain of at least three stations, i.e., a master and two or more slave stations all transmitting a pulsed signal at a carrier of 100 kHz. Pulsed groups from the master station are also transmitted by the slave stations, each delayed with respect to that from the master station by predetermined times. The pulse times are precisely controlled by means of atomic clocks so that time intervals can be measured to 0.1 microsecond. Position information is obtained by measuring the envelope and carrier time differences between the master and each of the slaves. For a constant time difference between the master and a slave, the receiving station will be somewhere on a curved line, known as a hyperbolic line of position. It will also be somewhere along another line of position determined by the master and the other slave station. The point where the hyperbolic lines cross determines the position of the receiver. With the Loran C system the pulses are not transmitted simultaneously, but are accurately delayed, so that the master pulse always arrives first. All of the Loran C information from all of the stations is received at 100 kHz.

4.4.3 System Description.

A conventional frequency modulated 403 MHz radiosonde is modified by the incorporation of a miniature solid state receiver which is fixed tuned to 100 kHz. The Loran C signals are collected by a fine wire dipole antenna. Each section is between 35 and 10 feet in length. After filtering and amplification, the Loran C signal is limited so that the output transistor can handle a wide range of signal levels that may be encountered. Signals are then fed to a varactor diode located across the 403 MHz tank circuit. This produces frequency modulation of the 403 MHz transmitter with the Loran C information together with the usual meteorological data. The ground receiving equipment is shown in Figure 4.4. This equipment consists of a 403 MHz sleeve dipole antenna, a preamplifier, a 403 MHz receiver, a signal attenuator, a 100 kHz receiver and selective amplifier, a 100 kHz antenna, a Loran C 100 kHz pulse generator and other data handling and readout components.

During discussions with the developers of this system, opinions were expressed that it could provide altitude data in addition to geographic position data and therefore, be adaptable to meteorological rocketsondes.

4.5 Micro-Miniature Voltage Controlled Oscillator

Sonex, Inc. has developed a micro-miniature isolated high level voltage controlled oscillator (TEX-3087) which may be useful in future meteorological rocket payloads as a subcarrier oscillator. All IRIG proportional and constant bandwidth subcarrier frequencies are available in this unit. Deviations of $\pm 7.5\%$ and 15% are available for proportion bandwidth channels and ± 2 kHz, ± 4 kHz, and ± 8 kHz for constant bandwidth channels. The input impedance is $750\text{ K}\Omega$ minimum for $\pm 7.5\%$ deviation and $375\text{ K}\Omega$ minimum for $\pm 15\%$ deviation. Output impedance is $47\text{ K}\Omega$ and output voltage is up to 1.4 volts peak-to-peak into a $10\text{ K}\Omega$ load or 8 volts with no load. The power requirements are +28 VDC at a nominal current of 25 mg. The size is $0.71'' \times 1.00'' \times 1.06''$ for a volume of 0.74 in^3 . The weight is 0.8 oz.

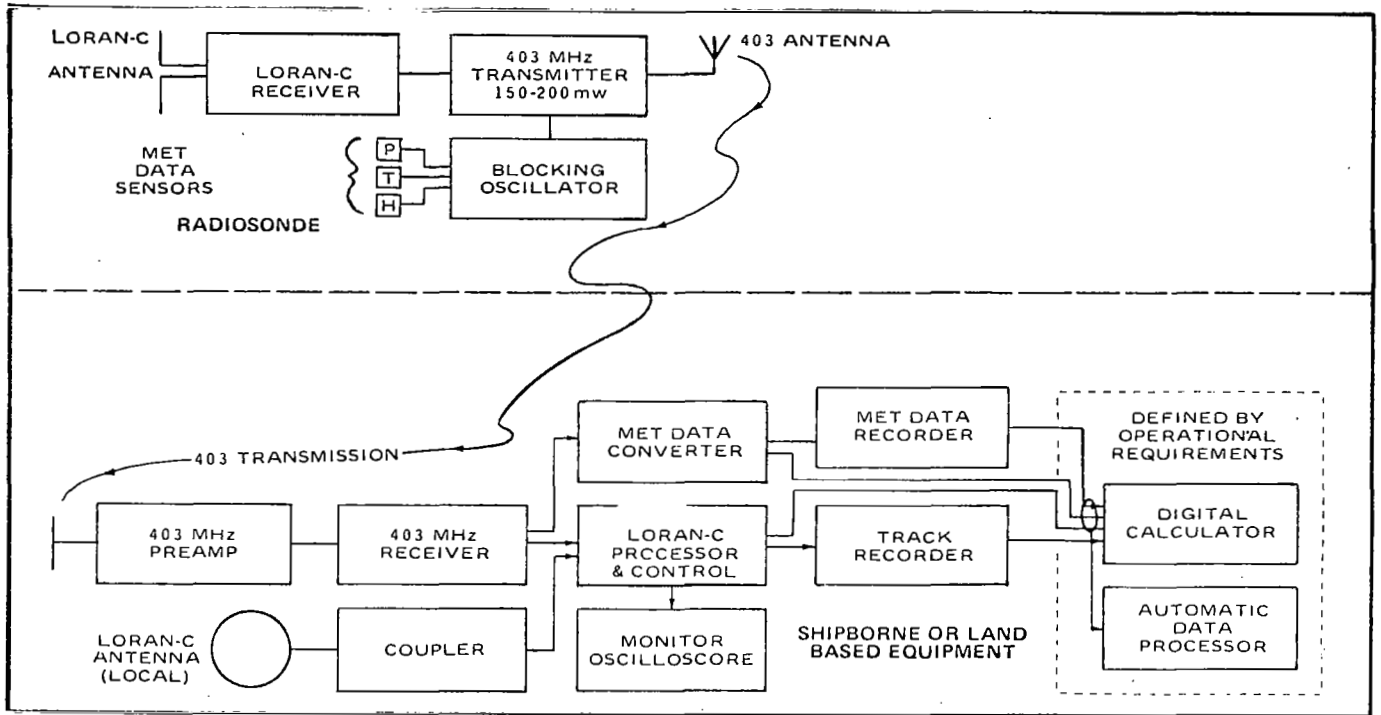


Figure 4.4 Loran C Radiosonde System

RECENT ROCKET VEHICLE ADVANCEMENTS

5.1 General.

Although the published literature over the past year has been scanty, there are currently three meteorological rocket vehicle developments.

5.2 Super Loki.

The Super Loki with a large diameter dart is being developed for AFCRL for their GMD-4 transponder payload. This vehicle has been successfully flight tested a number of times to altitudes of 76 km (250,000 feet). The rocket motor is identical to that developed for NASA-MSFC as reported in NASA CR-1529 Volume I Part 2, but the dart is increased in size to 2.125 inch diameter, 57.5 inch length to house the larger AFCRL payload and it weighs 18.3 lb. A hybrid vehicle has been developed and flight tested by the Air Force to eliminate the booster wind-drift problem. A standard Super Loki rocket motor is used with a heavy interstage and the standard PWN-8B Loki dart. The heavy interstage keeps the booster stable after dart separation so that the booster follows a ballistic trajectory and impact range is increased to about three miles. The dart achieves an altitude of about 70 km (230,000 feet).

5.3 Army RDT & E Rocket

The Army RDT and E rocket has been flight tested at WSMR to an altitude just short of 60 km (200,000 feet). For a sea level launch this is equivalent to an apogee of only 48 km (160,000 feet). Since this altitude is well below the stated performance requirement, the Army is currently redesigning the rocket vehicle.

5.4 Astrobee D

The Astrobee D is a 6 inch diameter solid propellant sounding rocket which is being developed by the Aerojet General Corporation for 100 km soundings. This rocket uses a slow burning hydroxyl-terminated polybutadiene (HTPB) propellant in a dual-thrust grain geometry to overcome the slow launch velocity problems of winds and dispersion, and at the same time to produce a long burning time to minimize drag losses in the atmosphere. Major design characteristics are presented in Table 5.1.

Table 5.1 Astrobe D Characteristics

Motor Length	110 inches
Motor Diameter	6 inches
Propellant Weight	133 lbs
Motor Weight	181 lbs
Total Impulse (Vacuum)	34,000 lb-sec
Boost Thrust	3,800 lb
Boost Duration	2 sec
Sustain Thrust	1,800 lb
Boost Acceleration Max.	25 g
Sustain Acceleration Max.	20 g
Sustain Duration	16 sec

The vacuum thrust curve is presented in Figure 5.1. The predicted apogee altitude is approximately 140 km (460,000 feet) from a sea level launch. However, the first flight tests at WSMR achieved about 98 km (320,000 ft) with a 33 lb payload. From a sea level launch site this altitude would be about 70 km (230,000 feet) with the large payload. It appears that with a 9-10 lb net payload performance will be about 140 km altitude which is required for the passive falling sphere measurements. Although the company has advertised a vehicle cost of less than \$1,000 for quantity production, their estimate for small quantities is on the order of \$3,000. The actual price for which eight vehicles were sold at AFCRL for evaluation was \$4,375 each including payload.

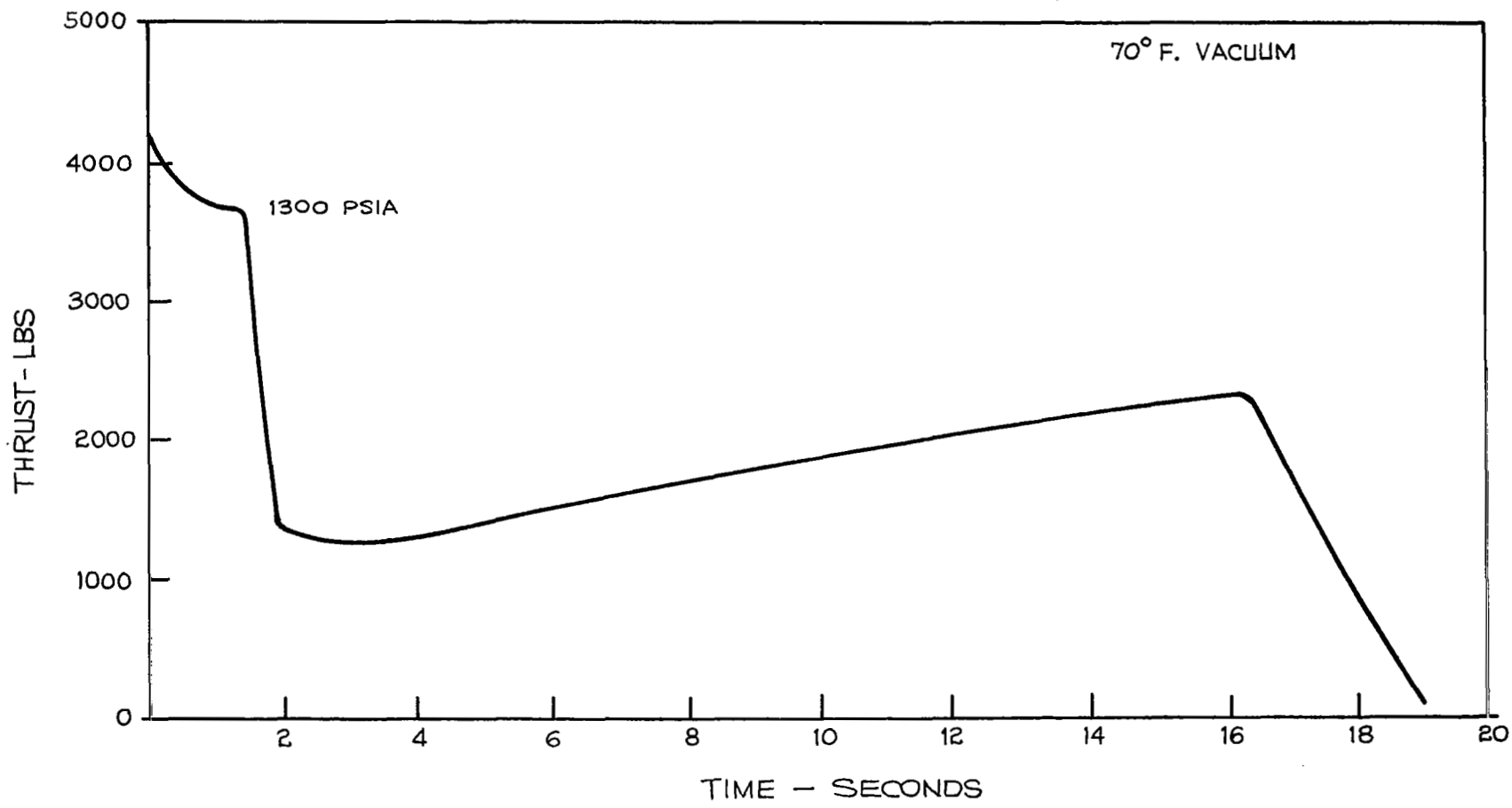


Figure 5.1 ASTROBEE D - Thrust vs. Time

6.

PITOT PROBE DESIGN STUDY

6.1 General.

There appears to be a need for a low cost 50 km to 100 km atmospheric density and wind measurement system for semi-synoptic missile and space vehicle support soundings. Currently used passive sphere techniques require sophisticated and costly radar for data acquisition, and the data accuracy has been rather questionable. Other density measurement techniques which have been used or evaluated to date are not satisfactory for routine use because of high cost or poor accuracy in this altitude region. The design of a small, relatively inexpensive pitot probe meteorological rocket system has been studied to improve the accuracy of the 50 to 100 km soundings as compared with the passive sphere systems and at the same time eliminate the requirement for radar support.

During the IGY, rather sophisticated pitot-static measurements made with the Aerobee-150 vehicle demonstrated the validity and accuracy of the density data derived from measurements of the ram pressure at the nose of the rapidly ascending vehicle. Since vehicle performance and attitude were monitored by on-board instrumentation during these flights, an error analysis could be conducted to assess the effects of such parameters as vehicle angle of attack, vehicle velocity and atmospheric winds. These analyses indicated that as long as the vehicle velocity was maintained above Mach 3 and vehicle attitude below a 10-degree angle of attack, accurate density data could be derived from a measurement of ram pressure alone. Under these conditions the effects of atmospheric winds on the calculated densities were found to be negligible.

As a result of the preceding experiments, NASA-Goddard Space Flight Center has scaled the pitot experiment down to the Nike-Apache vehicle. With the measurement of only ram pressure, the derived densities appear to be quite accurate. However, this system is too expensive for semi-routine meteorological soundings. The Sparrow Arcas Denpro program conducted by the Navy at the Pacific Missile Range demonstrated the feasibility of utilizing a relatively low cost vehicle and AN/GMD-2 telemetry, instead of radar, for this pitot measurement technique. The weak point of this system, however, was the inaccuracy of the pressure transducer which was used to measure the ram pressure.

This design study presents the background theory and systems design parameters for a low cost pitot probe system. The proposed vehicle is a two-stage Super Loki sounding rocket. The proposed telemetry and tracking instrumentation is compatible with the AN/GMD-2, but consideration is also given to the incorporation of the tone-range telemetry interferometer tracking system being developed at Goddard. After a review of pressure transducers was conducted, the primary selection in the vibrating diaphragm technique developed at NASA Ames Research Center. Subsequent discussions with Ames personnel indicate possible improvements and cost savings by modifying the existing unit for the pitot probe application.

In the proposed system, ram air pressure measurements are initiated after ejecting the vehicle nosecone at an altitude of 50 km during vehicle ascent. During the measurement period from 50 km to 100 km the Mach number ranges from 5.0 to 5.6, the speed ranges from 1365 mps to 1700 mps, and the angle of attack, due to the flight path angle profile, varies from 0° to 2.0° . Ram pressures will vary from about 2.8×10^1 to 3.7×10^{-3} mm Hg through the measurement region. The ram pressure will be about 2.2×10^{-4} mm Hg at 120 km. The total angle of attack depends upon vehicle coning or precession and flight path angle. A tradeoff between gyroscopic and aerodynamic effects is made to minimize the effect of vehicle attitude upon the density measurements.

After the ram pressure measurements are completed, the deployment of an inflatable sphere is proposed for wind measurement. The sphere is to be released from the rear of the pitot probe payload compartment between 130 km to 200 km during the upleg portion of the vehicle trajectory. Depending upon the available ground-based data acquisition equipment at a given launch site, the sphere would be either metalized for radar tracking or it would contain a lightweight instrument compatible with the GMD-2 or the Goddard tone-ranging interferometer. If FPS-16 type radar were available, redundant density measurements from the sphere could be made. To optimize wind response or sensitivity a larger sphere than the standard 1-m diameter is proposed, especially if the tracking instrumentation is required.

The systems operation is portrayed in Figure 6.1. The primary density measurement region is from 50 to 100 km where the accuracy of the pitot probe should be within 2 percent on an rms basis. The secondary density measurement region from 100 to 120 km can be considered as a region of less accuracy but worthwhile density measurements.

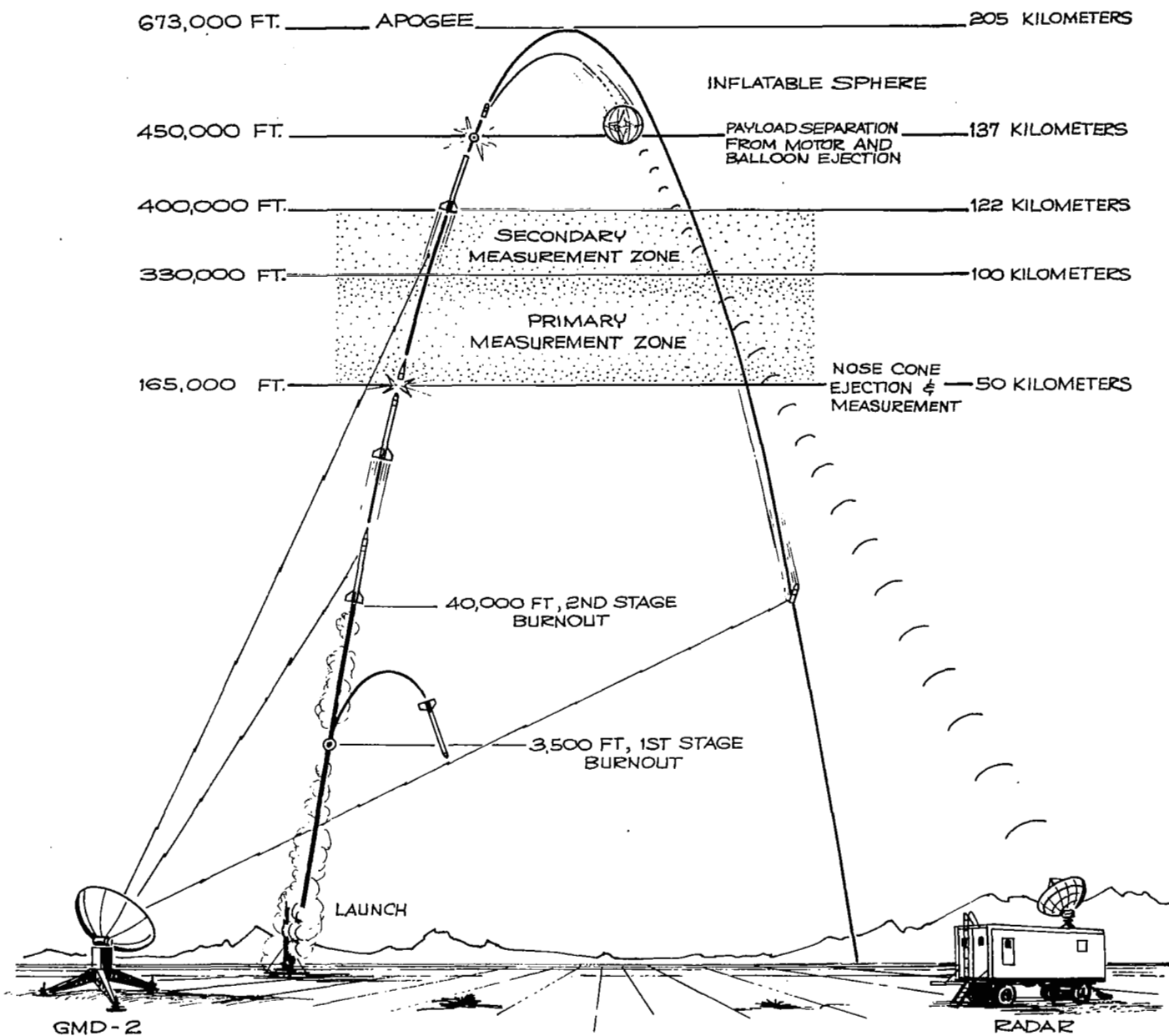


FIGURE 6.1 PITOT PROBE DENSITY MEASURING SYSTEM

6.2 Introduction.

Atmospheric density profiles can be determined from the measurement of ram pressure at the nose of a rapidly ascending sounding rocket. As early as 1952, density profiles were obtained by this technique; however, the rockets and instrumentation were large, complex and very costly. These early Aerobee-Hi pitot probe flights indicated that the complexity of the instrumentation could be reduced provided vehicle attitude and velocity were maintained within certain limits through the measurement region.

More recently NASA/GSFC has scaled the pitot probe instrumentation down in size, complexity and cost so that a limited number of flights can more economically be conducted each year with the Nike-Apache vehicle. Although quite accurate density profiles have been obtained with this system, the expendable cost has been on the order of \$18,000 per flight.

An attempt was made by the Navy at PMR and Atlantic Research Corporation about 1965 to adapt a low cost pitot probe to the two-stage Sparrow-Arcas vehicle with AN/GMD-2 (modified) telemetry and tracking instrumentation. During this program the vehicle, telemetry and GMD-2 tracking were demonstrated to be feasible. However, the payload required both a high and a low pressure gage to extend the measurements throughout the altitude region from 46 km to 107 km. During the flight test series, the high pressure gage produced reasonable density profiles to 65 km, but the low pressure gage did not perform. Thus, the feasibility of the low cost pitot probe system concept was demonstrated up to the point of the pressure gages. The estimated cost for this Sparrow-Arcas pitot probe system is as follows:

Sparrow-Arcas Vehicle	\$5,000
Payload Structures	500
Telemetry	500
High Pressure Gage	800
Low Pressure Gage	<u>1,200</u>
Total System Cost	\$8,000

Although this cost is considerably less than for the Nike-Apache system, it is still much greater than can be considered as reasonable for routine meteorological support.

This design study describes a pitot probe sounding rocket system which can be used for routine density soundings to an altitude of about 100 km at an economical cost. The vehicle is a two-stage Super Loki with a 4 inch diameter nose cone and an apogee altitude of approximately 230 km. Telemetry and tracking are accomplished with AN/GMD-2 (modified) type instrumentation. The ram pressure

sensing is accomplished with a vibrating diaphragm pressure transducer which has been developed by NASA Ames Research Center. In addition to the pitot probe sensor, it is also proposed to release an inflatable sphere prior to vehicle apogee to obtain winds and possibly a redundant density profile, depending upon the quality of the available ground-based radar at a given launch site.

6.3 Requirements.

Although the technical and logistic requirements for a pitot probe cannot be completely separated, they are discussed separately here for ease in presentation. Tradeoffs are made among the various factors to arrive at a reasonable system design. These subjects are discussed in the following sections.

6.3.1 Technical Requirements.

There are high altitude requirements to obtain atmospheric density measurements above current rocketsonde altitudes from 50 km to an altitude of about 100 km. Although precise measurements are desired throughout this region, technical and logistic factors, i. e., cost, require the formulation of measurement accuracy criteria such as that presented in Figure 6.2. Not only is it more difficult to measure density accurately as the altitude is increased, but the accuracy requirements for the data are generally less stringent with increasing altitude. The measurement aspects of the pitot probe technique are reviewed in the following paragraphs.

6.3.1.1 Normal Shock Wave Relationships.

The pitot probe measurements and data reduction are based upon the supersonic normal shock wave relationships. The equations of continuity, conservation of momentum, conservation of energy and the perfect gas laws are combined to derive the basic relationships which describe the conditions fore and aft of a normal shock wave.

Consider a stream column with a constant cross-sectional area and a normal shock wave as shown in Figure 6.3. The equation of continuity states that

$$\rho_1 V_1 = \rho_2 V_2 \quad (1)$$

The law of conservation of momentum states that

$$P_1 + \rho_1 V_1^2 = P_2 + \rho_2 V_2^2 \quad (2)$$

The law of conservation of energy states that for a compressible adiabatic flow the sum of the pressure energy and kinetic energy is as constant as:

$$\left(\frac{\gamma}{\gamma-1}\right) \frac{P_1}{\rho_1} + \frac{V_1^2}{2} = \left(\frac{\gamma}{\gamma-1}\right) \frac{P_2}{\rho_2} + \frac{V_2^2}{2} \quad (3)$$

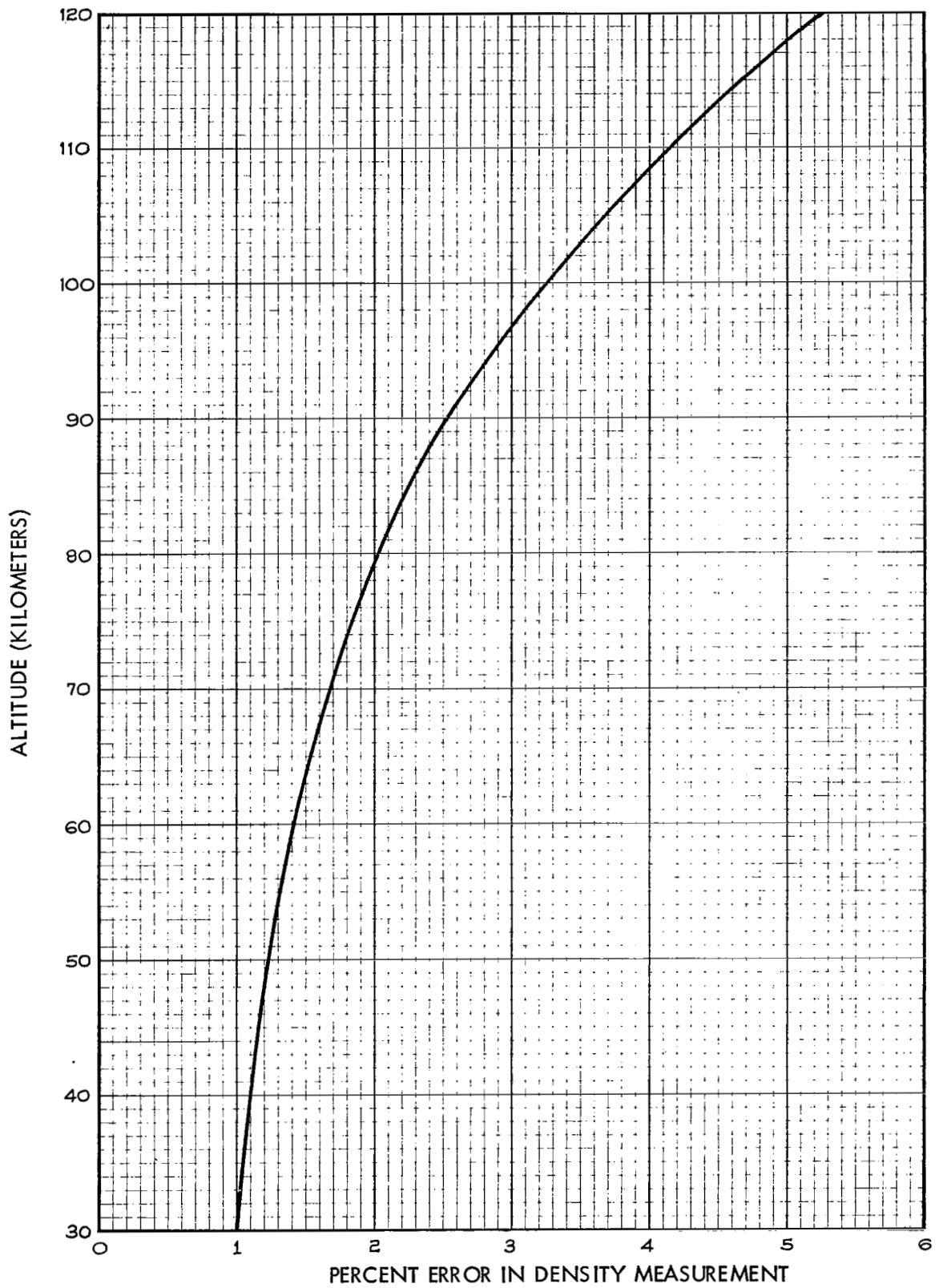
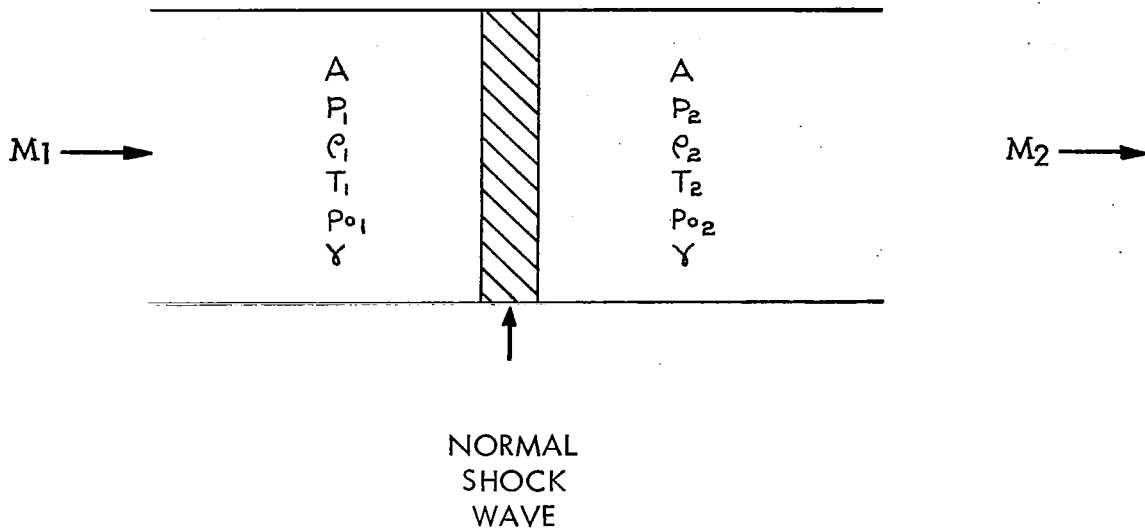


FIGURE 6.2 TYPICAL ATMOSPHERIC DENSITY MEASUREMENT ACCURACY REQUIREMENT



A	=	Cross-sectional Area
p	=	Pressure
ρ	=	Density
T	=	Absolute Temperature
p_0	=	Stagnation Pressure
M	=	Mach Number
γ	=	Ratio of Specific Heats

FIGURE 6.3 NORMAL SHOCK WAVE

By combining equations (1) and (2),

$$\frac{V_2}{V_1} = \left(\frac{1}{\gamma M_1^2} \right) \left(1 - \frac{P_2}{P_1} \right) + 1$$

and by substituting this expression into equation (3) with the perfect gas law

$$\frac{T_2}{T_1} = \left(\frac{P_2}{P_1} \right) \left(\frac{\rho_2}{\rho_1} \right)$$

the basic relationships which describe the conditions fore and aft of a normal shock wave are derived as follows:

Pressure

$$\frac{P_2}{P_1} = \frac{2 \gamma M_1^2 - (\gamma - 1)}{\gamma + 1} \quad (4)$$

Temperature

$$\frac{T_2}{T_1} = \frac{[2 \gamma M_1^2 - (\gamma - 1)][(\gamma - 1) M_1^2 + 2]}{(\gamma + 1)^2 M_1^2} \quad (5)$$

Density

$$\frac{\rho_2}{\rho_1} = \frac{(\gamma + 1) M_1^2}{(\gamma - 1) M_1^2 + 2} \quad (6)$$

Mach Number

$$M_2^2 = \frac{(\gamma - 1) M_1^2 + 2}{2 \gamma M_1^2 - (\gamma - 1)} \quad (7)$$

Stagnation Pressure

$$\frac{P_{o2}}{P_{o1}} = \left[\frac{(\gamma + 1) M_1^2}{(\gamma - 1) M_1^2 + 2} \right]^{\frac{\gamma}{\gamma - 1}} \left[\frac{2 \gamma M_1^2 - (\gamma - 1)}{\gamma + 1} \right]^{\frac{-1}{\gamma - 1}} \quad (8)$$

where the subscript 0 denotes the isentropic stagnation pressure.

The pitot probe constitutes a special case of the normal shock wave wherein the air flow is brought to rest inside the pitot tube and stagnation or total pressure is measured. Rayleigh derived the basic pitot equation from the above relationships as

$$\frac{P_{o2}}{P_1} = \left(\frac{\gamma+1}{2} M_1^2 \right)^{\frac{\gamma}{\gamma-1}} \left[\frac{2\gamma M_1^2 - (\gamma-1)}{\gamma+1} \right]^{\frac{-1}{\gamma-1}} \quad (9)$$

where, in this expression, P_{o2} denotes pressure measured in the impact tube.

The pitot stagnation pressure-to-static pressure ratio for the supersonic flow of air ($\gamma = 1.4$) is plotted against free stream Mach number in Figure 6.4. A main advantage of employing a pitot probe pressure measurement instead of a static or ambient pressure measurement from a fast moving supersonic vehicle at high altitudes is that the pitot pressure is from 10 to 30 times greater than the corresponding ambient pressure, and therefore, less sensitive pressure gages may be used. A second advantage is that the location of the pitot orifice at the nose of the vehicle is exactly determined; whereas, the static or ambient pressure position along the side of the vehicle is not accurately known. This static pressure position changes with Mach number and angle of attack during flight.

6.3.1.2 Simplified Pitot Probe Relationships.

In the continuum flow region the Rayleigh pitot equation for supersonic flow and the equation of state for an ideal homogeneous gas may be combined, with some simplifying assumptions, to yield a simple expression for ambient density as

$$\frac{1521.1 P_{o2}}{|V|^2} \quad \text{Kilograms/meter}^3 \quad (10)$$

This expression holds for Mach numbers between 3.5 and 7.2 and where $|V|$ is the component of rocket velocity normal to the pitot orifice. A similar expression used by Ainsworth, et al., is

$$P_1 = \frac{0.144 P_{o2} - 0.066 P_1}{|V|^2} \quad (11)$$

$$\frac{\text{gm}}{\text{m}^3} = \frac{\text{mm Hg}}{\left(\frac{\text{km}}{\text{Sec}}\right)^2}$$

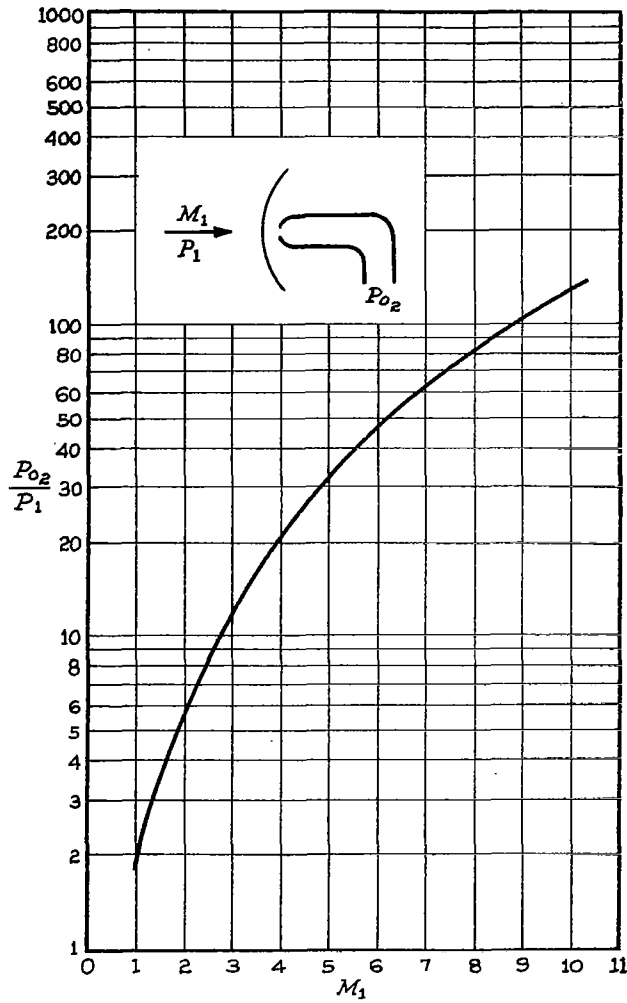


FIGURE 6.4 PITOT-STATIC PRESSURE RATIO FOR SUPERSONIC FLOW OF AIR ($\gamma = 1.4$)

In the free molecular flow region the shock wave disappears, and thermal transpiration governs the pressure relationships. The pressure ratio is then given by

$$\frac{P_{o2}}{P_{o1}} = \sqrt{\frac{T_{o2}}{T_{o1}}} F(s) \quad (12)$$

where

$$F(S) = e^{-S^2} + S \pi (1 + \operatorname{erf} S)$$

$$S = \frac{V \cos \alpha}{C_{m0}}$$

α = effective rocket angle of attack

C_{m0} = most probable particle velocity

Combining the above expression with the equation of state for an ideal and homogeneous gas yields the expression for ambient density as

$$\rho_1 = \frac{P_{o2}}{\sqrt{\frac{2 \pi R T_{o2}}{m}} \cdot V \cos \alpha} \quad (13)$$

where

R = universal gas constant

m = mean molecular mass of the gas

This expression results from simplifying assumptions made by Ainsworth regarding the vehicle velocity, angle of attack and the effect of atmospheric winds upon the measured impact pressure.

A number of factors must be considered in order to use the above simplified expressions to compute density from impact pressure with a reasonable degree of accuracy. These factors include the vehicle speed, the angle of attack, the effect of atmospheric winds, outgassing effects, transducer error, heating effects, viscous effects due to tube shape and Reynolds number and impact pressure deficiency compared to ideal pressure because of orifice size. In general, it was found that corrections to the measured data were less than 1 percent with the exception of the viscous effects, where the required correction in the free molecular flow region was 9 percent. A summary of the sources and probable magnitudes of error in the density determination is presented in Table 6.1 and discussed as follows.

TABLE 6.1 SUMMARY OF ERROR SOURCES IN PITOT-TUBE METHOD
(PER DENPRO FINAL REPORT BY ATLANTIC RESEARCH CORP., 1965)

Error Source	Effect on Computed Density	Magnitude of Correction	Remarks
1. Angle of Attack	Lowers	+ 0.2%	Correction applies if attack angle is less than 10-degrees
2. Vehicle Speed	Equation (4)	0	Correction applies for relatively constant Mach number range
3. Atmospheric Winds Vertical	Increases	- 0.15 to -0.3%	Correction must be estimated
4. Atmospheric Winds Horizontal	Increases	- 2.0%	Correction must be estimated
5. High Gas Temperature	Increases	- 0.8%	Varies with altitude
6. Chamber Response	Increases	- 0.2 to -0.5%	For membrane gage
7. Orifice Size	Decrease	+ 0.3%	During continuum flow region
8. Viscous Effects	Decrease	+ 1.0%	Continuum flow
		+ 9.0%	Free molecular flow
9. Gage Pressure Hysteresis	Increases	2.0 to 10%	Gages are calibrated for correction
10. Gage Thermal Response	--	--	Error can be calibrated out
11. Acceleration Sensitivity	--	--	Drag acceleration after thrust phase can be calibrated out
12. Outgassing Effect	Increases	0	Prudent design and preflight precautions eliminate significant error
13. Gage Accuracy	--	± 0.5%	Error analysis from lab calibration will determine correction

(a) Rocket Vehicle Speed.

The more general expression for density in the continuum flow region is

$$\rho_a = \frac{P_i}{V^2 \frac{\gamma+1}{2} \left[\frac{(\gamma+1)^2 M^2}{4\gamma M^2 - 2\gamma + 2} \right]^{\frac{1}{\gamma-1}}} \quad (14)$$

where

ρ_a = ambient density

P_i = ideal impact pressure

γ = ratio of specific heats (C_p/C_v)

M = free stream Mach number

V = free stream velocity

Examining the function of the denominator of Equation (14)

$$\frac{\gamma+1}{2} \left[\frac{(\gamma+1)^2 M^2}{4\gamma M^2 - 2\gamma + 2} \right]^{\frac{1}{\gamma-1}}$$

and assuming that γ has a constant value of 1.4, it is apparent that this part is a weak function of Mach number and approaches a constant value of about 1.3 for values of M greater than about 3. However, as M decreases below 3, significant changes occur which must be accounted for in the solution of equation (14). Hence, in order to simplify data reduction processes, it is desirable to maintain a high Mach number and a limited range thereof throughout the altitude region of interest.

(b) Angle of Attack and Wind Effects.

The term P_i refers to an ideal impact pressure which would be developed at a zero degree angle of attack of the pitot probe. Flight path angle variation and both horizontal and vertical winds cause the ideal impact pressure to be different from the actual measured impact pressure and the velocity term to be

different from the vehicle velocity. As the vehicle ascends an attack angle develops gradually between the longitudinal axis of the probe body and a tangent plane to its flight path. Under this situation it was determined that measured values of P_i can be adjusted with acceptable accuracy to correct values by dividing them by the cosine of α , the attack angle. It can be shown that for attack angles in the order of 10 degrees or less, the required correction is in the order of 0.2 percent. To achieve such low angles, however, the peak altitude capability of the vehicle usually must exceed, by far, the maximum measurement altitude.

The actual values used for V are intended to be the air stream velocity, not merely the rocket probe velocity. Based upon a few measurements of winds, it was determined that the maximum error in computed density, as a result of vertical wind components, may be 1.5 percent, but the root-mean-square error would be 0.1 to 0.3 percent. Corrections to be applied for horizontal components are a strong function of such parameters as flight path angle, initial zenith angle, and precession cone angles. Ideally, to minimize resulting errors from unknown horizontal winds, the rocket vehicle should be insensitive to low altitude winds so that high launch angles can be used. The vehicle should also be capable of achieving payload apogee values for in excess of measuring altitudes to maintain high flight path angles, and be spin stabilized to reduce precession angles to small values. It is interesting to note that spin stabilization is deleterious at the higher altitudes since it causes a divergence in the angle of attack as the flight path angle begins to flatten out.

(c) Outgassing Errors.

Measured impact pressure can be affected by the presence of gas molecules which are foreign to the ambient atmosphere. Such gas interference can stem from out-gassing of impact chamber walls, gas escaping from the interior of the vehicle, and gas evolving from hot exterior surfaces. Difficulties from this effect are likely to become particularly troublesome near the upper region of the desired altitude, above 80 kilometers, where residual gas pressure should be below 10^{-4} mm Hg. Special treatment of surfaces and rigorous out-gassing of all surfaces near the orifice prior to flight can reduce errors due to this contamination.

(d) Gage Errors.

The normal gage errors of accuracy, bias, repeatability, stability and range sensitivity in addition to response time, acceleration sensitivity, thermal sensitivity, zero stability and hysteresis are sources of error in the basic impact pressure measurement. These factors vary with the particular sensor gage used.

6.3.1.3 Measurement Requirements.

Pitot probe density measurements may be made from an altitude of 50 km to an altitude of 100 km with a relatively low cost system providing certain requirements through the measurement zone are satisfied. These requirements are as follows:

- a. Maintain the vehicle angle of attack below 10 degrees.
- b. Maintain the vehicle speed between Mach 3.5 and 7.2.
- c. Maintain a high flight path angle and attitude to minimize the effects of horizontal winds.
- d. Maintain ambient temperature of the pitot chamber by protecting it from aerodynamic heating with a nose cone during the lower altitude flight.
- e. Maximize orifice size to keep within continuum flow region as high as possible.
- f. Minimize outgassing effects.
- g. Locate the gage within the pitot chamber to minimize chamber time constant.
- h. Utilize a gage which is sensitive and accurate down to a pressure level of 10^{-4} mm Hg.

6.3.2 Logistic Requirements.

The primary logistic requirement for a routine pitot probe is low cost. The vehicle, telemetry and sensor instrumentation must be relatively inexpensive and the cost of the overall system should be less than \$2,000 for routine use. The annual requirement will probably be on the order of a few hundred systems. The vehicle must be small enough and simple enough for a two-man crew to launch at remote sites without handling equipment. The telemetry and sensor instrumentation must be relatively simple to operate and must be compatible with more or less standard AN/GMD-2 ground station equipment. The sensor instrumentation should not require elaborate calibration at the launch site. These are the essential logistic requirements for a routine pitot probe.

6.4 Pitot Probe Sensor.

6.4.1 General.

The pitot probe sensor consists of a truncated conical housing with a hemispherical tip, an orifice in the tip and a pressure transducer which resides within the conical housing section immediately aft from the tip as shown in Figure 6.5. During flight the ram air is driven through the orifice and creates a ram or impact pressure in the spherical chamber formed within the structure. The vibrating diaphragm pressure transducer developed by NASA Ames Research Center is proposed as the sensor. It is located at the rear of the impact chamber to minimize hydraulic lag. A detailed description of the various sensor parameters is presented in the following sections.

6.4.2 Hemispherical Tip and Structures.

The hemispherical tip has been chosen as the sensor forebody since this shape is relatively insensitive to angle of attack effects. Also, a great deal of theoretical and experimental work has been done with this shape to determine the high velocity pressure distributions under numerous flow conditions.

A number of authors have obtained pressure distribution solutions for the hemispherical forebody (references 15, 16, 17, 18, 19). Additional work has been done for conical forebodies with spherical tips. The data presented in Figure 6.6 for a zero angle of attack is representative of the previous work. The streamlines and meridian lines are coincident at zero angle of attack, and the pressure distribution is symmetrical about the longitudinal reference axis. For cone half angles $\theta < 45^\circ$ and $M > 3$ the sphere-cone junction is located in locally supersonic flow; hence the conical skirt has no effect on the pressure distribution over the spherical portion up to the sphere-cone junction.

At angles of attack (zero yaw) the stagnation point moves along the vertical meridian a distance

$$\frac{s}{R} = \alpha \quad (\text{radian}).$$

Streamlines then radiate from the stagnation point in a symmetrical pattern about the stagnation velocity vector for a distance

$$\frac{s_l}{R} = \left(\frac{\pi}{2} - \theta - \alpha \right)$$

which is the arc distance from the stagnation point to the sphere-cone junction at $\phi = 0$.

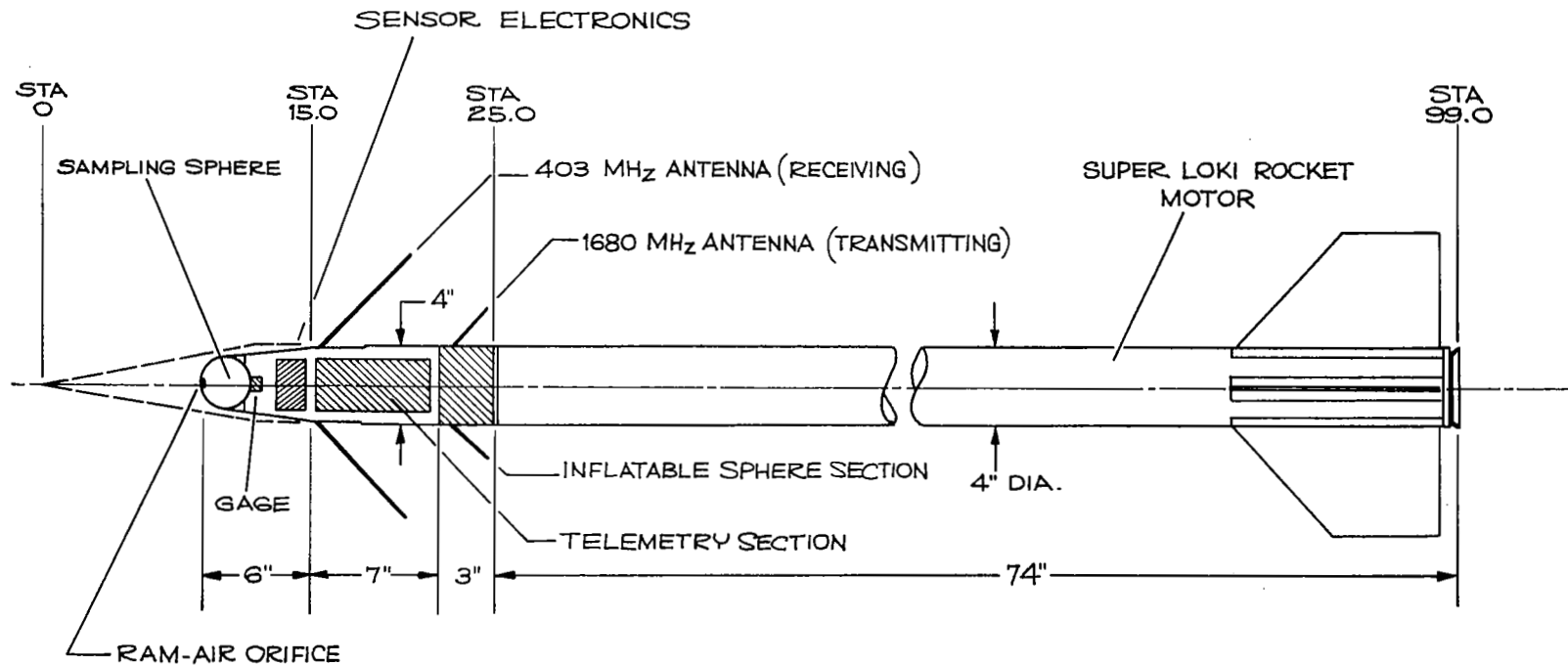
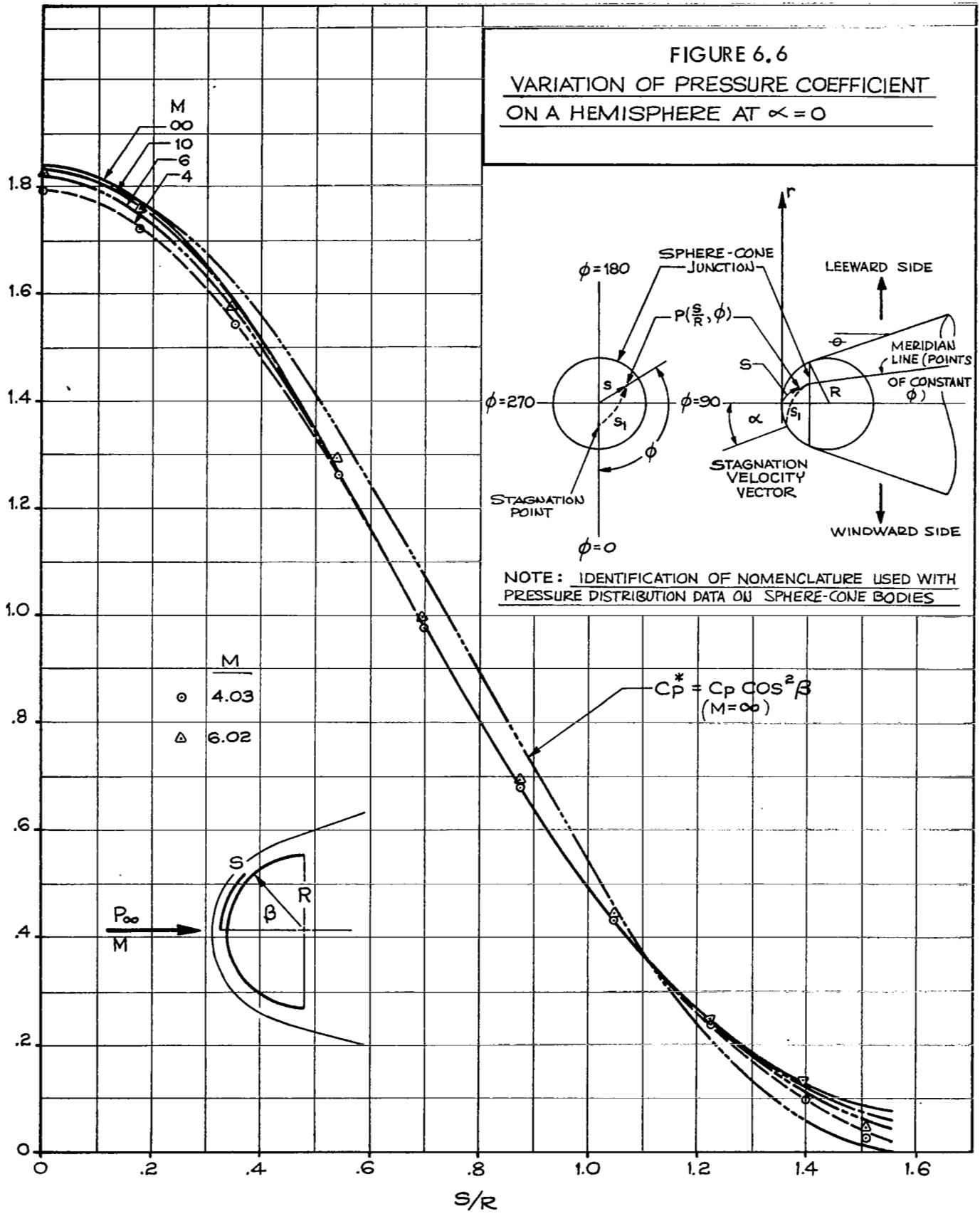


FIGURE 6.5 PITOT PROBE SENSOR

FIGURE 6.6
VARIATION OF PRESSURE COEFFICIENT
ON A HEMISPHERE AT $\alpha = 0$



Analytical results were not available to predict a pressure variation along the streamline path between

$$\frac{s_1}{R} = \left(\frac{\pi}{2} - \theta - \alpha \right) \text{ and } s_1/R = \frac{\pi}{2} - \psi$$

(spherecone junction) for meridians other than $\varnothing = 0$. For the purpose of this analysis it is assumed that all streamlines follow exactly a meridian path between the stagnation point and the sphere-cone junction, and that the pressure variation along the path is given by the data in Figure 6.6. It is believed that for moderate angles of attack the assumption yields good accuracy.

It now remains to compute the pressure distribution along meridian lines on the hemispherical nose. The relation between the sides and angles of an oblique spherical triangle is

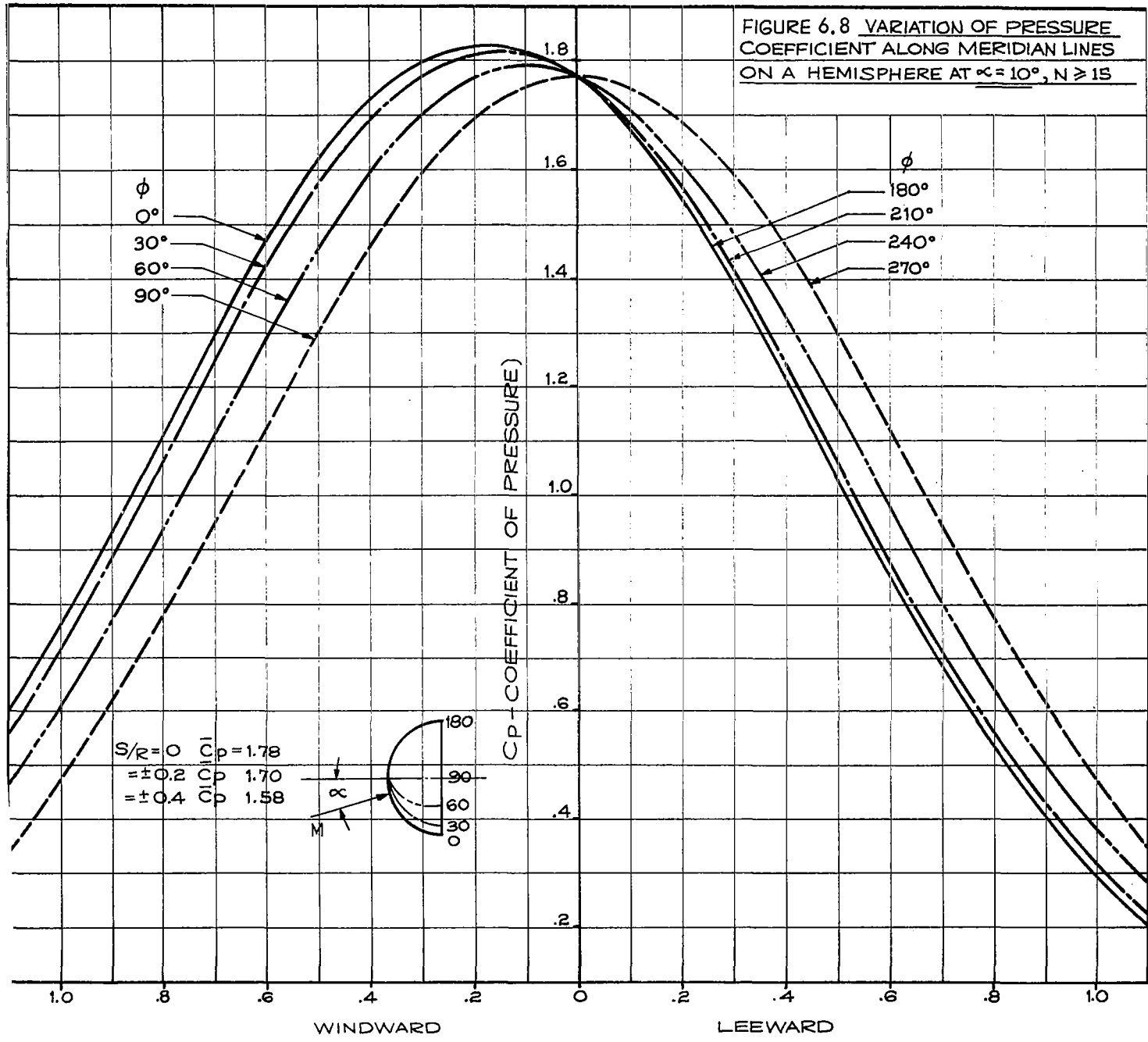
$$\cos \frac{s_1}{R} = \cos \frac{s}{R} \cos \alpha + \sin \frac{s}{R} \sin \alpha \cos \varnothing .$$

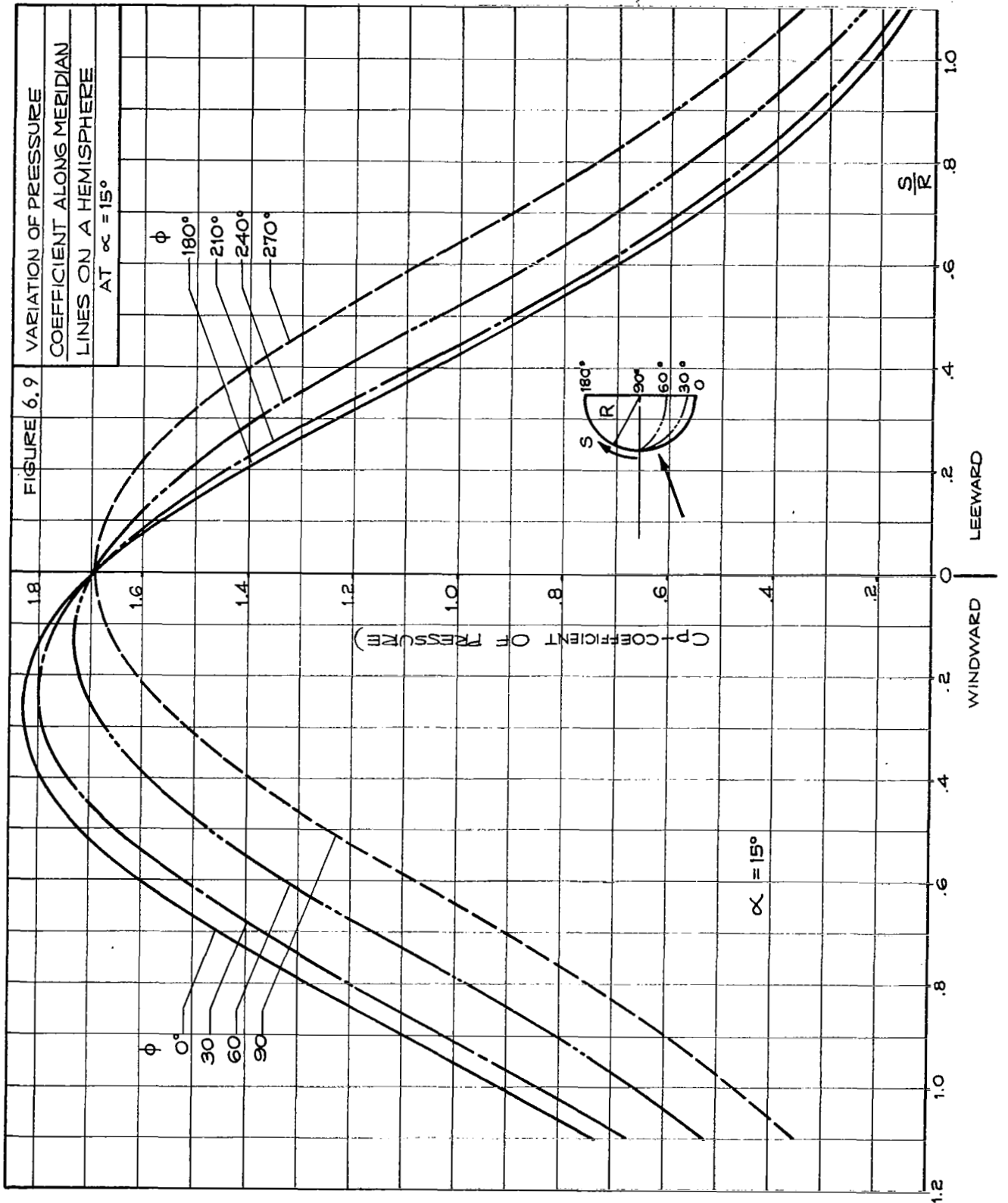
Using this equation for a given α and meridian line defined by \varnothing , a relation between $\frac{s_1}{R}$ and $\frac{s}{R}$ is obtained. Then, the pressure at any point p $(\frac{s}{R}, \theta)$ can be found by first finding its distance from the stagnation point, $\frac{s_1}{R}$, and then take the pressure corresponding to this distance from 6.6.

Figures 6.7, 6.8 and 6.9 present the pressure coefficient variation along eight meridian lines ($\varnothing = 0, 30, 60, 90, 180, 210, 240, 270$) to $\frac{s}{R} = 1.1$ for angles of attack of 5, 10 and 15 degrees respectively. From $\frac{s}{R}$ the above data, the pressure coefficient over a given orifice area can be integrated to yield the total ram pressure for any given orifice size and angle of attack. It can be seen that for angles of attack below 5° there is a negligible angle of attack effect. For $\alpha > 10^\circ$ there is an appreciable effect, and the angle of attack should be known for accuracy in the reduced density data. For $5^\circ < \alpha < 10^\circ$ the accuracy of the density data should be only slightly degraded without taking into account the angle of attack.

The pitot orifice diameter is selected in a trade-off between angle of attack effects and mean free path effects. For moderate α 's the angle of attack effect is minimized for small orifice diameters. On the other hand, continuum flow is maintained to a higher altitude for larger diameters. Previous rocket pitot probes have maintained an orifice diameter to hemisphere diameter ratio of 0.2 (Ainsworth, et al., and Drews).

FIGURE 6.8 VARIATION OF PRESSURE COEFFICIENT ALONG MERIDIAN LINES ON A HEMISPHERE AT $\alpha = 10^\circ$, $N \geq 15$





Economy and weight are important design criteria to be employed in the design of the pitot probe. The need to employ a nosecone shape during the high drag regime of rocket ascent in order to realize maximum altitude and velocity from the available thrust is beneficial to the probe design in two ways. First, it means that aerodynamic heating of the impact pressure surfaces, which could become a source of measurement error, would be avoided. Second, and as a result of negligible heating, the mass of the impact chamber and supporting members can be held to a minimum.

An outline of the sensor assembly is shown in Figure 6.10. The hemispherical leading surface contains the ram pressure orifice; the spherical pressure chamber serves to reduce angle of attack sensitivity; and the gage subassembly is attached directly to the pressure chamber. Beginning at the leading surface, a stainless steel sphere is attached to a machine tapered aluminum body of 4.0 inches length. The sphere is 3.5 inches in diameter and contains a 0.7 inch orifice at its leading edge center. The pressure gage is connected directly to the sphere.

The nosecone is secured to the conical side wall of the sensor assembly by means of three (3) brass shear screws. A pyrotechnic delay train is located within the ram orifice sealing column which is surrounded with a strong spring. The spring is restrained with a pull-pin arrangement which is released at the end of the timing cycle. The delay train is electrically initiated at launch. Also contained within the sealing column is a vacuum getter. The gage and sphere cavities are evacuated, allowed to outgas, and sealed by the manufacturer. No provision is made for reevacuating these cavities after final assembly. However, it is desirable to check gage calibration at a hard vacuum ($\sim 10^{-7}$ torr) to establish a sensitivity threshold prior to launch. To avoid the necessity of employing high vacuum test equipment in the field, a getter arrangement is employed as a part of the nose cone release assembly. This consists of a sealed brass tube, in which is installed a coated tungsten wire getter. The tube terminates in a brass flange which contains an o-ring on its face. The entire getter assembly is inserted within the coils of the ejection spring. When the nose cone is installed, the o-ring is seated around the outside of the impact pressure orifice. Copper tubing, inside the getter assembly, provides a means of evacuating the impact pressure sphere and gage and then sealing the entire assembly from contamination. With this arrangement the payload can be completely calibrated and assembled at the point of manufacture and prelaunch checkout can be accomplished in the field with a minimum of equipment.

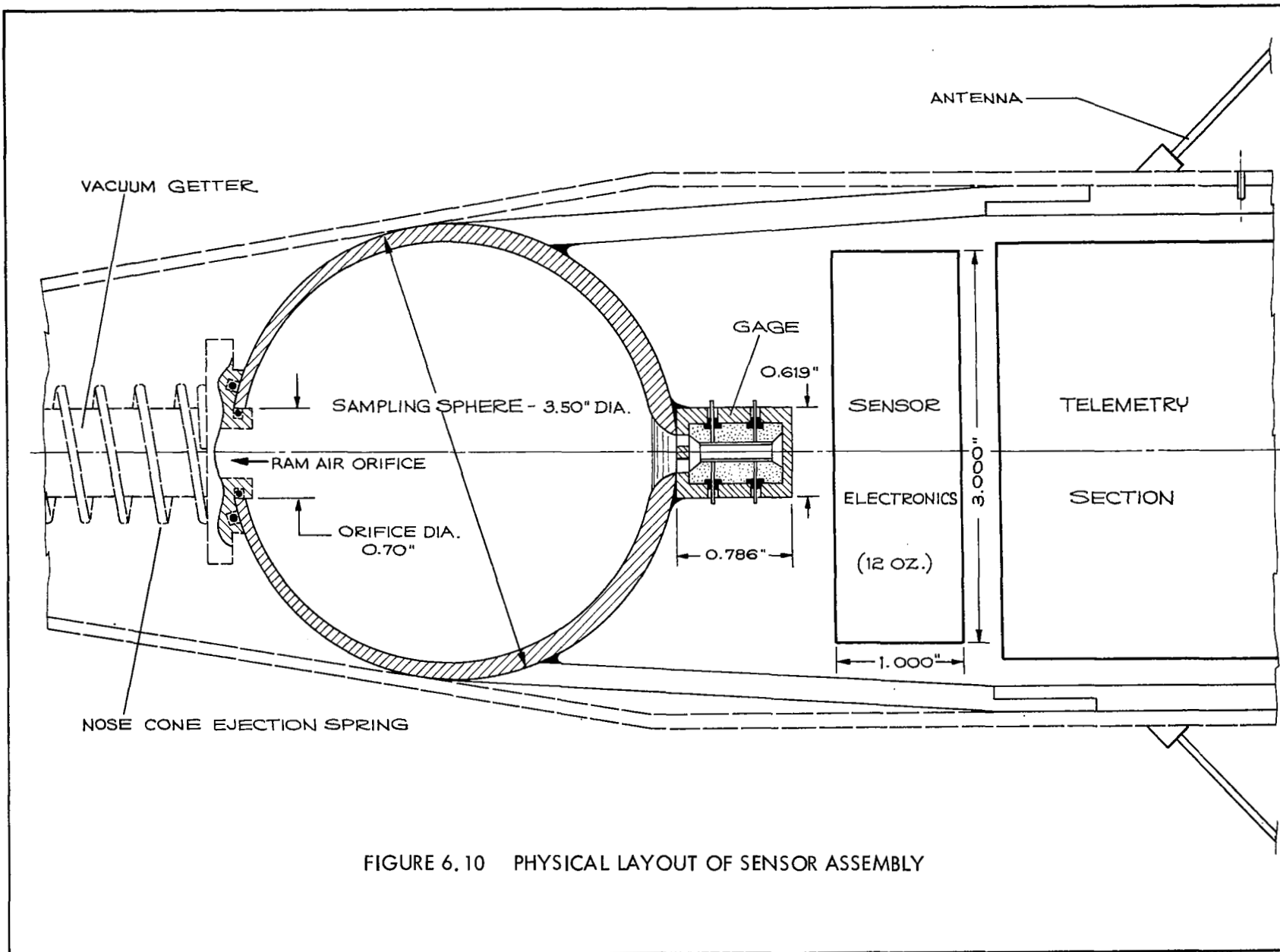


FIGURE 6.10 PHYSICAL LAYOUT OF SENSOR ASSEMBLY

6.4.3 Pressure Gage.

6.4.3.1 General.

Although a number of transducers, working on a variety of principles, have been developed for measuring pressures between 10^{-5} and 10^3 mm Hg, all have limitations for the pitot probe application. The most commonly encountered limitations are large size, slow response, dependence of response on gas composition, fragile construction, sensitivity to differential rather than absolute pressure, poor accuracy, and intermittent indication. A review of a number of pressure gage techniques is presented in Appendix A.

To overcome the many limitations of previous sensors when applied to the problem of monitoring pressures encountered in high-velocity wind tunnels, Dimeff, Lane, et al. (references 20,21,22) at NASA Ames Research Center developed a new transducer based on the principle of gas damping of a vibrating diaphragm. This device has been used for several years in the high-velocity wind tunnels at Ames Research Center and has given good results in measuring pressures from atmospheric down to about 10^{-5} mm Hg.

Since improved accuracy, speed and reliability in measuring pressure in this range have been accomplished with the Ames vibrating diaphragm transducer, this gage is considered as the primary candidate for the pitot probe application.

6.4.3.2 Principle of Operation.

The vibrating diaphragm pressure transducer is an instrument for measuring absolute gas pressure between 10^{-5} and 10^3 mm Hg. When used with appropriate electronic circuitry, continuous pressure indication is possible with an accuracy of better than one percent over most of this range.

The transducer measures pressure by sensing the damping effect of the gas to be measured on the vibration of a thin metal diaphragm. The diaphragm is under radial tension and is electrically maintained in continuous vibration at its mechanical resonant frequency. The vibrating diaphragm gage is a great improvement over the previous gas damping instruments which are delicate, difficult to use, and limited in their useful range. They also require a large gage volume, have long response times and do not provide continuous indication. In contrast, the Ames device is small, relatively rugged and reliable. It also has fast response, is not subject to damage by overpressure, does not require a vacuum reference and lends itself readily to automatic operation.

Figure 6.11 is a simplified sketch of the vibrating diaphragm transducer which is composed of a thin metallic diaphragm under radial tension between two closely spaced insulated metal plates. The two metal plates provide a means of electrically forcing and detecting the diaphragm's vibration. The space between the plates and the diaphragm is filled with gas at the pressure to be measured. Gas damping causes a loss of energy from the diaphragm to the gas, and this loss is sensed by its effect on the diaphragm damping factor. The electrical power required for a given amplitude of vibration is, therefore, a measure of the gas pressure.

The forcing plate of the transducer is supplied with a dc potential and an ac voltage from an electronic oscillator set at the mechanical resonant frequency of the tensioned diaphragm. The electrostatic forcing function thus generated causes the diaphragm to vibrate synchronously with the ac driving voltage and at an amplitude which is a function of the driving signal and the diaphragm damping factor Q . The diaphragm's vibration causes a corresponding periodic variation in the capacitance between the diaphragm and the sensing plate that may be detected and used to indicate the vibration amplitude. Since the power required for a given amplitude of vibration is a function of the damping of the diaphragm, the power can be monitored as an indication of the pressure.

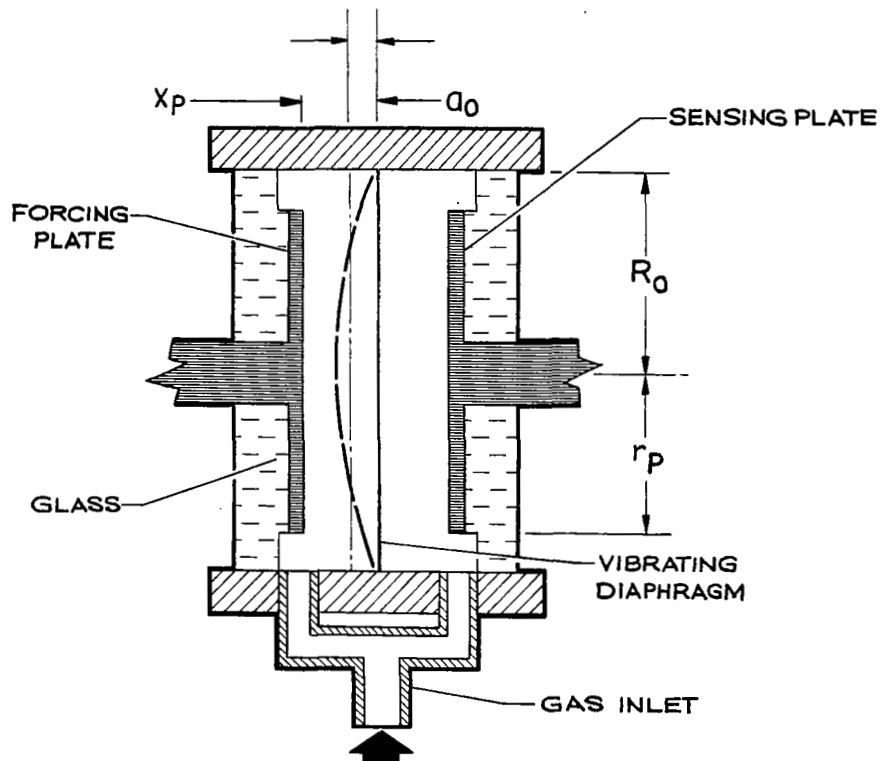
The difficulty in maintaining the driving oscillator at the exact mechanical resonant frequency of the diaphragm is overcome by the gage electronic system. The vibrating diaphragm transducer is used as the frequency-selective element of the electronic oscillator, so that the ac driving signal is automatically maintained at the diaphragm mechanical resonant frequency.

A dc potential, V_o , is applied to the transducer sensing plate through a very high resistance R_1 . The variation in capacitance between the diaphragm and the sensing plate produces an ac output voltage V_2 . If the change in capacitance occurs over a time interval that is short compared with the R_1C_o time constant, then

$$V_2 = V_o \cdot \frac{C_1}{C_o}$$

where C_1 is the change in capacitance and C_o is the static capacitance.

Since the vibration in capacitance is sinusoidal, V_2 is sinusoidal, with a peak value dependent on the peak value of the capacitance change (See Figure 6.12).

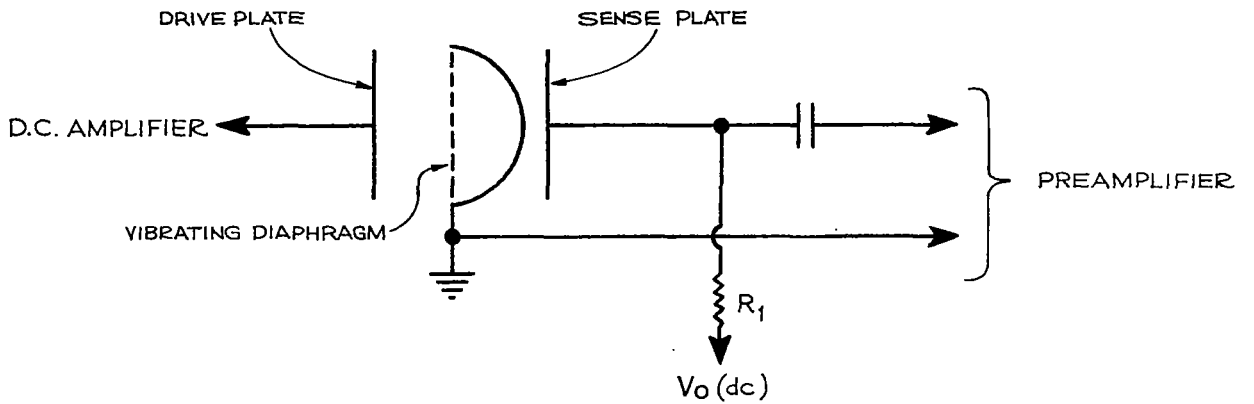


$$R_0 = 8.3 \times 10^{-3} \text{ m}$$
$$r_p = 7 \times 10^{-3} \text{ m}$$
$$X_p = 7.5 \times 10^{-5} \text{ m}$$
$$a_0 = 7.5 \times 10^{-10} \text{ m}$$
$$t = 2.5 \times 10^{-6} \text{ m}$$
$$\omega_0 = 3.6 \times 10^4 \text{ rad/sec.}$$
$$Q = 3 \times 10^4$$
$$Q = 2 \pi \frac{W}{\Delta W}$$

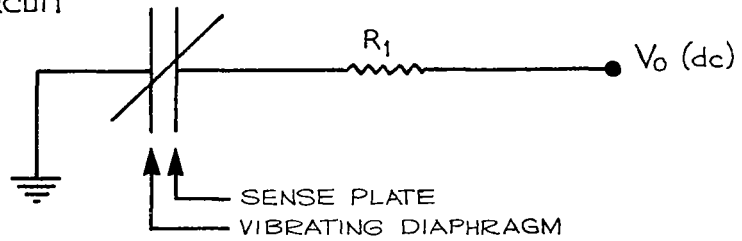
(Dimeff, Lane, et al)

FIGURE 6.11 SIMPLIFIED SKETCH OF THE ORIGINAL EMBODIMENT

$C_0, V_0 (dc)$
 $\Delta C, V_2 (ac)$ } BETWEEN DIAPHRAGM AND SENSE PLATE



EQUIVALENT CIRCUIT



FOR R_1 LARGE SO THAT $R_1 C_0$ TIME CONSTANT IS GREATER THAN VIBRATION OR OSCILLATION PERIOD.

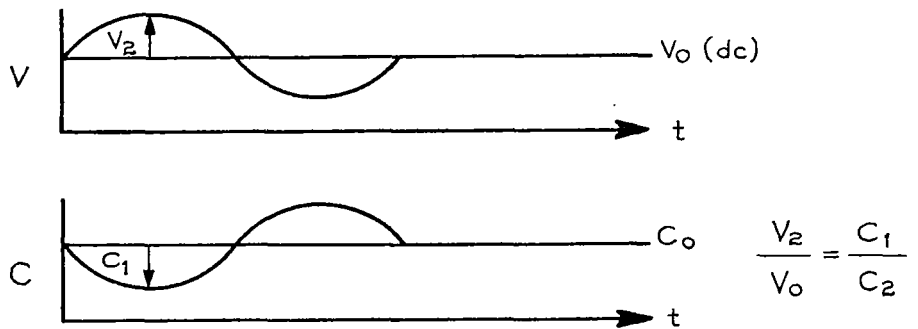


FIGURE 6.12 PRINCIPLE OF OPERATION

V_2 is amplified and the output connected to an ac-to-dc amplitude detector and through a phase shifter to a peak-to-peak clipper circuit that produces an output with a fixed peak-to-peak amplitude. A portion of the clipper output is fed back to the forcing plate of the transducer. If the amplifier gain is sufficient to overcome the gage energy losses, the circuit will oscillate at the resonant frequency of the transducer diaphragm with an amplitude dependent on the setting of the clipper output.

To control automatically the feedback amplitude, the output of the ac-to-dc amplitude detector is compared with a fixed dc reference potential in a differential amplifier. Any difference between the detector level and the dc reference level is reduced by altering both the dc applied to the transducer plates and the portion of the clipper output applied to the forcing plate. The control action is such that as the gas pressure is decreased, a smaller portion of the clipper output is used because of the decreased loss of energy from the diaphragm to the gas. To increase the pressure range, the dc voltage applied to the fixed transducer plates is also reduced as the damping is decreased. Therefore, high diaphragm vibration levels are necessary to maintain the detector output voltage equal to the fixed reference at the input to the differential amplifier. A transistorized electronic feedback system has been designed to provide a dc output voltage proportional to pressure ($V_{out} \propto P$). This system has a frequency response of up to 100 cycles per second and has provisions for an expanded scale over selected portions of the pressure range. This transistorized system is proposed for the pitot probe application.

The range of the vibrating diaphragm transducer is limited by the energy losses of the diaphragm. The energy dissipated by the periodic motion of the gas is reduced as the gas pressure is reduced until it is equal in magnitude to the energy lost within the diaphragm as a result of the inelastic deformation of the metal. Such unwanted losses can be caused either by stress concentrations near the edge of the diaphragm where it is attached to the body of the transducer by spot welding, or by viscoelastic losses due to the periodic stress applied to the diaphragm. At pressures significantly lower than this value, use of the transducer requires measurement of a small gas effect in the presence of relatively large losses in the metal diaphragm. The higher pressure range of the transducer is limited when the viscous losses associated with the gas at high pressures become so great that resonance can no longer be sustained.

Energy lost through diaphragm vibration must be replaced for the diaphragm to vibrate at a required amplitude. The total energy loss is the sum of the electrical energy losses, the mechanical energy losses, and the energy losses caused by the gas. Electrical energy losses result from resistance and dielectric losses in the transducer driving and sensing circuit. Mechanical losses are caused by the presence of viscous foreign materials on the diaphragm, the vibration of the diaphragm-edge support, and the transfer of energy from the transducer housing to the transducer support. For good transducer sensitivity and accuracy, the electrical and mechanical losses must be very constant and preferably very small compared with the energy loss from gas damping. The low-pressure end of the range is determined by the smallest electrical and mechanical losses possible in a practical instrument as compared with the loss from gas damping.

(a) Electrical Input Power.

The electrical power required to maintain diaphragm vibration can be determined by the method of Dimeff, et al. (reference 21). The electrostatic force between the diaphragm and the forcing plate is given by

$$F = \frac{V^2}{2 \epsilon x_p^2} \quad (15)$$

where

- F = force per unit area
- ϵ = dielectric constant
- V = voltage applied to the forcing plate
- x_p = distance between forcing plate and diaphragm

For a sinusoidal input voltage of the form $V = V_s + V_v \sin \omega t$, only the fundamental frequency is transferred through the transducer and

$$F = \frac{\epsilon V_s V_v \sin \omega t}{x_p^2} \quad (16)$$

By integrating the product of the electrostatic force times the diaphragm velocity over the area of the stationary forcing plate for a complete cycle of displacement, the following expression is obtained for the electrical work per cycle

$$W_e = \frac{\pi^2 \epsilon V_s V_v r_p^2}{x_p} \frac{\Delta C}{C} \quad (17)$$

where

- r_p = effective radius of forcing plate
- ΔC = peak capacitance change
- C = capacitance between forcing plate and undisturbed diaphragm

For small displacement occurring at the first vibrational mode of the diaphragm and for assumed spherical deformation

$$\frac{\Delta C}{C} = \frac{A_0}{x_p} \quad (18)$$

where A is the peak displacement of the diaphragm averaged over the area of the fixed plate.

The average electrical power input is given by

$$P_e = \frac{\pi r_p^2 \epsilon V_s V_v A_0 w}{2 x_p^2} \quad (19)$$

$$= \frac{A \epsilon V_s V_v A_0 w}{2 x_p^2} \quad (20)$$

where w is the resonant frequency of the diaphragm in radians per second and A is the area of the diaphragm.

(b) Gas Damping Losses.

For the frequencies and dimensions used in the transducer, the gas damping power losses can be expressed as

$$P_g = \frac{8\pi x_p}{9\mu} A_0^2 \cdot P_0^2 \quad \text{or} \quad (21)$$

$$= \left(\frac{\pi \gamma^2}{6\mu} \right) x_p x_2^2 \cdot P_0^2 \quad (22)$$

for the continuum region, and as

$$P_a = 16\pi A_0^2 \beta \bar{c} \cdot P_0 \quad \text{or} \quad (23)$$

$$= \left(\frac{\pi RT}{2 \bar{\alpha}, \bar{c}} \right) x_2^2 \cdot P_0 \quad \text{or} \quad (24)$$

$$= \left(\frac{\pi^2 \bar{c} m \gamma^2}{16 \bar{\alpha}_1} \right) \chi_2^2 \cdot P_0 \quad (25)$$

for the free molecular region where the gas mean free path is large compared with X_p and the following definitions apply:

P_0 = equilibrium pressure being measured by transducer

β = momentum transfer accommodation coefficient, characteristics of the gas and surface involved

\bar{c} = molecular velocity

μ = viscosity coefficient

γ = ratio of specific heats

R = gas constant

T = temperature

$\tilde{\alpha}_1$ = analogous shear stress coefficient

m = molecular weight of the gas

x_2 = peak diaphragm displacement in center
($\approx (\pi/2) A_0$)

The above alternate equations converge to the same expression for air and the gage parameters under consideration.

The input power lost to gas dampening is determined by equating the expression for electrical input power to the respective gas damping expressions to derive the following:

$$\frac{V_s V_v}{A_0} = \frac{\pi^3 \gamma^3}{12 A \epsilon \mu \omega} X_p^3 \cdot P_0^2 \quad \begin{array}{l} \text{Continuum} \\ \text{Region} \end{array} \quad (26)$$

$$\frac{V_s V_v}{A_o} = \frac{\pi^4 \bar{c} m Y^2}{32 A \epsilon \omega \bar{\alpha}_1} x_p^2 \cdot P_o \quad \text{Free Molecular Region} \quad (27)$$

or

$$= \frac{\pi^{7/2} (2RT_m)^{1/2} Y^2}{16 A \epsilon \omega \bar{\alpha}_1} x_p^2 \cdot P_o \quad \text{Free Molecular Region} \quad (28)$$

Although laboratory tests have shown good agreement with these theoretical expressions, some of the factors are not precisely known and the mechanical and electrical losses are not included. Therefore, in practice, the relationship between $\frac{V_s V_v}{A_o}$ and pressure is determined by means of laboratory calibrations as

$$\frac{V_s V_v}{A_o} = P_g + P_m + P_r \quad (29)$$

where

P_m = mechanical losses

P_r = electrical losses

The two voltages can be measured and the value of A_o determined from the variation in capacity between the diaphragm and the sensing plate.

Not only is power dissipated in the gas, it is also lost in the mechanical structure and in the electrical circuit used to read out the transducer signal. The mechanical loss is difficult to completely describe analytically, since it is primarily controlled by minor factors in assembly; however, such factors as the diaphragm material and the overall design are important. The diaphragm vibrates at its lowest natural resonant frequency. The most conventional measure of the internal loss for a system is the Q , defined as $2\pi(W/\Delta W)$ where ΔW is the energy loss per cycle and W is the maximum energy of the system. Using this definition for Q and noting that $W = (\rho/2)\pi r_p^2 d A_o^2 \omega^2$, an expression may be written as

$$Q^{-1} = \frac{32 \pi \beta \bar{c}}{M \omega^3} P_o + Q_{int}^{-1} \quad (30)$$

where

d = membrane thickness

ρ = membrane density

M = membrane mass

An investigation is currently being undertaken at Ames Research Center of the internal losses arising from thermoelastic effects, point defects, and dislocation phenomena. Results experienced with heat treatment of the transducers suggest that one should be able to obtain diaphragms routinely with Q's greater than 50,000.

The mechanical loss is indicated by the transducer Q at pressures so low that gas damping is insignificant. The major factors affecting the value of the structure Q are the purity of resonance in the diaphragm as determined by equal radial tension, the dimensional accuracy of the diaphragm effective diameter in all directions, the presence of viscous foreign material deposits on the diaphragm, and the variation of the diaphragm-mount contact points during the vibration cycle. Design of the diaphragm mount to minimize energy loss to the transducer structure is also important. A high Q structure is desirable, since the lower limit of the range is determined by the level at which the internal losses become large compared with the gas damping losses. The electrical loss is primarily the energy dissipated in the input impedance of the amplifier which follows the transducer. For this reason the input impedance of the transducer amplifier and any resistance furnishing a path for the dc potential to the transducer plates must be high to prevent lowering of the transducer Q.

(c) Response Speed.

The transducer response speed is limited by two factors - the time required for the diaphragm to assume a new equilibrium energy level after a change in pressure, and the time for the change in pressure to become the effective pressure within the transducer sensing region. The first factor is dependent on the effective Q. A lightly damped, freely vibrating first-order system decays to an amplitude of 1/e of its initial value after completely n cycles, where

$$n = \frac{Q}{\pi}$$

Since the time t or n cycles is

$$t = \frac{n}{f_0}$$

where f_0 is the resonant frequency. The time constant for the system is

$$T = \frac{Q}{\pi f_0} = \frac{3.4 Q}{\omega_0} \quad (31)$$

The effective time constant of the transducer at low pressures has been found to be of the above form, but with an empirically determined constant of 3.4 instead of 2.0.

Because of the transducer's large Q in the free molecule region, the response time for low-pressure measurements is controlled primarily by this factor. At high pressures the transducer Q becomes small, and the response time is limited by the airflow through the inlet tubes. By using circuitry that maintains a constant amplitude of diaphragm vibration, the effective time constant of the transducer at low pressures can be greatly reduced and made to approach that at higher pressures. Since the stored energy in the diaphragm remains constant with this mode of operation, the time to restore equilibrium energy does not directly affect the response time.

(d) Gas-Composition and Temperature Effects.

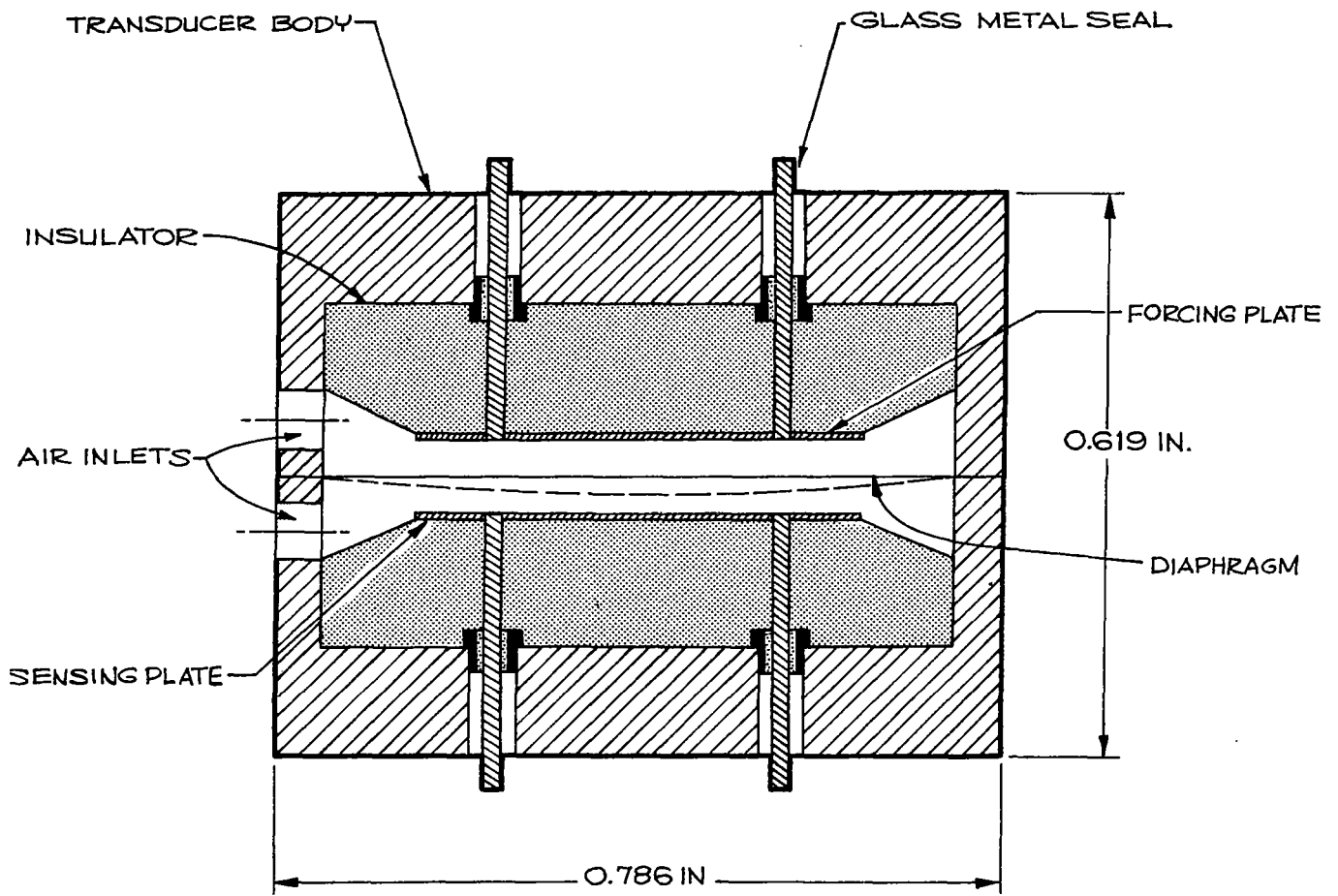
In the higher pressure ranges the ratio $V_s V_v / A_o$ is dependent on the ratio γ^2 / μ . The viscosity varies with temperature much more than the specific heat ratio. Therefore, gas temperature is expected to affect the calibration. Through the choice of materials and transducer design, the temperature effect can be so minimized that either or both X_p and ω vary to compensate for the change in the ratio γ^2 / μ as a function of temperature.

In the free molecule region the ratio $V_s V_v / A_o$ is dependent on the gas properties as given by the factors $[(TM)^{1/2} \gamma^2] / \tilde{\alpha}_1$. Here again the transducer sensitivity is generally expected to vary with both gas composition and temperature. Very possibly, the transducer design and materials selection can minimize this effect by changes in X_p or ω , or both.

6.4.3.3 Gage Construction.

The selection of materials and the care taken in fabrication determine, to a large extent, the ultimate performance of the transducer. The diaphragm material must have low internal losses to insure a high mechanical Q . The thermal expansion coefficients must be well matched for all materials, and the internal losses in the diaphragm should remain constant to reduce temperature effects. The diaphragm must be under equal radial tension in all directions. Lint, dust, viscous materials, and other foreign matter on the diaphragm or at the diaphragm attachment point will cause a reduction in the mechanical Q .

The proposed gage is shown in Figure 6.13. The gage body is made from 42 percent nickel-iron, and the ceramic insulators are Al_2O_3 . The diaphragm material is 44 percent nickel-iron annealed at 960° F. While under tension, the 0.0001 inch thick diaphragm membrane is mounted to one-half of the body with an overlapping spot weld. Commercially available hermetic feed-throughs are used to the fixed plates.



(Dimeff, Lane, et al)

FIGURE 6.13 TRANSDUCER ASSEMBLY DETAILS

With this design, the overall outside diameter is 0.786 inch, the vibrating diaphragm is 0.728 inch in diameter, the fixed plates 0.562 inch in diameter, and the overall thickness is 0.619 inch. The diaphragm is spaced 0.003 inch from the fixed plates and tensioned to achieve a resonant frequency of 2500 cps.

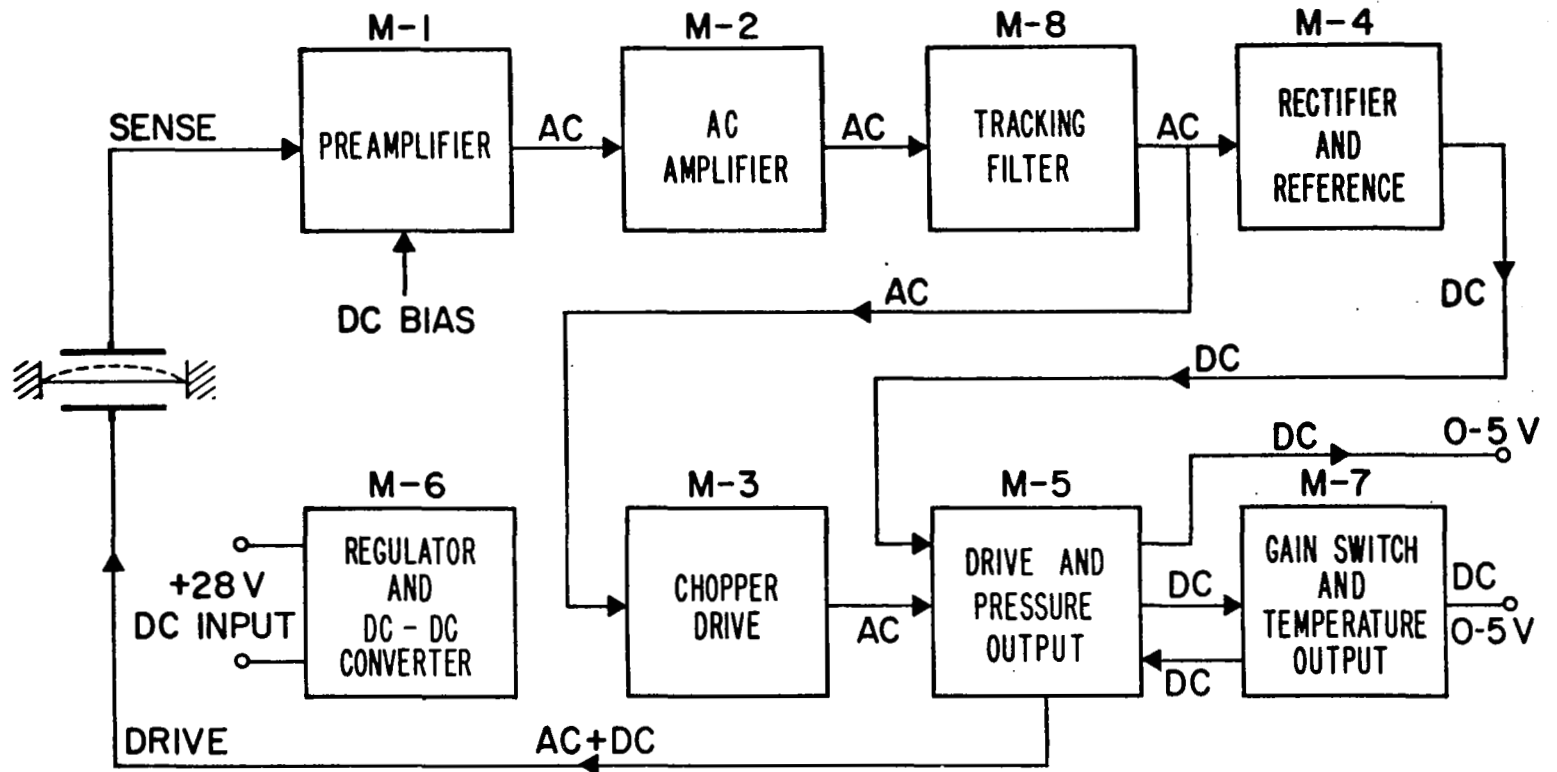
The vibrating diaphragm gage weighs about 12 ounces, has a volume of 8 cubic inches, requires 0.650 watts of power and has a time response of about 0.050 seconds. The unit has been environmentally tested to a vibration level of ± 10 g along all axes from 0 to 2000 Hz, an acceleration level of 50 g and a shock level of 250 g parallel to the diaphragm.

6.4.3.4 Gage Electronics.

The gage electronics consists of a feedback system to maintain the diaphragm oscillating at its mechanical resonant frequency and at a fixed amplitude.

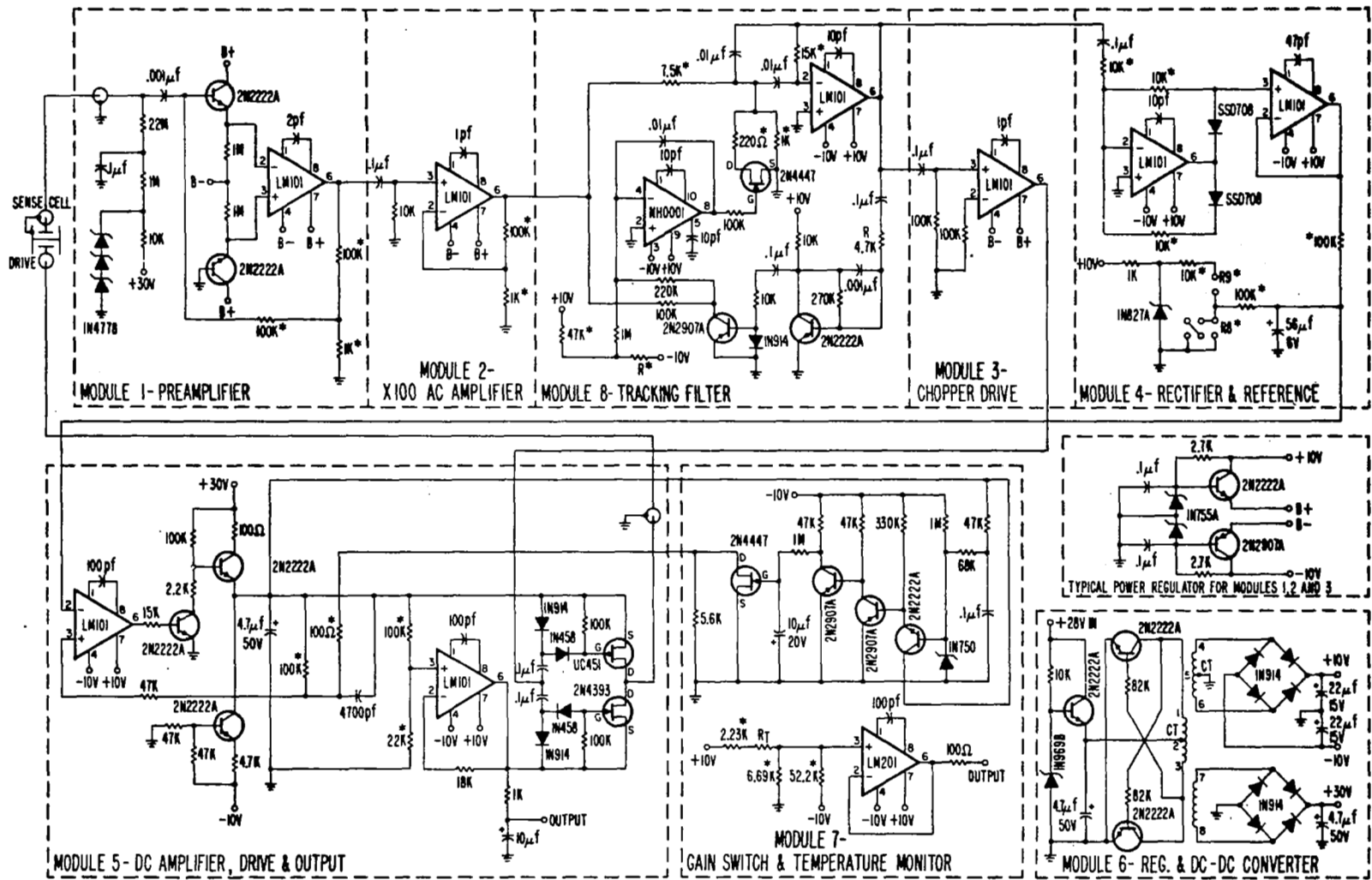
The operation of the system can best be understood by reference to Figure 6.14. In this arrangement the displacement of the diaphragm causes a capacitance change, which in turn, generates an input to a velocity sensing preamplifier. The output of the preamplifier is then amplified, filtered, rectified, and compared to a pre-set dc reference voltage in the rectifier-reference module. This unit generates a dc voltage input to the drive-output module whose dc output is periodically switched by the output of module 3, the chopper-drive module. Since this output is synchronized with the membrane velocity, the voltage drives the diaphragm at its resonant frequency and at an amplitude sufficiently large that the input voltage to M4 after rectification is equal to the reference voltage.

The function of each block may be described as follows. M1 is a preamplifier and differentiator, and the cell itself is the capacitor required to effect the differentiation. This preamplifier provides the 90° phase shift necessary to provide the proper phase shift for the cell driving force. M2 is an ac amplifier with a gain of 100. M8 is a narrow band tracking filter which self-tunes to the resonant frequency of the transducer and also maintains zero phase shift from its input to output. M4 is a precision rectifier, and contains the temperature-stable dc reference. M3 converts the sine wave from M8 into the square wave necessary to drive M5. M5 provides the ac-dc electrostatic drive to the transducer as well as the system output voltage. M7 is an automatic gain switch which reduces the open-loop gain of the system to insure stability when the cell Q changes to values above approximately 1000. M6 is a dc to dc converter and regulator which converts an input power supply voltage of approximately 28 volts to the voltages necessary to power the various modules. A schematic of the gage electronics is presented in Figure 6.15.



(Dimeff, Lane, et al)

FIGURE 6.14 BLOCK DIAGRAM FOR THE VIBRATING DIAPHRAGM SYSTEM



(Dimeff, Lane, et al)

FIGURE 6.15 VIBRATING DIAPHRAGM PRESSURE CELL ELECTRONICS SYSTEM

The electronic unit controls the resonant deflection of the membrane vibration to a value established by the reference voltage and by the gain of the linear ac amplifiers. The condition actually being controlled is that ΔV (the preamplifier output voltage) be constant, independent of the pressure being measured. It can be shown that the following expression is valid for the preamplifier:

$$\frac{\Delta V}{V_{bias}} = K_1 \frac{\Delta C}{C_o} \frac{\omega}{\omega_o} = K_2 A_o \frac{\omega}{\omega_o} \quad (32)$$

where

- ΔC is the detected change in capacitance
- C_o is the rest capacitance of the transducer
- A_o is the amplitude of the diaphragm motion
- ω_o is the frequency of the transducer at high vacuum
- ω is the frequency at the pressure being measured
- K_1 & K_2 are constants

It then follows that the controlling condition in the loop requires that $A_o \omega$ be held constant. For a wide range of pressures,

$$\frac{V_s V_v}{A_o} = K_3 P_o \quad (33)$$

where

- P_o is the pressure being measured
- K_3 is a constant

V_s and V_v are both derived from the dc output of the rectifier-reference module and are linearly related. Eq. (13) may, therefore, be written in the form $V_s^2 = KP_o/\omega$. It is worth noting that in addition to this square law dependence, the system readily lends itself to operation in either a mode where the pressure is proportional to the first or third power of the voltage. For example, if V_s were held constant and equal to V_{bias} . It can be seen from Eq. (13) that V_v would be linearly related to the pressure. V_{bias} may also be equal to V_s , thereby being changed as the pressure is varied. For this mode of operation, A_o then also varies with pressure, and from the arguments given above, it can be shown that $V_s^3 = KP_o/\omega$.

6.4.3.5 Gage Evaluation.

A typical calibration curve for the vibrating diaphragm gage is presented in Figure 6.16. This curve has been corrected for mechanical and electrical losses. Comparison measurements conducted at Ames with other pressure gage techniques indicate that the vibrating diaphragm gage error is within an rms error as shown in Figure 6.17.

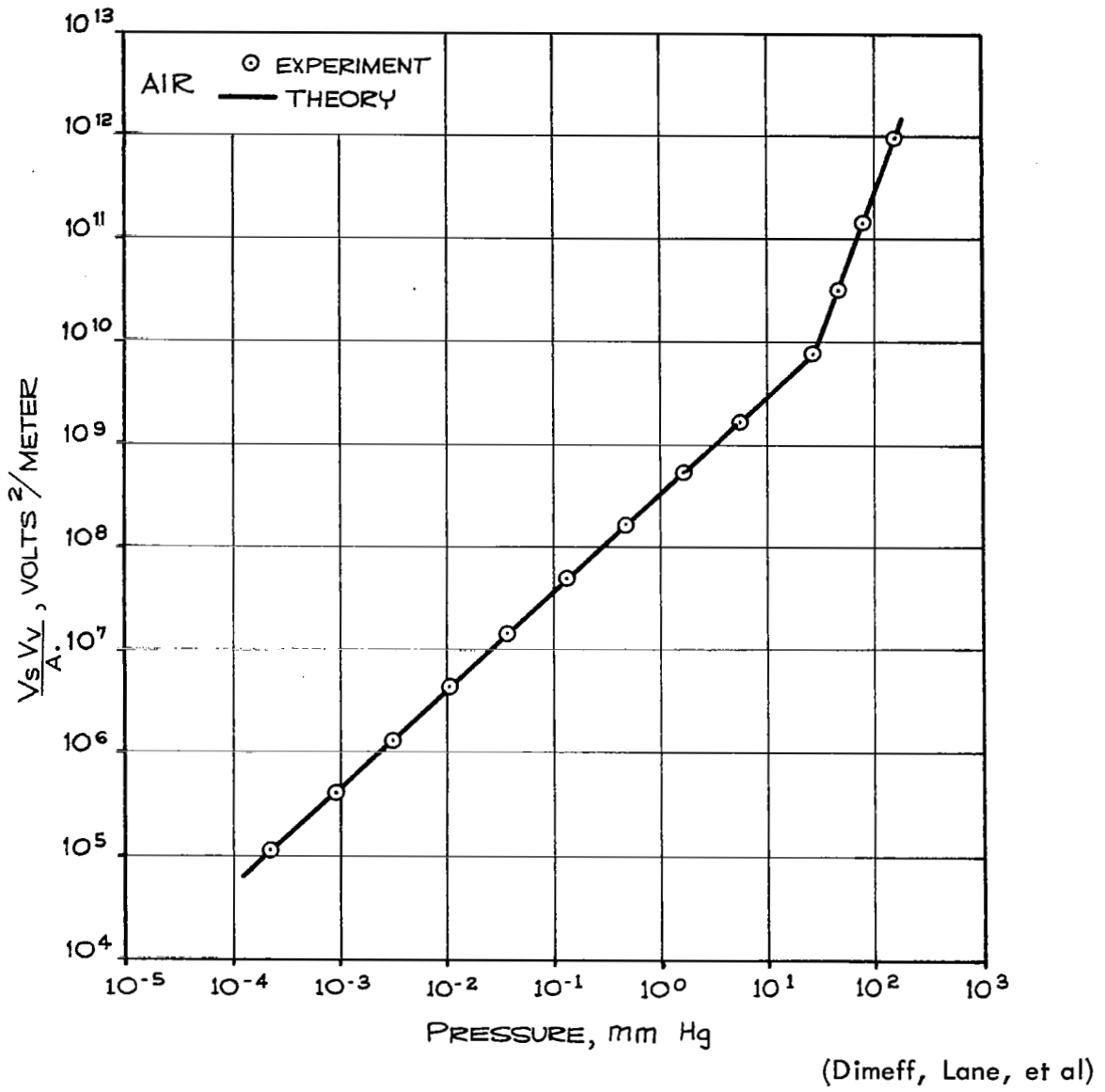


FIGURE 6.16 PERFORMANCE CURVES OBTAINED FOR AIR, CORRECTED FOR MECHANICAL AND ELECTRICAL LOSSES

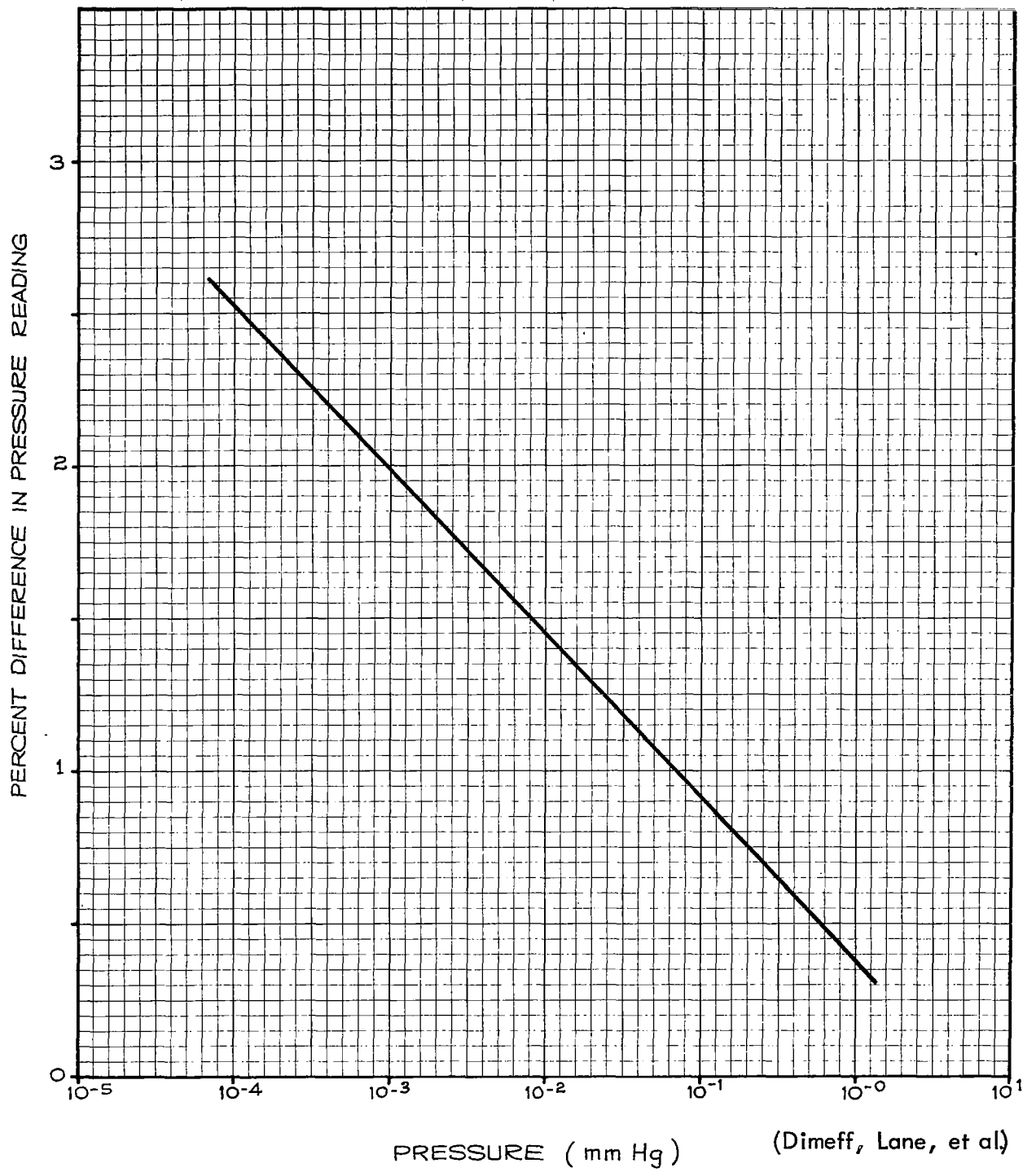


FIGURE 6.17 VIBRATING DIAPHRAGM TRANSDUCER RMS DEVIATION FROM STANDARD GAGE TECHNIQUES

The gage output stability over a period of several weeks is presented in Figure 6.18. The experimentally determined Q of the gage is presented in Figure 6.19 and the time constant in Figure 6.20. A summary of major transducer characteristics is presented in Table 6.2.

During a recent meeting at the Ames Research Center, it was suggested that the gage and gage electronics could be simplified for the pitot probe application by eliminating the control of the vibration amplitude, A_0 , and by basing the pressure measurement on the variation of the diaphragm resonant frequency with pressure. Such a calibration for the higher pressure levels has been made as in Figure 6.21. This frequency variation is extremely significant since it changes from approximately 5,000 Hz to 70,000 Hz over the interval from 10^{-3} torr to 760 torr. This large frequency variation makes this configuration particularly attractive when it is desirable to determine the pressure from frequency measurements. It is evident that frequency deviations as a function of temperature could cause errors for this mode of operation. However, the frequency deviation observed for the standard transducer at vacuum is approximately $0.014\%/^{\circ}\text{C}$. Because of construction a new configuration should be even less sensitive to temperature change and hence the problem should not be serious. This new embodiment offers a further advantage in that it is much easier to fabricate than the standard transducer configuration. Gage characteristics can be optimized for the region of interest, i.e., 10^{-4} to 10^1 mm Hg, and the cost of both the gage and the associated electronics can be considerably reduced.

6.4.3.6 Pressure Gage Calibration.

6.4.3.6.1 Each pressure gage must be individually calibrated in the laboratory, sealed and evacuated to a hard vacuum by means of a getter prior to launch. The gages must be individually calibrated against pressure in the laboratory for eventual flight data reduction purposes. The gage assemblies together with the pitot structures are then to be evacuated and sealed to prevent contamination from water vapor and other constituents during shipment, storage and preflight handling. Just prior to launch a vacuum getter is fired to evacuate the system below a pressure of 10^{-7} mm Hg in order to establish a threshold level of gage sensitivity, i.e., where the electrical and mechanical losses are much greater than the gas damping losses. Providing this low pressure can be sustained until the pitot measurements are initiated, any shifting in the original laboratory calibration due to temperature rise of the gage from aerodynamic heating may be determined.

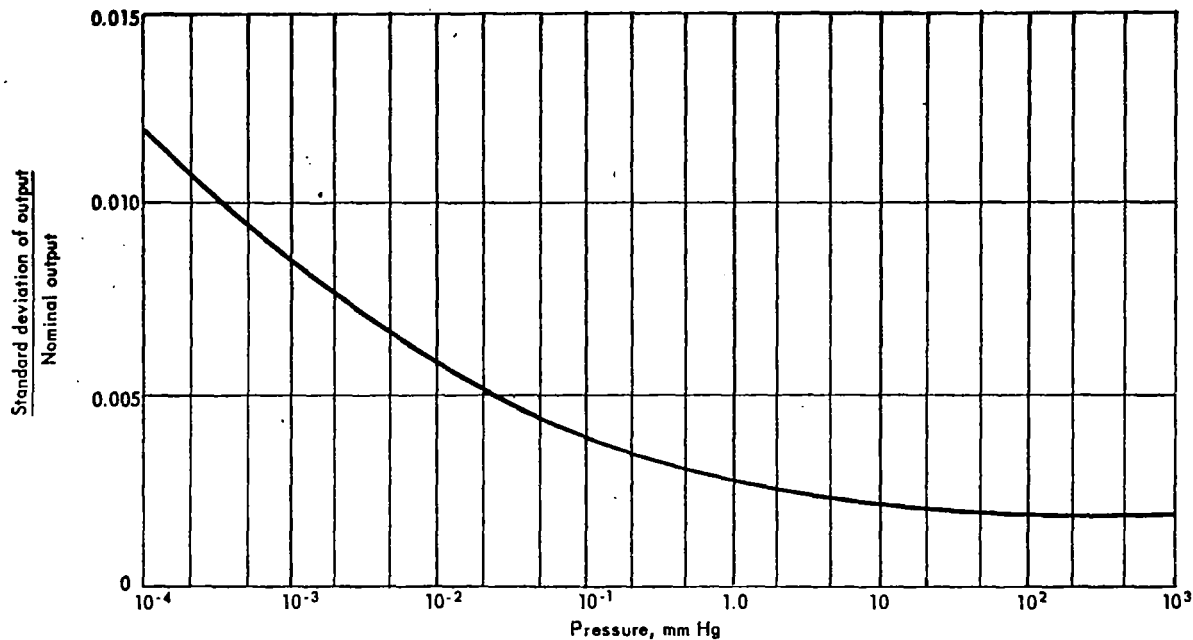


FIG. 6. 18 Output stability shown as a function of pressure.

(Dimeff, Lcne, et al)

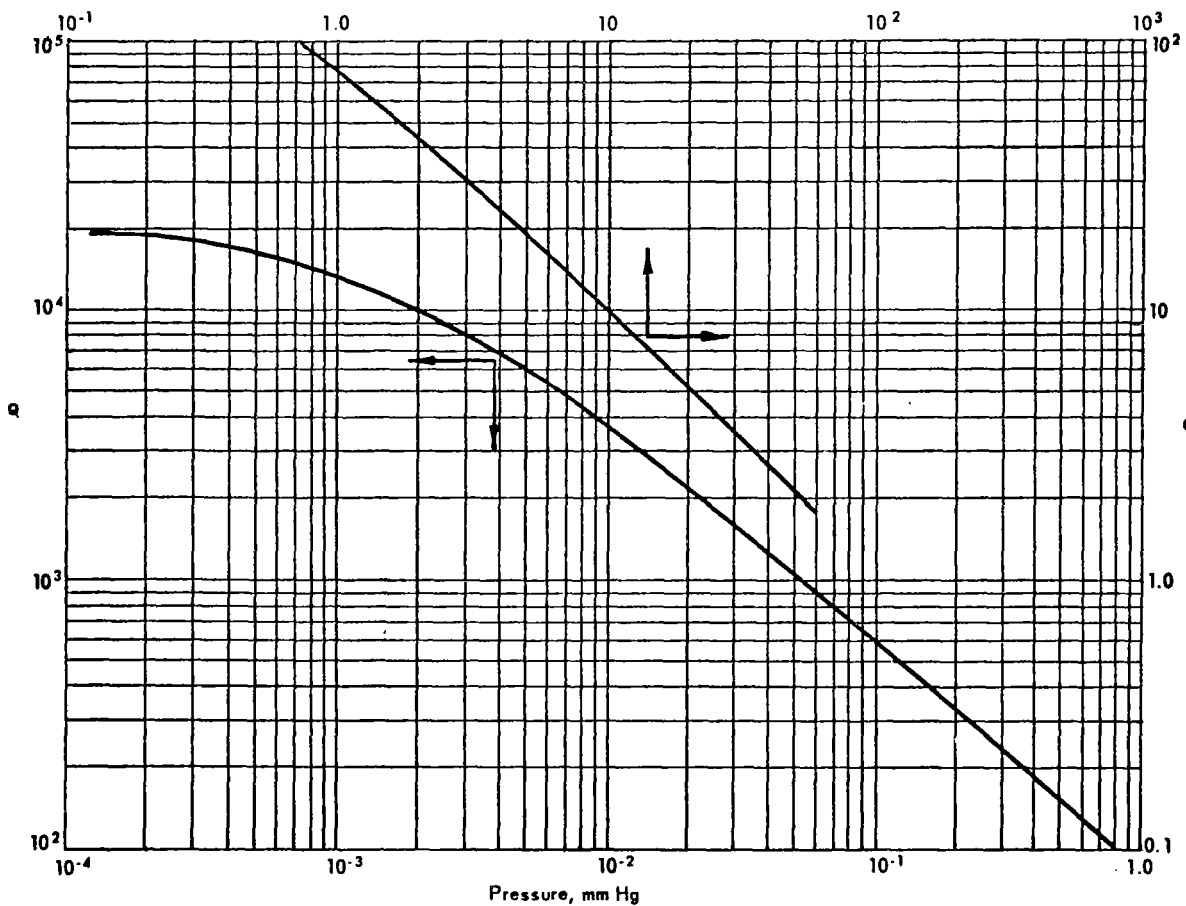


FIG. 6. 19 Transducer Q plotted against pressure.

(Dimeff, Lcne, et al)

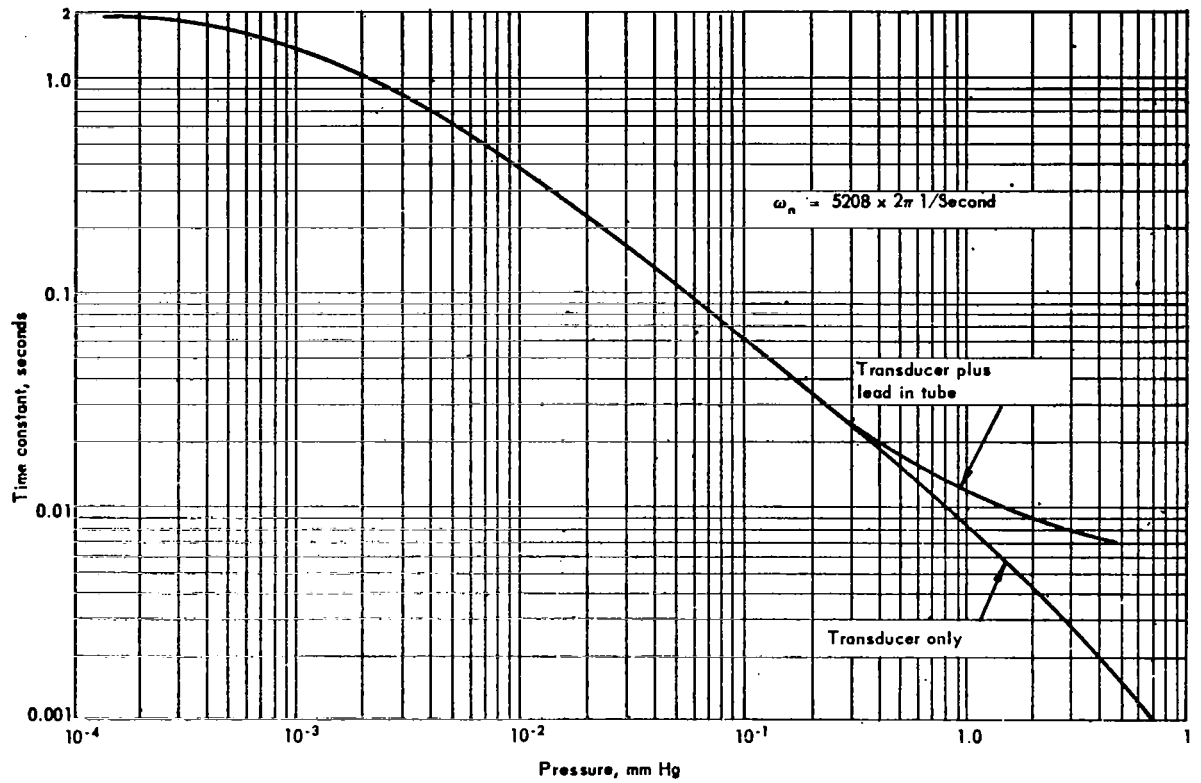


FIG. 6.20 Time constant plotted against pressure.

Table 6.2 Transducer Measurements

Factor	New Value
$Q^{-1} = \Delta f/f$ (Mechanical Filter Bandwidth)	$4 \cdot 10^{-6}$
Low Pressure Resolution	10^{-6} Torr
High Pressure Limit	$5 \cdot 10^3$ Torr
Frequency Change with Pressure (f_0 = Low Pressure Resonant Frequency)	$0.2 f_0$

(Dimeff, Lane, et al)

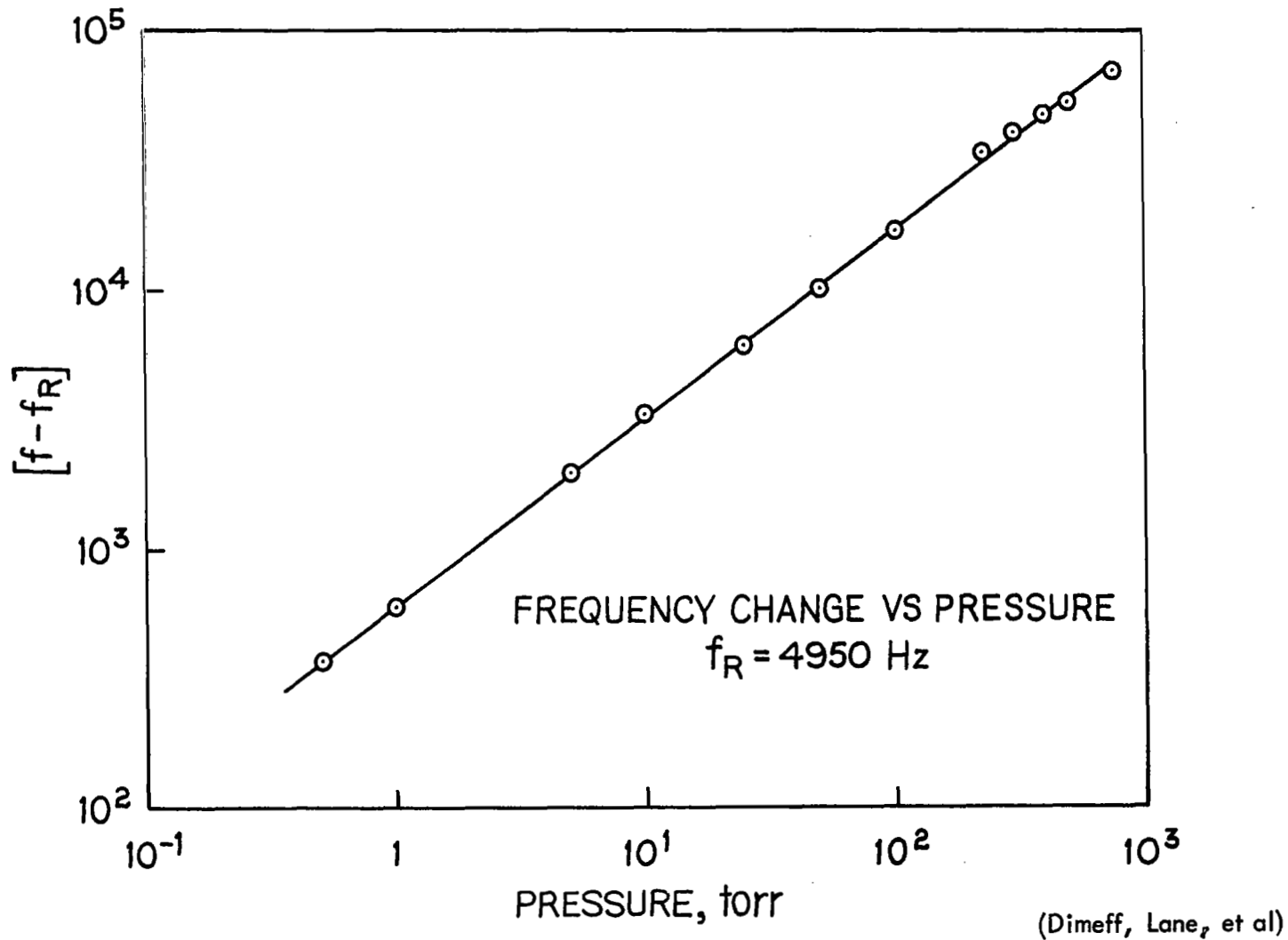


FIGURE 6.21 PRESSURE CALIBRATION FOR A NEW TRANSDUCER DESIGN

6.4.3.6.2 Vacuum Calibration Equipment. The vacuum calibration system will be designed for an ultimate vacuum of 10^{-7} torr. This pressure level is deemed adequate for a "zero pressure" reference point for calibration and a suitable pressure level to activate the getter in the gage system of the pitot probe. A typical vacuum calibration system is composed of a Cenco Hyvac 2 forepump, a Cenco Pressovac 4 roughing pump, a Cenco Supervac OD-25 oil diffusion pump, a 24 litre vacuum chamber and four liquid nitrogen traps. Three manually operated valves can be employed in the pumping circuit to permit rapid pull-down and venting sequences without turning off the pumps. Two Edwards solenoid valves can be used in the discrete volume air admittance arrangement. A block diagram of the system is shown in Figure 6.22. Standard pressure gages which can be used are as follows: (1) a Wallace and Tiernan dial manometer, Model FA 160110, range 0-50 torr, accuracy 0.33 percent F.S.; (2) a Wallace and Tiernan dial manometer, Model FA 160150, range 0-20 torr, accuracy 0.33 percent F.S.; (3) a Cenco McLeod gage, range 2×10^{-6} to 1 torr, accuracy 0.1 percent at the lowest pressure it is expected to be used (1×10^{-4} torr); (4) a Consolidated Vacuum Corporation Ionization Gage, Model GIC-110A, range 10^{-3} to 10^{-9} torr; (5) a thermistor and electronics manufactured by Space Data Corporation

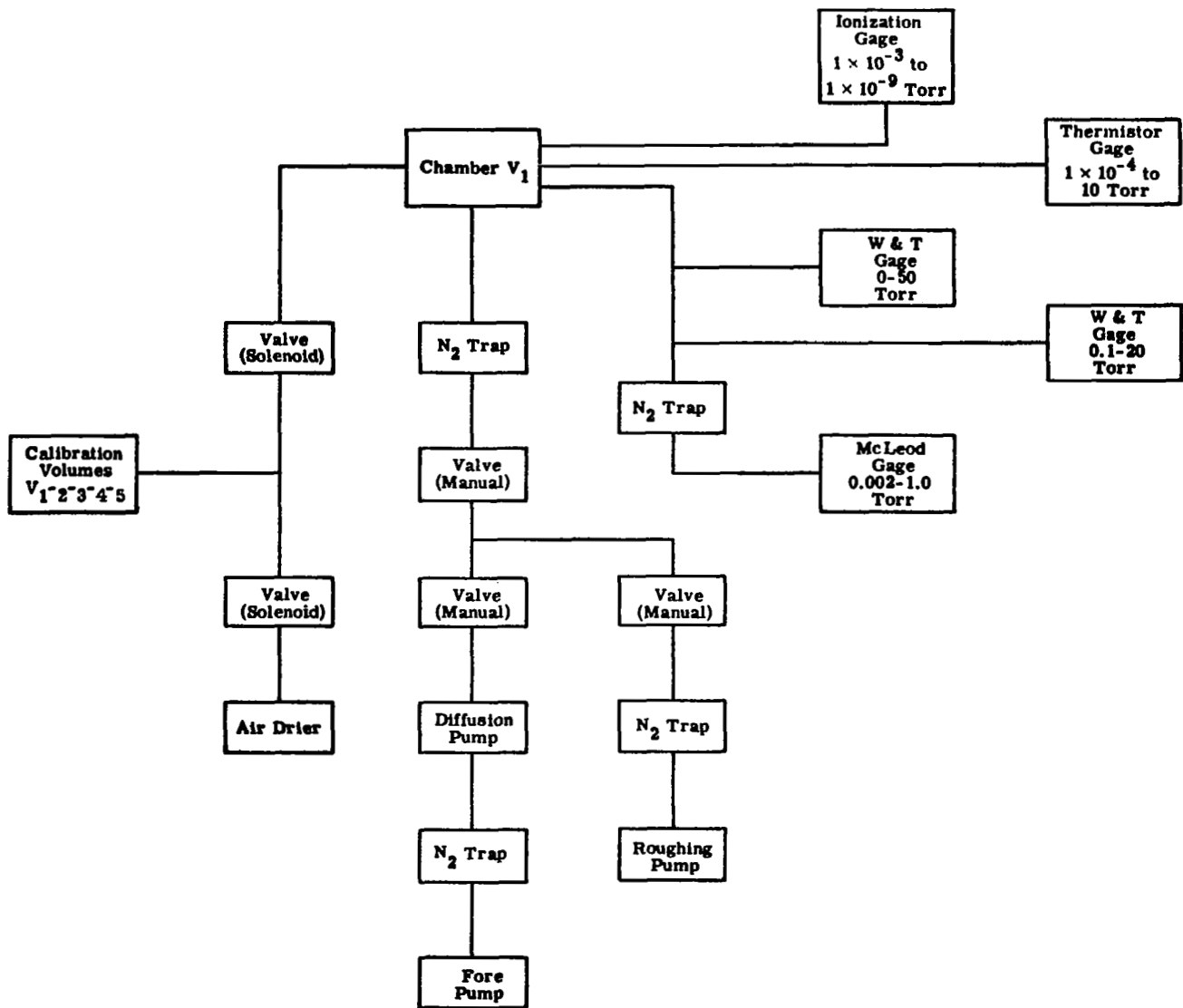
Accuracy of the ionization gage is not precisely known, but measurements agree with the McLeod gage in their common pressure range to within 15 percent. This will not adversely affect the calibration results since the ionization gage will be used only for establishment of the "zero pressure" reference point at about 10^{-7} torr. The range of the thermistor gage is about 10^{-4} to 10 torr. Since it will be calibrated against the other standards, it should have an accuracy of better than 1 percent.

6.4.3.6.3 Calibration Method. Provision is made for admitting discrete volumes of dry atmospheric air to the vacuum system. The calibrating volumes are interchangeable, and volumes are calculated to provide desired pressure steps. By measuring the atmospheric pressure and monitoring the temperature, the pressure at any step can be calculated from the relationship:

$$P_j = P_0 + \frac{(P_n - P_0)j}{n} \frac{\left[1 - \frac{(j-1)}{2} \frac{V_2}{V_1}\right]}{\left[1 - \frac{(n-1)}{2} \frac{V_2}{V_1}\right]} \quad (34)$$

where

- P_j = Pressure after j volumes have been admitted
- P_0 = Initial pressure
- n = Total number of volumes admitted
- P_n = Final pressure
- V_2 = Volume of calibrating chamber being used
- V_1 = Volume of system



(Draws)

FIGURE 6.22 TYPICAL VACUUM CALIBRATION SYSTEM

Each pressure gage-telemetry system combination will be calibrated with the vacuum system. Calibration will be started with each gage at a pressure at least two orders of magnitude below that which causes a detectable change in electrical signal. Under these "zero" conditions, the gage and telemetry output parameters will be measured. Step changes in applied pressure will then be made as all of the quantities about are measured and recorded. In addition, the reading of one or more pressure sensors will be taken as a check on the incremental pressure increase expected. For each gage and telemetry system two sets of calibration plots will be made, the first being output gage parameters versus applied pressure and the second output telemetry pulse rate versus gage applied pressure. In use, this allows two independent adjustments to be made for gage zero shift and blocking oscillator circuit drift. Oscillator drift is determined just prior to flight by injecting test voltages into the test point in the gage electronics. Zero shift of the gage is checked both before nose cone ejection and after ram pressures became insignificant.

From the results of the observations made before and during flight, it can be determined how much change in the calibration curves is required for final data reduction.

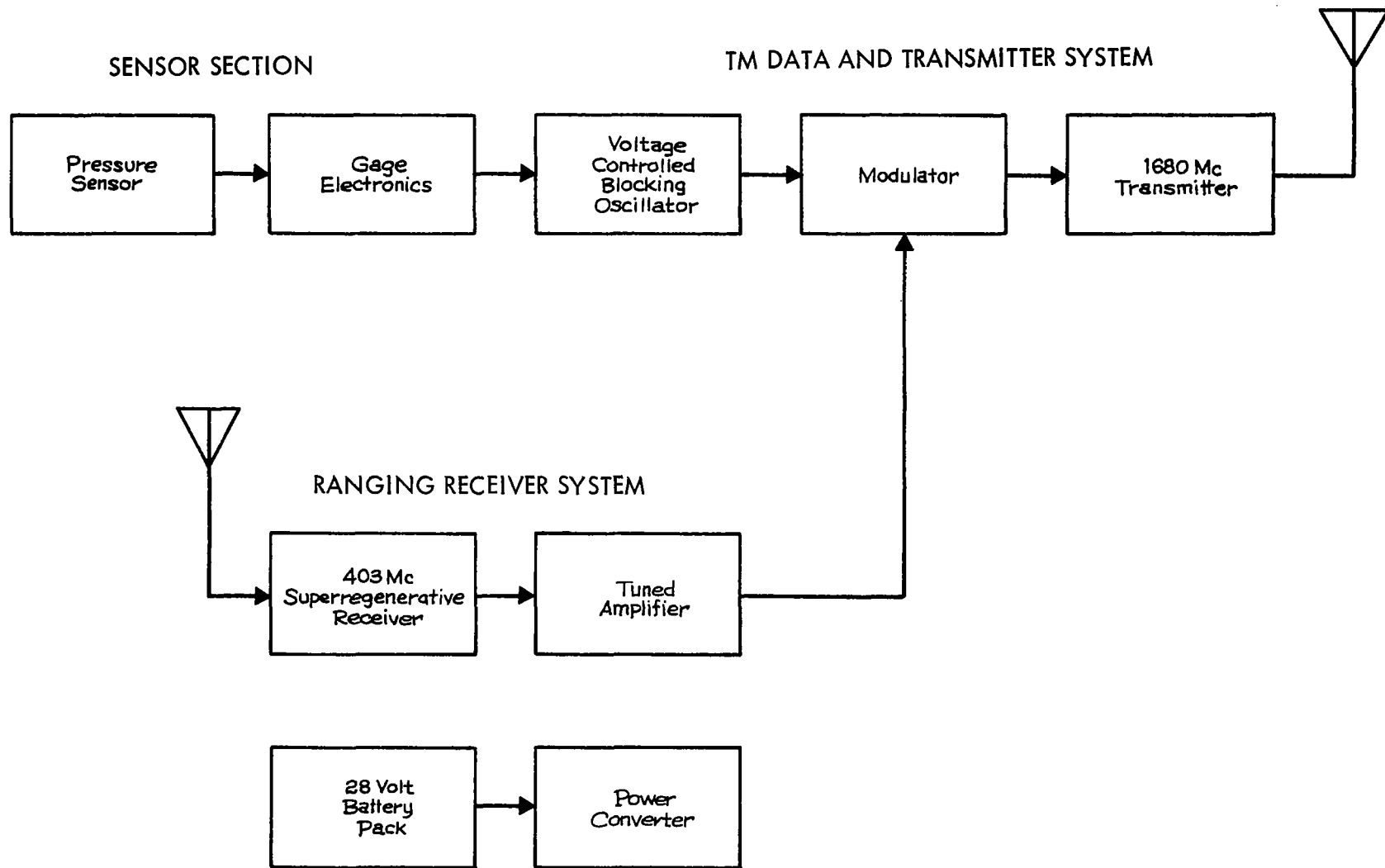
6.5 Tracking and Telemetry Instrumentation.

6.5.1 General.

The primary tracking and telemetry instrumentation for the proposed pitot probe is compatible with the AN/GMD-2 meteorological ground equipment so that radar will not be required for the density measurement system. The standard GMD-1 or GMD-2 equipment will require some modification, however, to update its capability to receive the high velocity tracking data and fast response telemetry data. The pitot probe pressure sensor produces a 0 to 5 volt dc output, and the on-board telemetry system has been designed to be compatible with this signal as an input. A single channel of telemetry is all that is required to telemeter the ram pressure data.

Although the GMD-2 is the proposed telemetry system, consideration will be given during the development program to the new tone-range telemetry interferometer tracking system currently being developed by NASA-Goddard Space Flight Center. However, since a majority of the meteorological rocket network stations are equipped with the standard GMD equipment, it appears that for the immediate future the GMD system would find more immediate acceptance and application.

The telemetry system for the pitot probe has two functions, i. e. , to telemeter one channel of ram pressure data from the pitot pressure sensor and to provide a tracking signal for both slant range and angular data. Referring to Figure 6.23, the gage electronics convert the output of the pressure transducer into a 0 to 5 volt dc



-157-

FIGURE 6.23 TELEMETRY BLOCK DIAGRAM

signal which is compatible with standard telemetry voltage controlled oscillators. The VCO, of a blocking oscillator type, provides an output pulse rate which is a function of sensor signal amplitude. These pulses frequency-modulate the transmitter and allow ground detection of the pulse rate. The pitot probe telemetry system also contains a 403 Mc super-regenerative receiver as a portion of the 81.94 kc slant range link. Retransmission of the detected signal is by frequency modulation of the 1680 Mc transmitter. Positive telemetry data pulses and the 81.94 kc sine wave are combined into one complex waveform by the modulator for application to the transmitter. Power for the telemetry package is derived from a series-connected pack of nickel-cadmium rechargeable cells. Transmitter and receiver plate potentials are provided by a dc to dc converter. Filament potentials are obtained from an accessory transformer coupled into the converter circuitry.

6.5.2 Payload Telemetry System.

The basic concept of payload telemetry system is compatibility with Rawin sets that operate in the 1660 to 1700 megacycle band for telemetering and the 400 to 406 megacycle band for range measurement. Hence, the basic telemetry modules are a transmitter operating at a nominal frequency of 1680 megacycles and a receiver of the super-regenerative type operating at a nominal frequency of 403 megacycles.

6.5.2.1 Voltage Controlled Blocking Oscillator.

Conversion of the output of the sensor electronics to a proportional pulse rate is accomplished by the blocking oscillator shown in Figure 6.24. For a given input potential, the pulse rate is determined by the charging time constant of R_1C_1 , the gain of the transistor and the characteristics of the transformer. T_1 is not a standard blocking oscillator transformer, since pulse widths on the order of 50 to 100 microseconds cannot be obtained with such transformers of small size. Proper blocking action is obtained using a small audio interstage transformer. If the emitter of Q_1 is grounded, the oscillator will not function satisfactorily for inputs below a fraction of one volt, and ceases oscillation for inputs more positive than zero volts. The split power source shown provides excellent operation for input potentials between plus 1 and minus 30 volts with pulse rates from 150 to 3,800 pps.

6.5.2.2 Modulator-Transmitter.

Positive pulses from the voltage controlled blocking oscillator and a sine wave of 81.94 kc from the ranging receiver must be combined to modulate the transmitter. The circuitry used for this is shown in Figure 6.25. Diodes D_3 and D_4 prevent all but a very small fraction of the overshoots developed by the blocking oscillator from reaching the mixing point, the base of Q_1 . Resistors R_3 and R_5 provide a proper balance of the two waveforms at the mixing point. The output of the gain stage, Q_1 , is fed to the emitter follower, Q_2 , which provides the necessary low

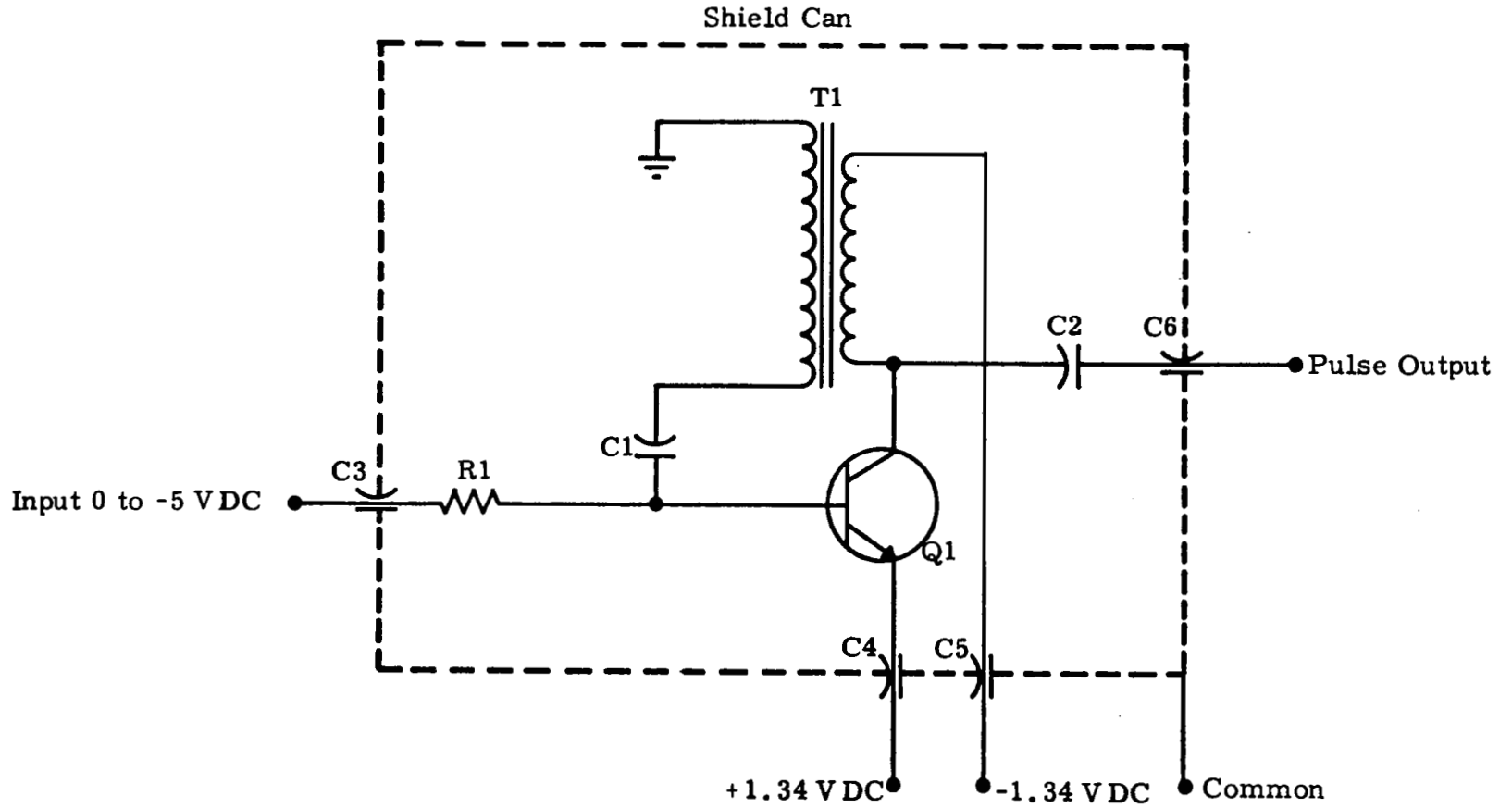


FIGURE 6.24 VOLTAGE CONTROLLED BLOCKING OSCILLATOR SCHEMATIC

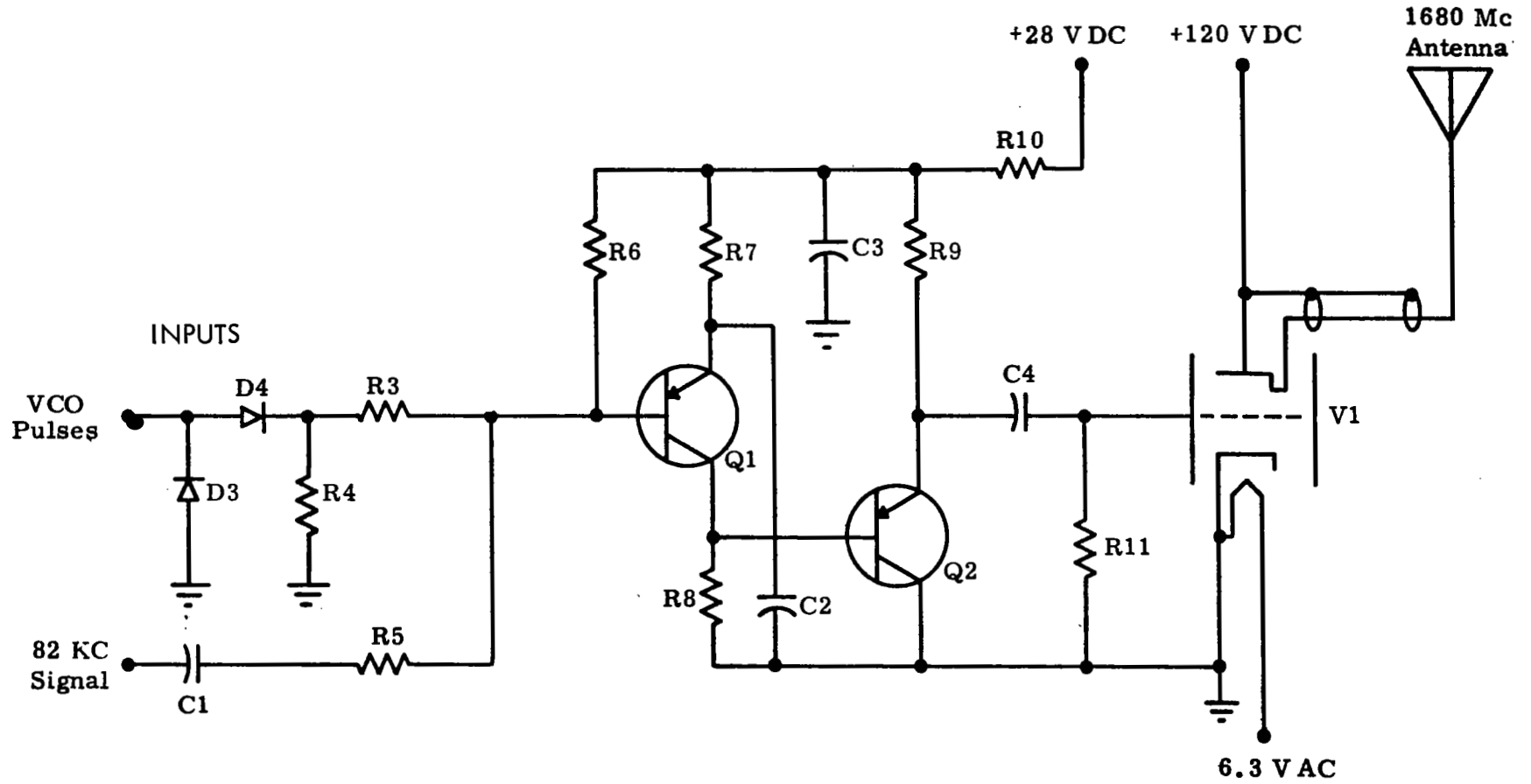


FIGURE 6.25 MODULATOR-TRANSMITTER SCHEMATIC

output impedance for driving the grid of the integral cavity oscillator-transmitter. Resistor R₁₁ in the grid current return path provides the necessary self-bias for the oscillator. The magnitude of modulation signal on the grid for proper frequency modulation is one volt peak for each component. Because of differentiation in the early stages of the Rawin set, the pulse data is strong in the ground signal even if barely noticeable in the oscillator grid waveform.

The cavity oscillator V₁ provides an inexpensive source of about 500 milliwatts or radio frequency power at 1680 Mc, but care must be exercised in its use since it is basically designed for radiosonde use where the shock and vibration problems are negligible and necessary lifetime is only a few hours. To overcome these possible trouble areas, the tube must be securely mounted and prelaunch testing of the transmitter kept moderate in time.

6.5.2.3 Superregenerative Receiver and Tuned Amplifier.

To provide the 403 Mc reception link in the pitot probe slant range system, the receiver shown in Figure 6.26 is included. It is a superregenerative detector with separate quench followed by an amplifier tuned to the frequency of the desired modulation signal, 81.94 kc. The detector tube V₁ is provided with a tuned circuit in an oscillator configuration at the desired 403 Mc. The tube bias is set nominally in the quasi-oscillation area such that an increase of the plate potential by a few volts will prevent oscillation. The state of the circuit is constantly moved between these two extremes by a sinusoidal quench oscillator made up of Q₁, T₁, and associated circuitry. Quench frequency is approximately 700 kc.

As shown in Figure 6.26, L₇ and C₇ form a parallel tuned load for the tube at 81.94 kc. To remove as much quench component as possible, the tuned load is followed by two sections of low passing filtering. This is followed by an amplifier, Q₂, which is tuned to the modulation frequency by L₁₀ and C₁₅.

6.5.2.4 Antenna Connections.

Pairs of quarterwave dipoles are used for the transmitter and receiver antennas. Figure 6.27 shows the electrical schematic of both systems. The cavity oscillator rf output is at plate potential with respect to ground, thus capacitors are provided between the coax shield and the frame ground to prevent a direct short circuit. These capacitors are 3/8 inch diameter copper washers secured to the frame walls with a thin ring of insulating material between the two. The dipoles are left at the plate potential. Since each cavity oscillator had a different output impedance angle, the length of coax "a" is adjusted for maximum radiated power.

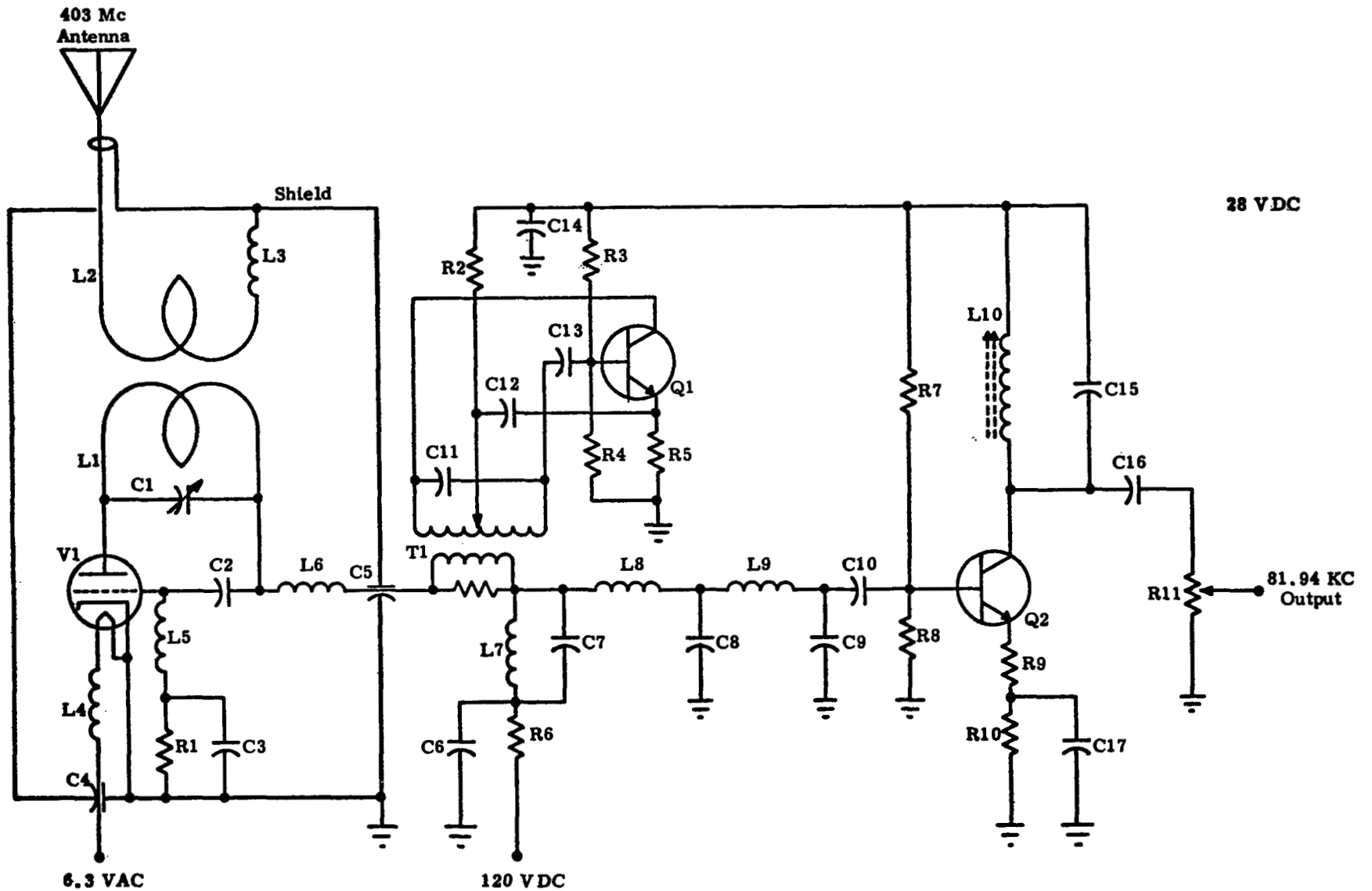


FIGURE 6.26 SUPERREGENERATIVE RECEIVER AND TUNED AMPLIFIER SCHEMATIC

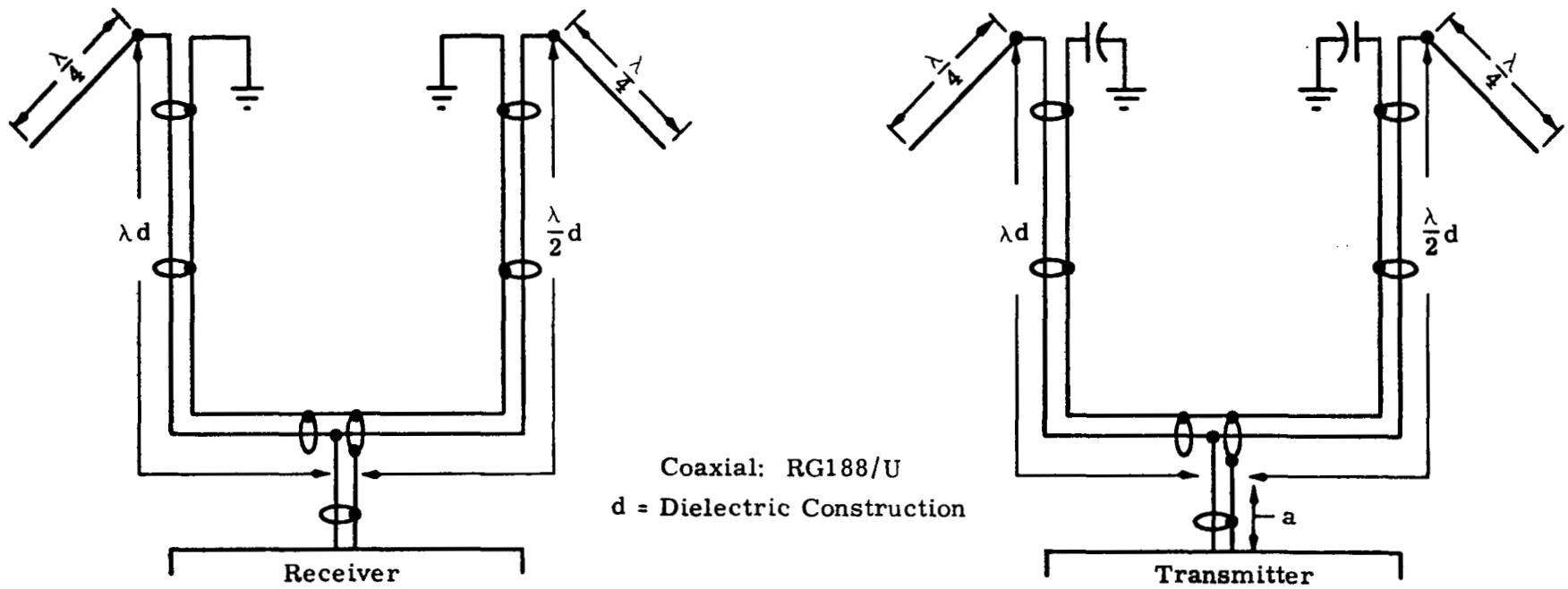


FIGURE 6.27 ANTENNA SCHEMATIC

6.5.2.5 Power Supply.

The power supply used with the telemetry payload is shown in Figure 6.28. Basic power was provided by nickel-cadmium rechargeable cells which provided a nominal 28 vdc. For other potentials, a dc to dc converter is excited from the battery source. The nominal output of the converter is 120 volts under load at the output of the two section RC filter. Filament voltage for the receiver and transmitter tubes is provided by stepping down the ac output of T₁ and T₂ to provide 6.3 volts. Since only two filaments are involved and each is different in current drain, any other method of providing filament power would waste power or cause unequal battery cell drain.

For testing and standby power provisions, the jacks J₁ and J₂ allow power to be brought into the power supply. Diodes D₁ and D₂ prevent reversal of current flow if the external source should be lower than the battery potential. Switch S₁ allows external power to be fed to the gage electronics only in the lower position, while full operation is obtained in the upper position.

6.5.2.6 Packaging.

The packaging volume for the telemetry system consists of an 8-inch length of the cylindrical 4-inch diameter payload section of the vehicle. Thus the vehicle nose cone would be available for installation of the impact pressure probe, gages and sensor electronics. A second consideration has been to provide an assembly of functional modules such as transmitters, receivers, signal conditioners, which can be interchanged or replaced in the field. The resulting assembly is depicted in Figures 6.29 and 6.30.

In order to conserve vehicle performance, consideration will be given to stowing the antennas during the high drag portion of the rocket's ascent. This can be accomplished by mechanically coupling the antenna pair on each of two phenolic side plates, so that they will all erect simultaneously upon nose cone release as shown in Figure 6.31.

Intermodular connections are made, wherever practical, with AMP Inc. printed circuit connectors. Modules are installed by sliding into milled slots in the two aluminum plates which contain the antenna assemblies. These plates are machined to the inner contour of the cylindrical payload section and, together with four cylindrical spacers form the structural skeleton for the electronic package. The final assembly slides smoothly into the cylindrical payload section from its forward end to form an integral unit.

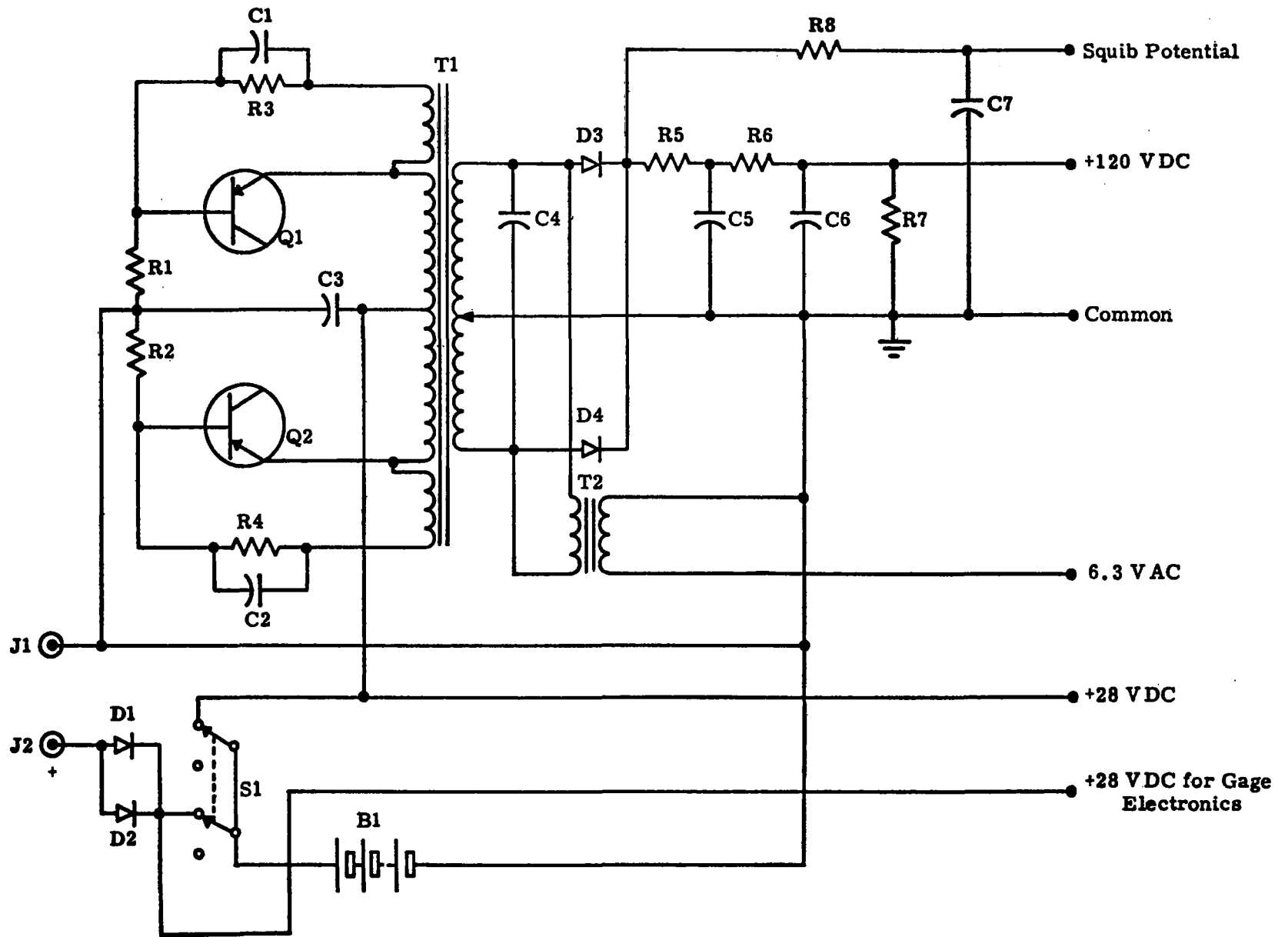


FIGURE 6.28 POWER SUPPLY SCHEMATIC

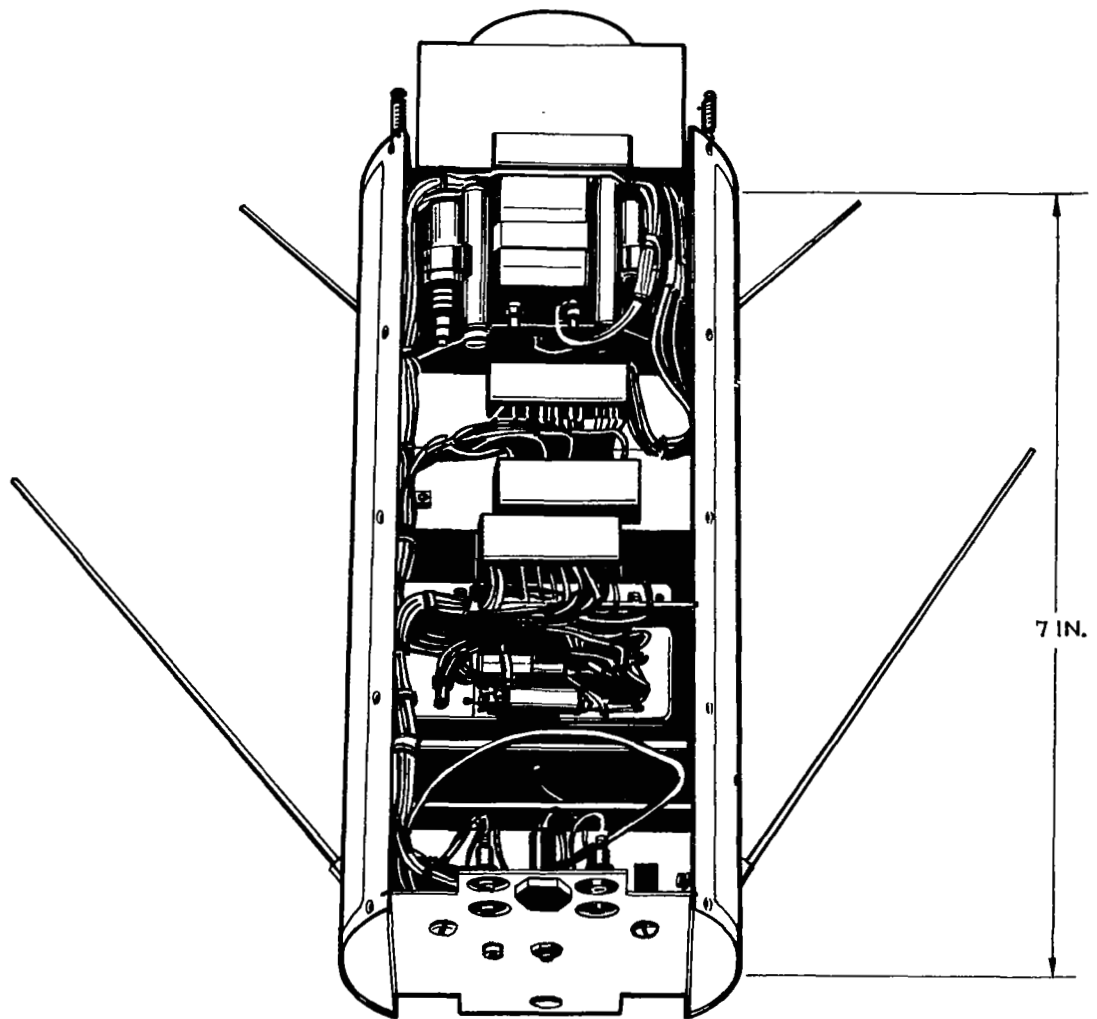


FIGURE 6.29 TELEMETERING MODULE ASSEMBLY

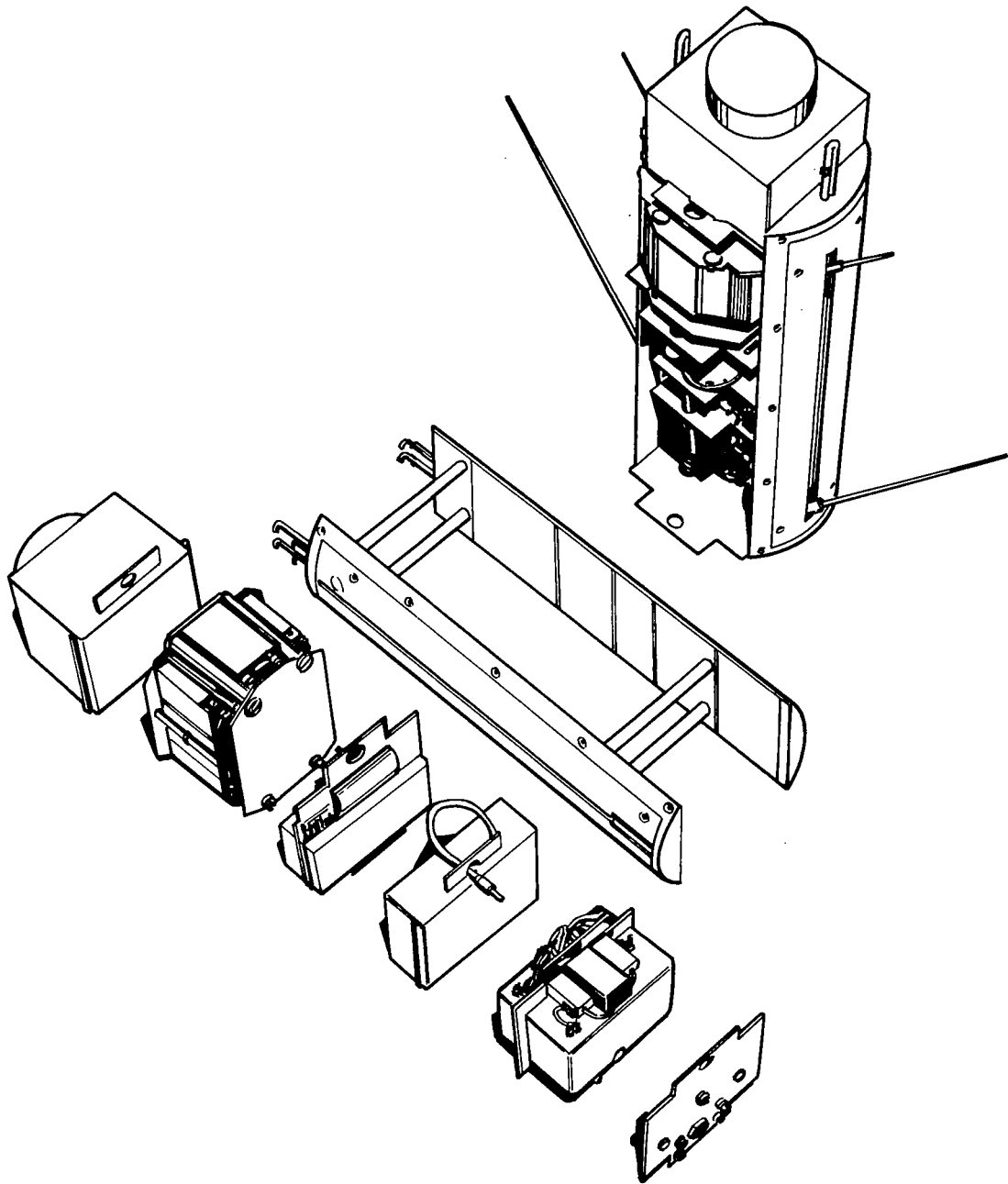


FIGURE 6.30 TELEMETERING MODULE SUBASSEMBLIES

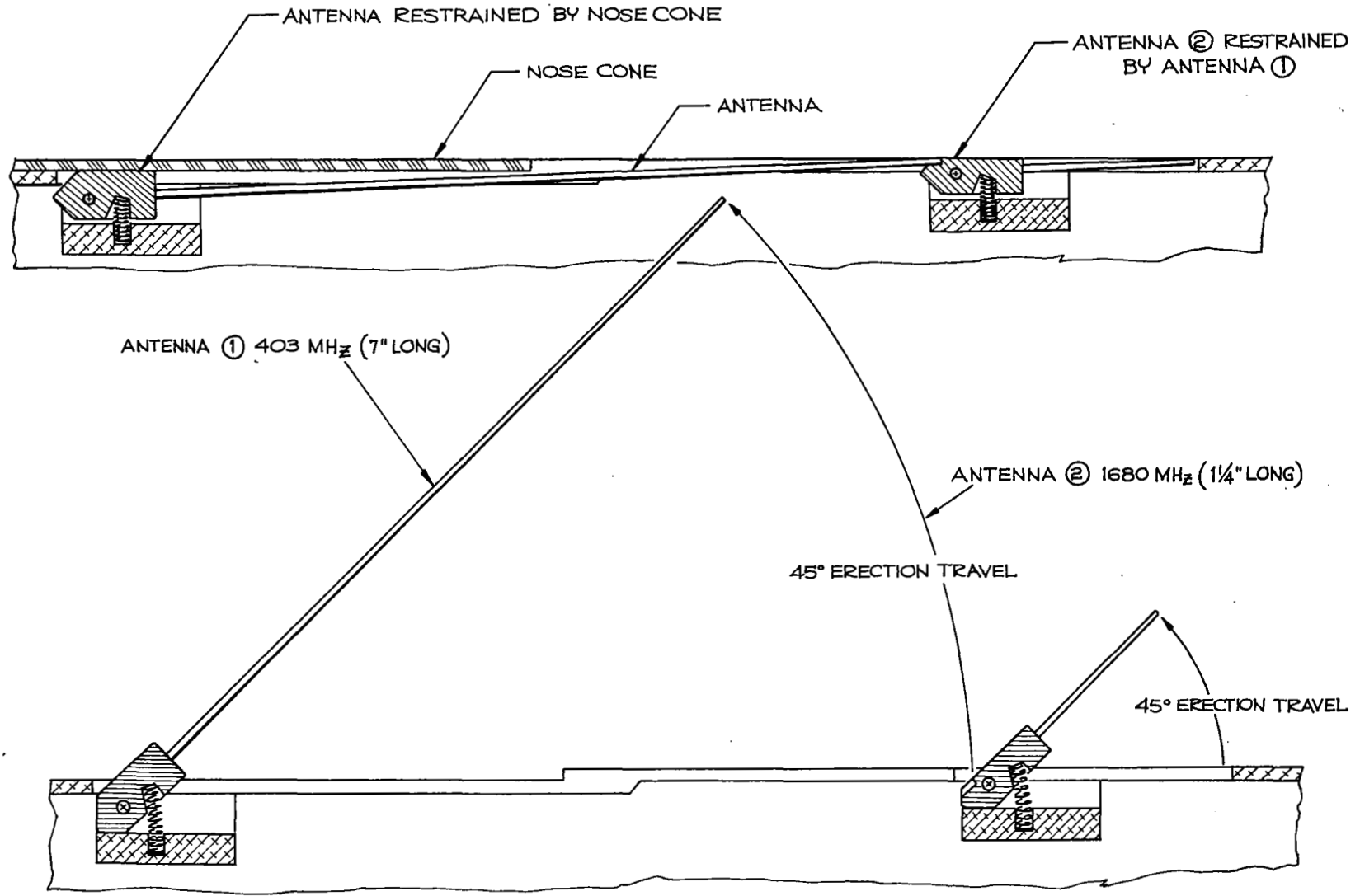


FIGURE 6.31 CENTRIFUGALLY ERECTED ANTENNA SYSTEM

6.5.3 Ground Equipment.

A basic Rawin Set AN/GMD-1B or GMD-2 can be employed for tracking the rocket-borne telemetry transmitter and detecting the modulation data contained in the tracking signal. The standard equipment must be modified, however, for considerably faster tracking rates and telemetry response times. These modifications have been made during the Denpro Program by the U.S. Army Electronics Command, Fort Monmouth, New Jersey. A detailed description of the modifications is beyond the scope of this proposal, but may be found in reference (15). A block diagram of the resulting ground equipment is depicted, however, in Figure 6.32. Major modifications were:

- a) The provision of a preamplifier of the tunnel diode type at the input of the Rawin receiver.
- b) Removal of Meteorological Recorder AN/TMQ-5 from the ground system and substituting a seven channel magnetic tape recorder for telemetered data.
- c) Addition of Transmitter T-456 ()/GMD-2 and Signal Comparator CM63 ()/GMD-2 to the Rawin set to provide for measurement of slant range.
- d) Addition of circuitry and components necessary for detecting and recording the rapidly pulsed telemetry data.
- e) Addition of control features and auxiliary timing data to enable accurate data reduction and payload acquisition after lift-off of the vehicle.

The location and distance relation between launching and tracking equipment may be chosen to enable acquisition of the payload telemetry, after lift-off, under conditions which result in low slew rate of the antenna. Rawin Set AN/GMD-1 will not track an ascending rocket from lift-off unless the separation distance between launcher and tracker is several miles. This is because of limited angular slewing rate (6 degrees/sec) of the antenna drive mechanism. An alternate location which may be adopted is to locate the tracker very near the launcher area and to train the antenna to a high vertical angle, chosen so that the antenna beam will intercept the rocket trajectory at some selected altitude. In practice, the beam should illuminate the trajectory for a considerable distance so that sufficient time is allowed for acquisition of the telemetry signal and lock-on of the automatic tracking circuits. The antenna train can be selected so as to acquire the rocket-borne signal at 12,000 feet altitude.

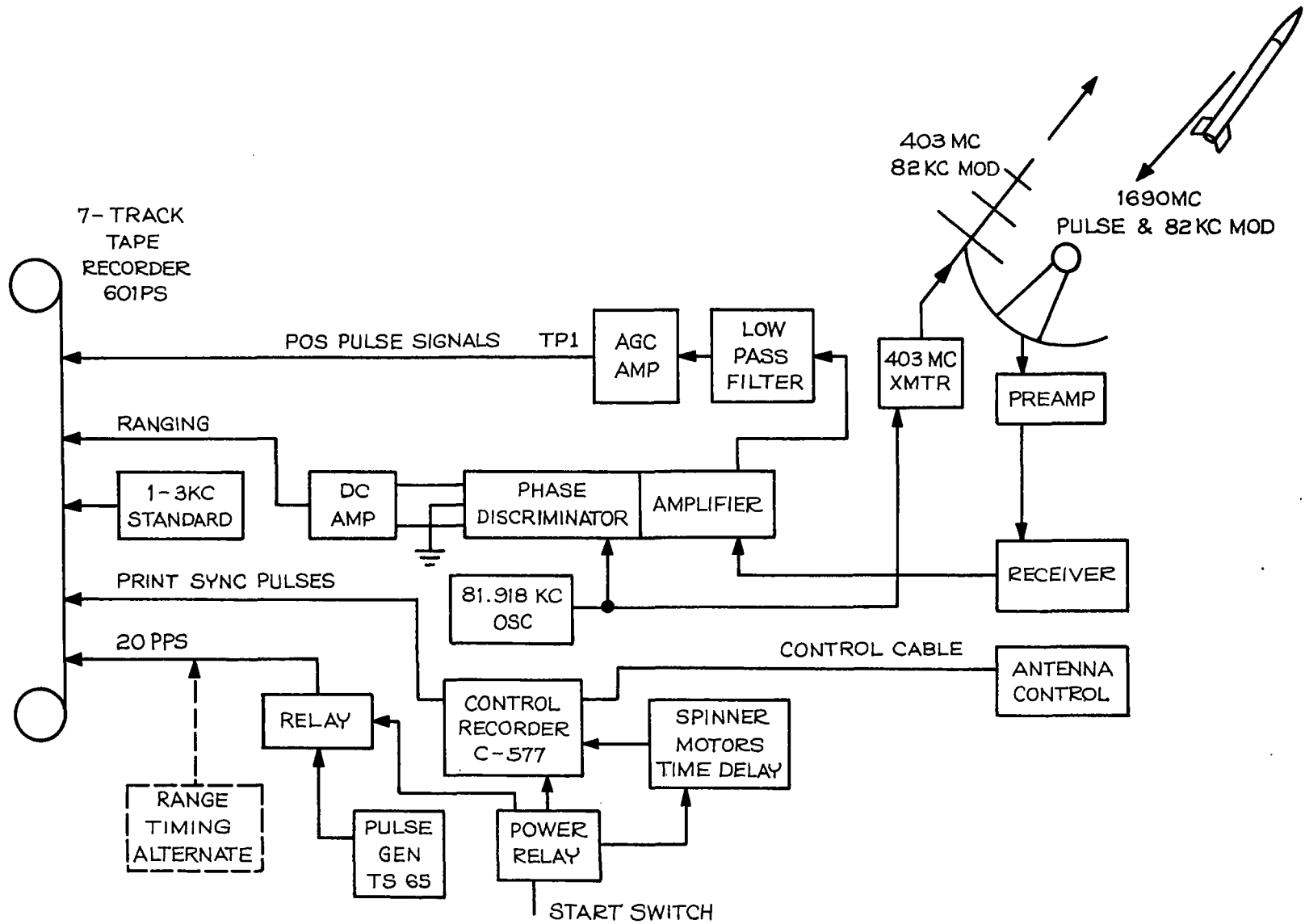


FIGURE 6.32 GROUND EQUIPMENT BLOCK DIAGRAM

Antenna drive motors are disabled after the antenna is trained to the intercept angles so that it will remain in position during countdown and prelaunch checkout. The proximity of the ground equipment to the payload when the latter is on the launch rail allows monitoring of all signals in spite of the fact that the antenna is trained away from the payload. The elapsed time after lift-off, at which acquisition is to occur, is determined from computer trajectory data and antenna drive motors are automatically energized by a preset elapsed time control relay which is installed as part of the ground equipment.

Flight and telemetry data are recorded on two mediums; azimuth and elevation angles on Control Recorder C-577, modified for a faster print rate than the standard recorder provides; and, telemetered data, range timing, time correlation pulses, and slant range data on a multichannel magnetic tape recorder.

From the block diagram of Figure 6.32, it is seen that all data necessary to compute the payload trajectory as an altitude-time relation, to compute the payload velocity, to reduce the telemetered data, and to correlate an altitude-density profile is present in the recordings.

6.6 Vehicle Design.

6.6.1 General.

The proposed pitot probe vehicle is a two-stage Super Loki sounding rocket. Previous studies have shown that for the pitot probe application a small two-stage solid-propellant rocket is considerably more efficient in terms of performance, cost, size and launching ease than a single stage vehicle.

6.6.2 Vehicle Description.

The two-stage Super Loki vehicle consists of two Super Loki rocket motors which were originally developed and flight tested for NASA Marshall Space Flight Center under Contract NAS8-20797. The vehicle configuration is shown in Figure 6.33. The forward end of the first stage is slip-fitted into the aft end of the second stage as shown in Figure 6.34 in the same manner as for the Nike boosted vehicles. Fin plan-form areas will be larger than for the original Super Loki motor to maintain two-stage stability and second stage stability at the higher Mach numbers. A pyrotechnic delay igniter will be used for the second stage so that both first and second stage igniters can be initiated at launch. The pre-ignition coast time of the second stage will be optimized for the pitot measurement by trading off factors of vehicle performance with flight path angle.

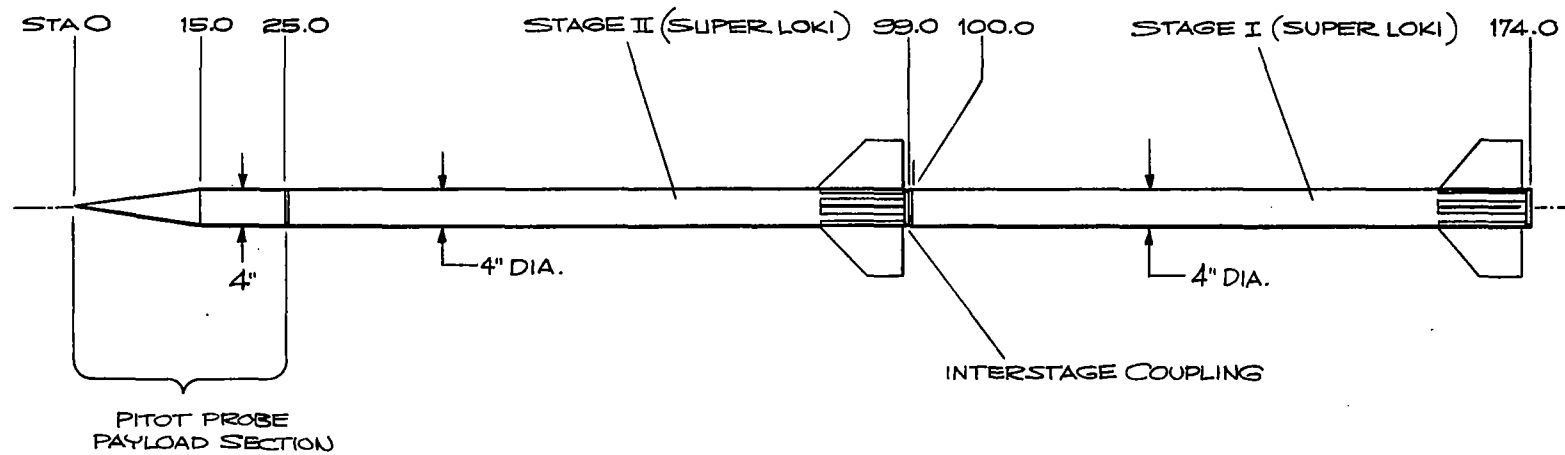


FIGURE 6.33 TWO-STAGE SUPER LOKI VEHICLE CONFIGURATION

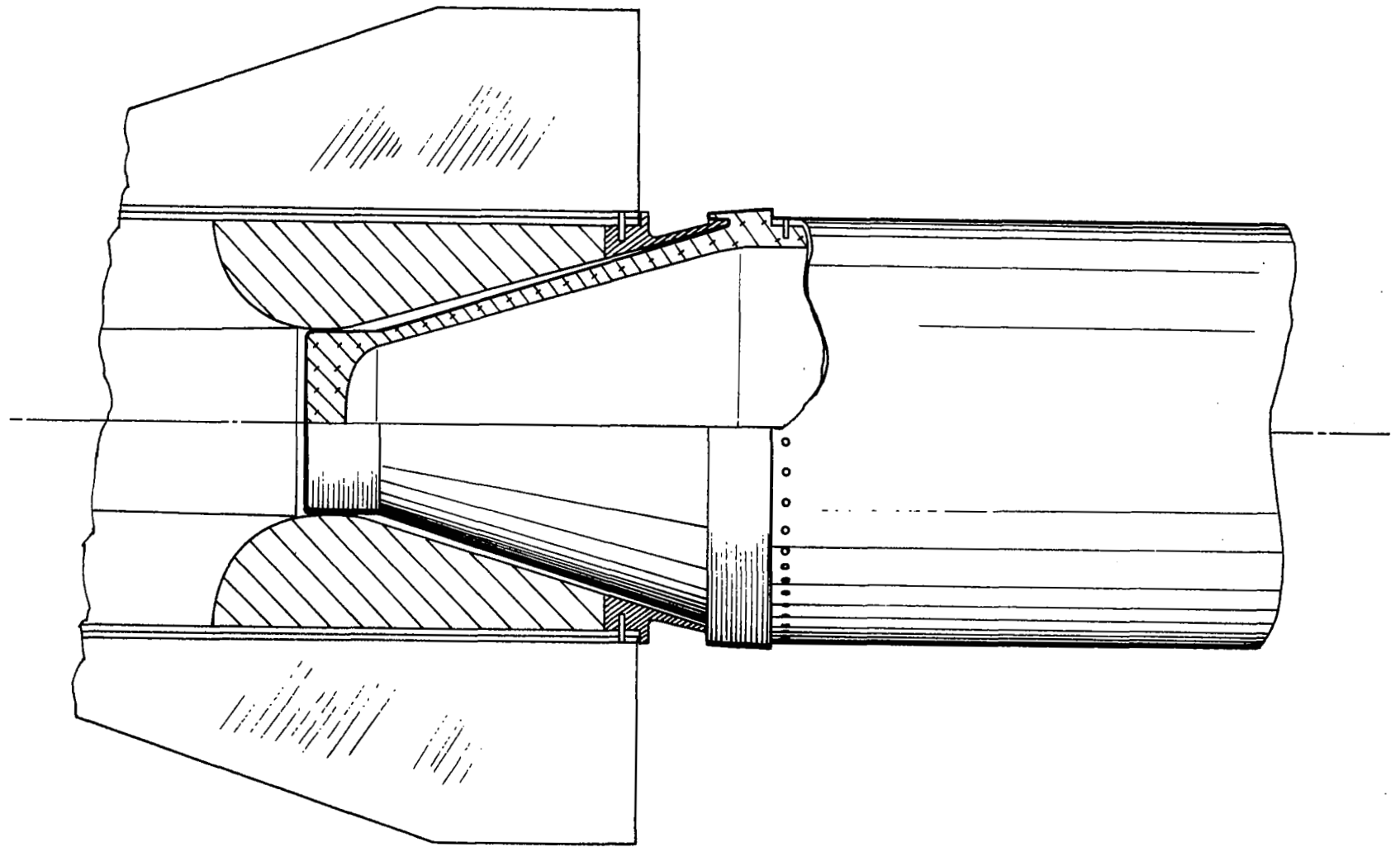


FIGURE 6.34 INTERSTAGE COUPLING DESIGN

The Super Loki rocket motor consists of an aluminum case with an internal burning cast-in-the-case solid propellant. Major design characteristics of the rocket motor are presented in Table 6.3. The propellant fuel is a polysulfide polymer and the oxidizer is ammonium perchlorate. A photograph of the rocket motor is shown in Figure 6.35. The igniter consists of two parallel 1 watt/1 ampere no-fire squibs and an appropriate ignition charge. The igniter is separable from the motor and is installed at the launch site. A cross-section view of the Super Loki rocket motor with the igniter installed is shown in Figure 6.36.

The proposed payload weight is 10 lb contained in a 4.00-inch cylindrical payload section and a conical nosecone as shown in Figure 6.37. The cylindrical payload section contains the telemetry and tracking electronics and an inflatable sphere payload. The nosecone section contains the pitot probe and associated sensor electronics. Pyrotechnic delay trains are initiated at launch from both a nosecone ejection system and a payload separation system. At 50 km the nosecone is ejected, spring-out telemetry antennae are released, and the pitot measurements commence. After the pitot measurements are completed at an altitude of about 120 km, the payload section is separated from the expended second stage motor and the inflatable sphere is released from the aft end of the payload section. More detailed descriptions of the payloads and payload systems are presented in other sections of this proposal.

A vehicle weight breakdown is presented in Table 6.4. Rocket motor thrust and propellant weight vs. time data are presented in Table 6.5. The vehicle drag coefficient data are represented in Table 6.6 and in Figure 6.38.

6.6.3 Vehicle Performance.

The two-stage Super Loki Pitot Probe vehicle reaches an apogee altitude of about 205 km (673,000 feet) when launched from sea level at an 85-degree QE. The exact altitude and performance variables depend upon the interstage coast period which is to be optimized for the pitot probe measurement during the development program. Vehicle apogee altitude vs. interstage coast time is presented in Figure 6.39. Vehicle impact range vs. interstage coast period is presented in Figure 6.40. A summary of the major performance characteristics is presented in Table 6.7 for various interstage coast periods.

Since the preliminary analysis of the pitot measurement requirements indicate an optimum coast period of 20 seconds, detailed performance curves are presented for this configuration as follows:

Figure 6.41	Altitude vs. Time
Figure 6.42	Altitude vs. Range
Figure 6.43	Altitude vs. Velocity
Figure 6.44	Altitude vs. Mach No.
Figure 6.45	Altitude vs. Attitude Parameters

TABLE 6.3

SUPER LOKI ROCKET MOTOR
DESIGN CHARACTERISTICS SUMMARY

Length (inches)	78
Diameter (inches)	4
Weights:	
Inert Motor with Interstage (kg)	5.26 (11.6 lb)
Propellant (kg)	16.87 (37.2 lb)
Total (kg)	22.14 (48.8 lb)
Motor Mass Fraction	0.76
Burning Time (seconds)	2.0
Chamber Pressure:	
Maximum (Atmospheres)	100.02 (1470 psig)
Average (Atmospheres)	83.69 (1230 psig)
Thrust at Sea Level:	
Maximum (kg)	2608.20 (5750 lb)
Average (kg)	2018.52 (4450 lb)
Total Impulse at Sea Level (nt-sec)	3.96 (8900 lb-sec)
Specific Impulse at Sea Level (sec)	239
Loaded Weight	22.19 kg (48.93 lb)
Expended Weight	5.28 kg (11.63)
Loaded Center-of-Gravity	85.6 cm (33.70 inches) from aft end of motor
Expended Center-of-Gravity	85.09 cm (33.50 inches) from aft end of motor
Load Pitch Moment of Inertia	7.28 kg-m ² (5.27 slug/ft ²)
Expended Pitch Moment of Inertia	3.08 kg-m ² (2.27 slug/ft ²)

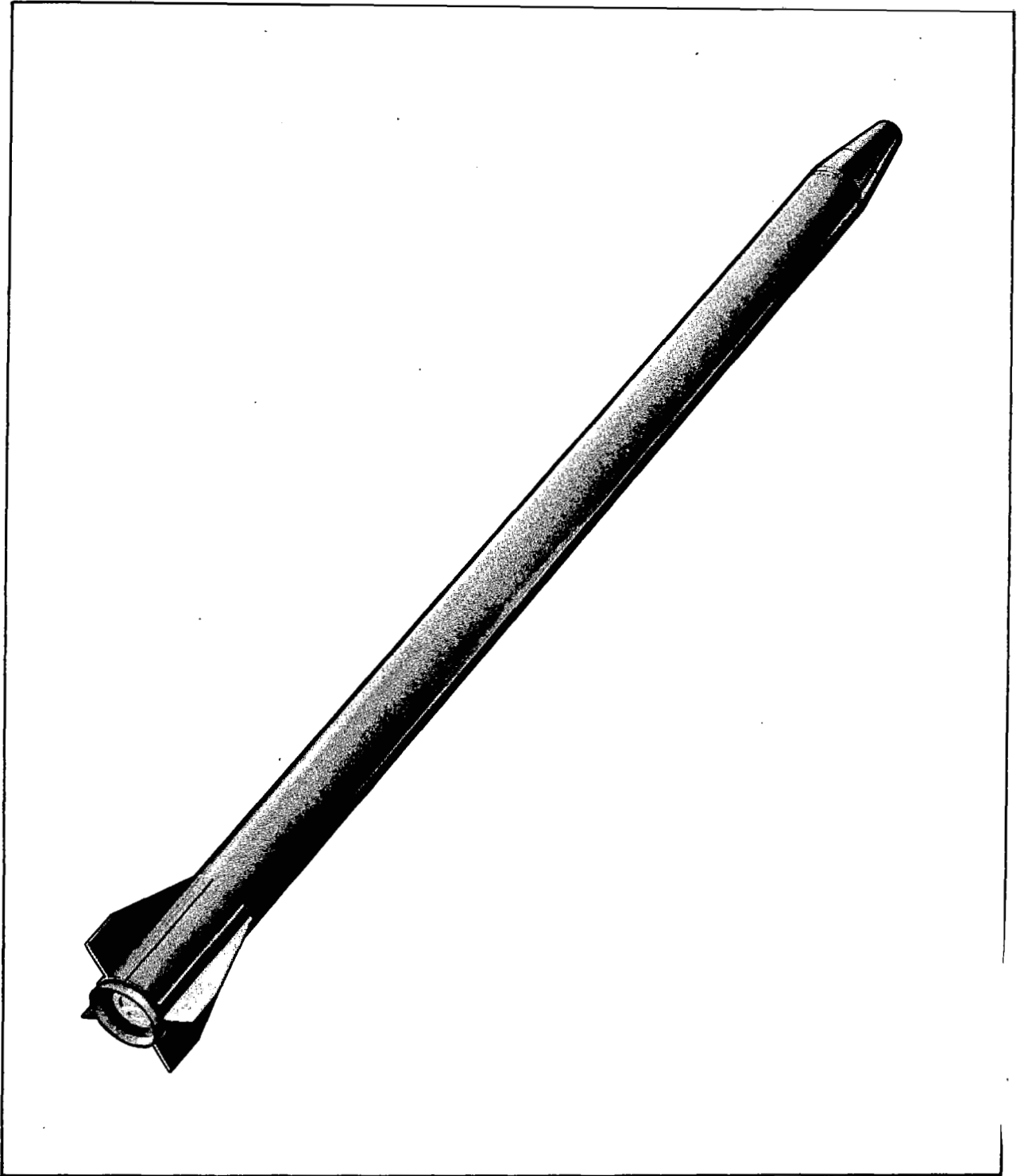


FIGURE 6.35 SUPER LOKI ROCKET MOTOR

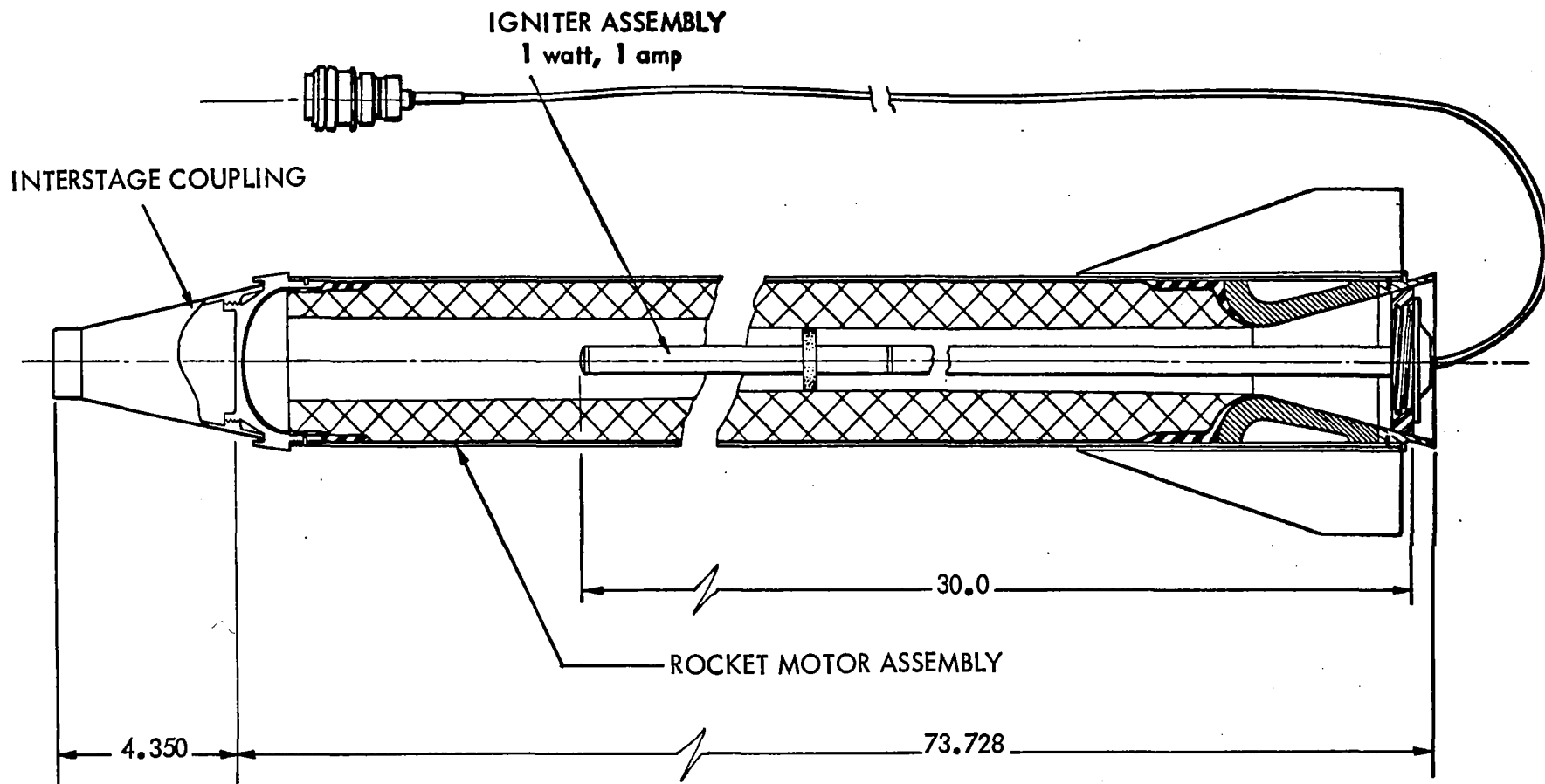


FIGURE 6.36 CROSS SECTION VIEW OF FIRST STAGE SUPER LOKI MOTOR

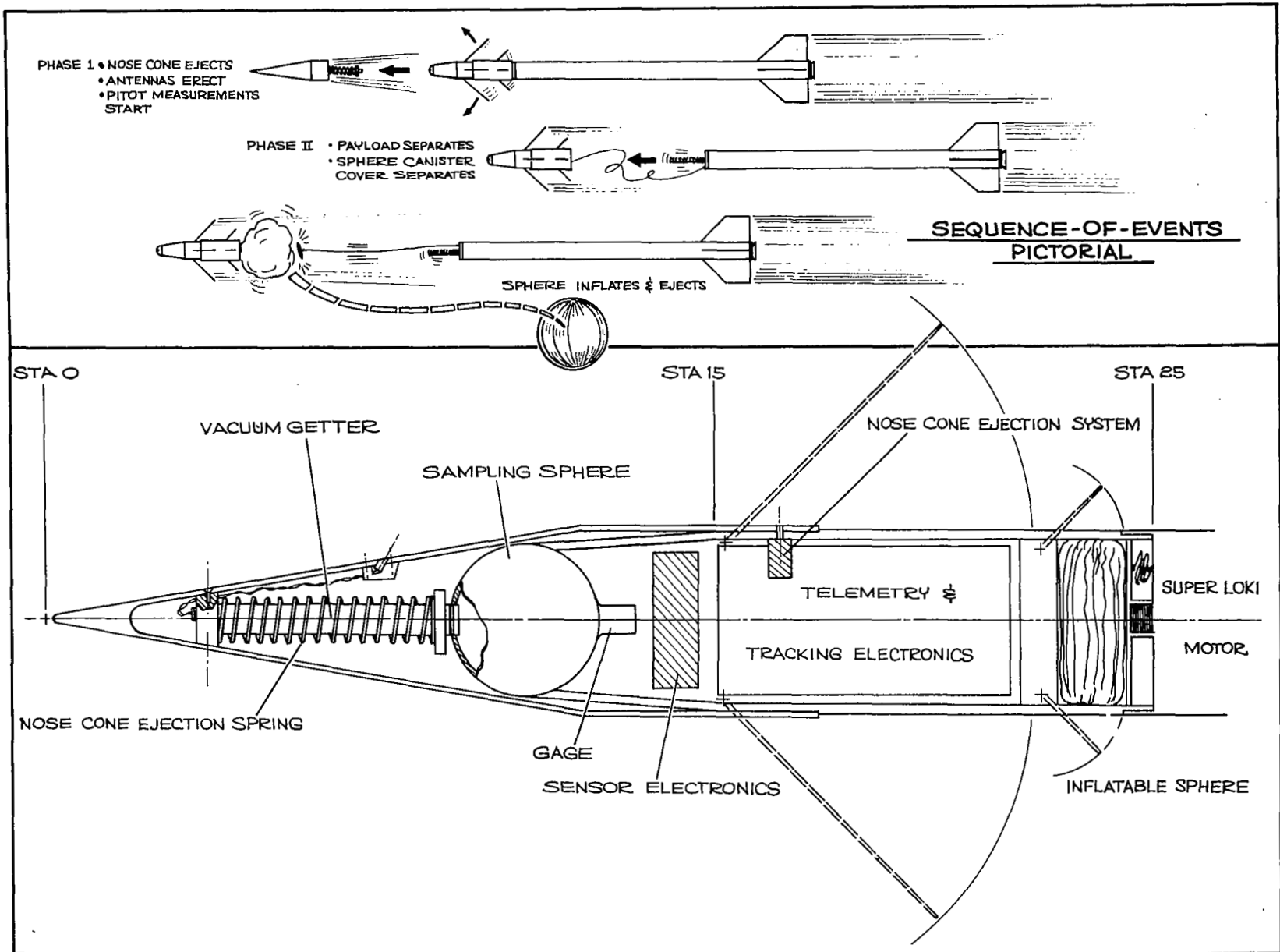


FIGURE 6.37 PROPOSED PAYLOAD DESIGN

TABLE 6.4

TWO-STAGE SUPER LOKI WEIGHT BREAKDOWN

Components

Loaded Rocket Motor	48.93 lb
Expended Rocket Motor	11.63
Propellant	37.20
Liner	0.10
Stage 1 Fins	6.00
Stage 2 Fins	4.00
Interstage	2.00
Payload	10.00

Stage Weights

Payload	10.00 lb	
Expended Motor	11.63	
Stage 2 Fins	4.00	
Stage 2 Expended		25.63 lb
Propellant and Liner	37.30	
Stage 2 Loaded		62.93
Expended Motor	11.63	
Stage 1 Fins	6.00	
Interstage	2.00	
Stage 1 Expended		82.56
Propellant and Liner	37.30	
Stage 1 Launch		119.86

TABLE 6.5

SUPER LOKI THRUST AND PROPELLANT
WEIGHT VS TIME (SEA LEVEL CONDITIONS)

Time (sec)	Thrust (lbf)	Time (sec)	Propellant Weight (lb)
0.	0.	0.	37.2
.1	2887.85	0.025	37.
.2	2927.15	0.05	36.7
.3	3041.38	0.10	36.0
.4	3254.71	0.2	34.8
.5	3512.59	0.3	33.5
.6	3774.52	0.5	30.7
.7	4067.81	0.8	25.6
.8	4366.64	1.0	21.6
.9	4627.70	1.2	17.3
1.	4877.97		
1.1	5073.51		
1.2	5154.32		
1.3	5188.26		
1.4	5237.69	1.4	12.8
1.5	5277.57	1.5	10.6
1.6	5231.42	1.6	8.3
1.7	5331.74	1.8	3.7
1.8	5468.90	1.9	1.6
1.9	4322.60	1.95	0.8
2.0	1755.03	2.0	0.2
2.1	69.77	2.02	0.0

TABLE 6.6

TWO-STAGE SUPER LOKI DRAG COEFFICIENT DATA

Two-Stage Drag Coefficients
(Thrusting) Reference Area 0.0873 ft²

<u>Mach No.</u>	<u>C_D</u>
0.0	.362
0.2	.419
0.4	.475
0.6	.600
0.8	1.358
1.0	1.663
1.2	1.063
1.4	.950
1.6	.894
1.8	.849
2.00	.815
2.20	.792
2.40	.769
2.60	.747
2.80	.724
5.0	.701

Second Stage Drag Coefficients
Reference Area 0.0873 ft²

Thrusting		Coasting	
<u>Mach No.</u>	<u>C_D</u>	<u>Mach No.</u>	<u>C_D</u>
0.	.283	0.	0.311
.6	.291	0.6	.32
.8	.301	0.8	.332
1.	.387	1.0	.426
1.1	.581	1.1	.64
1.2	.610	1.2	.671
1.4	.597	1.4	.650
1.6	.561	1.6	.618
1.8	.533	1.8	.586
2.0	.500	2.0	.550
2.5	.426	2.5	.469
3.0	.363	3.0	.399

FIGURE 6.38 TWO-STAGE SUPER LOKI
DRAG COEFFICIENTS

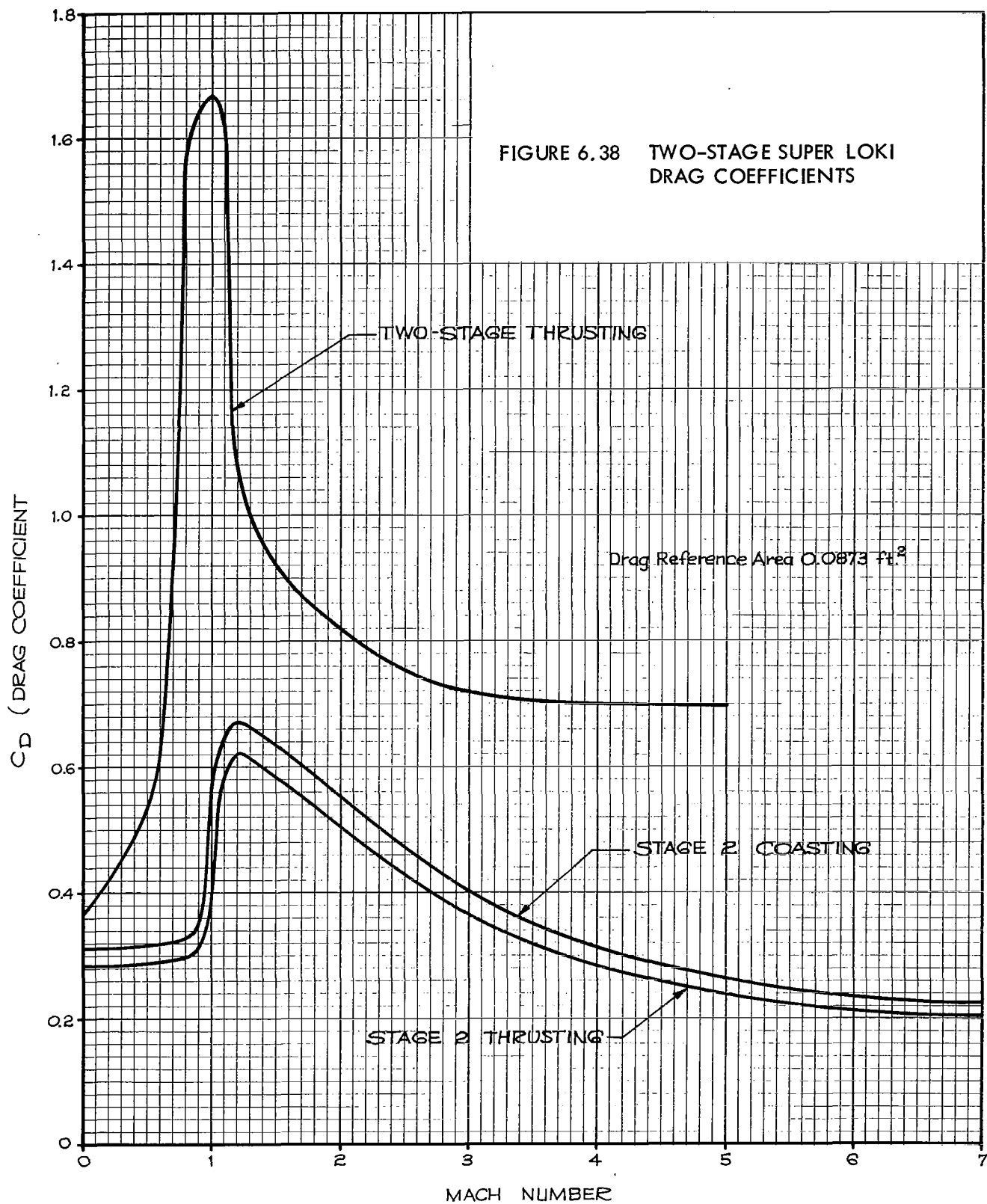
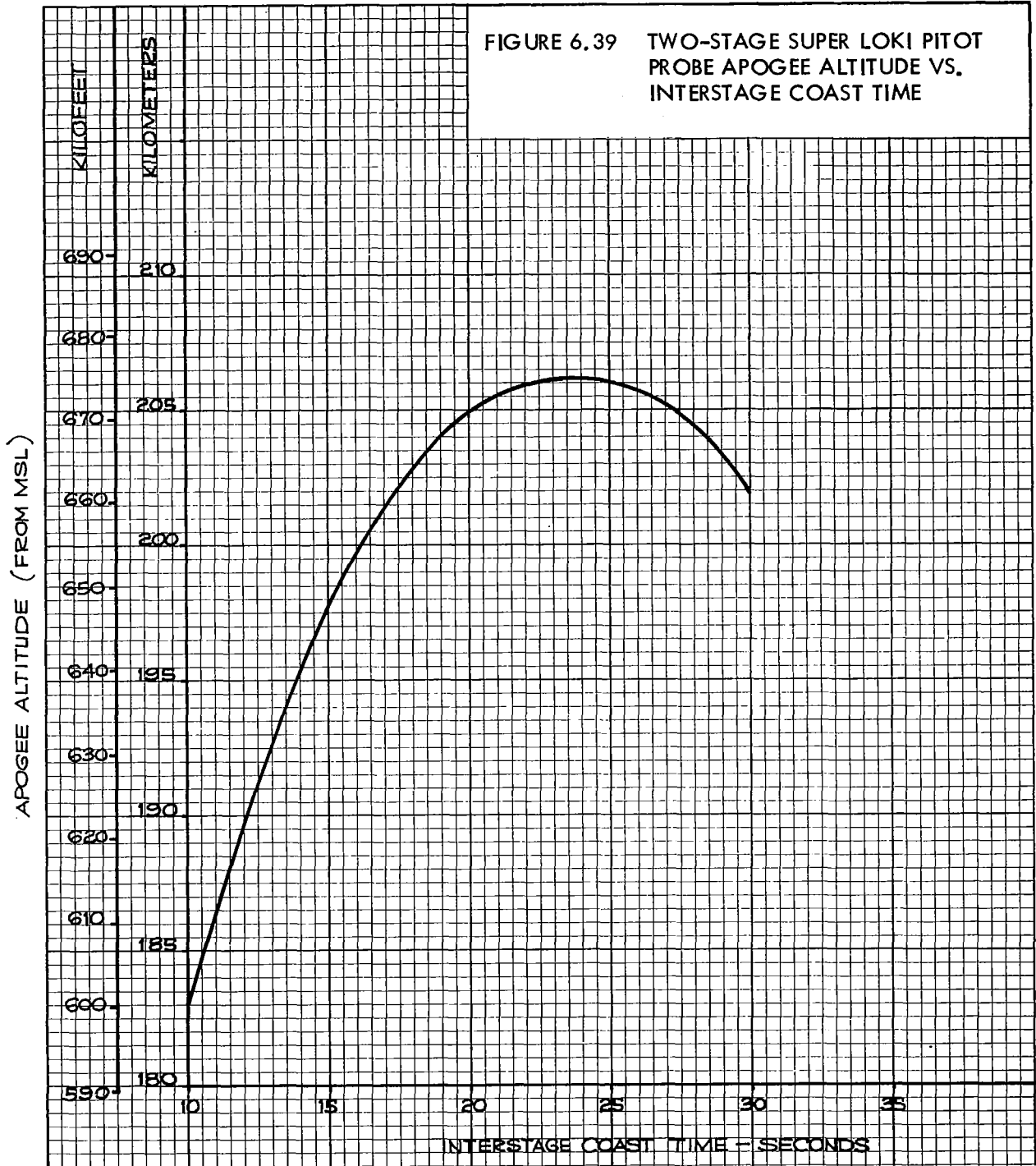


FIGURE 6.39 TWO-STAGE SUPER LOKI PITOT PROBE APOGEE ALTITUDE VS. INTERSTAGE COAST TIME



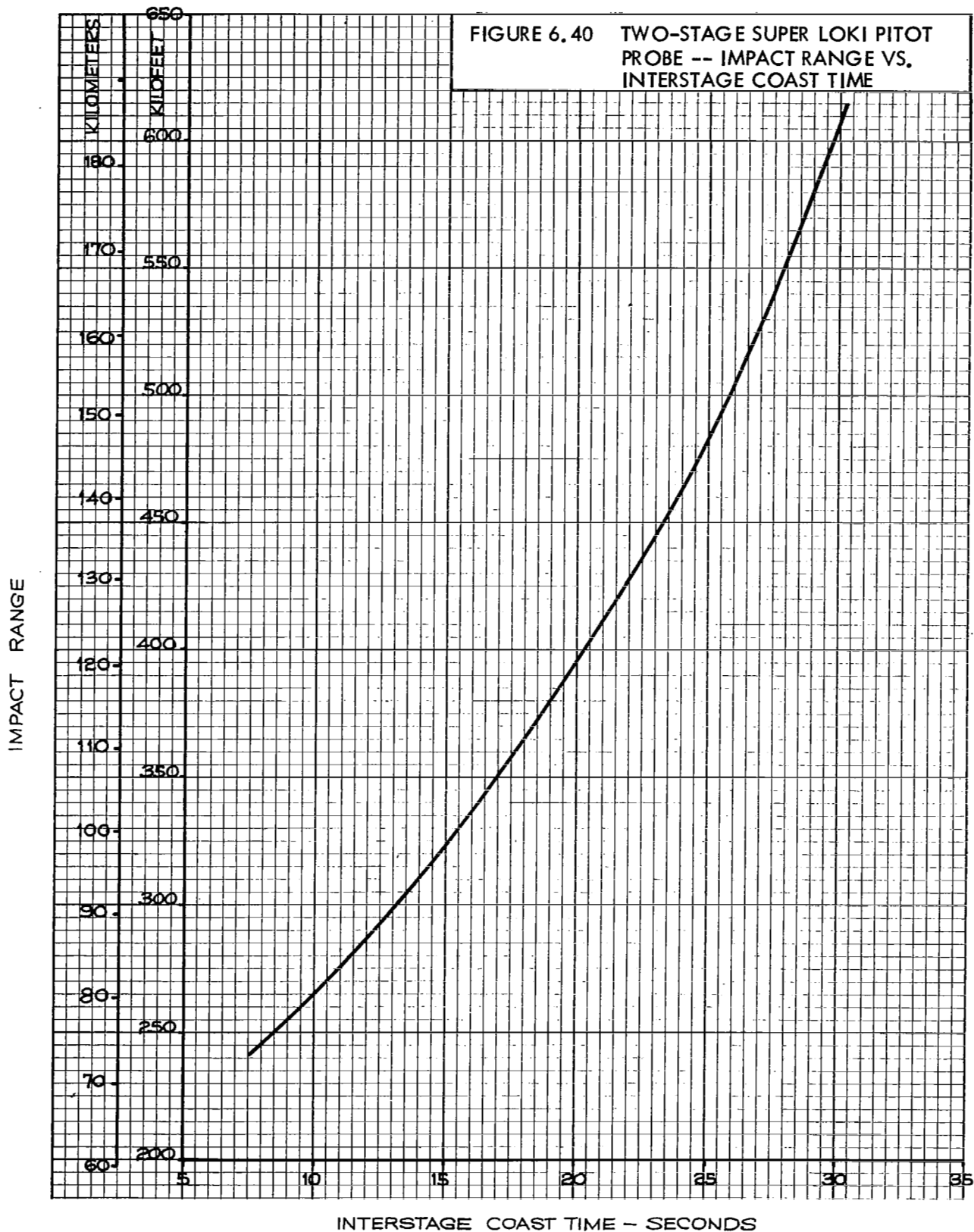


Table 6.7 Two-Stage Super Loki Pitot Probe Vehicle Performance Summary
85° QE Sea Level Launch with Various Interstage Coast Times

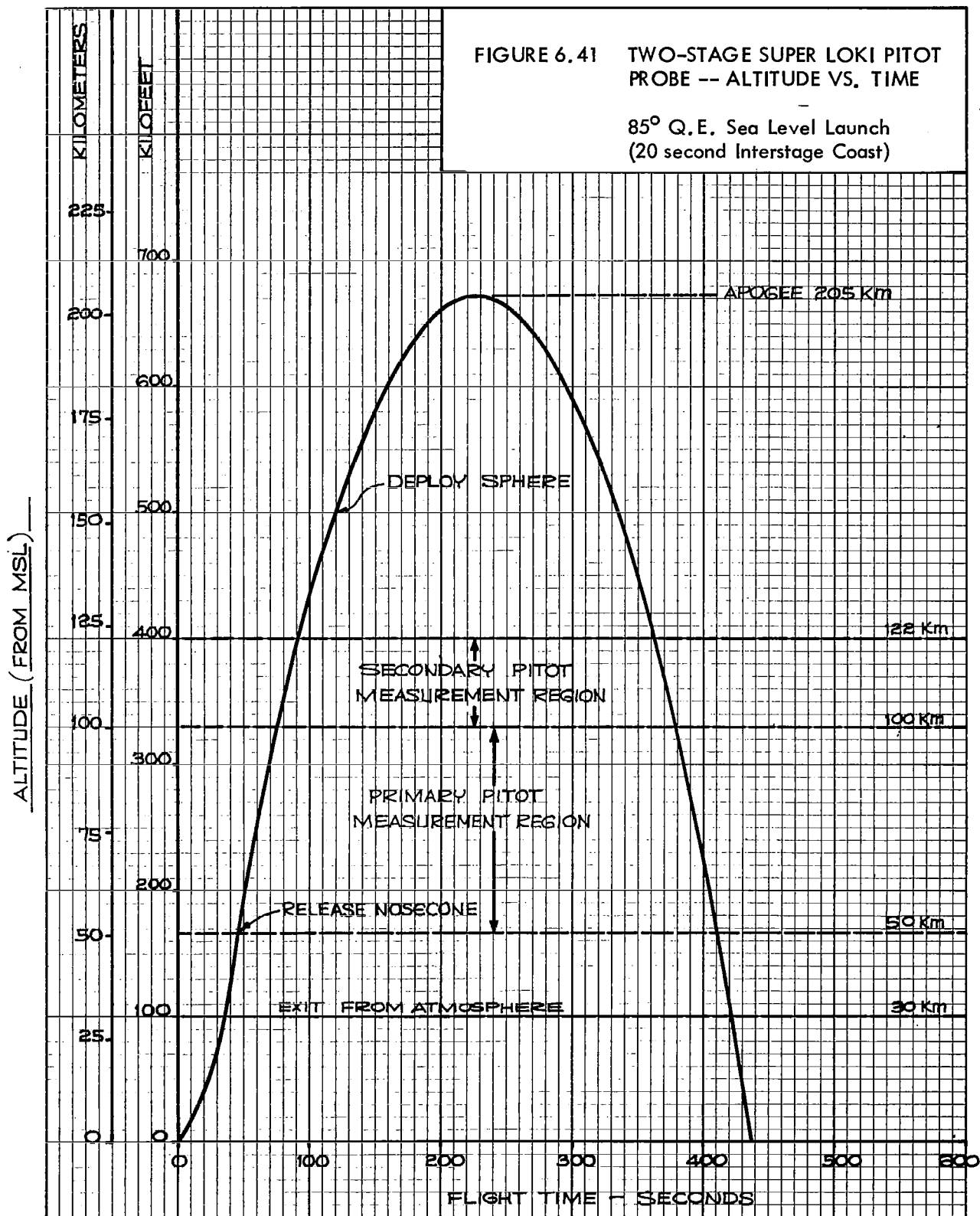
Coast Period (sec)	Apogee Altitude		Max. Velocity (fps)	Burnout Conditions			Atmospheric Exit		
	(km)	(ft)		Mach No.	Altitude (ft)	Flt. Path Angle (deg)	Dynamic Pressure (lb/ft ²)	Altitude (ft)	Flt. Path Angle (deg)
10	183	600,000	7674	7.7	30,114	83.4	26,132	108,684	82.9
15	197	647,000	7507	7.7	35,933	82.5	20,075	104,476	82.0
20	205	673,000	7374	7.6	40,613	81.2	15,515	97,608	80.8
25	206	676,000	7246	7.5	44,217	79.3	12,606	100,792	78.8
30	202	662,000	7118	7.4	47,047	76.3	10,625	102,870	75.7

Table 6.7 Two-Stage Super Loki Pitot Probe Vehicle Performance Summary
 85° QE Sea Level Launch with Various Interstage Coast Times
 Continued

Coast Period (sec)	50 KM Conditions				100 KM Conditions				120 KM Conditions			
	Mach No.	Velocity (fps)	Flt. Path Angle (deg)	Angle of Attack (deg)	Mach No.	Velocity (fps)	Flt. Path Angle (deg)	Angle of Attack (deg)	Mach No.	Velocity (fps)	Flt. Path Angle (deg)	Angle of Attack (deg)
10	4.8	5260	82.5	0.4	4.6	4135	80.4	2.5	4.0	3645	79.1	3.8
15	5.0	5548	81.5	0.5	5.0	4489	79.4	2.6	4.4	4000	78.2	3.8
20	5.1	5675	80.2	0.6	5.2	4684	78.1	2.7	4.7	4258	76.9	3.9
25	5.2	5716	78.0	0.8	5.3	4734	75.5	3.3	4.8	4314	74.1	4.7
30	5.2	5730	74.8	0.9	5.3	4741	71.5	4.2	4.8	4330	69.7	6.0

FIGURE 6.41 TWO-STAGE SUPER LOKI PITOT PROBE -- ALTITUDE VS. TIME

85° Q.E. Sea Level Launch
(20 second Interstage Coast)



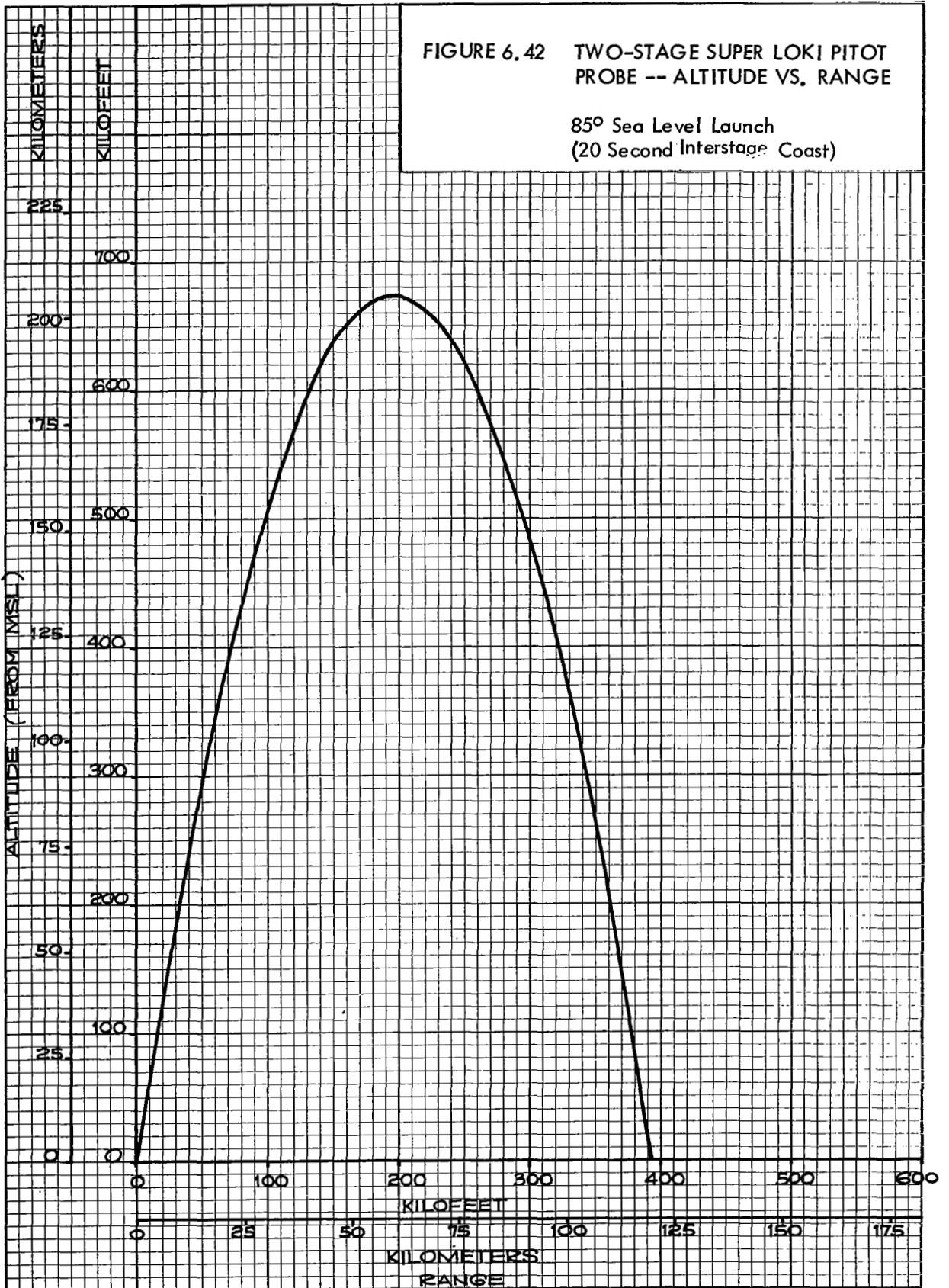


FIGURE 6.43 TWO-STAGE SUPER LOKI PITOT PROBE -- ALTITUDE VS. VELOCITY

85° Q.E., Sea Level Launch
(20 Second Interstage Coast)

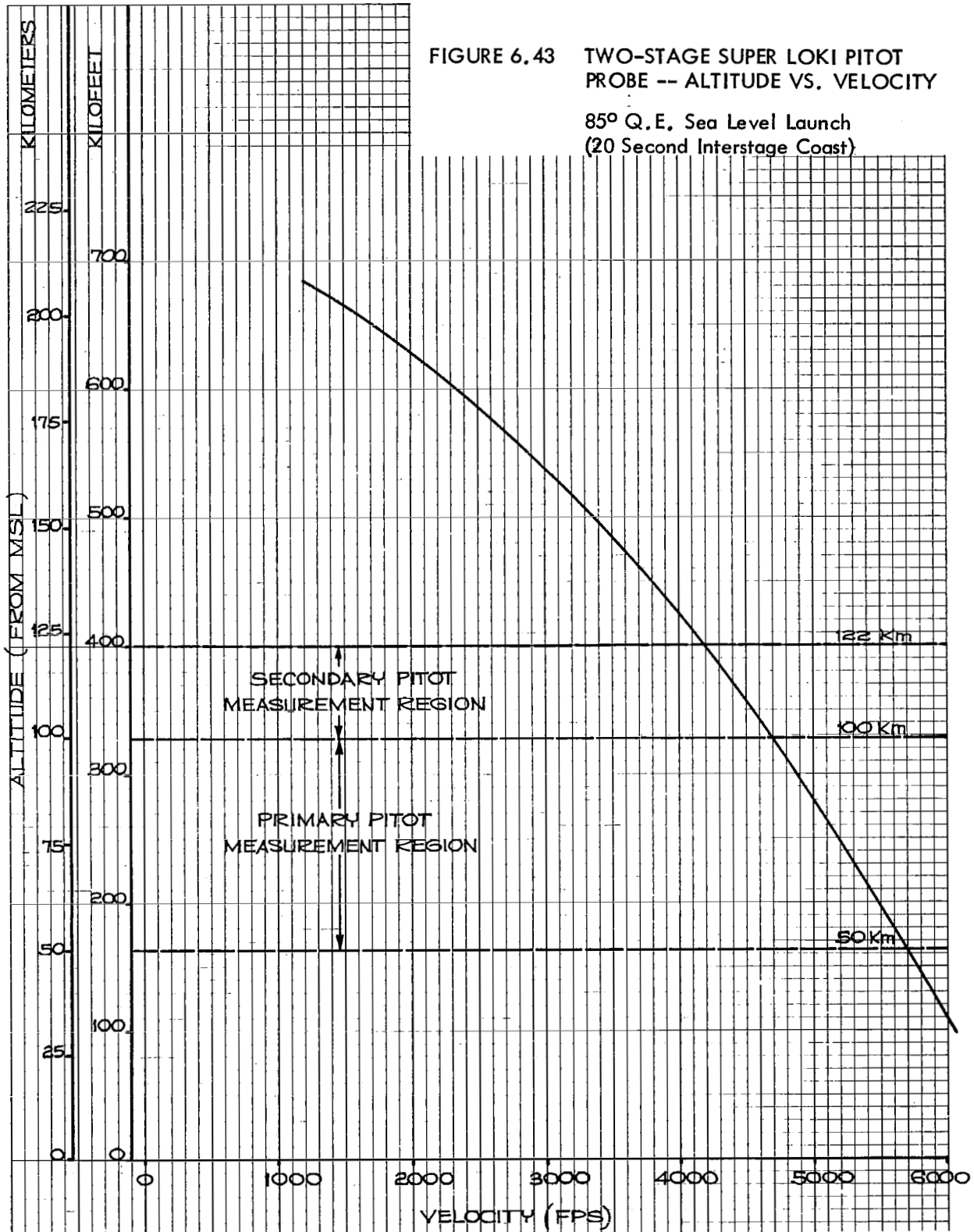
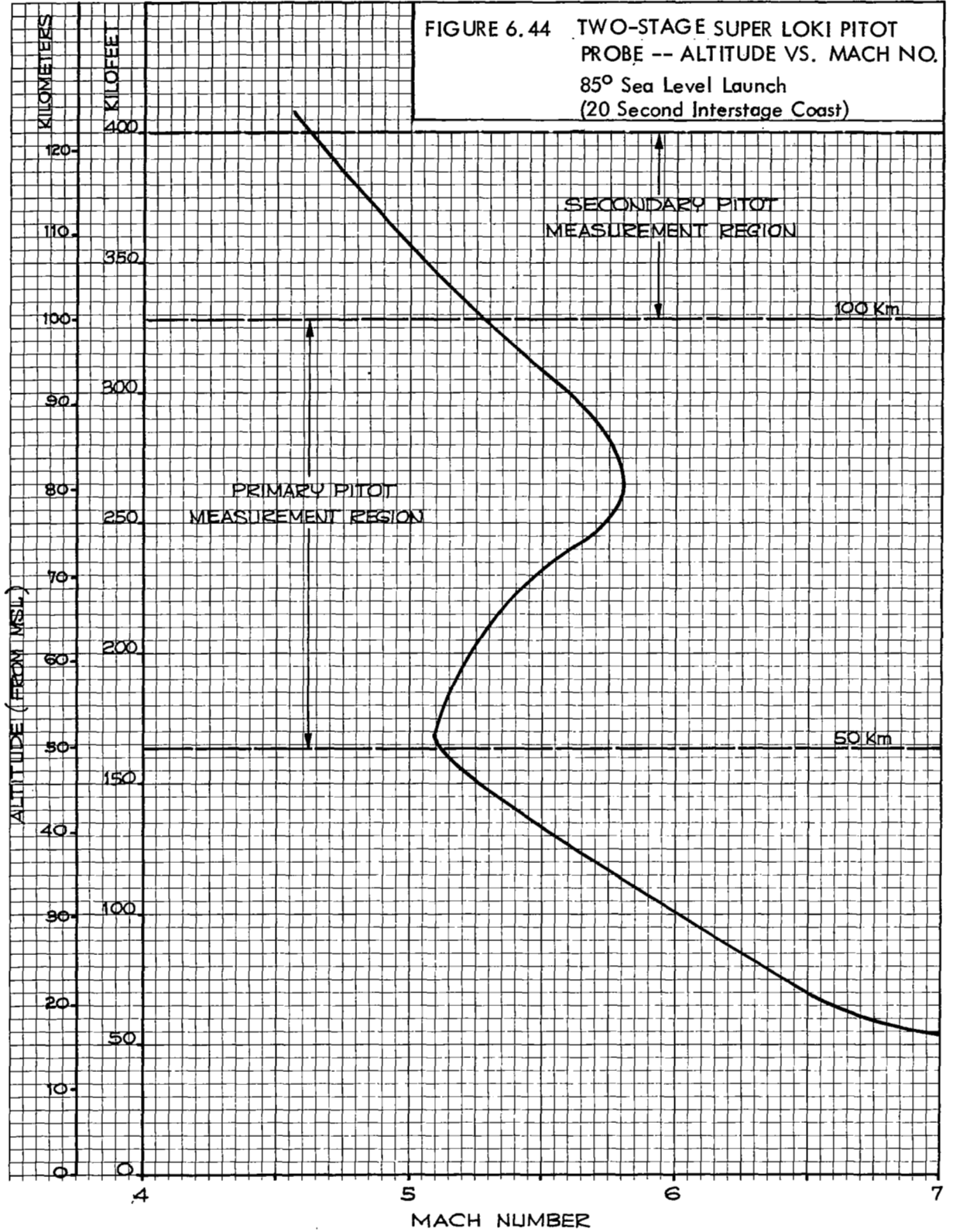


FIGURE 6.44 TWO-STAGE SUPER LOKI PITOT PROBE -- ALTITUDE VS. MACH NO.
 85° Sea Level Launch
 (20 Second Interstage Coast)



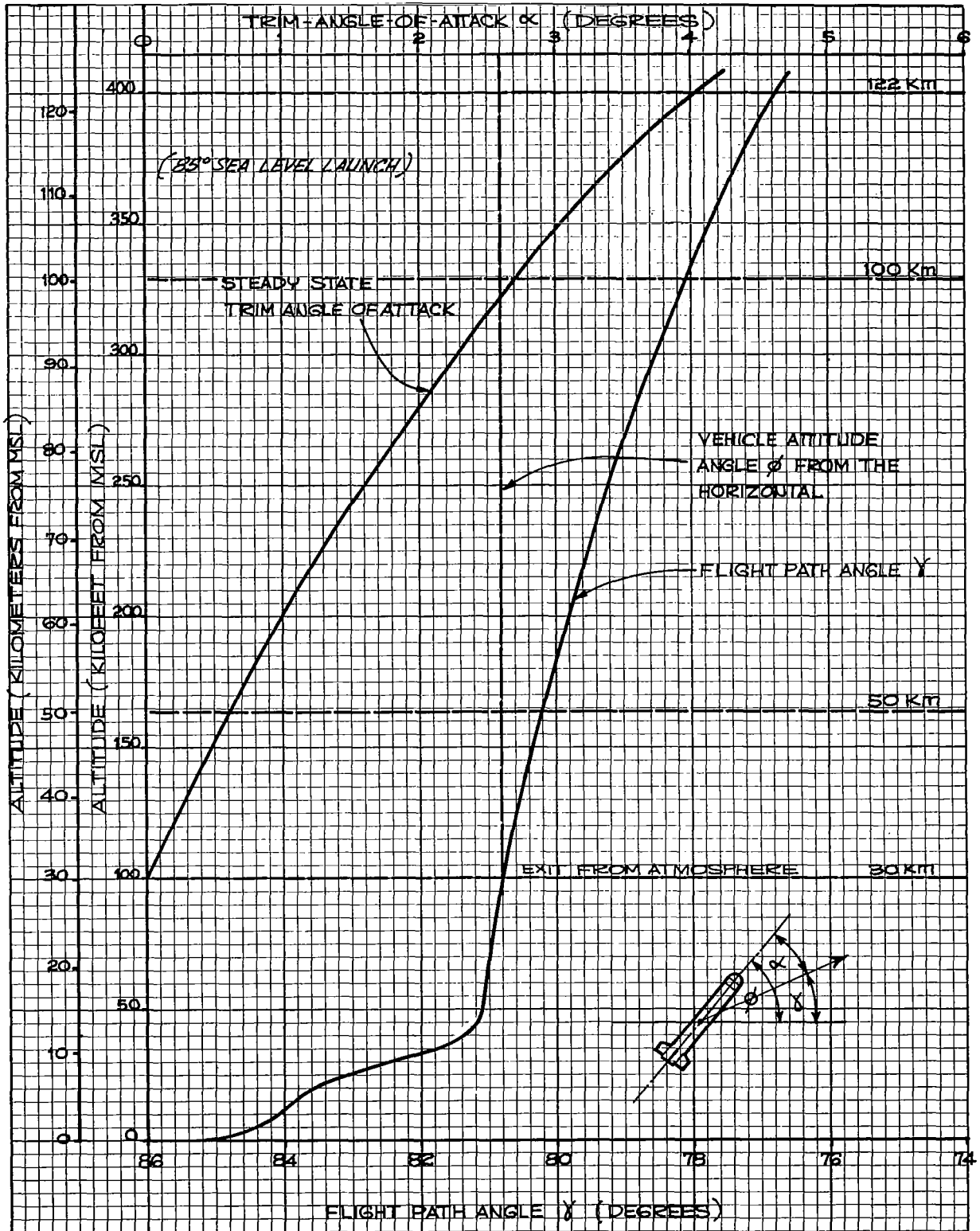


FIGURE 6.45 TWO-STAGE SUPER LOKI PITOT PROBE -- ATTITUDE PARAMETERS VS. ALTITUDE

A copy of the computed trajectory output is presented for the 20-second interstage coast period in Table 6.8.

A preliminary dynamic analysis indicates that the vehicle precession or coning angles should not exceed a 2-degree half cone angle throughout the measurement region. Since the steady state trim angle is less than 3-degrees to 100 km and less than 4-degrees to 120 km, the total angle of attack should be less than 5-degrees to 100 km and less than 6-degrees to 120 km. The vehicle attitude should not deviate more than 11.2 degrees from the vertical throughout the measurement regions. The Mach No. varies between 4.6 and 5.8 throughout the measurement regions.

The results of the preliminary stability analysis for the two-stage Super Loki with the pitot probe payload are presented in Table 6.9 and Figure 6.46. For preliminary design purposes 50 in² fins were assumed for the first stage and 80 in² fins were assumed for the second stage. After reviewing the stability data presented in Figure 6.46, it appears that considerably smaller fins can be used for the first stage.

6.7 System Performance.

6.7.1 General.

A number of system parameters affect the accuracy of the resulting density measurements. The accuracy of the density data is a function of measurement altitude since gage response and accuracy becomes less at the lower pressures, and the flow properties change from continuum to free molecular flow with a transition region between. The overall accuracy of the density measurements at a given altitude can be defined by the systematic errors or biases and the resultant of the random errors. In certain cases the systematic errors can be significantly reduced by applying correction factors to the data. Since the pressure gage errors, which contribute a major error source, are a function of the impact pressure, an estimate of the expected impact pressure profile must first be made to estimate the expected density measurement errors.

6.7.2 Expected Impact Pressures.

The expected impact pressure profile can be estimated by calculating the ideal impact pressure profile based upon the vehicle performance parameters and the 1962 Standard Atmosphere. Since the variations in density about this standard atmosphere are on the order of thirty percent, the impact pressures will vary by about $\pm 30\%$ about this mean profile. The 1962 Standard Atmosphere density and pressure profiles are shown in Figure 6.47. The mean free path profile is shown in Figure 6.48.

TABLE 6.8

TWO DEGREE OF FREEDOM - POINT MASS SIMULATION SPACE DATA CORP

TWO STAGE SUPER LOKI WITH PITOT PROBE PAYLOAD
 10 LB PAYLOAD WEIGHT 4 INCH DIAMETER
 85 DEG QE/SEA LEVEL LAUNCH/20 SECOND COAST

0.050	0.087	85.000	119.860	1.000
1.000	400000.063	0.000	0.000	1000.000
0.000	0.000	0.000	2.000	
82.560	37.200	1.000	160.000	

** OUTPUT UNITS **

FEET	SECONDS	POUNDS(FORCE)	POUNDS(MASS)	DEGREES
------	---------	---------------	--------------	---------

TABLE 6.8 - Continued -

TIME	ALT	VEL	RANGE	MACH	Q	ANG	THRUST	DRAG	MASS	ACC/G	VVERT	VHOR
0.0	0.	0	0.	0.0	0.	85.0	0.	0	119.8	-0.99	0	0
1.0	401.	968	36.	0.9	1101.	84.6	4877.	140	104.1	43.67	964	89
2.0	2161.	2542	202.	2.3	7213.	84.5	1755.	491	82.7	21.94	2531	239
2.1	2542.	2545	238.	2.3	7146.	84.5	0.	486	81.2	-6.54	2534	240

COAST STAGE	A=	0.0873	M=	62.93	T1=	22.1	T2=	2.0	N=	1		
3.0	4630.	2392	437.	2.2	5927.	84.5	0.	269	62.9	-5.27	2381	228
5.0	9082.	2094	871.	1.9	3962.	84.3	0.	192	62.9	-4.04	2083	205
7.0	13010.	1862	1265.	1.8	2769.	84.1	0.	138	62.9	-3.19	1853	189
9.0	16525.	1677	1631.	1.6	2002.	83.9	0.	108	62.9	-2.70	1667	176
11.0	19696.	1516	1974.	1.5	1473.	83.7	0.	82	62.9	-2.29	1507	166
13.0	22570.	1378	2298.	1.3	1103.	83.4	0.	63	62.9	-1.99	1369	157
15.0	25186.	1258	2607.	1.2	838.	83.0	0.	48	62.9	-1.76	1249	151
17.0	27575.	1150	2904.	1.1	644.	82.7	0.	36	62.9	-1.57	1141	145
19.0	29760.	1055	3192.	1.1	500.	82.2	0.	24	62.9	-1.37	1045	141
21.0	31766.	972	3472.	1.0	394.	81.7	0.	14	62.9	-1.21	962	139
22.1	32802.	930	3625.	0.9	347.	81.4	0.	12	62.9	-1.17	920	137

POWER ON	TM=	1.015	FO=	0.0	WM=	1.000	W=	25.6	T2=	1.00		
22.1	32802.	930	3625.	0.9	347.	81.4	0.	12	62.9	-1.17	920	137
23.1	34544.	2969	3890.	3.0	3313.	81.2	4951.	103	47.2	99.24	2935	449
24.1	39520.	7316	4656.	7.6	16093.	81.2	1782.	297	25.8	80.75	7231	1115
24.2	40613.	7374	4825.	7.6	15515.	81.2	0.	287	24.3	-11.21	7288	1125

COAST STAGE	A=	0.0873	M=	25.63	T1=	*****	T2=	2.0	N=	0		
25.1	46671.	7066	5763.	7.3	10660.	81.1	0.	217	25.6	-9.48	6983	1082
27.1	60154.	6626	7863.	6.8	4919.	81.1	0.	100	25.6	-4.90	6546	1024
29.1	72984.	6382	9881.	6.6	2452.	81.0	0.	50	25.6	-2.93	6304	996
31.1	85427.	6227	11858.	6.4	1281.	80.9	0.	26	25.6	-2.00	6149	982
33.1	97608.	6115	13813.	6.1	694.	80.8	0.	14	25.6	-1.53	6036	974
35.1	109589.	6025	15757.	5.9	382.	80.7	0.	7	25.6	-1.28	5946	969
37.1	121402.	5947	17695.	5.7	213.	80.6	0.	4	25.6	-1.15	5867	967
39.1	133353.	5873	19677.	5.5	121.	80.5	0.	2	25.6	-1.07	5793	966
41.1	144871.	5805	21608.	5.3	72.	80.4	0.	1	25.6	-1.03	5725	965
43.1	156254.	5740	23538.	5.2	44.	80.3	0.	1	25.6	-1.01	5658	964

TABLE 6.8 - Continued -

45.1	167504.	5675	25468.	5.1	28.	80.2	0.	0	25.6	-0.99	5592	964
47.1	178625.	5611	27396.	5.1	18.	80.1	0.	0	25.6	-0.98	5528	964
49.1	189617.	5548	29325.	5.2	11.	79.9	0.	0	25.6	-0.97	5464	964
51.1	200481.	5485	31253.	5.3	7.	79.8	0.	0	25.6	-0.97	5400	963
53.1	211218.	5423	33181.	5.3	5.	79.7	0.	0	25.6	-0.96	5337	963
55.1	221828.	5361	35109.	5.4	3.	79.6	0.	0	25.6	-0.96	5273	963
57.1	232312.	5299	37037.	5.5	2.	79.5	0.	0	25.6	-0.96	5210	963
59.1	242670.	5237	38965.	5.6	1.	79.3	0.	0	25.6	-0.96	5147	963
61.1	252901.	5175	40893.	5.7	0.	79.2	0.	0	25.6	-0.95	5084	963
63.1	263007.	5113	42820.	5.8	0.	79.1	0.	0	25.6	-0.95	5021	963
65.1	272987.	5051	44749.	5.7	0.	78.9	0.	0	25.6	-0.95	4959	963
67.1	282841.	4990	46677.	5.6	0.	78.8	0.	0	25.6	-0.95	4896	963
69.1	292570.	4928	48605.	5.6	0.	78.7	0.	0	25.6	-0.95	4833	963
71.1	302174.	4867	50533.	5.4	0.	78.5	0.	0	25.6	-0.95	4771	963
73.1	311652.	4806	52461.	5.4	0.	78.4	0.	0	25.6	-0.95	4708	963
75.1	321006.	4745	54389.	5.3	0.	78.2	0.	0	25.6	-0.94	4646	963
77.1	330235.	4684	56317.	5.2	0.	78.1	0.	0	25.6	-0.94	4583	964
79.1	339339.	4623	58245.	5.1	0.	77.9	0.	0	25.6	-0.94	4521	964
81.1	348318.	4562	60174.	5.1	0.	77.7	0.	0	25.6	-0.94	4459	964
83.1	357172.	4501	62102.	5.0	0.	77.6	0.	0	25.6	-0.94	4396	964
85.1	365903.	4440	64030.	4.9	0.	77.4	0.	0	25.6	-0.94	4334	964
87.1	374508.	4379	65958.	4.9	0.	77.2	0.	0	25.6	-0.94	4272	964
89.1	382990.	4319	67887.	4.8	0.	77.1	0.	0	25.6	-0.94	4210	964
91.1	391347.	4258	69815.	4.7	0.	76.9	0.	0	25.6	-0.93	4148	964
93.1	399581.	4198	71743.	4.6	0.	76.7	0.	0	25.6	-0.93	4086	964
95.1	407690.	4138	73671.	4.6	0.	76.5	0.	0	25.6	-0.93	4024	964

TABLE 6.8 - Continued

EXOATMOSPHERE RESULTS									
TIME	ALT	RANGE	ALT(KM)	RANGE(KM)	TIME	ALT	RANGE	ALT(KM)	RANGE(KM)
0.108219E	03	0.457690E	06	0.861878E	05	0.139504E	03	0.262701E	02
0.122946E	03	0.507690E	06	0.997758E	05	0.154744E	03	0.304117E	02
0.140147E	03	0.557690E	06	0.116255E	06	0.169984E	03	0.354346E	02
0.161733E	03	0.607690E	06	0.136259E	06	0.185224E	03	0.415321E	02
0.195609E	03	0.657690E	06	0.167802E	06	0.200464E	03	0.511464E	02
0.293449E	03	0.607690E	06	0.257176E	06	0.185224E	03	0.783876E	02
0.315035E	03	0.557690E	06	0.277181E	06	0.169984E	03	0.844850E	02
0.332236E	03	0.507690E	06	0.293660E	06	0.154744E	03	0.895079E	02
0.346963E	03	0.457690E	06	0.307248E	06	0.139504E	03	0.936496E	02
0.360043E	03	0.407690E	06	0.319764E	06	0.124264E	03	0.974646E	02
0.371925E	03	0.357690E	06	0.331120E	06	0.109024E	03	0.100925E	03
0.382884E	03	0.307690E	06	0.341589E	06	0.937843E	02	0.104116E	03
0.393104E	03	0.257690E	06	0.351350E	06	0.785443E	02	0.107092E	03
0.402713E	03	0.207690E	06	0.360529E	06	0.633042E	02	0.109889E	03
0.411808E	03	0.157690E	06	0.369222E	06	0.480642E	02	0.112539E	03
0.420461E	03	0.107690E	06	0.377786E	06	0.328241E	02	0.115149E	03
0.428730E	03	0.576905E	05	0.385687E	06	0.175841E	02	0.117557E	03
0.436660E	03	0.769050E	04	0.393536E	06	0.234407E	01	0.119950E	03
0.444287E	03	0.423095E	05	0.401082E	06	0.128959E	02	0.122250E	03

ORBITAL PARAMETERS

E	A	P	QC
0.998608E	00	0.108074E	08
0.300622E	05	0.259507E	-01

APOGEE CONDITIONS

TIME	ALT	RANGE	ALT(KM)	RANGE(KM)
0.227591E	03	0.673105E	06	0.196718E
0.205163E	03	0.599598E	02	

IMPACT CONDITIONS

TIME	ALT	RANGE	ALT(KM)	RANGE(KM)
0.120353E	03			

TABLE 6.9

TWO STAGE SUPER LOKI SECOND STAGE / FIN AREA 80 SQ.IN.

BODY NO.	2	LENGTH =	74.00 IN.	DIAMETER=	4.00 IN.	CP STA.=	37.00
BODY NO.	3	LENGTH =	10.00 IN.	DIAMETER=	4.00 IN.	CP STA.=	79.00
OGIVE NO.	4	DIAMETER=	4.00 IN.	CP STA.=	89.00		
FIN SET NO.	6	AREA =	80.00 SQ.IN.	CP STA.=	3.33 IN.		

REF.AREA= 12.58 SQ.IN. NEP STA = 99.20 IN.

MACH NO.	CNALPHA (1/RAD)	CNALPHA (1/DEG)	C.P. LOC. (STATION)	C.P. LOC. (IN FWD NEP)
1.25	37.59	0.6562	9.61	89.58
1.50	26.43	0.4613	12.26	86.93
1.75	21.39	0.3733	14.37	84.82
2.00	18.36	0.3205	16.19	83.00
2.25	16.30	0.2845	17.82	81.37
2.50	14.78	0.2580	19.31	79.88
2.75	13.61	0.2375	20.68	78.51
3.00	12.67	0.2212	21.96	77.23
3.25	11.90	0.2078	23.17	76.02
3.50	11.26	0.1966	24.30	74.89
3.75	10.71	0.1870	25.37	73.82
4.00	10.24	0.1788	26.38	72.81
4.25	9.83	0.1717	27.34	71.85
4.50	9.47	0.1654	28.25	70.94
4.75	9.15	0.1598	29.12	70.07
5.00	8.87	0.1548	29.95	69.24
5.25	8.61	0.1503	30.74	68.45
5.50	8.38	0.1463	31.50	67.69
5.75	8.17	0.1426	32.23	66.96
6.00	7.98	0.1392	32.93	66.26

TABLE 6.9 - Continued -

6.25	7.80	0.1362	33.60	65.59
6.50	7.64	0.1333	34.24	64.95
6.75	7.49	0.1307	34.86	64.33
7.00	7.35	0.1283	35.46	63.73
7.25	7.22	0.1260	36.03	63.16
7.50	7.10	0.1239	36.59	62.60
7.75	6.99	0.1220	37.12	62.07
8.00	6.88	0.1201	37.64	61.55
8.25	6.78	0.1184	38.13	61.06
8.50	6.69	0.1168	38.62	60.57
8.75	6.60	0.1153	39.08	60.11
9.00	6.52	0.1138	39.53	59.66
9.25	6.44	0.1125	39.97	59.22
9.50	6.37	0.1112	40.39	58.80
9.75	6.30	0.1100	40.80	58.39
10.00	6.23	0.1088	41.20	57.99

TABLE 6.9 - Continued -

TWO STAGE SUPER LOKI BOOSTER FIN AREA 50 SQ. IN.

FIN SET NO.	1	AREA =	50.00 SQ. IN.	CP STA.=	3.33 IN.		
BODY NO.	4	LENGTH =	74.00 IN.	DIAMETER=	4.00 IN.	CP STA.=	37.00
BODY NO.	5	LENGTH =	74.00 IN.	DIAMETER=	4.00 IN.	CP STA.=	111.00
FIN SET NO.	6	AREA =	70.00 SQ. IN.	CP STA.=	77.11 IN.		
BODY NO.	7	LENGTH =	10.00 IN.	DIAMETER=	4.00 IN.	CP STA.=	153.00
OGIVE NO.	8	DIAMETER=	4.00 IN.	CP STA.=	163.00		

REF. AREA = 12.58 SQ. IN. NEP STA = 173.20 IN.

MACH NO.	CN ALPHA (1/RAD)	CN ALPHA (1/DEG)	C.P. LOC. (STATION)	C.P. LOC. (IN FWD NEP)
1.20	62.68	1.0940	51.73	121.46
1.39	44.10	0.7698	53.99	119.20
1.59	35.71	0.6233	55.78	117.41
1.79	30.65	0.5350	57.33	115.86
1.99	27.19	0.4746	58.73	114.46
2.19	24.63	0.4299	60.02	113.17
2.39	22.65	0.3953	61.21	111.98
2.59	21.06	0.3675	62.33	110.86
2.79	19.75	0.3447	63.39	109.80
2.99	18.65	0.3255	64.39	108.80
3.19	17.71	0.3091	65.35	107.84
3.39	16.90	0.2950	66.26	106.93
3.59	16.19	0.2826	67.13	106.06
3.79	15.57	0.2717	67.96	105.23
3.99	15.01	0.2620	68.76	104.43

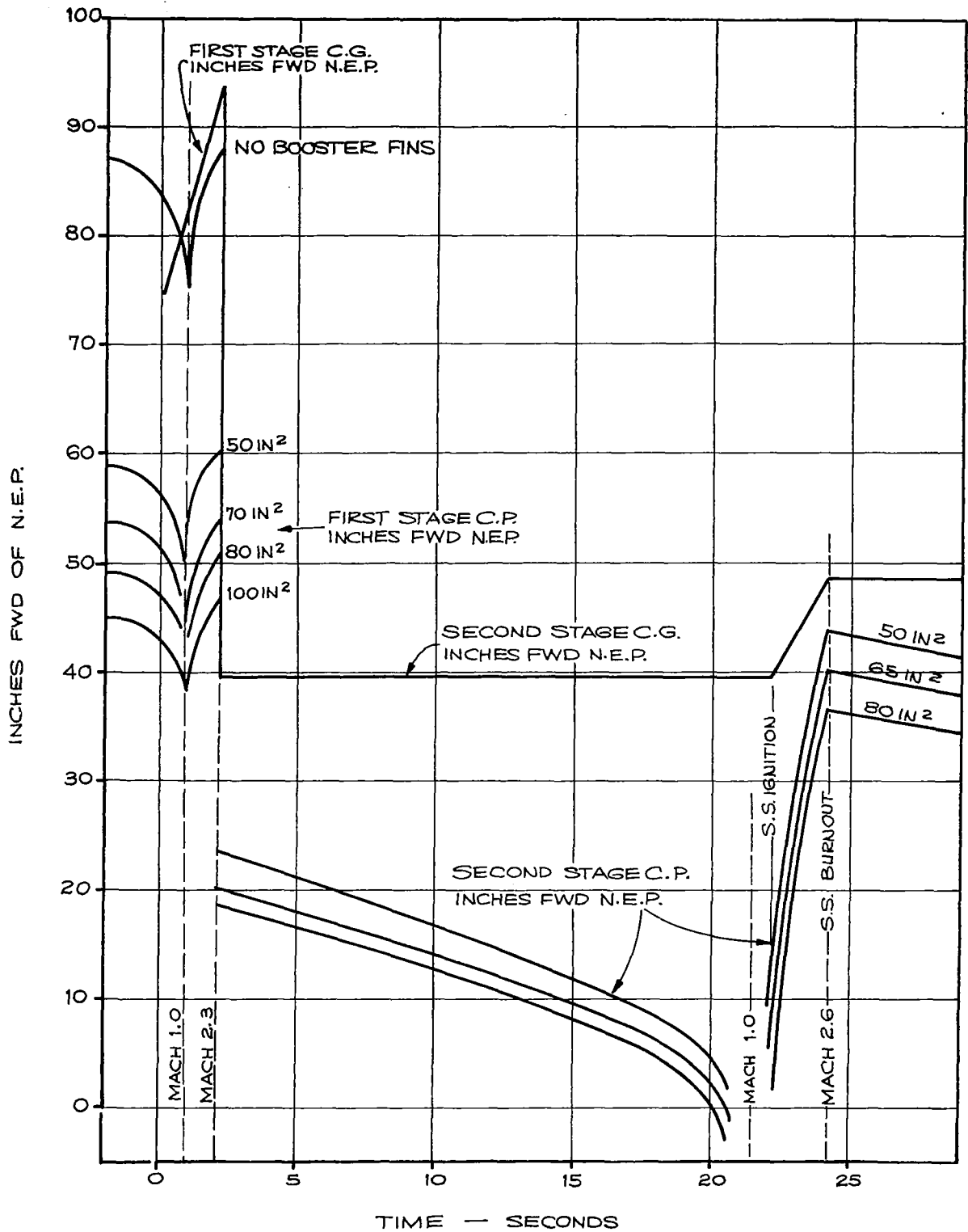


FIGURE 6.46 TWO-STAGE SUPER LOKI PITOT PROBE VEHICLE STATIC STABILITY DATA

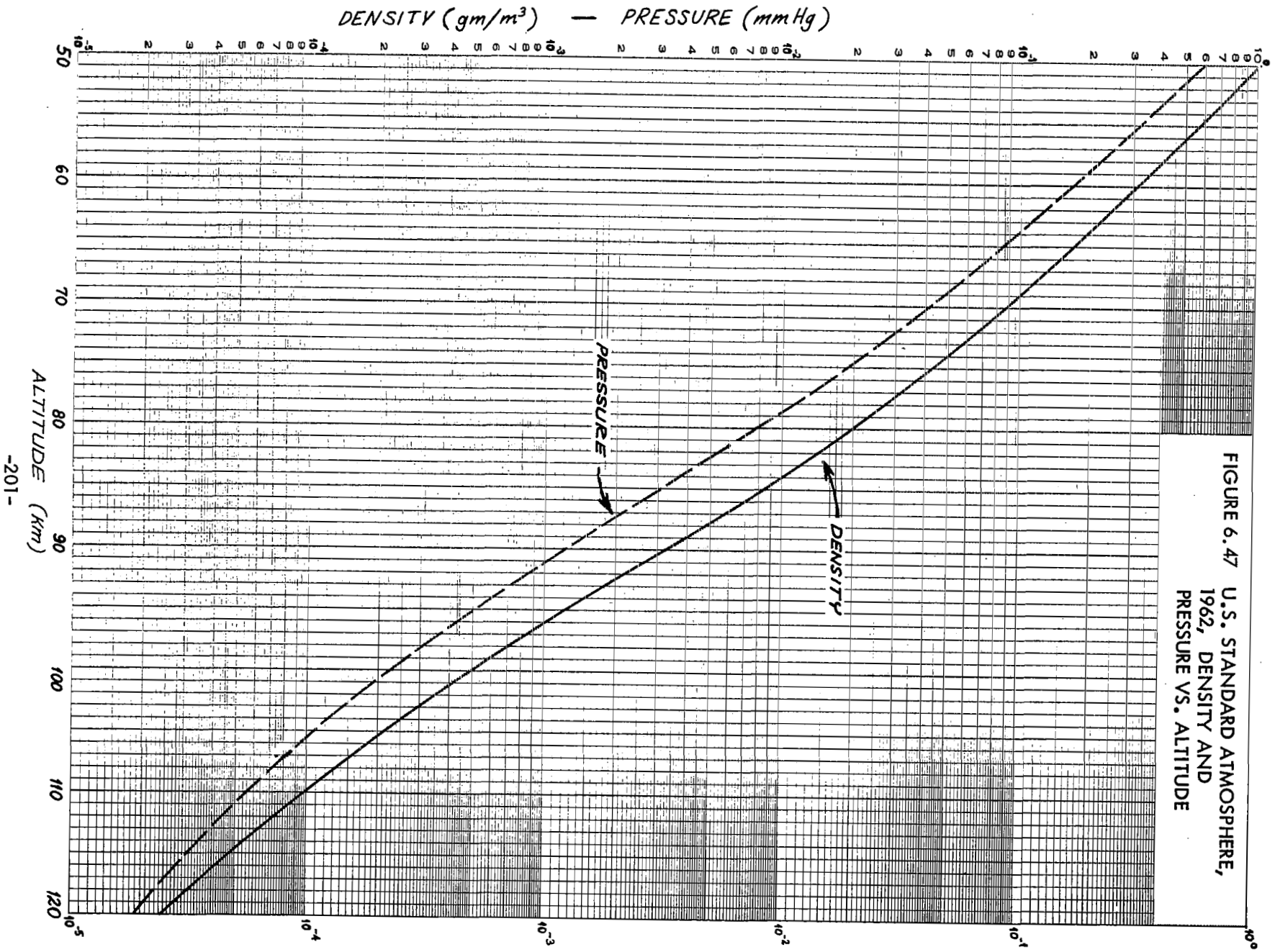


FIGURE 6.47 U.S. STANDARD ATMOSPHERE,
1962, DENSITY AND
PRESSURE VS. ALTITUDE

MEAN FREE PATH (cm)

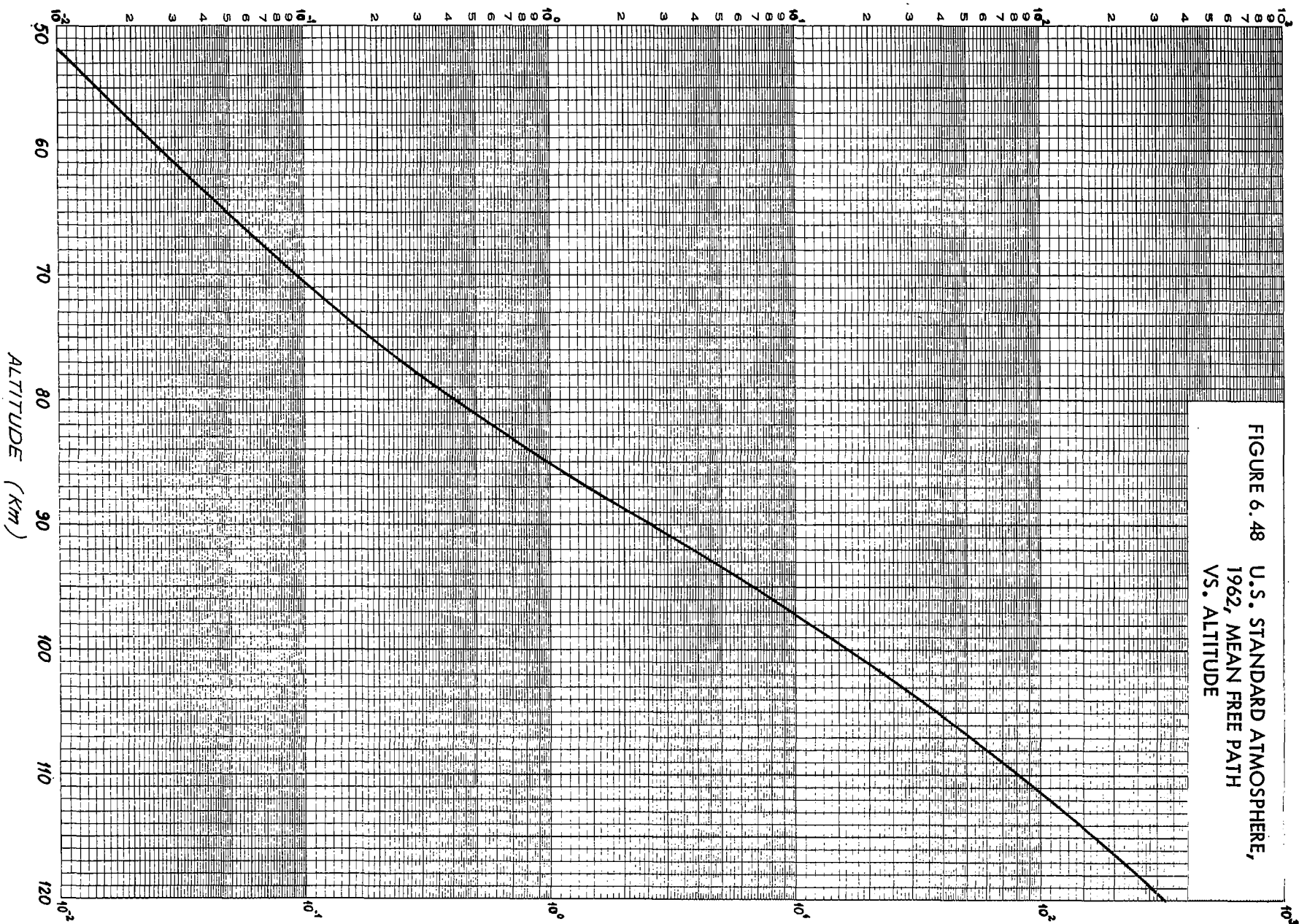


FIGURE 6. 48 U.S. STANDARD ATMOSPHERE,
1962, MEAN FREE PATH
VS. ALTITUDE

In the continuum flow region, where the impact chamber diameter of 9.05 cm is larger than the atmosphere mean free path, the ideal impact pressure may be computed by equation (11). When the mean free path becomes larger than the impact chamber diameter, the normal shock wave disappears, and thermal transpiration governs the pressure relationships as described by equations (12) and (13). This is the free molecular flow region. A simplifying expression as used by Ainsworth, Fox and LaGow (reference 23) for calculating density in the free molecular flow region is:

$$\rho = \frac{P_{O_2}}{\sqrt{\pi} \mu' |V| \cos \alpha}$$

where μ' = most probable molecular velocity

The ideal impact pressure is then given by

$$P_{O_2} = 1.773 \rho_1 \mu' V$$

for small angles-of-attack, i. e., below 7-degrees.

If the input units used are as follows:

$$\rho \text{ ————— in } \frac{\text{gm}}{\text{m}^3}$$

$$\mu' \text{ ————— in } \frac{\text{m}}{\text{sec}}$$

$$V \text{ ————— in } \frac{\text{km}}{\text{sec}}$$

then the resulting value for P_{O_2} must be multiplied by 0.752×10^{-2} to obtain P_{O_2} in mm Hg. The above calculations were made for the proposed pitot probe and the data is presented in Table 6.10.

The expected ideal impact pressure profile is plotted in Figure 6.49. The flow regime undergoes a transition from continuum to free molecule at about 97 km. The maximum expected impact pressure is about 2.80×10^1 mm Hg at 50 km and the minimum is about 1.52×10^{-4} mm Hg at 120 km.

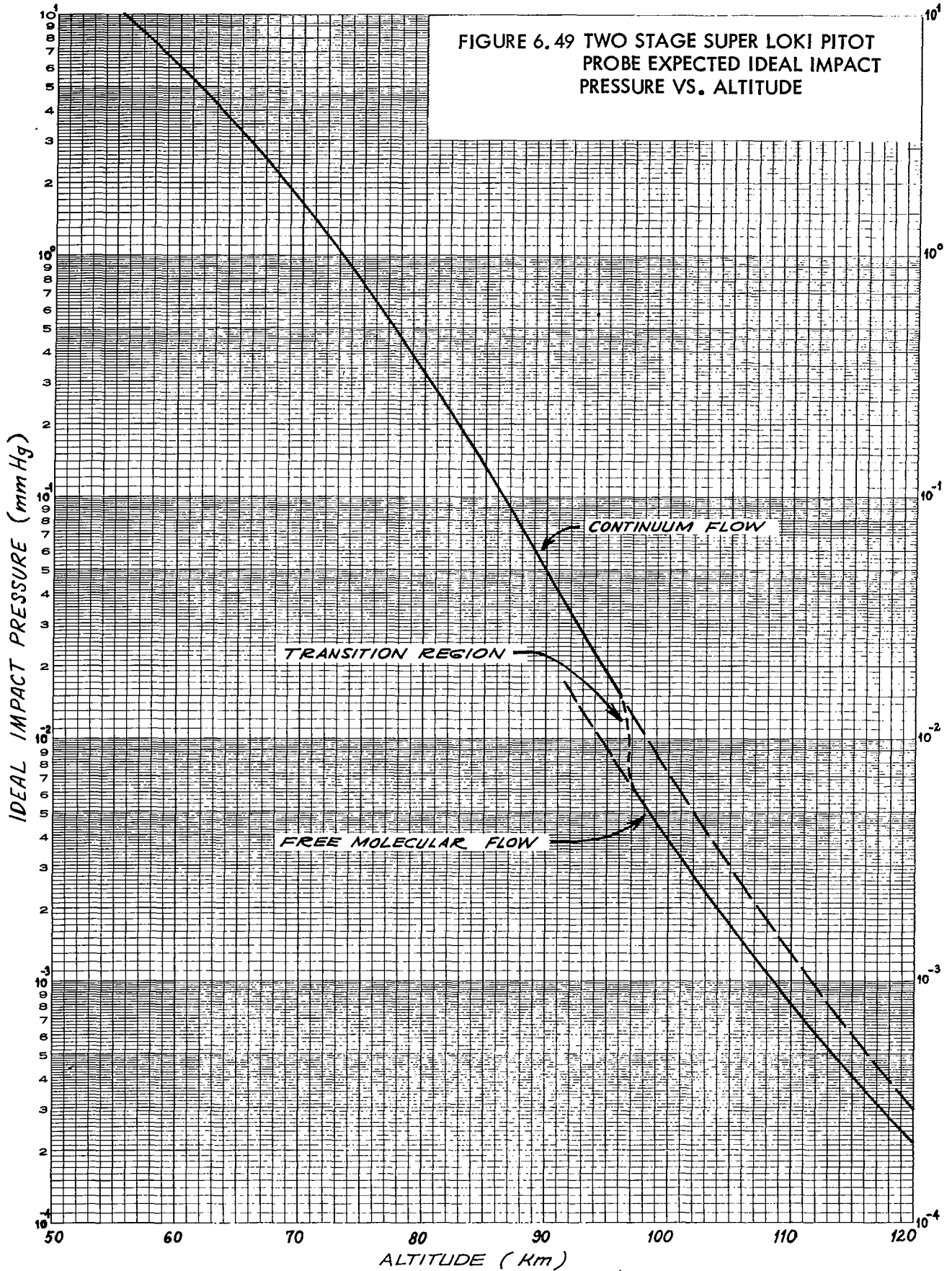
Table 6.10 Pitot Probe Density Measurement Parameters

Altitude (km)	50	60	70	80
1962 Std. Density (gm/m ³)	1.027×10^0	3.059×10^{-1}	8.754×10^{-2}	1.999×10^{-2}
1962 Std. Pressure (mm Hg)	5.984×10^{-1}	1.685×10^{-1}	4.141×10^{-2}	7.775×10^{-3}
Vehicle Velocity (km/sec)	1.730	1.670	1.615	1.540
Angle-of-Attack (deg)	0.60	0.96	1.34	1.78
Mean Free Path (cm)	7.91×10^{-3}	2.66×10^{-2}	9.28×10^{-2}	4.07×10^{-1}
Most Probable Molecular Velocity (m/sec)	444.79	432.39	400.74	363.4
Ideal Impact Pressure:				
Continuum Flow (mm Hg)	2.160×10^1	6.00×10^0	1.613×10^0	3.34×10^{-1}
Free Molecule Flow (mm Hg)	-	-	-	1.490×10^{-1}
Ratio of Impact Pressure to Static Pressure for Continuum Flow	36.0	35.6	39.0	42.9
Ratio of Impact Pressures for Continuum Flow: Free Molecule Flow	-	-	-	2.24
Pitot Cavity Diameter	9.05 cm			
Orifice Diameter	1.78 cm			

Table 6.10 Pitot Probe Density Measurement Parameters
Continued

Altitude(km)	90	100	110	120
1962 Std. Density (gm/m ³)	3.170×10^{-3}	4.974×10^{-4}	9.829×10^{-5}	2.436×10^{-5}
1962 Std. Pressure (mm Hg)	1.233×10^{-3}	2.256×10^{-4}	5.516×10^{-5}	1.891×10^{-5}
Vehicle Velocity (km/sec)	1.490	1.430	1.350	1.300
Angle-of-Attack (deg)	2.22	2.70	3.22	3.90
Mean Free Path (cm)	2.56×10^0	1.63×10^1	8.15×10^1	3.23×10^2
Most Probable Molecular Velocity (m/sec)	363.4	392.4	436.5	513.4
Ideal Impact Pressure:				
Continuum Flow (mm Hg)	4.95×10^{-2}	7.18×10^{-3}	1.268×10^{-3}	2.940×10^{-4}
Free Molecule Flow (mm Hg)	2.290×10^{-2}	3.710×10^{-3}	7.720×10^{-4}	2.165×10^{-4}
Ratio of Impact Pressure to Static Pressure for Continuum Flow	40.2	31.6	23.0	15.5
Ratio of Impact Pressures for Continuum Flow: Free Molecule Flow	2.16	1.93	1.64	1.35

FIGURE 6.49 TWO STAGE SUPER LOKI PITOT PROBE EXPECTED IDEAL IMPACT PRESSURE VS. ALTITUDE



6.7.3 Systematic Errors.

The major systematic errors are associated with the fundamental flow characteristics and to a large degree can be significantly reduced by applying correction factors. However, in general, the larger the error or bias, the larger the residual error after the correction is applied.

A primary systematic error source is viscous effects which are a function of the orifice size. For the chosen orifice these effects cause the measure impact pressure to be lower than the ideal by less than 0.3% in the continuum flow region. Viscous corrections are about 1% at 85 km and 9% in the transition flow region at about 97 km. This correction becomes less as altitude is increased above the transition region to a value of about 5% at 100 km. The reduction in this bias occurs when the mean free path of the gas in the impact chamber is greater than the interior dimension of the cavity and when the orifice diameter is small compared with the cavity's interior dimension so that the gas entering from the outside region has adequate time to assume the chamber temperature.

A second correction to the measured impact pressure is required because of the high gas temperatures which exist in the vicinity of the nose of the pitot tube at high Mach numbers. These high temperatures cause a reduction in the ratio of the specific heats which is known as caloric imperfection, and which causes the measured impact pressure for a given ambient atmospheric density and pressure to be greater than the ideal impact pressure. It is the ideal impact pressure which is computed by using the Rayleigh pitot-tube equation and which is required in Equation 11 for computing density. For the particular Mach numbers of interest here, the values of the measured impact pressure are determined to be greater than the ideal impact pressure by approximately 0.8 percent from 50 to 80 km. Since this error affected computations employing Equation 11, corrections can be made to the computed density profiles and these should be generally 0.5 percent or less.

Systematic errors in the gage, gage electronics and telemetry system should be negligible, except for temperature/effects, since the complete system will be calibrated under vacuum conditions. Aerodynamic heating temperature rise of the impact chamber and gage must be minimized and taken into account during the development phases of the program. It is expected that the temperature rise will be repeatable, predictable and small in value.

Systematic errors in tracking are not particularly troublesome in the critical calculation of vehicle velocity which is derived from differences rather than the absolute values. The absolute altitude may be in error by as much as 0.03 km, but this should not be an important effect.

Angle-of-attack biases due to atmospheric winds, flight path angle and vehicle coning are negligible due to the relatively vertical vehicle attitude and small coning angles through the measurement regions.

Gage and impact chamber flow response characteristics will govern the systematic errors due to the system time constant. The current Ames gage has a time constant of about 2 seconds at 10^{-4} mm Hg. This appears to be a bit long, but indications are that a modified gage design could improve this parameter.

6.7.4 Radom Errors.

The major error contribution will be due to the gage random rms error. This error is plotted vs altitude for the proposed pitot probe in Figure 6.50. The gage rms error should be less than 2-percent up to 100 km and less than 2.5-percent to 120 km.

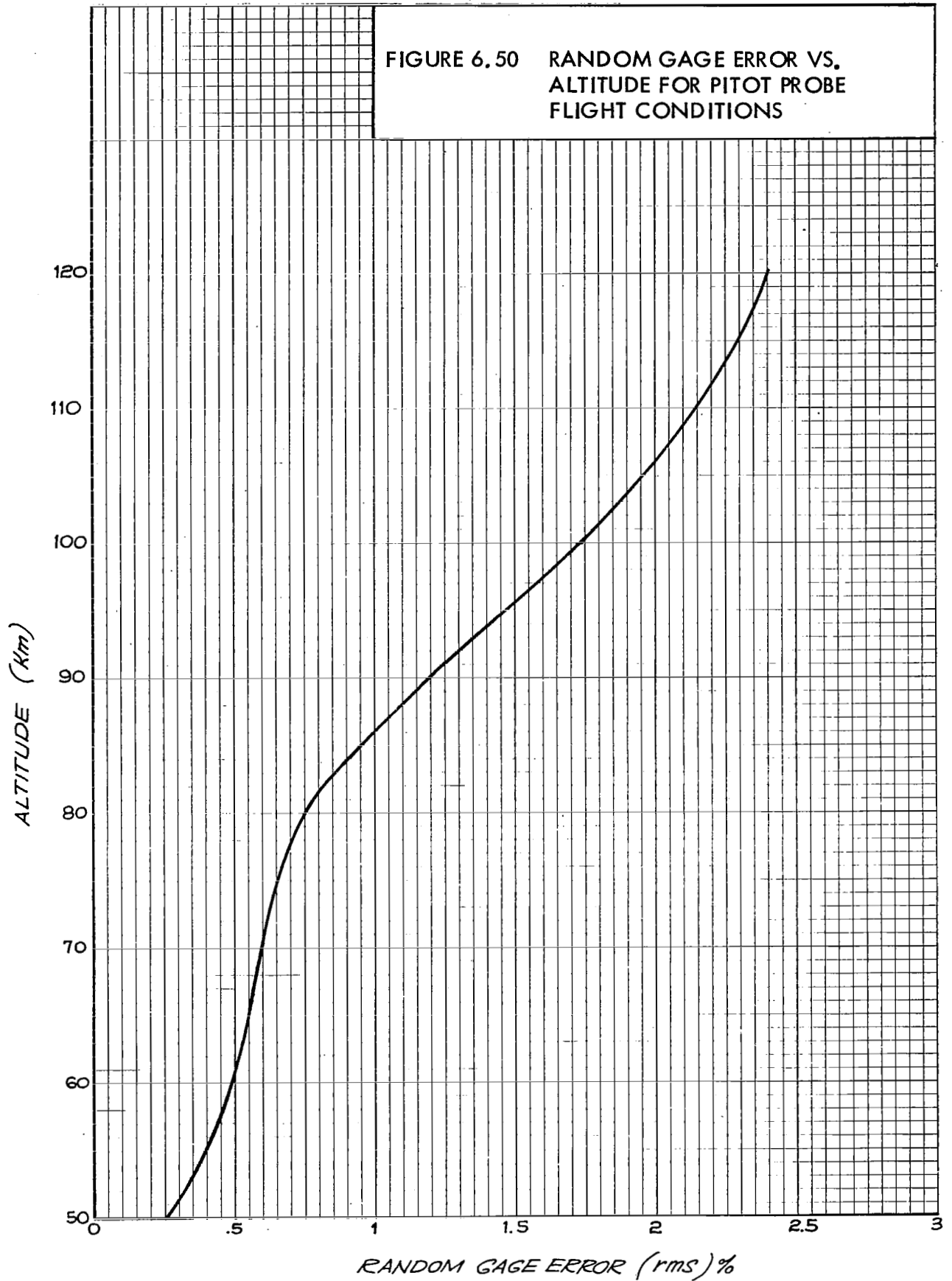
The only other significant random error will be in the tracking. Since the vehicle will be in essentially a drag-free trajectory through the measurement regions and above, the random tracking errors may be considered to have an insignificant effect upon either the velocity or altitude position. This is true because the entire set of vehicle position data points may be used to estimate the one unique drag-free (or vacuum) trajectory which is completely determined by any one altitude and velocity point. Thus, statistical averaging or curve fitting may be employed to use all the tracking data above 50 km to determine the one unique trajectory. This procedure should reduce the random tracking error to a negligible value.

6.8 Inflatable Sphere Sensor.

A lightweight inflatable sphere will be deployed from the pitot probe vehicle at about an altitude of 150 km after the ram pressure measurements have been completed. This sphere may be tracked by lower resolution radars than the AN/FPS-16 for wind data. If an FPS-16 radar or the equivalent is available, redundant density measurements can also be obtained.

To optimize the sphere for wind measurement it will be made as large and as light as possible. Packaging volume and structural strength will determine the size limit. The sphere will be aluminized instead of using corner reflectors to minimize its weight. The sphere will be fabricated from 1/4-mil mylar and will be inflated with a capsule of isopentane during deployment. A tradeoff study will be made to optimize the size of the sphere with the packaging volume and length somewhat flexible in the early design phases of the program.

FIGURE 6.50 RANDOM GAGE ERROR VS. ALTITUDE FOR PITOT PROBE FLIGHT CONDITIONS



At remote sites where radar is not available, a lightweight GMD-2 transponder tracking beacon may be used within the sphere for wind data. The instrument could be located inside an inflatable strut within the sphere, and the battery weight could be minimized by requiring tracking from release to only 50 km. Thus, the instrument turn-on time would be limited to only about ten minutes. The development of this transponder payload is within the current state-of-the-art.

6.9 System Operation.

At the launch site the first stage will be slid onto a simple rail launcher, and then the second stage motor will be slip-fitted into the interstage coupling. The payload sections will have been calibrated and assembled at the factory, and all that will be necessary at the launch site is a brief prelaunch checkout. This is performed by electrically firing the vacuum getter and operating the gage electronics and telemetry on external power through an umbilical connection. After establishing the gage low pressure calibration point and the base leg for the GMD-2 ranging signal, the payload may be switched off and assembled to the vehicle. Prior to launch the rocket motor igniters and payload pyrotechnic delay initiators are electrically hooked up and the payload instrumentation is switched to internal power. The system is then ready for launch.

During flight a number of sequential events take place as follows:

<u>Time</u> <u>(sec)</u>	<u>Event</u>
0	Lift-off and initiation of all pyrotechnic devices.
2	First stage burnout and separation of second stage.
22	Second stage ignition.
24	Second stage burnout.
44	Nosecone ejection, antennae erection and initiation of ram pressure measurements (50 km).
91	Ram pressure measurements become insensitive (120 km).
120	Payload section separation and deployment of inflatable sphere (150 km).
220	Sphere apogee (200 km).
600	Sphere down to 50 km.

The entire data run for both density and winds is gathered in ten minutes.

REFERENCES

1. Staffanson, F. L.; Alsaji, S.; and Fazzio, R., Entry Length for the Rocket Meteorological Radiation Shield, NASA CR-1200, October 1968.
2. Staffanson, F. L., Theoretical Comparison of Beads, Wires and Films as Rocketsonde Temperature Sensors in the Mesosphere, NASA CR-1286, February 1969.
3. Haak, E. L.; and Noreen, R. A., Wind Tunnel Calibration of the "Arcasonde 1-A" at Simulated Altitudes Between 35 and 56 km, NASA CR-66638, May 1968.
4. Morrissey, J. F., Rocketsonde/Radiosonde Temperature Compatability, Paper Presented at 4th National Conference on Aerospace Meteorology, May 4-7, 1970, Las Vegas, Nevada.
5. McWatters, K. D.; and Peterson, J. W., Adequacy of the Passive Inflated Falling Sphere Technique, Paper Presented at Langley Research Center Hampton, Virginia, Sept 23-24 1969, NASA SP-219.
6. Rigali, D. J.; and Touryan, K. J., Analysis of Pressure Measurements Taken at Altitudes Between 30 and 90 km by Cone-Cylinder Pitot-Static Probes, Sandia Laboratories, SC-RR-67-251, June 1967.
7. LeBel, P. J., Analysis of the Gamma-Ray-Backscatter Technique for Direct Measurement of the Density of the Martian Atmosphere, NASA TN D-5431, September 1969.
8. Sellers, B.; and Ziegler, C. A., Development of an Atmospheric Density Gauge Based on the Bremsstrahlung Effect, DDC AD 652-236, April 1965.
9. Gilmour, A. S., Jr., Radio-Frequency Mass Spectrometers and Their Applications in Space, Paper Presented at Aerospace Support Conference, Washington, D. C., August 1963.
10. Krueger, A. J.; and McBride, W. R., Rocket Ozondesonde (ROCOZ)-Design and Development, NWC TP-4512, July 1968.
11. Krueger, A. J.; and McBride, W. R., Sounding Rocket-OGO-IV Satellite Ozone Experiment: Rocket Ozonesonde Measurements, NWC TP-4667, December 1968.

REFERENCES

12. Krueger, A.J., Rocket Measurements of Ozone over Hawaii, Paper Presented par J. London au X^e Symposium international de l'Ozone, Monaco, 2-7 September 1968.
13. Hudgins, J.I.; and Lease, J.R., The Tone Range/Telemetry Interferometer Tracking System for Support of Sounding Rocket Payloads, Paper Presented at Langley Research Center, Hampton, Virginia, September 23-24, 1969, NASA SP-219.
14. Harmantas, C., Winds Aloft Measurements Through LORAN C Navigation Aid, ESSA Technical Memorandum WBTM EDL 6, October 1968.
15. Ellett, D.M., Pressure Distribution on Sphere Cones, SC-RR-64-1796, January 1965.
16. Van Dyke, M.D.; and Gorden, H.D., Supersonic Flow About a Family of Blunt Axisymmetric Bodies, NASA TR R-1, 1959.
17. Inouye, M.; and Lomax, H., Comparison of Experimental and Numerical Results for the Flow of a Perfect Gas About Blunt-Nosed Bodies, NASA TN-D-1426, September 1962.
18. Gravalos, F.G.; Edelfelt, I.H.; and Emmons, H.W., The Supersonic Flow About a Blunt Body of Revolution for Gases at Chemical Equilibrium, Proc. IX Int. Astron. Cong., Amsterdam, Vol. 1; August 1958, pp 312-322.
19. Vaglio-Laurin, R.; and Trella, M., A Study of Flow Fields About Some Typical Blunt-Nosed Slender Bodies, PIBAL Report No. 623.
20. Dimeff, J.; Lane, J.; and Coon, G., Rev. Sci. Instr., Vol. 33, p 804, 1962.
21. Technology Utilization Report, Technology Utilization Division, Vibrating Diaphragm Pressure Transducer, NASA SP-5020.
22. Dimeff, J.; Lane, J.W.; Deboo, G.J.; and Hendlund, R.C., A Vibrating Diaphragm Pressure Measuring System, Ames Research Center, NASA (To Be Published)
23. Ainsworth, J.E.; Fox, D.F.; and LaGow, H.E., Measurement of Upper-Atmosphere Structure by Means of the Pitot-Static Tube, NASA TN D-670, February 1961.